

**APPLYING CYCLE-SCALED MAGNETOSTRATIGRAPHY FOR
GLOBAL CORRELATION OF SELECTED MAJOR PALEOCLIMATIC
EVENTS IN THE TRIASSIC, CRETACEOUS AND QUATERNARY**

by

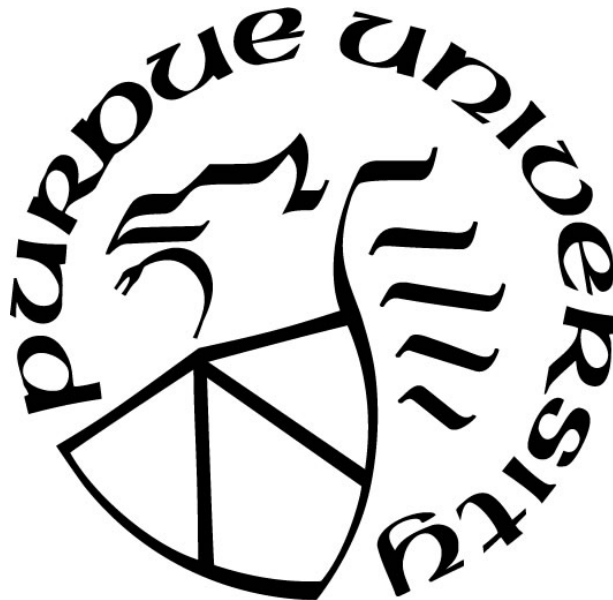
Yang Zhang

A Dissertation

Submitted to the Faculty of Purdue University

In Partial Fulfillment of the Requirements for the degree of

Doctor of Philosophy



Department of Earth, Atmospheric, and Planetary Sciences

West Lafayette, Indiana

December 2019

**THE PURDUE UNIVERSITY GRADUATE SCHOOL
STATEMENT OF COMMITTEE APPROVAL**

Dr. James G. Ogg, Co-Chair

Department of Earth, Atmospheric, and Planetary Sciences

Dr. Darryl Granger, Co-Chair

Department of Earth, Atmospheric, and Planetary Sciences

Dr. Matthew Huber

Department of Earth, Atmospheric, and Planetary Sciences

Dr. Kenneth D. Ridgway

Department of Earth, Atmospheric, and Planetary Sciences

Dr. Nathaniel A. Lifton

Department of Earth, Atmospheric, and Planetary Sciences

Dr. Chunju Huang

School of Earth Sciences, China University of Geosciences, Wuhan, China

Approved by:

Dr. Daniel J. Cziczo

*I dedicate this dissertation to my Mother,
whose family name was used for my given name.*

Dear Mom,

*As a very ordinary mom, you have successfully made me long for extraordinary.
Your caring and worrying always remind me that I am not alone when life is not easy.
Your diligence, perseverance and hard working have been coined into my personality and have
taught me that one earns his/her own life.
Your tolerance and good temper let me be a loving person.
Your not being interfering makes me grow up into an independent woman.
And your sentimentality and fragility as getting elder let me to realize that I should behave like a
real grown-up and cherish every moment that we could spend together.*

*Thank you! Mother.
For bringing me to the world,
And for your being open-minded and supportive to my life-changing decisions.*

*Sincerely from your daughter,
-- Yang Zhang*

ACKNOWLEDGMENTS

I thank all my advisory committee members:

Dr. James G. Ogg, my major research advisor, for him being my Bó Lè, and for his constructive advice and confidence throughout my PhD program;

Dr. Matthew Huber, for him providing valuable insights and comments whenever requested for my manuscript writing and career development.

Dr. Darryl Granger, my official advisor, for him being kind to “take me over” after Dr. Ogg’s semi-retirement, and for his help in my academic career.

Dr. Kenneth D. Ridgway, for him being strict with my academic performance at EAPS and “pushing” me to broaden my geological background.

Dr. Nathaniel A. Lifton, for him agreeing to serve on my committee and encouraging me to learn more geochronology, and also his warm smiles when meeting in the hallway.

I thank my dear family members, friends and colleagues:

Firstly, my Mom and Dad, for them not expecting me to make miracles or change the world, but to do good in what I chose/have chosen; my two big brothers, for taking care of our parents when I cannot be physically with them, and for always treating me like a little sister, in need of caring and love; my “two-month” husband, Ting Hao, for being my “loyal” and tolerant boyfriend for the past 8 years, 7 out of which are distant relationship; this being said, my parents-in-law and siblings-in-law are sincerely thanked for their belief and confidence in me. Dr. Gabi Ogg (and their two great sons), thank you for treating me like a daughter (a sister) – I like your quote of “parents by birth, parents by law, and parents by choice”.

My only several life-time friends in China, for them always being there when I need a talk, and their honest though harsh remarks when I face choices. Two of you are giving birth soon – you have a baby, I have a dissertation. (“Good friends are like stars. You don't always see them, but you know they're always there.” – Quote from Christy Evans). My friends made while studying abroad, who are often graduate students, for sharing experiences (good and bad) pursuing this degree. No PhD is a piece of cake; yes, I know that. Specially to my landlord and roommate, Ms. Teri Egly, for taking me in and let Baby and Marshi be my kitties, too. And finally, my colleagues, for your great contributions to my research projects.

TABLE OF CONTENTS

LIST OF TABLES.....	8
LIST OF FIGURES	9
ABSTRACT.....	17
CHAPTER 1. INTRODUCTION	19
1.1 Geologic time scale.....	19
1.2 Methods used to build a geologic time scale	20
1.3 Cyclostratigraphy and Astrochronology	21
1.4 Magnetostratigraphy and Geomagnetic Time Scale.....	23
1.5 Geologic time intervals and geologic events of interest	25
1.5.1 Carnian Pluvial Episode (Late Triassic).....	25
1.5.2 Cretaceous Oceanic Anoxic Events (e.g., OAE 1a)	28
1.5.3 Mid-Pleistocene Transition.....	29
1.6 References.....	32
CHAPTER 2. LATE TRIASSIC MAGNETOSTRATIGRAPHY FROM THE GERMANIC BASIN AND THE GLOBAL CORRELATION OF THE CARNIAN PLUVIAL EPISODE	41
2.1 Introduction.....	42
2.2 Geologic Setting and Chronostratigraphic Control on the Keuper Group.....	45
2.3 Materials and Methods.....	49
2.3.1 Paleomagnetic sampling	49
2.3.2 Paleomagnetic analyses of Germanic Basin samples	50
2.4 Results.....	54
2.4.1 Demagnetization behaviors	54
2.4.2 Mean characteristic directions	54
2.4.3 Magnetostratigraphy and inter-well correlation	56
2.5 Discussion.....	58
2.5.1 Composite magnetostratigraphy of the Germanic Basin.....	58
2.5.2 Correlation of the Germanic Basin magnetostratigraphy to the reference magnetic polarity scale.....	60
2.5.3 Correlation with Italian magnetostratigraphy sections	66

2.5.4	Correlation with Qingyangou section, South China	67
2.5.5	The Carnian polarity time scale and implied chronostratigraphy of the Germanic Basin formations.....	68
2.6	Conclusions.....	72
2.7	References.....	73
	Appendix A Additional stratigraphic and paleomagnetic information.....	81
CHAPTER 3. MAGNETOSTRATIGRAPHY OF U/PB-DATED BOREHOLES IN SVALBARD, NORWAY, IMPLIES THAT THE BARREMIAN–APTIAN BOUNDARY (BEGINNING OF CHRON M0R) IS 121.2 ±0.4 MA		
		104
3.1	Introduction.....	104
3.2	Materials and methods	106
3.3	Results and discussion	108
3.4	Implications and conclusions.....	110
3.5	References cited.....	113
	Appendix B GSA data repository	116
CHAPTER 4. PLIOCENE-PLEISTOCENE MAGNETO-CYCLOSTRATIGRAPHY OF IODP SITE U1499 AND IMPLICATIONS FOR CLIMATE-DRIVEN SEDIMENTATION IN THE NORTHERN SOUTH CHINA SEA		
		138
4.1	Introduction.....	139
4.2	Materials and methods	141
4.2.1	Lithology, paleomagnetic sampling and NGR logging.....	141
4.2.2	Methods	142
4.3	Results.....	145
4.3.1	Rock magnetic properties	145
4.3.2	Paleomagnetic results (Post-expedition).....	146
4.3.3	Astrochronology and the time-calibrated magnetostratigraphy	149
4.4	Discussion.....	155
4.4.1	Accuracy of the astronomically-tuned magnetostratigraphy.....	155
4.4.2	Regional sedimentation responses to the East Asia climate evolution during the Pliocene-Pleistocene	157
4.4.3	Pliocene and Early Pleistocene.....	158

4.4.4	Mid-Pleistocene Transition.....	162
4.4.5	Mid-Brunhes Event and Middle Pleistocene Glacial Cycles.....	163
4.4.6	Synchronicity of northern SCS and southern SCS sedimentation history	164
4.5	Conclusions.....	165
4.6	References.....	167
	Appendix C Additional rock magnetic studies and data.....	178
CHAPTER 5. SUMMARY.....		189
VITA.....		191

LIST OF TABLES

Table 2.1. Carnian paleomagnetic mean directions and virtual geomagnetic poles for the three boreholes (Fig. 5, this study) and results from outcrops by Hahn (1984). The statistics of samples from each borehole that yielded good-quality (N/NP and R/RP), poor (NPP/RPP) and very poor (N?/R?/INT) ratings are indicated. Hahn (1984) had interpreted that the deposition of Stuttgart Formation was diachronous as a delta advanced from North (outcrops dominated by N polarity recorded in Weserbergland) to Southwest Germany (outcrops dominated by R polarity in Swabia); but our results suggest that this may have been an artifact of the available exposures in each region. 56

Table 4.1. Correlation of the magnetostratigraphy of IODP Hole U1499A (0-333 mbsf) to the Plio-Pleistocene geomagnetic polarity time scale (from GTS2016; Ogg et al., 2016). The uncertainties in depth for the placement of magnetozone boundaries are given (e.g. ± 1.2 (m)). The two right columns are the apparent offsets in the age and in the time-span between the reference magnetochron ages from GTS2016 and astronomical-tuned age model for the magnetozones in this study. Offsets to a younger age or to shorter durations are indicated by red-colored negative numbers. 154

LIST OF FIGURES

- Figure 1.1. The construction of a geologic time scale, adopted from GTS2012 (Gradstein et al., 2012). It is a result of merging a chronometric scale (measured in years) and a chronostratigraphic scale (standardized global stratigraphic units, an agreed convention, such as “Triassic”, “X ammonite zone”, “polarity Chron C25r”)..... 20
- Figure 1.2. The astrochronology (astronomical time scale, ATS) coverage in GTS2012 (Gradstein et al., 2012). (Modified from Chapter 3 (Hinnov and Hilgen, 2012a) in GTS2012).. 21
- Figure 1.3. The La2004 model from 235 to 240 Ma (Laskar, 2004) showing predicted astronomical-cycle frequencies (E = long eccentricity, e = short eccentricity, O = obliquity, P = precession) for early Carnian age. 22
- Figure 1.4. (Left) Earth's magnetic field showing the present-day magnetic North Pole and Earth's rotational axis that are not overlapped. (Right) A sketch showing the nomenclature of magnetic polarity chrons. Newark Basin locates at the north hemisphere and thus when an interval shows a declination toward North (South) while inclination pointing down (up), which is same as (opposite to) present-day magnetic field, we call it Normal (Reversed). See text for detailed explanation. 24
- Figure 1.5. Studied areas where the anomalous facies changes correspond to the mid-Carnian Event. Modified from Nakada et al. (2014) and Chris Scotese of the localities (circles in yellow) on a Late Triassic paleogeography. 1: pelagic environment during Carnian based on chert samples collected from the Ladinian–Carnian strata in the Tamba–Mino–Ashio Belt, Japan.(Nakada et al., 2014); 2: Wrangellia Large Igneous Province (Greene et al., 2010). 3: Chinle Group of Southwestern USA (Lucas et al., 1997); 4: North Curry Sandstone Member and Arden Sandstone Member (Simms and Ruffell, 1989, 1990); 5: Schilfsandstein (Stuttgart) Formation of Germanic Basin (Kozur and Bachmann, 2010); 6: Reingraben Turnover event in Austrian Hallstatt facies (Hornung and Brandner, 2005; Roghi et al., 2010); 7: Heiligkreuz Formation into Carnian platforms of Italian Dolomites (Preto and Hinnov, 2003); 8: Prograding Carnian deltas Barents sea (Hochuli and Vigran, 2010); 9: Sheina and Tikhaya Reka Formations in Kotel'nyi Island off Siberia (Bragin et al., 2012); 10: Yangtze platform, South China (Enos et al., 2006; Lehrmann et al., 2005). Modified from Ogg (2015)..... 26
- Figure 1.6. The proposed Mid-Pleistocene Transition (MPT) in a global view (modified based on Figures 1&2 in Head et al., 2008). *A.* The geomagnetic polarity time scale (Ogg et al., 2016; generated using TSCreator); the boundary of Brunhes/Matuyama (0.77 Ma) is marked. Abbreviated magnetochrons: JAR = Jaramillo Subchron, C = Cobb Mountain Event. *B.* The compiled benthic foraminiferal $\delta^{18}\text{O}$ records (LR04 stack; Lisiecki and Raymo, 2005) for the last 1.5 myr with MIS 1-49 labeled. The estimated MPT interval is denoted in semi-opaque blue. *C.* The interpreted main transitions by the wavelet spectrum of LR04 stack by Head et al. (2008). *D.* Contemporary geologic events shown for reference. The global ice expansion interval (Clark et al., 2006), stepwise uplifting stages of the Tibetan Plateau (green triangles with possible uncertainties in dashed line) by stratigraphic and paleomagnetic evidences (e.g. Li et al. (1997); Liu et al. (2010)) and the major intensification of East Asia Winter Monsoon supported by a Chinese loess records (Heslop et al., 2002)..... 30

Figure 1.7. Current Ocean drilling sites in the South China Sea (SCS) including ODP Leg 184 (1999), IODP 349 (2014), and IODP 367&368 (2017) (see legend in lower left corner for symbols of sites-leg) (modified from Sun et al. (2016)). The geographic location of SCS is also shown as an inset in the upper right corner with the monsoon system simplified in arrows. WJ = Westerly Jet (modified from Han et al. (2012)), EAWM = East Asia Winter Monsoon, EASM = East Asia Summer Monsoon, ISM = Indian Summer Monsoon. 31

Figure 2.1. An example of previous Carnian stratigraphic scales from the GTS2012/2016 syntheses (Gradstein et al, 2012, using their "long Norian" option; Ogg et al., 2016). The early Carnian portion of the geomagnetic polarity column incorporates magnetostratigraphy scaled by astronomical cycles (Zhang et al., 2015) for magnetozones UT1 through UT4 of Hounslow and Muttoni (2010). The late Carnian to early Norian polarity patterns compares the magnetozones ages projected for the Newark Series (Kent and Olsen, 1999; Kent et al., 2017; although E1-E6 lack direct astronomical cycle calibration) to the "reference" synthesis of UT10-UT13 by Hounslow and Muttoni (2010) that had biostratigraphic age constraints. The grey-hatched interval above UT4 indicates the lack of magnetostratigraphic data in the Hounslow and Muttoni (2010) and GTS2016 compilations. Note that the base of the Norian had been placed erroneously at the base of E7n in that scale, but the current proposed marker of the lowest occurrence of conodont *Metapolygnathus parvus* (Mazza et al., 2018) occurs in latest E7n. The onset of the Carnian Pluvial Episode in the latest Julian is at the beginning of the sandy Stuttgart Formation (also called the Schilfsandstein). The salt ablation/residual bed in uppermost Weser Formation is according to the Morsleben borehole (e.g., Barnasch, 2010). Mb = Member. The Cordevolian substage of lowest Carnian is generally merged with the Julian substage into a single Julian substage by most Triassic stratigraphers. The diagram was generated using the databases in TSCreator v.7.4 (<https://timescalecreator.org>)..... 44

Figure 2.2. Paleogeography map of the Germanic Basin (Central European Basin) based on the Geological Atlas of Europe (Ziegler, 1990) and re-drawn from Franz et al. (2014). Red dots show the locations of the studied boreholes at Morsleben (Dp Morsleben 52A/95), Neubrandenburg (Gt Neubrandenburg 2/85) and Tarnow (Kb Tarnow 1/65). The hatched area is the extent of the brackish-marine Neubrandenburg Member of the Stuttgart Formation, and light grey is the correlative fluvial clastics. The massifs and highlands are in darker grey, and EAS is the central Eichsfeld–Altmark Swell. The Tethys ocean to the southeast of the basin is denoted in white..... 46

Figure 2.3. The Stuttgart Formation (Schilfsandstein) is highlighted in light blue within a general time frame provided by brief marine transgressions in the left panel (redrawn from Franz et al. (2014)). Vertical lines in green mark the approximate span of the three studied wells with abbreviated names: M.= Morsleben, N.= Neubrandenburg, and T.= Tarnow. The other three panels are the lithostratigraphy of these three studied wells. Gamma-ray logs of the Neubrandenburg and Tarnow boreholes are from LUNG M-V (under the copyright of Leibniz Institute for Applied Geophysics), and of the Morsleben borehole is digitized from Barnasch (2010) with artificial relative intensity scale of 1 to 8. Vertical red lines with numbers are possible correlation among the three wells as guided by lithology. Details on Stuttgart Formation lithologic subdivisions are given the Supplementary Material. Abbreviations: Chronostrat.= chronostratigraphy; Mb.= member; Neu. Mb= Neubrandenburg Member; Lower S.= Lower Schilfsandstein Member; G. Mb = Gaildorf Member; Upper S. = Upper Schilfsandstein Member;

B Mb= Beaumont Member; N= north; S= south; TST= transgressive system tract; RS = regressive system tract. 49

Figure 2.4. Typical examples of polarity ratings (N/R, NP/RP, and NPP/RPP) of samples from Morsleben. In each diagram, the lower-left subplot is the equal-area projection (solid/open squares are downward/upward vectors, respectively), the upper-left subplot is the magnetization intensity during progressive thermal (or AF) demagnetization steps, and the right subplot is the orthogonal projections of the vectors (Zijderveld, 1967) (solid squares are the projection onto the horizontal plane or declination, while open squares are projection onto a vertical plane or inclination). Steps used for ChRM are highlighted in red. The Principal Component Analysis (PCA) (Kirschvink, 1980) vectors are denoted in blue for N(P)/R(P) rated samples. The original declinations have been re-oriented based on the removed overprints at early demagnetization steps (see Methods section for details). Sample M346.2 – Polarity rating of “N” with ChRM direction assigned to the 550-575-600-625°C cluster. Sample M330.1 (330.1 m; pale reddish brown claystone; middle Weser Formation) – “NP” with ChRM computed from cluster of 4 steps between 575° and 640°C, with the P-quality rating because the ChRM inclination is anomalously shallow compared to the expected Carnian paleolatitude (Stampfli and Kozur, 2006). Sample M272.9 – “NPP” with ChRM calculated from the 4 steps, for which NPP is assigned due to being far (15°) from the expected Carnian normal-polarity declination; therefore, this sample was not used in computing the Carnian mean direction, although its normal-polarity is quite apparent. Sample M389.5 – “R” with ChRM calculated from a cluster of 5 steps during 480° to 575°C. For this sample, an interpreted storage overprint is removed at AF 5 mT and 150°C, followed by removal of a Brunhes north at 250°C; then a progressive great-circle movement toward the southwest with an upward inclination. Sample M384.4 – “RP” with ChRM computed from the cluster of 4 steps. Rated as RP due the counterclockwise rotation toward a Carnian-age reversed-polarity direction after removal of a downward drilling-induced overprint, but its ChRM declination was still significantly clockwise rotated from that expected Carnian reversed-polarity direction; therefore, it was not given full-weight in computing the mean paleomagnetic pole. Sample M401.2 – “RPP” with ChRM computed from 585°-655°C. The low-quality PP-rating was assigned due to having a trend toward an expected reversed-polarity direction, but not reaching an end point consistent with other re-oriented samples. 52

Figure 2.5. Equal-area projection of the characteristic directions (ChRM) for all re-oriented samples rated as N-NP- and R-RP-that were used for computation of mean directions (red star) and approximate 95% confidence (α_{95} , red circle) for each polarity cluster of the three boreholes (Table 1). Green triangle is the present-day geomagnetic field direction of modern Berlin (52.5°N, 13.4°E): 3.5° declination and 67.9° inclination computed from <https://www.ngdc.noaa.gov/geomag-web/#igrfwmm>. Cyan squares are the outcrop-derived mean paleomagnetic directions by Hahn (1984). 55

Figure 2.6. Magnetostratigraphy with polarity quality-ratings (open circles superimposed on the black-white polarity column) and lithology of the Morsleben borehole. Half-width bars indicate a single sample with an interpreted polarity opposite to the polarity of adjacent samples. Declinations, inclinations, maximum angle deviation (MAD, in degrees) and intensity (mA/m) are given for the ChRMs calculated by Principle Component Analysis (PCA) (Kirschvink, 1980). All MADs are less than 15°, thereby indicating a relatively good quality for these PCA directions. Declinations are after re-orientation to the early-removed overprint that was interpreted as the

Brunhes North component. Gd.= Gaildorf Member; U.= Upper; M.= Middle; L.= Lower. See Figure 3 for the lithology legend. 57

Figure 2.7. Inter-well correlation based on litho-magnetostratigraphy of the three boreholes in northern Germany (panel B) and the corresponding composite magnetostratigraphy for the generalized lithological units of Morsleben, northern Germany (panel A). The Lehrberg Horizon denotes the lower/middle Weser Formation by dolomitic-claystone variations (Barnasch, 2010). Note that the vertical scaling is enlarged for the Neubrandenburg and Tarnow boreholes. The Stuttgart Formation is highlighted in light blue with solid blue lines marking the formation base/top. In the composite polarity column, 7 main magnetic zones are denoted from LK0-MK6 (LK = Lower Keuper; MK = Middle Keuper) with the boreholes noted that were the sources for the relative widths of the polarity patterns. Red dashed lines indicate the interpreted correlation of the generalized polarity magnetozones of three boreholes; for example, the Morsleben normal-polarity magnetozones M5n in the upper Stuttgart Formation correlates to Neubrandenburg N4n and possibly to Tarnow T4n. 59

Figure 2.8. Proposed correlations of the main magnetostratigraphy features as guided by biostratigraphy and lithology of the Germanic Basin composite (B) of this study to other biostratigraphically-constrained magnetostratigraphy sections. Note that the originally defined MK5 in Fig. 7 is divided into six subchrons from lower to upper: MK5n.1n, MK5n.1r, MK5n.2n, MK5n.2r, MK5r.1r, MK5r.1n, and MK5r.2r. Circled numbers along with red lines (solid/dashed) denote the proposed correlations, with the solid lines of more confidence. (A) The reference polarity pattern used in GTS2016 (Ogg et al., 2016), which adopted the most recent synthesis in Maron et al. (2019). The Carnian/Norian (C/N) boundary is placed at the top of E7r according to Kent et al. (2017) and Maron et al. (2019) (translucent yellow box). (C) Upper Carnian sections including Lower Trench section at Silická Brezová (= SB) (Channell et al., 2003) and Pizzo Mondello (= PM), Sicily (Muttoni et al., 2004). The proposed C/N boundary GSSP is defined as the first occurrence of conodont *M. pavus* in the uppermost PM4n by Mazza et al. (2018) (narrow yellow bar). (D) Latest Ladinian to lower Carnian magnetostratigraphy in Prati di Stuores section (Italy) (= S) (Loriga et al., 1999) and upper Mayerling section (Austria) (= MA) (Gallet et al., 1998). The GSSP of base Carnian is marked at Lower Trench section. 62

Figure 2.9. (A) Age model for the Carnian Stage with the magnetic polarity scale developed in this study, selected biostratigraphic zones, published radiometric dates and the projected first occurrences of dinosaur footprints and nannoplankton. The nomenclature for the main magnetochrons in indicate the main reference compilations: MA from Mayerling in Austria (Maron et al., 2018), WY from Wayao in South China (Zhang et al., 2015), MK4 and MK5 from the composite Germanic Basin magnetostratigraphy (Fig. 8), PM3r from Pizzo Modello in Italy (Muttoni et al., 2004), and E7-E9 from the Newark series (Kent et al., 2017). Tethyan conodont zonations are rescaled from Rigo et al. (2018) with the Carnian-Norian boundary correlations from Mazza et al. (2018) and with nomenclature of genera as recommended by Michael Orchard (pers. commun., Nov 2019). Spinicaudata (formerly called conchostracans) zones are from Geyer and Kelber (2018) using correlations to Germanic basin stratigraphy from Franz et al. (2018). Radiometric dates are from Furin et al. (2006), Ezcurra et al. (2017) and Mietto et al. (2012). (B) Rescaled composite lithostratigraphy of the northern Germanic Basin, and of magnetostratigraphy reference sections from South China, from a portion of the Pignola-2 section in the Lagonegro Basin and from the Dibona section in the Italian Dolomites (Maron et al., 2017). The scaling for the HWQ section of South China is based on the biostratigraphy and

carbon isotope interpretation of Jin et al. (2018a, b) as detailed in Section 5.3. The “B, C & D” labels in the Dibona section are siliciclastic pulses (Roghi et al., 2010) and the red line marks the Julian/Tuvalian (J/T) boundary based on conodonts (Maron et al., 2017). (C) Composite of negative carbon isotope excursions from NW Tethys (Dal Corso et al., 2018b) and from the Longchang section in South China (Sun et al., 2016, 2019) rescaled to this age model. 70

Figure 3.1. Radiometric dates used in Geologic Time Scale 2012 (GTS2012; Gradstein et al., 2012) (left panel) compared to selected radiometric dates published since 2012 that imply a systematic offset to younger ages (right panel). Dates are positioned according to their constraints from biostratigraphy or magnetic polarity. Two dates from MIT Guyot ([2], in green) were re-positioned in the right column to align with a reinterpreted correlation to polarity chrons. [1] Germany, Selby et al., 2009; [2] MIT Guyot, Pacific; [3] Great Valley, California; [4] and [5] Ontong Java Plateau, Pacific; [6] Argentina; [7] Shatsky Rise, Pacific; [8] Reversed-polarity basalt in North China; [9] Svalbard (in red), Midtkandal et al., 2016; and [10 through 13] Argentina. All $40\text{Ar}/39\text{Ar}$ dates are calibrated to a Fish Canyon Tuff monitor standard of 28.20 Ma (Kuiper et al., 2008). [Full references are given in GSA Data Repository Table DR1.] 105

Figure 3.2. Magnetostratigraphy across the U/Pb-dated horizons in Svalbard borehole DH1 (B), and correlation (blue lines) to (A) the GTS2012/2016 magnetic polarity scale (Ogg et al., 2016) in which the base Aptian was 126.3 Ma. Biostratigraphic constraints on DH1 core are palynomorphs of Barremian (M. t. = *Muderongia tetracantha*, S. g. = *Sirmiodinium grossii*) and Hauterivian (M. a. = *Muderongia australis*) and a dinoflagellate cyst of Aptian (V. l. = *Vesperopsis longicornis*). Carbon isotope curve from DH1 (Midtkandal et al., 2016) is compared to (C) the Cismon core of Italy that has carbon isotope trends, OAE1a (gray shaded interval) and magnetostratigraphy. The level of the U/Pb date (in red) in the DH1 core is projected from the two nearby volcanic ash-bearing cores (DH3 and DH7). (D) Locations of the DH cores (modified from Midtkandal et al., 2016). 108

Figure 3.3. The astronomically tuned grayscale data with the 405-kyr cycles (Gauss filter; passband: 0.00245 ± 0.00052), and with multitaper and evolutionary spectral analysis with significant frequencies/cycles marked. Bases of planktonic foraminifer zones (and P. columnata nannofossil) are from Larson et al. (1993) for this Piobbico core. The top E31 is the same long-eccentricity number as Huang et al. (2010), but underlying E's are different. The three shaded intervals were not directly tuned due to ambiguous/distorted signals (see GSA Data Repository). 110

Figure 3.4. New Aptian time scale based on the cyclostratigraphy of the Piobbico core (Fig. 3) with ages of selected zones of Sub-Mediterranean ammonites (modified from Reboulet et al., 2014), planktonic foraminifers (Huber and Petrizzo, 2014; and pers. commun.), calcareous nannoplankton, major sea-level sequences (Haq, 2014) and generalized trends of $\delta^{13}\text{C}$ with widespread organic-rich shale events (compiled from Föllmi et al., 2006; Kennedy et al., 2014; and other sources). 111

Figure 4.1. Location of Site U1499 (star in yellow) in the South China Sea (SCS) (modified from Liu et al., 2016). Sites 1148, 1146 and 1143 of ODP Leg 184 are marked by pinkish squares. Major river systems discharging into the SCS are shown. The cyan and the red arrows indicate the dominant directions of the East Asian Winter Monsoon (EAWM) and of the East Asian Summer Monsoon (EASM), respectively. 141

Figure 4.2. Rock magnetic properties of 4 samples from U1499A: Sample 26.8 (Core 26X, core catcher), Sample 28.2 (Core 28X, Section 2), Sample 31.1 (Core 31X, Section 1), and Sample 34.6 (Core 34X, Section 6). R is the ratio of saturation remanence, demagnetized to the remanent coercive force value, to undemagnetized saturation remanence. Values equal to and above 0.5 are characteristic of non-interacting single domain (SD) grains (Dunlop, 1972; Wohlfarth, 1958). H_{cr} is intersection of acquisition and AF demagnetization of IRM that approximates the remanent coercive force field, at which the magnetization re-aligned by the reversed field should equal the magnetization unaffected by the reversed field. NRM: Natural remanent magnetization; IRM: isothermal remanent magnetization; ARM: anhysteretic remanence magnetization. 145

Figure 4.3. Merger of shore-based and shipboard paleomagnetic results. (A) Composite magnetostratigraphy of Hole U1499A (0-333 m) combining both shipboard and post-cruise results (detailed correlation is shown in Fig s6 in the Supplement 2). Divisions of magnetochrons/subchrons are named from S4 to S1 using a nomenclature style similar to that recommended by Kent et al. (1995). (B) Shore-based post-cruise magnetostratigraphy of the ChRM directions against lithostratigraphic units and cored intervals. Magstrat = magnetostratigraphy. MAD = maximum angular deviation. The dashed red line in the Inclination column indicates the present-day magnetic inclination at this location. “S” of the magnetozones S4r to S1n is for South China Sea. (C & D) Representative examples of demagnetization behaviors (intensity and magnetic vectors) of samples interpreted as high-quality-rated normal- and reversed-polarity. In the orthogonal projection of the magnetic vectors (Zijderveld, 1967), the open/solid squares are the projections of the vectors on the vertical/horizontal planes. The blue line indicates the ChRM direction computed in the PuffinPlot program based on the subset of steps shown in red. PCA = Principal component analysis. Dec = declination. Inc = inclination. 148

Figure 4.4. Spectral analysis of the detrended natural gamma radiation (NGR) data (dark green) after removal of the slumped interval of lithologic Unit II. The dashed red line and solid blue line represent the two dominating cycles at ~30-m and 8-m, respectively (Gauss filter, passband: 0.033 ± 0.015 and 0.125 ± 0.04 , respectively). The ‘raw’ NGR data (solid black line; with the fake high/low values deleted) and the 74-m LOWESS trend (dashed line in orange) are shown against the lithology units, core images and core numbers. An interpolation of 0.2 m is applied before the spectral analysis. Evolutionary power spectrum uses a 50-m window. The 2π MTM power spectrum shows that the dominant cycles have wavelengths of 25-43, 5-10, ~2.5 and ~1.5 m. 150

Figure 4.5. COCO analysis of NGR of Hole U1499A (0-333 m). The upper to lower panels are (A) the *Correlation coefficient* ρ with higher- ρ sediment accumulation rates (in cm/kyr) labeled, (B) the *Null hypothesis* (H_0 = no astronomical forcing) results showing that all the high- ρ sediment accumulation rates are less than 0.01 but only the 4.3 and ~10-11.1 cm/kyr range less than 0.001, and (C) the *Number of astronomical terms* (#) identified in the tested sediment accumulation range from 1 to 20 cm/kyr. The step used for the COCO analysis is 0.2 cm/kyr The target series is the La2004 astronomical solution for the late Pliocene (0 to 3 Ma). 151

Figure 4.6. The eCOCO sediment-accumulation rate mapping of NGR of Hole U1499A (0-333 m) after removing slumped interval of Lithologic Unit II. Columns from left to right are the evolutionary correlation coefficient, the evolutionary H_0 significance level, and the evolutionary map of the number of astronomical terms identified in the NGR data series. The sliding window is 50 m using 5-m steps. All periodograms were analyzed with the AR(1) red noise model

removed. The number of Monte Carlo simulations is 2000. The tested sedimentation rates range from 1 to 20 cm/kyr with a step of 0.2 cm/kyr. The tracked sediment accumulation rates shown by the black line in the Correlation coefficient map (leftmost column) were used to generate the age model in this study. The translucent hatched areas point is the non-recovery interval of Core 25X, for which the eCOCO results spanning that window might not be valid. 152

Figure 4.7. Time calibrated magnetostratigraphy of Hole U1499A and its correlation with other geologic events. (A) The chronostratigraphy of the past 4.7 Myr from GTS2016 (Ogg et al., 2016) with magnetochrons and ages of stage boundaries. (B) The time-calibrated composite magnetostratigraphy of U1499. Blue-colored double-headed lines are the correlation of the composite magnetostratigraphy to the GTS2016 geomagnetic polarity time scale. This scale assumes that ~200-300 kyr is missing from magnetozones S2r (the recovery gap of Core 25X) (Table A.1). The shipboard microfossil datums (Sun et al., 2018) have ages according to GTS2016; B = Bottom of range (FAD), and T = Top of range (LAD). The columns on the right are sediment accumulation rates, with the thick blue line of Hole U1499A being the same as the thick black line of its sediment-accumulation rates in Fig. 6 but converted to the time domain. These U1499A sediment accumulation rates are averaged over 50-m windows with the values centered on the corresponding projected age; which is why the curve does not extend to the base and top of the studied interval. Published sediment accumulation rates for other Ocean Drilling sites in the SCS (locations in Fig. 1) are included for comparison: ODP Site 1148 in green based on intervals between benthic oxygen-isotope excursions correlated to major MIS events (modified from Tian et al., 2008; Table A.2), ODP Site 1143 in solid line is from a detailed visual correlation of benthic oxygen-isotope excursions record to the LR04 benthic stack (Lisiecki and Raymo, 2005) (from Ao et al., 2011; Table A.3) and Site 1143 dashed line are average rates within each polarity zone (modified from Wu et al., 2017; Table A.4). The numbered blue arrows and shaded areas highlight the major intervals of lower sediment accumulation rates in Hole U1499A during the Quaternary and their possible equivalents at Site 1143, which separated the sedimentation into four main phases (Phase I to Phase VI discussed in the main text). 156

Figure 4.8. The Mid-Pleistocene Transition (MPT) and Mid-Brunhes Event (MBE) recorded in the NGR series of Hole U1499A (A) Geomagnetic polarity time scale of GTS2016 (Ogg et al., 2016); JAR = Jaramillo Subchron, C = Cobb Mountain Event. (B) Benthic foraminifer $\delta^{18}\text{O}$ records (LR04 stack; Lisiecki and Raymo, 2005) for the past 1.55 Myr with even-numbered marine isotope stages (MIS) corresponding to the cold events. The Early-Middle Pleistocene Transition (from 1.25-0.7 Ma, (Head and Gibbard, 2015)) is shaded in light blue. (C) The shift of dominating periodicity interpreted from the wavelet spectrum of LR04 stack by Head et al. (2008). (D) Evolutive spectra of the astronomically tuned NGR series of Hole U1499A (right), with its 2π MTM power spectrum (left) showing peaks at 405-kyr long-eccentricity 'E', ~100-kyr short-eccentricity 'e', ~40-kyr obliquity 'O' and ~20-kyr precession 'p' frequencies. The evolutionary power spectrum (right) displays the distribution of these orbital cycles. The sliding window applied here is 300 kyr with 4 kyr steps. (E) The astronomical-tuned NGR of the past 1.55 Myr. After compensating for the slump in lithologic Unit II, then the peaks and troughs of the time-calibrated NGR series show a reasonably good consistency with the benthic foraminifer $\delta^{18}\text{O}$ curve. The numbers denote the possible correlations to the MIS cold intervals. (F) Ratio of fine to intermediate grain-sizes in the sediments of ODP Site 1146 (location in Fig. 1) (modified from Figure 7 in Boulay et al., 2007) with the dashed line indicating the long-term trend. Note

that the scale is inverted, so that relatively clay-rich compositions are below the dashed line. (G) Contemporary geologic events in Asia, i.e., the global ice expansion interval (Clark et al., 2006), stepwise uplifting stages of the northeast Tibetan Plateau (green triangles with uncertainties in dashed line) estimated by stratigraphic and paleomagnetic evidences in Yellow River drainage basins (e.g. Li et al., 1997, 2014; Liu et al., 2010) and the major intensification of East Asia Winter Monsoon supported by a Chinese loess records (Heslop et al., 2002). 160

ABSTRACT

As climate change became a major international hot topic, scientists look to the geologic past for potential analogues of global warming and cooling events. However, the underlying triggering mechanisms and rates are enigmatic and difficult to unravel, especially when good reference time scale do not exist.

Reversals of the Earth's magnetic field are recorded by preferential orientation of iron oxide grains during their deposition in all types of sediments. When combined with cyclostratigraphy, magnetostratigraphy has proved to be one of the robust ways to build portions of the geologic time scale and to enable global correlation among various settings. For this PhD research projects, Yang Zhang (Y. Z.) utilized the combination of magnetic polarity scales with astronomical-cycle tuning to resolve long-debating time scaling of time intervals where major climate shifts (e.g., major excursions in Earth's carbon cycle reflected in isotopic anomalies) took place. Other stratigraphical tools such as geochemistry data, radiometric dating, and biostratigraphy help constrain the validity and accuracy of cycle-scaled magnetic polarity scales.

The major achievements that have been accomplished during this PhD program include:

1) Successfully constructed the entire Carnian (Late Triassic) polarity time scale. The Upper Carnian portion implies that: (a) the lowermost Upper Carnian is dominated by reversed-polarity magnetozone; (b) The middle two-thirds of the Upper Carnian is a major normal-polarity-dominated magnetozone; and this interval correlates with the basal portion of the Newark magnetic polarity reference series. This enhanced polarity scale is independently supported by results from South China and western Tethys sections, therefore provide great opportunity to correlate the Carnian Pluvial Episode in various depositional settings, plus calibrate other major geologic episodes, like the earliest dinosaur-bearing beds in South America.

2) Magnetostratigraphy of U/Pb-dated boreholes in Svalbard that placed the base M0r (proposed as the base Aptian) at 121.2 ± 0.4 Ma, which is about 5 myr younger compared to that in GTS2016. This revised scaling put lots of topics, like the cause and effect between the Ontong Java Plateau and the Oceanic Anoxic Event 1a (OAE1a), the faster spreading and the global highstand during the Cretaceous Normal Super-chron, and the seafloor spreading model from the Middle Jurassic to the Early Cretaceous, etc.

3) The first cycle-scaled magnetostratigraphy for Plio-Pleistocene in the north margin of the South China Sea. The cycle-scaled natural gamma ray data since the Middle Pleistocene Transition indicate a trend of more contributions from coarse grains as global temperature cools, especially during the Mid-Brunhes Cooling Event when the first major sand influx happened.

CHAPTER 1. INTRODUCTION

The ultimate goals of this dissertation are 1) to establish high-resolution geologic time scales, during which major paleoclimate/paleoceanography changes occur, so that these geologic events or episodes could be correlated globally, 2) by comparing to contemporaneous disruptive events, such as large igneous province emplacement, asteroid impact, or astronomical nodes, the underlying triggering mechanisms could be investigated, and 3) to contribute to better understand concurrent life evolutions/migrations under unfavorable conditions.

Magnetostratigraphy and cyclostratigraphy are the main tools to reach the goals.

1.1 Geologic time scale

Arther Holmes (1890-1965), credited as “the father of the geologic time scale”, first combined radiogenic isotope ages (linear time, or chronometric scale) with geologic formations (rock record or chronostratigraphic scale) (Fig 1.1) to create the framework for deciphering and understanding Earth’s history. However, as Arther Holmes wrote “To place all the scattered pages of earth history in their proper chronological order is by no means an easy task” (Holmes, 1965, p. 148). Plenty of geologic time scale version are present since 1980s with the book series of A Geologic Time Scale (coined GTS followed by publish years, such as GTS04, GTS12) being mostly widely accepted and used. The construction of a geologic scale is more than just giving a number or proposing a unit (as reviewed in GTS2012 by Gradstein et al., 2012) while uncertainties should be aware of when discussing past geologic events. Numerous efforts from (geo)scientists of various backgrounds and continual improvements in data coverage, methodology and the standardization of chronostratigraphic units stay a permanent job and topic. In addition, correlation among global locations is essential since successions of time derived in one area are too unique to represent earth history elsewhere.

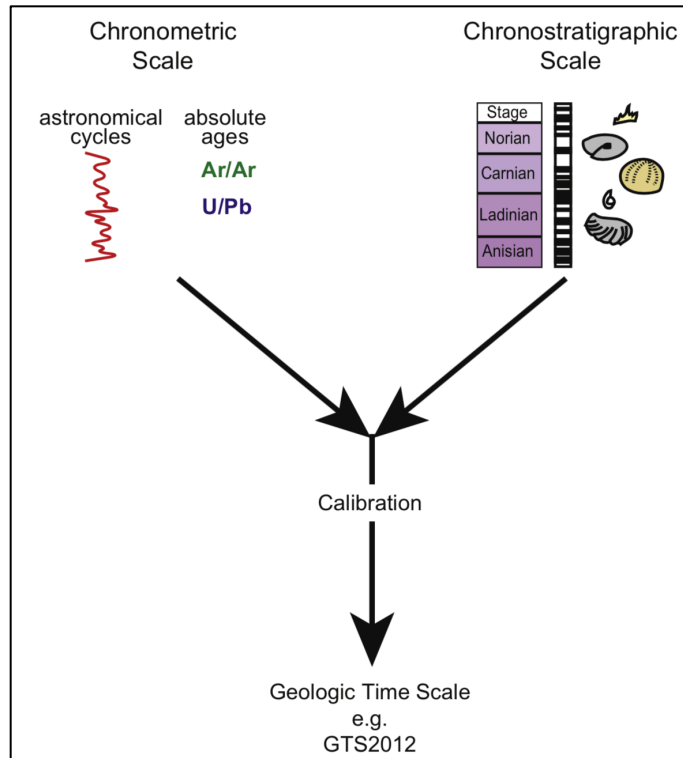


Figure 1.1. The construction of a geologic time scale, adopted from GTS2012 (Gradstein et al., 2012). It is a result of merging a chronometric scale (measured in years) and a chronostratigraphic scale (standardized global stratigraphic units, an agreed convention, such as “Triassic”, “X ammonite zone”, “polarity Chron C25r”)

1.2 Methods used to build a geologic time scale

There are three main types of global events recorded in all types of settings – climate shifts induced by periodic “Milankovitch” changes in Earth’s orbit and tilt, major excursions in Earth’s carbon cycle reflected in isotopic anomalies, and reversals in the Earth’s geomagnetic field. None of these methods provide a unique time-stamp signature, but when combined with general biostratigraphy and a few radiometric dates, then the merger of these global events provides both high-resolution correlation horizons among continents and depositional settings, plus the ability to measure durations using the periodic astronomical “clock”.

In the research, cyclo- and magnetostratigraphy are the two major tools. Till now, the Neogene and Oligocene portion has been calibrated by astronomical cycles to be within an orbital-precession oscillation (~20 kyr). Parts of Paleogene, Cretaceous, Jurassic and Triassic are also scaled using Milankovitch cycle durations, with the 405-kyr eccentricity oscillation being a stable tuner (Gradstein et al., 2012) (Fig. 1.2). The geomagnetic polarity time scale for the Late

Cretaceous to Neogene (termed C-sequence) and Middle Jurassic to Early Cretaceous (termed M-sequence) are established and calibrated through patterns of marine magnetic anomalies to bio- and cyclostratigraphy and in some cases radiometric ages (Ogg, 2012); for the pre-Jurassic, however, the polarity patterns still require additional verification by outcrop-based magnetostratigraphy studies, due to the lack of magnetic anomaly records in oceanic crust.

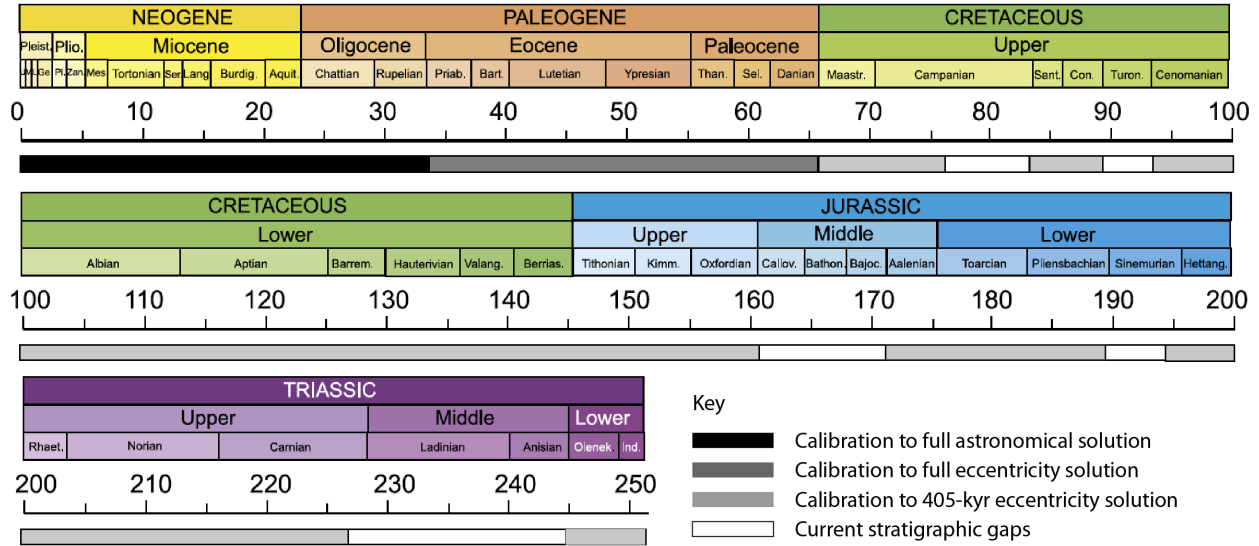


Figure 1.2. The astrochronology (astronomical time scale, ATS) coverage in GTS2012 (Gradstein et al., 2012). (Modified from Chapter 3 (Hinnov and Hilgen, 2012a) in GTS2012).

1.3 Cyclostratigraphy and Astrochronology

It has been documented in detailed sedimentary record in both marine and continental deposits (such as stacking patterns of beds, disconformities, facies changes, fluctuations in biological composition, and/or changes in geochemical composition) that small changes in the Earth's orbit around the sun can result in the variation in Earth's climate through time, as a consequence of the interaction between the Earth, the Sun, and other planets in the solar system (Hays et al., 1976; Hinnov and Hilgen, 2012b; House, 1995; Strasser et al., 2006). The main cycles (Fig. 1.3) in the Milankovitch band of precession, obliquity (or tilt) and eccentricity combine to influence the amount of solar energy (or insolation) reaching the outer atmosphere of the Earth and thus influence the climate.

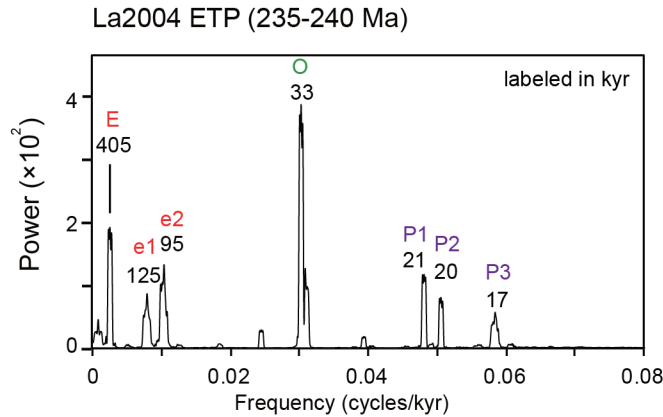


Figure 1.3. The La2004 model from 235 to 240 Ma (Laskar, 2004) showing predicted astronomical-cycle frequencies (E = long eccentricity, e = short eccentricity, O = obliquity, P = precession) for early Carnian age.

Eccentricity reflects the ellipticity of Earth's orbit around the Sun and has varied between 0.002 and 0.067 (~ 0.0167 for present) over the past 10 myr (Hinnov, 2013; Hinnov and Hilgen, 2012b; Laskar, 2004) with major periods of ~ 100 kyr and 405 kyr. It also has a long-period component of 2.4 myr. The 405-kyr-long-eccentricity, related to Jupiter and Venus, remains extremely stable over the full 250 myr period and exists in geologic records (Kent et al., 2018; Laskar, 2004). The obliquity is the angle between Earth's axis of rotation and the perpendicular of the plane of the Earth's orbit. The value ranges from 22° to 24° and the present day tilt (23.5°) is in near the middle of the range and is decreasing (Hinnov, 2013; Laskar, 2004; Laskar et al., 1993). The dominant period is 41 kyr in Cenozoic and shorter in pre-Cenozoic with a 1.25 myr amplitude modulation (Hilgen et al., 2003; Shackleton et al., 1999). The climatic precession reflects the combined effects of Earth's orbital rotation and axial precession with principal periods at 19 kyr and 23 kyr, which was shorter earlier in time because of faster rotation rates. This parameter is the result of the pull of the Moon and Sun on the Earth's equatorial bulge and acts in an opposite role in each hemisphere (180° out of phase) (Berger, 1988; House, 1995; Weedon, 2003). The length of seasons changes due to the precession but the total insolation remains balanced annually (Weedon, 2003).

Changes in eccentricity have a direct effect in modulating the amplitude of precession cycles (Kent, 1999). Therefore, if the couplets in sedimentary rhythmicity could be combined into groups of about five couplets as bundles (an approximate 5:1 ratio), it may indicate orbital control with the periods of ~ 20 kyr precession and ~ 100 -kyr short eccentricity cycles. Indeed,

geologists now are seeking quantitative records in sediments, corals, trees, ice cores and cave calcite and these records are known as time series. Once the relationship between the sedimentary record and the orbital forcing is established, we can use the astronomical cycles of known periodicities to date and thus to integrate into the global chronostratigraphic framework (Hinnov and Ogg, 2007; Palike and Hilgen, 2008; Strasser et al., 2006).

1.4 Magnetostratigraphy and Geomagnetic Time Scale

The Earth's magnetic field can be approximated as a huge dipole magnet including negative and positive poles on opposite sides (Figure 1.4). As is shown, the magnetic poles do not necessarily coincide with Earth's rotational axis. The present-day polarity is conventionally labeled as Normal with geographic-north-toward declination with downward inclination of the magnetic field in North Hemisphere and upward in South Hemisphere. The Reversed polarity is just the opposite. Recognition of the older opposite magnetization directions to the present magnetic field in volcanic rocks are from the early pioneering work of Brunhes (1906) and Matuyama (1929) (e.g. reviewed in Cox et al. (1964) and Hounslow and Muttoni (2010)). Magnetostratigraphy is the discipline that studies the geomagnetic polarity sequence documented in stratified rocks by means of natural magnetic acquisition processes, and then constructs high-resolution geomagnetic polarity timescale to correlate to "standard reference scales", like in the Geologic Time Scale series. It is also utilized to inter-correlate globally among various sections based on the distinctive patterns of normal and reversed sequence and the potentially contemporary record of polarity reversals (Ogg, 2012). The correlation of magnetostratigraphy includes two aspects—correlation of "bar-code" pattern over a stratigraphic interval and correlation of boundaries or transitions of magnetozones (Hounslow and Muttoni, 2010).

The geomagnetic polarity timescale has been astronomically and biostratigraphically calibrated for the majority of the Cenozoic and for portions of the Mesozoic. However, for the Triassic there is not yet an agreed geomagnetic polarity timescale (GPTS) but a composite GPTS based on incomplete marine and non-marine successions from sections in North America, Europe and Asia (Lucas, 2010).

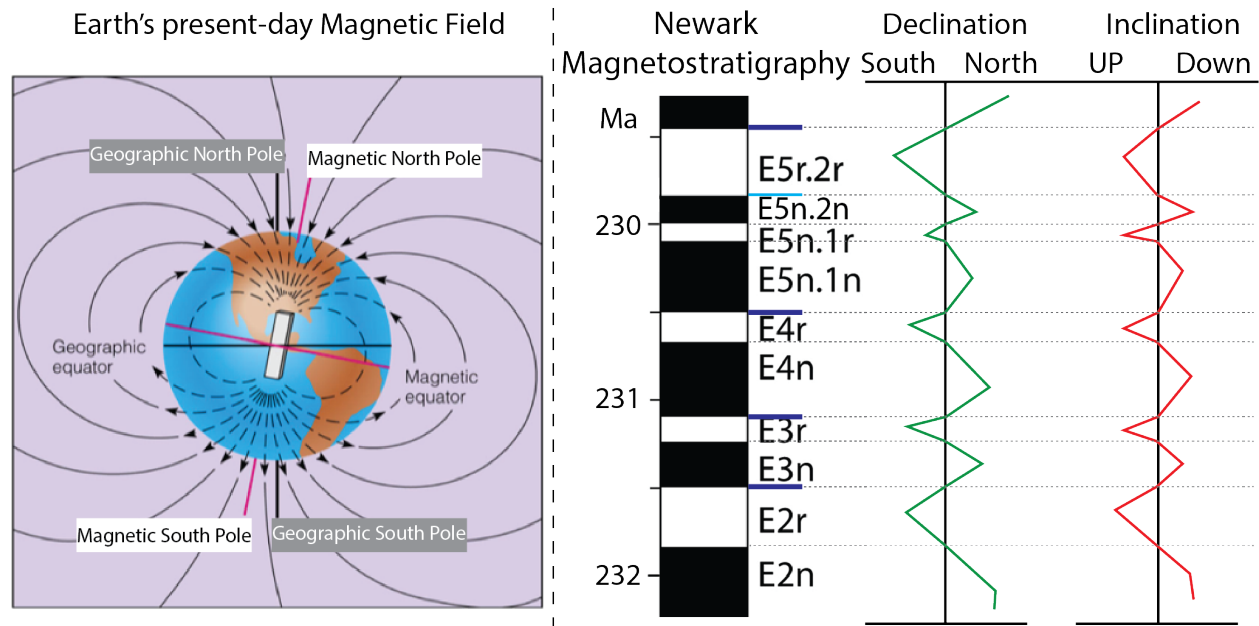


Figure 1.4. (Left) Earth's magnetic field showing the present-day magnetic North Pole and Earth's rotational axis that are not overlapped. (Right) A sketch showing the nomenclature of magnetic polarity chrons. Newark Basin locates at the north hemisphere and thus when an interval shows a declination toward North (South) while inclination pointing down (up), which is same as (opposite to) present-day magnetic field, we call it Normal (Reversed). See text for detailed explanation.

Through Earth's history, the orientation and intensity of Earth's magnetic field did not remain unchanged but have varied at irregular times of which the causes are yet to be determined. The characteristic result of the non-periodic reversals is the "bar code" of alternating normal and reversed polarity chrons with varying durations. The nomenclatures (Figure 1.4) for the polarity magnetozone identification generally adopted among authors are based on Kent et al. (1995): successive pairs of dominant Normal and Reversed patterns are classified with one magnetozone, from base upwards these magnetozones are assigned to integers in ascending numerical order with the prefix i.e. the acronym for the magnetostratigraphy source (usually the outcrop or borehole name) and correspondingly the predominant Normal and Reversed included in this magnetozone with the suffix 'n' (for Normal) and 'r' (for Reversed), respectively. Sometimes for a magnetozone with more than one pair of Normal and Reversed polarity intervals are named submagnetozones and can be labeled in a similar manner. One thing is that a decimal point is used after which subordinal integers are appended ascending upsection. For example, in Kent et al. (2017), the magnetostratigraphy is from Newark, North America and the fifth magnetozone is

therefore with a prefix E (rather than N, in order to distinguish from Normal), i.e. E5 and the Normal polarity interval is E5n while E5r is the Reversed interval. But since there are brief subchrons within E5n, from older to younger, they are named as E5n.1n, .1r, and .2n, ascending upward.

1.5 Geologic time intervals and geologic events of interest

Earth has been in a relatively cooler state (icehouse) for the past 30 myr while in a warmer state (greenhouse) for most of the Phanerozoic Eon. The cooler icehouse is often related to the waxing and waning of glaciation near the polar regions while the warmer greenhouse state, usually featured by much higher temperatures globally and few-to-no ice sheets, is often attributed to large igneous province emplacements. Although not being exact analogues for present and/or future climate, research on the climates of Earth's deep past could provide important insights into how geologic and biological processes operate under warmer and cooler conditions. Even though the PhD research is not directly investigating the past climate events, the work on time scale calibration is essential to better understand the rates of paleoclimate changes (like light carbon injection into the atmosphere) and the underlying causes and effects. Next a brief introduction of the climate events or episodes involved in the interested geologic time intervals would be discussed.

1.5.1 Carnian Pluvial Episode (Late Triassic)

During the middle of the Carnian Age (~230 Ma) of the early Late Triassic, the sedimentary records in different regional basins display dramatic changes. For example, tropical carbonate platforms abruptly ended, and engorged river systems left widespread sand-rich layers across inland basins and coastal regions. Correspondingly, a global disruption of Earth's climate-ocean-biological system was recorded. As is shown in Fig. 1.5, 1, 6, 7, 10 are carbonate platform crises while 3, 4, 5, 8, and 9 are fluvial surges. Generally, the combination of increased atmospheric carbon dioxide and moisture content will increase the rates of continental weathering. Therefore, basins and margins near uplifts with exposed silicate-rich sediments, will receive an enhanced delivery of clastics (e.g. Algeo and Twitchett (2010)); for oceanic and shelf settings, a warmer and more equable climate, coupled with additional carbon release into the Earth system, could lead to deposition of organic-rich "black shales" under expanded oxygen-

minimum zones. In addition, relatively high extinction rates of several groups such as ammonoids, crinoids, bryozoa and conodonts, and a dramatic increase of conifer resin exudation and amber formations (Gianolla et al., 1998) are also reported.

This episode was short-lived (Hornung and Brandner, 2005; Preto and Hinnov, 2003; Rigo et al., 2007) and lasted two or three 405-kyr long eccentricity cycles (Kozur and Bachmann, 2008; Kozur and Bachmann, 2010; Roghi et al., 2010). The recovering world saw the first widespread dinosaurs on land and the emergence of the calcareous nanoplankton in the oceans that now govern Earth's carbon cycle (Dal Corso et al., 2012; Preto et al., 2013). Benton et al. (2014) thought that these earliest dinosaurs were possibly more adaptable to climate shifts from arid to humid and back to arid.

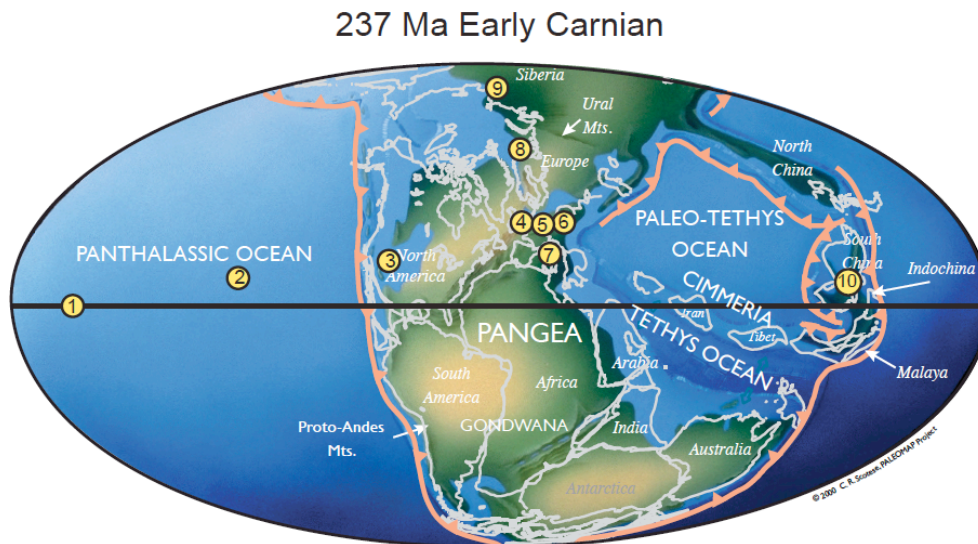


Figure 1.5. Studied areas where the anomalous facies changes correspond to the mid-Carnian Event. Modified from Nakada et al. (2014) and Chris Scotese of the localities (circles in yellow) on a Late Triassic paleogeography. 1: pelagic environment during Carnian based on chert samples collected from the Ladinian–Carnian strata in the Tamba–Mino–Ashio Belt, Japan.(Nakada et al., 2014); 2: Wrangellia Large Igneous Province (Greene et al., 2010). 3: Chinle Group of Southwestern USA (Lucas et al., 1997); 4: North Curry Sandstone Member and Arden Sandstone Member (Simms and Ruffell, 1989, 1990); 5: Schilfsandstein (Stuttgart) Formation of Germanic Basin (Kozur and Bachmann, 2010); 6: Reingraben Turnover event in Austrian Hallstatt facies (Hornung and Brandner, 2005; Roghi et al., 2010); 7: Heiligkreuz Formation into Carnian platforms of Italian Dolomites (Preto and Hinnov, 2003); 8: Prograding Carnian deltas Barents sea (Hochuli and Vigran, 2010); 9: Sheina and Tikhaya Reka Formations in Kotel'nyi Island off Siberia (Bragin et al., 2012); 10: Yangtze platform, South China (Enos et al., 2006; Lehrmann et al., 2005). Modified from Ogg (2015).

What caused Carnian Pluvial Episode?

Despite the current investigations of the mid-Carnian Event, the triggering mechanism is still under discussion and varied among authors. There are mainly three possible explanations.

1. Tectonic activity (Enos et al., 2006; Enos et al., 1998; Hornung and Brandner, 2005; Kozur and Bachmann, 2010; Lehrmann et al., 2005). During the formation of the Neo-Tethys, the Cimmerian microcontinent (located at the northern margin of the Tethys realm) collided with the continental splinters that detached from Eurasia, and the following uplift related to this collision enhanced the monsoonal circulation in the Tethys realm (Stamfli and Kozur, 2006).
2. Eruption of Wrangellia Large Igneous Provinces (LIPs) lasting ~2 myr and covering ~100,000 km³ (Furin et al., 2006; Greene et al., 2009). In Earth history, many LIPs have been bound up with mass extinctions and climate changes due to the massive emission of greenhouse gases and heat (Greene et al., 2010; Wignall, 2001), for example, the Siberian Traps (end-Permian mass extinction) (Renne et al., 1995), Central Atlantic Magmatic Province (CAMP; end-Triassic mass extinction) (Ruhl et al., 2011), Ontong Java Plateau (early Aptian oceanic anoxic event) (Keller et al., 2011), and North Atlantic Igneous Province (Paleocene-Eocene boundary Thermal Maximum, "PETM") (Storey et al., 2007) . The Wrangellia plateau has been highlighted as a mantle plume origin for most of the volcanic series and showed a geochemical similarity to the basalts of the Caribbean and Ontong Java Plateaus (Greene et al., 2010; Greene et al., 2009). Therefore, in analogy with other LIPs, this massive eruption could have caused a global climate and oceanographic perturbation.
3. Mega-monsoonal climates of Pangaea and the Tethys realm (Colombi and Parrish, 2008; Hay et al., 1994). Due to the very large landmass of Pangaea, the Carnian Pluvial Event may record the peak of a mega-monsoon system featured by widespread occurrence of humid conditions.

Actually, it is possible that multiple factors were involved. The increased greenhouse gases resulting from the Wrangellia LIP eruption could lead to a warmer atmosphere with more evaporation and seasonal precipitation at regional scale. Meanwhile, the land-surface heating would draw in oceanic moisture and, in turn increase the magnitude of monsoon-associated summer rainfall and flooding.

1.5.2 Cretaceous Oceanic Anoxic Events (e.g., OAE 1a)

As being one of the warmest periods in Earth's history, the Cretaceous has been known for the recurrence of global Oceanic Anoxic Events (OAEs) (e.g., Jenkyns (2010)). An Oceanic Anoxic Event is a palaeoceanographic phenomenon characterized by the deposition of approximately coeval carbon-rich deposits (black shales) under oxygen-poor conditions on a global scale (Dr. Hugh C. Jenkyns, personal communication, August 2018). Currently available data suggest that OAEs are driven by abrupt rise in global temperature that was probably caused by rapid influx of CO₂ into the atmosphere from volcanism emplacement or methane releases. Changes in redox-sensitive isotope systems support the enhanced contribution of mantle-derived hydrothermal fluids (such as the positive excursion of ϵ Nd and less radiogenic trend of Sr isotopes; e.g., (Jones and Jenkyns, 2001; MacLeod et al., 2008)) as well as brief intensified continental weathering (like a pulse of radiogenic Sr and Os; e.g., (Bodin et al., 2015)) due to accelerated hydrologic cycles under global warming (as reviewed in Jenkyns (2010), although intermittent coldhouse climate were also recorded (e.g., Bodin et al., 2015)).

OAEs that manifestly caused major chemical change in the Cretaceous Ocean include the early Aptian (*Selli* event, or OAE 1a, ~120 Ma), early Albian (*Paquier* event, or OAE 1b, ~111 Ma), and Cenomanian–Turonian (*Bonarelli* event, or OAE 2, ~93 Ma) (as reviewed in Jenkyns (2010)). Estimates according to the biostratigraphically-constrained astrochronology indicate that the durations of OAEs typically fall in the range of a few hundred thousand years (e.g., (Sageman et al., 2006; Voigt et al., 2008)), although longer span is expected for the OAE1a (e.g., (Huang et al., 2010; Li et al., 2008b)). It has been suggested that some (but perhaps not all) of the OAEs were periodic events and coincided with insolation nodes and dampened seasonality (e.g., Mitchell et al. (2008)). Therefore, one could perhaps identify potential OAEs that were not well preserved.

The OAE1a (*Selli Event*) of early Aptian Stage has been favorably associated with the Greater Ontong Java Plateau (OJP) volcanism (e.g., (Erba et al., 2015; Olierook et al., 2019)), which also caused the “nannoconid crisis” that is about 40-100 kyr preceding the OAE1a (Erba, 1994). The OAE1a has been recognized worldwide in various settings, including pelagic (e.g.,(Weissert, 1989)), neritic ((Jenkyns, 1995)), and terrestrial records (e.g., (Ando et al., 2002)), Recently, the High Arctic Large Igneous Province (HALIP) has been reported to play a similarly key role as the OJP emplacement (e.g., Polteau et al. (2016)), causing the organic-rich

deposits in higher latitudes of North Hemisphere evidenced by carbon isotope excursions. However, this cause and effect association is questioned due to the yet-to-be-settled age of the Barremian-Aptian boundary. We thus strive to resolve this debated age boundary by integrating biostratigraphy, magnetostratigraphy, chemostratigraphy and cyclostratigraphy (Chapter III).

1.5.3 Mid-Pleistocene Transition

The Middle Pleistocene Transition (MPT) was first reported by Berger et al. (1993) using deep marine materials recovered by ODP Leg 130 from the Ontong Java Plateau of the South Pacific Ocean. A mis-match of the ‘template’ deep-sea records from the ‘target’ simulated climate cyclicity from the ice cores revealed the climate cyclicity shift centered at ~900,000 years ago. The MPT represents a major episode in Earth history (*ca.* 1.2-0.6 Ma), featured by the change of dominating climatic cyclicity from 41-kyr to an average of 100-kyr rhythms. In addition, climate and environmental changes are recognized in both land and marine settings, plus the evolution and migration of biota, including hominids. The span of this transition has been recently defined as an onset at ~1.2 Ma, a center at the boundary of marine isotope stages (MIS 23/22) at ~0.9 Ma and an end at ~0.6 Ma (Head and Gibbard, 2015).

Although this transition has been recognized in both marine and terrestrial settings from equatorial regions to high latitudes, there is not much data from the western Pacific, especially the marginal seas. The South China Sea, the largest marginal sea along the western Pacific, has thick deposits of Quaternary sediments and thus could provide excellent climatic records of sea-land interaction. Conveniently, the last Earth’s magnetic reversal boundary (Brunhes/Matuyama) has been placed at ~0.77 Ma, close to the MPT ‘center’ (Fig 1.6), which can be used as a correlation age control; and similarly, the subchrons (Jaramillo, Cobb Mountain Event) within the Matuyama reversed-polarity zone provide crucial age constraints on sediments and thus better global correlation of the MPT. Chapter IV attached the published work based on Site U1499 (location in Fig. 1.7).

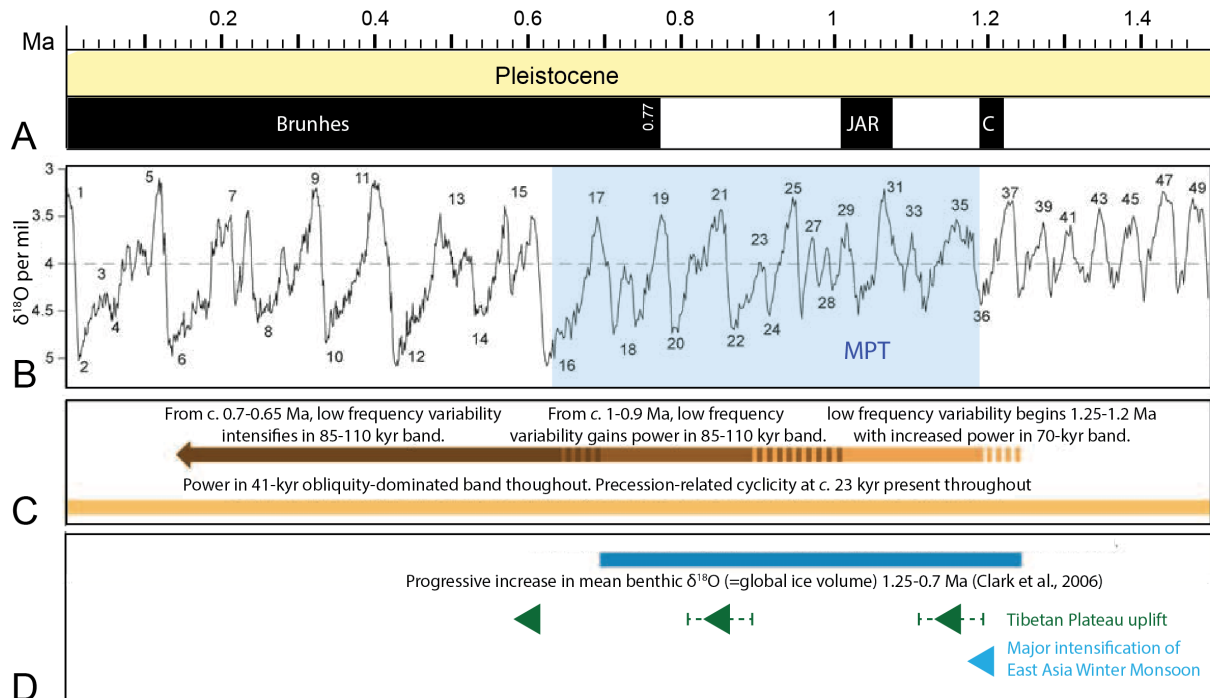


Figure 1.6. The proposed Mid-Pleistocene Transition (MPT) in a global view (modified based on Figures 1&2 in Head et al., 2008). *A.* The geomagnetic polarity time scale (Ogg et al., 2016; generated using TSCreator); the boundary of Brunhes/Matuyama (0.77 Ma) is marked. Abbreviated magnetochrons: JAR = Jaramillo Subchron, C = Cobb Mountain Event. *B.* The compiled benthic foraminiferal $\delta^{18}\text{O}$ records (LR04 stack; Lisiecki and Raymo, 2005) for the last 1.5 myr with MIS 1-49 labeled. The estimated MPT interval is denoted in semi-opaque blue. *C.* The interpreted main transitions by the wavelet spectrum of LR04 stack by Head et al. (2008). *D.* Contemporary geologic events shown for reference. The global ice expansion interval (Clark et al., 2006), stepwise uplifting stages of the Tibetan Plateau (green triangles with possible uncertainties in dashed line) by stratigraphic and paleomagnetic evidences (e.g. Li et al. (1997); Liu et al. (2010)) and the major intensification of East Asia Winter Monsoon supported by a Chinese loess records (Heslop et al., 2002).

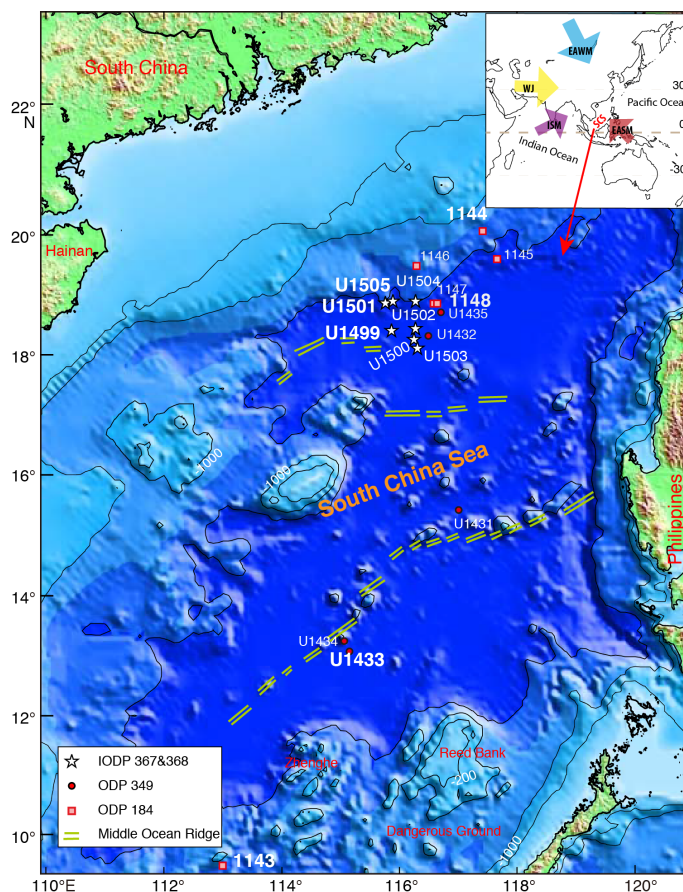


Figure 1.7. Current Ocean drilling sites in the South China Sea (SCS) including ODP Leg 184 (1999), IODP 349 (2014), and IODP 367&368 (2017) (see legend in lower left corner for symbols of sites-leg) (modified from Sun et al. (2016)). The geographic location of SCS is also shown as an inset in the upper right corner with the monsoon system simplified in arrows. WJ = Westerly Jet (modified from Han et al. (2012)), EAWM = East Asia Winter Monsoon, EASM = East Asia Summer Monsoon, ISM = Indian Summer Monsoon.

The “Mysterious” Middle Pleistocene Transition

In terms of the causes, however, no agreement has been reached among several possible candidates, such as tropical forcing processes (e.g. sea surface temperature (SST) change), ice sheet expansion, and global carbon reservoir changes due to enhanced weathering (as summarized in Li et al. (2008a)). Head et al. (2008) applied wavelet analysis on the LR04 stack (Lisiecki and Raymo, 2005) of marine benthic foraminiferal $\delta^{18}\text{O}$ records to reveal that the obliquity and precession-related cyclicality are present throughout the past 1.5 myr, whereas low-frequency components started to gain power from 1.25-1.2 Ma. This timing seems to be at or just

after the onset of increasing global ice volume (Clark et al., 2006), and thus they proposed a major forcing by the glacial development (Fig 1.6).

The dominating forcing factor of this transition may differ depending on location, especially for the reported vegetation changes in both low and high latitudes. For example, Suc and Popescu (2005) reported the extinction of thermophilous (warm-loving) plants in pollen records from northwestern Mediterranean and southern Italy, which indicates a lowering of temperature during Early-Middle Pleistocene transition (at ~1 Ma); whereas in the northern Mediterranean, no major vegetation change has been found. Using tropical Atlantic Ocean records, Schefuß et al. (2003) obtained a record of increasing C4 plant abundance from 1.2-0.45 Ma (ODP Site 1077 and surface samples), and the most significant driving force of this increase is proposed to be an intensified aridity produced by a combination of tropical sea surface temperature change and African monsoon variation.

In Mainland China, the MPT is also recognized in various locations. The most prominent signals are from the Chinese Loess record. For example, Han et al. (2012) proposed a remarkable two-step shift of the 100-kyr cyclicity with onset at ~0.9 Ma and stabilization at ~0.64 Ma, which is consistent with the enhancement of East Asian monsoons; and they suggest the driving force for the MPT was the stepwise rapid uplift of the Tibetan Plateau. This assumption seems to be in accordance of a recent publication (Liu et al., 2017) on the connection of proto-Yangtze River into the East China Sea, which started at around 1.2-1.0 Ma (Jaramillo subchron), as evidenced by the surge of magnetic mineral concentrations by 5-10 times.

1.6 References

- Algeo, T. J., and Twitchett, R. J., 2010, Anomalous Early Triassic sediment fluxes due to elevated weathering rates and their biological consequences: *Geology*, v. 38, no. 11, p. 1023-1026.
- Ando, A., Kakegawa, T., Takashima, R., and Saito, T., 2002, New perspective on Aptian carbon isotope stratigraphy: data from $\delta^{13}\text{C}$ records of terrestrial organic matter: *Geology*, v. 30, no. 3, p. 227-230.
- Benton, M. J., Forth, J., and Langer, M. C., 2014, Models for the Rise of the Dinosaurs: *Current Biology*, v. 24, no. 2, p. R87-R95.

- Berger, A., 1988, Milankovitch Theory and Climate: *REVIEWS OF GEOPHYSICS*, v. 26, no. 4, p. 624-657.
- Berger, W., Bickert, T., Jansen, E., Wefer, G., and Yasuda, M., 1993, The central mystery of the Quaternary ice age: a view from the South Pacific: *Oceanus*, v. 36, no. 4, p. 53-57.
- Bodin, S., Meissner, P., Janssen, N. M. M., Steuber, T., and Mutterlose, J., 2015, Large igneous provinces and organic carbon burial: Controls on global temperature and continental weathering during the Early Cretaceous: *Global and Planetary Change*, v. 133, p. 238-253.
- Bragin, N. Y., Konstantinov, A., and Sobolev, E., 2012, Upper Triassic stratigraphy and paleobiogeography of Kotel'nyi Island (New Siberian Islands): *Stratigraphy and Geological Correlation*, v. 20, no. 6, p. 541-566.
- Clark, P. U., Archer, D., Pollard, D., Blum, J. D., Rial, J. A., Brovkin, V., Mix, A. C., Pisias, N. G., and Roy, M., 2006, The middle Pleistocene transition: characteristics, mechanisms, and implications for long-term changes in atmospheric pCO₂: *Quaternary Science Reviews*, v. 25, no. 23, p. 3150-3184.
- Colombi, C. E., and Parrish, J. T., 2008, bragin: *Palaios*, v. 23, no. 12, p. 778-795.
- Cox, A., Doell, R. R., and Dalrymple, G. B., 1964, Reversals of the earth's magnetic field: *Science*, v. 144, no. 3626, p. 1537-1543.
- Dal Corso, J., Mietto, P., Newton, R. J., Pancost, R. D., Preto, N., Roghi, G., and Wignall, P. B., 2012, Discovery of a major negative ¹³C spike in the Carnian (Late Triassic) linked to the eruption of Wrangellia flood basalts: *Geology*, v. 40, no. 1, p. 79-82.
- Enos, P., Lehrmann, D. J., Jiayong, W., Youyi, Y., Jiafei, X., Chaikin, D. H., Minzoni, M., Berry, A. K., and Montgomery, P., 2006, Triassic Evolution of the Yangtze Platform in Guizhou Province, People's Republic of China, v. 417, p. 1-105.
- Enos, P., Wei, J., and Lehrmann, D. J., 1998, Death in Guizhou — Late Triassic drowning of the Yangtze carbonate platform: *Sedimentary Geology*, v. 118, no. 1-4, p. 55-76.
- Erba, E., 1994, Nannofossils and superplumes: The Early Aptian “nannoconid crisis”: *Paleoceanography*, v. 9, no. 3, p. 483-501.

- Erba, E., Duncan, R. A., Bottini, C., Tiraboschi, D., Weissert, H., Jenkyns, H. C., and Malinverno, A., 2015, Environmental consequences of Ontong Java Plateau and Kerguelen Plateau volcanism: The origin, evolution, and environmental impact of oceanic large igneous provinces. *Geological Society of America Special Paper*, v. 511, p. 271-303.
- Furin, S., Preto, N., Rigo, M., Roghi, G., Gianolla, P., Crowley, J. L., and Bowring, S. A., 2006, High-precision U-Pb zircon age from the Triassic of Italy: Implications for the Triassic time scale and the Carnian origin of calcareous nannoplankton and dinosaurs: *Geology*, v. 34, no. 12, p. 1009.
- Gianolla, P., Ragazzi, E., and Roghi, G., 1998, Upper Triassic amber from the Dolomites (Northern Italy). A paleoclimatic indicator?: *Rivista Italiana di Paleontologia e Stratigrafia*, v. 104, p. 381-390.
- Gradstein, F. M., Ogg, J. G., Schmitz, M. D., and Ogg, G. M., 2012, *The Geologic Time Scale 2012*, Elsevier, p. 1-1144.
- Greene, A. R., Scoates, J. S., Weis, D., Katvala, E. C., Israel, S., and Nixon, G. T., 2010, The architecture of oceanic plateaus revealed by the volcanic stratigraphy of the accreted Wrangellia oceanic plateau: *Geosphere*, v. 6, no. 1, p. 47-73.
- Greene, A. R., Scoates, J. S., Weis, D., Nixon, G. T., and Kieffer, B., 2009, Melting history and magmatic evolution of basalts and picrites from the accreted Wrangellia oceanic plateau, Vancouver Island, Canada: *Journal of Petrology*, p. egp008.
- Han, W., Fang, X., and Berger, A., 2012, Tibet forcing of mid-Pleistocene synchronous enhancement of East Asian winter and summer monsoons revealed by Chinese loess record: *Quaternary Research*, v. 78, no. 2, p. 174-184.
- Hay, W., Thompson, S., Pollard, D., Wilson, K., and Wolc, C., 1994, Results of a climatic model for Triassic Pangea: *Zbl Geol Palöntol Teil*, v. 1, p. 1253-1265.
- Hays, J. D., Imbrie, J., and Shackleton, N. J., 1976, Variations in the Earth's Orbit: Pacemaker of the Ice Ages: *Science*, v. 194, no. 4270, p. 1121-1132.
- Head, M. J., and Gibbard, P. L., 2015, Early–Middle Pleistocene transitions: linking terrestrial and marine realms: *Quaternary International*, v. 389, p. 7-46.

- Head, M. J., Pillans, B., and Farquhar, S. A., 2008, The Early-Middle Pleistocene transition: characterization and proposed guide for the defining boundary: *Episodes*, v. 31, no. 2, p. 255-259.
- Heslop, D., Dekkers, M., and Langereis, C., 2002, Timing and structure of the mid-Pleistocene transition: records from the loess deposits of northern China: *Palaeogeography, Palaeoclimatology, Palaeoecology*, v. 185, no. 1, p. 133-143.
- Hilgen, F. J., Abdul Aziz, H., Krijgsman, W., Raffi, I., and Turco, E., 2003, Integrated stratigraphy and astronomical tuning of the Serravallian and lower Tortonian at Monte dei Corvi (Middle–Upper Miocene, northern Italy): *Palaeogeography, Palaeoclimatology, Palaeoecology*, v. 199, no. 3–4, p. 229-264.
- Hinnov, L., and Hilgen, F., 2012a, Cyclostratigraphy and astrochronology: The Geologic Time Scale 2012: vol. 1, p. 63-83.
- Hinnov, L. A., 2013, Cyclostratigraphy and its revolutionizing applications in the earth and planetary sciences: *Geological Society of America Bulletin*.
- Hinnov, L. A., and Hilgen, F. J., 2012b, Chapter 4 - Cyclostratigraphy and Astrochronology, *in* Gradstein, F. M., Schmitz, J. G. O. D., and Ogg, G. M., eds., *The Geologic Time Scale*: Boston, Elsevier, p. 63-83.
- Hinnov, L. A., and Ogg, J. G., 2007, Cyclostratigraphy and the astronomical time scale: *Stratigraphy*, v. 4, no. 2-3, p. 239-251.
- Hochuli, P. A., and Vigran, J. O., 2010, Climate variations in the Boreal Triassic — Inferred from palynological records from the Barents Sea: *Palaeogeography, Palaeoclimatology, Palaeoecology*, v. 290, no. 1–4, p. 20-42.
- Hornung, T., and Brandner, R., 2005, Biochronostratigraphy of the Reingraben Turnover (Hallstatt Facies Belt): Local black shale events controlled by regional tectonics, climatic change and plate tectonics: *Facies*, v. 51, no. 1-4, p. 460-479.
- Hounslow, M. W., and Muttoni, G., 2010, The geomagnetic polarity timescale for the Triassic: linkage to stage boundary definitions: *Geological Society, London, Special Publications*, v. 334, no. 1, p. 61-102.
- House, M. R., 1995, *Orbital forcing timescales: an introduction*: Geological Society, London, Special Publications, v. 85, no. 1, p. 1-18.

- Huang, C., Hinnov, L., Fischer, A. G., Grippo, A., and Herbert, T., 2010, Astronomical tuning of the Aptian Stage from Italian reference sections: *Geology*, v. 38, no. 10, p. 899-902.
- Jenkyns, H. C., Carbon-isotope stratigraphy and paleoceanographic significance of the Lower Cretaceous shallow-water carbonates of Resolution Guyot, Mid-Pacific Mountains, *in* *Proceedings of the Ocean Drilling Program, Scientific Results 1995*, Volume 143, Ocean Drilling Program, College Station, p. 99-104.
- Jenkyns, H. C., 2010, Geochemistry of oceanic anoxic events: *Geochemistry Geophysics Geosystems*, v. 11.
- Jones, C. E., and Jenkyns, H. C., 2001, Seawater strontium isotopes, oceanic anoxic events, and seafloor hydrothermal activity in the Jurassic and Cretaceous: *American Journal of Science*, v. 301, no. 2, p. 112-149.
- Keller, C. E., Hochuli, P. A., Weissert, H., Bernasconi, S. M., Giorgioni, M., and Garcia, T. I., 2011, A volcanically induced climate warming and floral change preceded the onset of OAE1a (Early Cretaceous): *Palaeogeography, Palaeoclimatology, Palaeoecology*, v. 305, no. 1-4, p. 43-49.
- Kent, D. V., 1999, Orbital tuning of geomagnetic polarity time-scales: *Philosophical Transactions of the Royal Society A: Mathematical, Physical and Engineering Sciences*, v. 357, no. 1757, p. 1995-2007.
- Kent, D. V., Olsen, P. E., and Muttoni, G., 2017, Astrochronostratigraphic polarity time scale (APTS) for the Late Triassic and Early Jurassic from continental sediments and correlation with standard marine stages: *Earth-Science Reviews*, v. 166, no. Supplement C, p. 153-180.
- Kent, D. V., Olsen, P. E., Rasmussen, C., Lepre, C., Mundil, R., Irmis, R. B., Gehrels, G. E., Giesler, D., Geissman, J. W., and Parker, W. G., 2018, Empirical evidence for stability of the 405-kiloyear Jupiter-Venus eccentricity cycle over hundreds of millions of years: *Proc Natl Acad Sci U S A*, v. 115, no. 24, p. 6153-6158.
- Kent, D. V., Olsen, P. E., and Witte, W. K., 1995, Late Triassic-earliest Jurassic Geomagnetic Polarity Sequence and Paleolatitudes: *Journal of Geophysical Research*, v. 100, no. B8, p. 14965-14998.

- Kozur, H. W., and Bachmann, G. H., 2008, Updated correlation of the Germanic Triassic with the Tethyan scale and assigned numeric ages: Upper Triassic Subdivisions, Zonations and Events, v. 76, p. 53-58.
- Kozur, H. W., and Bachmann, G. H., 2010, The Middle Carnian Wet Intermezzo of the Stuttgart Formation (Schilfsandstein), Germanic Basin: Palaeogeography, Palaeoclimatology, Palaeoecology, v. 290, no. 1-4, p. 107-119.
- Laskar, J., 2004, A long-term numerical solution for the insolation quantities of the Earth: *Astronomy & Astrophysics*, v. 428, no. 1, p. 261-285.
- Laskar, J., Joutel, F., and Boudin, F., 1993, ORBITAL, PRECESSIONAL, AND INSOLATION QUANTITIES FOR THE EARTH FROM -20 MYR TO +10 MYR: *Astronomy & Astrophysics*, v. 270, no. 1-2, p. 522-533.
- Lehrmann, D. J., Enos, P., Payne, J. L., Montgomery, P., Wei, J., Yu, Y., Xiao, J., and Orchard, M. J., 2005, Permian and Triassic depositional history of the Yangtze platform and Great Bank of Guizhou in the Nanpanjiang basin of Guizhou and Guangxi, south China: *Albertiana*, v. 33, no. 1, p. 147-166.
- Li, J. J., Fang, X. M., Van der Voo, R., Zhu, J. J., Niocaill, C. M., Ono, Y., Pan, B. T., Zhong, W., Wang, J. L., and Sasaki, T., 1997, Magnetostratigraphic dating of river terraces: Rapid and intermittent incision by the Yellow River of the northeastern margin of the Tibetan Plateau during the Quaternary: *Journal of Geophysical Research: Solid Earth*, v. 102, no. B5, p. 10121-10132.
- Li, Q., Wang, P., Zhao, Q., Tian, J., Cheng, X., Jian, Z., Zhong, G., and Chen, M., 2008a, Paleooceanography of the mid-pleistocene south china sea: *Quaternary Science Reviews*, v. 27, no. 11, p. 1217-1233.
- Li, Y.-X., Bralower, T. J., Montañez, I. P., Osleger, D. A., Arthur, M. A., Bice, D. M., Herbert, T. D., Erba, E., and Silva, I. P., 2008b, Toward an orbital chronology for the early Aptian oceanic anoxic event (OAE1a, ~ 120 Ma): *Earth and Planetary Science Letters*, v. 271, no. 1, p. 88-100.
- Lisiecki, L. E., and Raymo, M. E., 2005, A Pliocene-Pleistocene stack of 57 globally distributed benthic $\delta^{18}\text{O}$ records: *Paleoceanography*, v. 20, no. 1.

- Liu, D., Fang, X., Song, C., Dai, S., Zhang, T., Zhang, W., Miao, Y., Liu, Y., and Wang, J., 2010, Stratigraphic and paleomagnetic evidence of mid-Pleistocene rapid deformation and uplift of the NE Tibetan Plateau: *Tectonophysics*, v. 486, no. 1, p. 108-119.
- Liu, X., Chen, J., Maher, B. A., Zhao, B., Yue, W., Sun, Q., and Chen, Z., 2017, Connection of the proto-Yangtze River to the East China Sea traced by sediment magnetic properties: *Geomorphology*.
- Lucas, S. G., 2010, *The Triassic timescale: an introduction*: Geological Society, London, Special Publications, v. 334, no. 1, p. 1-16.
- Lucas, S. G., Heckert, A. B., Estep, J. W., and Anderson, O. J., 1997, Stratigraphy of the Upper Triassic Chinle group, four corners region: *New Mexico Geological Society Guidebook*, v. 48, p. 81-107.
- MacLeod, K. G., Martin, E. E., and Blair, S. W., 2008, Nd isotopic excursion across Cretaceous ocean anoxic event 2 (Cenomanian-Turonian) in the tropical North Atlantic: *Geology*, v. 36, no. 10, p. 811-814.
- Mitchell, R. N., Bice, D. M., Montanari, A., Cleaveland, L. C., Christianson, K. T., Coccioni, R., and Hinnov, L. A., 2008, Oceanic anoxic cycles? Orbital prelude to the Bonarelli Level (OAE 2): *Earth and Planetary Science Letters*, v. 267, no. 1-2, p. 1-16.
- Nakada, R., Ogawa, K., Suzuki, N., Takahashi, S., and Takahashi, Y., 2014, Late Triassic compositional changes of aeolian dusts in the pelagic Panthalassa: Response to the continental climatic change: *Palaeogeography, Palaeoclimatology, Palaeoecology*, v. 393, p. 61-75.
- Ogg, J. G., 2012, Chapter 5 - Geomagnetic Polarity Time Scale, *in* Gradstein, F. M., Schmitz, J. G. O. D., and Ogg, G. M., eds., *The Geologic Time Scale*: Boston, Elsevier, p. 85-113.
- Ogg, J. G., 2015, The Mysterious Mid-Carnian “Wet Intermezzo” Global Event: *Journal of Earth Science*, v. 26, no. 2, p. 181-191.
- Olierook, H. K., Jourdan, F., and Merle, R. E., 2019, Age of the Barremian–Aptian boundary and onset of the Cretaceous Normal Superchron: *Earth-Science Reviews*, p. 102906.
- Palike, H., and Hilgen, F., 2008, Rock clock synchronization: *Nature Geosci*, v. 1, no. 5, p. 282-282.

- Polteau, S., Hendriks, B. W. H., Planke, S., Ganerød, M., Corfu, F., Faleide, J. I., Midtkandal, I., Svensen, H. S., and Myklebust, R., 2016, The Early Cretaceous Barents Sea Sill Complex: Distribution, $^{40}\text{Ar}/^{39}\text{Ar}$ geochronology, and implications for carbon gas formation: *Palaeogeography, Palaeoclimatology, Palaeoecology*, v. 441, p. 83-95.
- Preto, N., Agnini, C., Rigo, M., Sprovieri, M., and Westphal, H., 2013, The calcareous nannofossil *Prinsiosphaera* achieved rock-forming abundances in the latest Triassic of western Tethys: consequences for the $\delta^{13}\text{C}$ of bulk carbonate: *Biogeosciences*, v. 10, no. 9, p. 6053-6068.
- Preto, N., and Hinnov, L. A., 2003, Unraveling the origin of carbonate platform cyclothems in the Upper Triassic Durrenstein Formation (Dolomites, Italy): *Journal of Sedimentary Research*, v. 73, no. 5, p. 774-789.
- Renne, P. R., Zichao, Z., Richards, M. A., Black, M. T., and Basu, A. R., 1995, Synchrony and causal relations between Permian-Triassic boundary crises and Siberian flood volcanism.
- Rigo, M., Preto, N., Roghi, G., Tateo, F., and Mietto, P., 2007, A rise in the Carbonate Compensation Depth of western Tethys in the Carnian (Late Triassic): Deep-water evidence for the Carnian Pluvial Event: *Palaeogeography, Palaeoclimatology, Palaeoecology*, v. 246, no. 2-4, p. 188-205.
- Roghi, G., Gianolla, P., Minarelli, L., Pilati, C., and Preto, N., 2010, Palynological correlation of Carnian humid pulses throughout western Tethys: *Palaeogeography Palaeoclimatology Palaeoecology*, v. 290, no. 1-4, p. 89-106.
- Ruhl, M., Bonis, N. R., Reichert, G. J., Sinninghe Damste, J. S., and Kurschner, W. M., 2011, Atmospheric carbon injection linked to end-Triassic mass extinction: *Science*, v. 333, no. 6041, p. 430-434.
- Sageman, B. B., Meyers, S. R., and Arthur, M. A., 2006, Orbital time scale and new C-isotope record for Cenomanian-Turonian boundary stratotype: *Geology*, v. 34, no. 2, p. 125.
- Schefuß, E., Schouten, S., Jansen, J. F., and Damsté, J. S. S., 2003, African vegetation controlled by tropical sea surface temperatures in the mid-Pleistocene period: *Nature*, v. 422, no. 6930, p. 418-421.
- Shackleton, N. J., Crowhurst, S. J., Weedon, G. P., and Laskar, J., 1999, Astronomical calibration of Oligocene--Miocene time: *Philosophical Transactions of the Royal Society A: Mathematical, Physical and Engineering Sciences*, v. 357, no. 1757, p. 1907-1929.

- Simms, M. J., and Ruffell, A. H., 1989, Synchronicity of climatic change and extinctions in the Late Triassic: *Geology*, v. 17, no. 3, p. 265.
- Simms, M. J., and Ruffell, A. H., 1989, 1990, Climatic and biotic change in the late Triassic: *Journal of the Geological Society*, v. 147, no. 2, p. 321-327.
- Stamfli, G. M., and Kozur, H. W., 2006, Europe from the Variscan to the Alpine cycles: Geological Society, London, *Memoirs*, v. 32, no. 1, p. 57-82.
- Storey, M., Duncan, R. A., and Swisher, C. C., 3rd, 2007, Paleocene-Eocene thermal maximum and the opening of the Northeast Atlantic: *Science*, v. 316, no. 5824, p. 587-589.
- Strasser, A., Hilgen, F. J., and Heckel, P. H., 2006, Cyclostratigraphy – concepts, definitions, and applications: *Newsletters on Stratigraphy*, v. 42, no. 2, p. 75-114.
- Suc, J.-P., and Popescu, S.-M., 2005, Pollen records and climatic cycles in the North Mediterranean region since 2.7 Ma: Geological Society, London, *Special Publications*, v. 247, no. 1, p. 147-158.
- Sun, Z., Stock, J., Jian, Z., McIntosh, K., Alvarez-Zarikian, C., and Klaus, A., 2016, Expedition 367/368 scientific prospectus: South China Sea rifted margin: International Ocean Discovery Program.
- Voigt, S., Erbacher, J., Mutterlose, J., Weiss, W., Westerhold, T., Wiese, F., Wilmsen, M., and Wonik, T. J. N. o. S., 2008, The Cenomanian–Turonian of the Wunstorf section–(North Germany): global stratigraphic reference section and new orbital time scale for Oceanic Anoxic Event 2, v. 43, no. 1, p. 65-89.
- Weedon, G. P., 2003, *Time Series Analysis and Cyclostratigraphy: Examining Stratigraphic Records of Environmental Cycles*, Cambridge University Press.
- Weissert, H., 1989, C-isotope stratigraphy, a monitor of paleoenvironmental change: a case study from the Early Cretaceous: *Surveys in Geophysics*, v. 10, no. 1, p. 1-61.
- Westerhold, T., Röhl, U., and Laskar, J., 2012, Time scale controversy: Accurate orbital calibration of the early Paleogene: *Geochemistry, Geophysics, Geosystems*, v. 13, no. 6, p. n/a-n/a.
- Wignall, P. B., 2001, Large igneous provinces and mass extinctions: *Earth-Science Reviews*, v. 53, no. 1–2, p. 1-33.

CHAPTER 2. LATE TRIASSIC MAGNETOSTRATIGRAPHY FROM THE GERMANIC BASIN AND THE GLOBAL CORRELATION OF THE CARNIAN PLUVIAL EPISODE

Yang Zhang^a, James G. Ogg^{b,a*}, Matthias Franz^c, Gerhard H. Bachmann^d, Michael Szurlies^e, Heinz-Gerd Röhling^f, Mingsong Li^g, Yan Chen^h, Christian Rolfⁱ, Karsten Obst^j

^a*Dept. of Earth, Atmospheric and Planetary Sciences, Purdue University, 550 Stadium Mall Drive, West Lafayette, Indiana, 47907-2051, USA*

^b*State Key Laboratory of Oil and Gas Reservoir Geology and Exploitation, Chengdu University of Technology, Chengdu 610059, Sichuan, P.R. China*

^c*Geowissenschaftliches Zentrum der Universität Göttingen, Abteilung Angewandte Geologie, Goldschmidtstraße 3,*

D-37077 Göttingen, Germany

^d*Institut für Geowissenschaften, Martin-Luther-Universität Halle-Wittenberg, D-06120 Halle (Saale), Germany*

^e*Bundesanstalt für Geowissenschaften und Rohstoffe (BGR), Stilleweg 2, D- 30655 Hannover, Germany*

^f*Erich-Baron-Weg 100, D-12623 Berlin, Germany*

^g*Department of Geosciences, Pennsylvania State University, University Park, PA 16802, USA*

^h*State Key Laboratory of Biogeology and Environmental Geology, School of Earth Sciences, China University of Geosciences, Wuhan 430074, Hubei, P.R. China*

ⁱ*Leibniz-Institut für Angewandte Geophysik, Sektion 5 Gesteinsphysik und Bohrlochgeophysik, Stilleweg 2, D-30655 Hannover, Germany*

^j*Landesamt für Umwelt, Naturschutz und Geologie Mecklenburg-Vorpommern, Goldberger Str. 12, D-18273 Güstrow, Germany*

* Corresponding author: jogg@purdue.edu

Abstract: The Stuttgart Formation (traditionally called the Schilfsandstein) in the Germanic Basin (or Central European Basin) is a sand-rich episode representing the Mid-Carnian Episode within the gypsum-rich clayey semi-arid Keuper facies. That regional Mid-Carnian Episode is now recognized to be a manifestation of a significant global disruption of Earth's climate-ocean-biological system during the early Late Triassic. In South China, the termination of the long-lived Yangtze carbonate platform by an influx of clastic-rich sediments potentially

corresponds to the Mid-Carnian Episode. However, due to a lack of an accurate time frame and means for high-resolution correlations, the understanding of the temporal relations among continental and marine records is hindered. We obtained a high-resolution composite magnetostratigraphy spanning the entire Carnian from three boreholes in the Germanic Basin. This composite shows a good consistency with earlier published magnetostratigraphy results from South China and enables the construction of a complete Carnian polarity time scale. The Upper Carnian (Tuvalian substage) portion implies that: (1) The lower quarter of the Tuvalian is dominated by a reversed-polarity magnetozone; (2) The upper three-fourths of the Tuvalian is a major normal-polarity-dominated magnetozone; and this interval correlates with the basal E1-E6 portion of the Newark magnetic polarity reference series; (3) The polarity patterns of portions of the Upper Carnian from the western Tethys sections of Lower Trench at Silická Brezová in Austria and Pizzo Mondello in Italy are verified; (4) The termination of the Yangtze Platform is coeval with deposition of the Stuttgart Formation in the Germanic Basin; (5) The radiolarian-rich green-colored clay horizon of the Pignola-2 section in south Italy that is below a volcanic ash bed dated as ca. 231 Ma correlates with the D pulse of siliciclastics in Dibona section of north Italy in the middle of the Tuvalian ; (6) The base of the Arnstadt Formation of the Germanic Basin, which had been traditionally assigned as the Carnian/Norian boundary, instead begins within the lower portion of Newark reversed-polarity zone E8r of earliest Norian. This Carnian composite is an enhanced polarity time scale for calibration of other global Carnian successions and events, such as the appearance of the earliest dinosaurs in fossiliferous beds of South America.

Keywords: Geomagnetic polarity time scale, Tuvalian, Julian, Central European Basin, South China, Pignola-2

2.1 Introduction

A rather short-term global disruption of Earth's climate-ocean-biological system in the middle of the Carnian Age of Late Triassic (~235 Ma) resulted in widespread sand-rich layers across inland basins and coastal regions from engorged river systems and the abrupt termination of many tropical carbonate platforms (e.g., Hornung et al., 2007a; Ruffell et al., 2016; Dal Corso et al., 2018a; and references therein). This episode has been subject to numerous studies in the last decades contributing to a profound database (reviews in Ogg, 2015; Ruffell et al., 2016; Dal

Corso et al., 2018a, b). After Simms and Ruffell (1989) had coined the term Carnian Pluvial Event, other names implementing a supposed shift to pluvial/humid or wet climate were proposed, such as Middle Carnian Wet Intermezzo (Kozur and Bachmann, 2010) or Carnian Pluvial Episode (Dal Corso et al., 2018a). In contrast, descriptive terms like Reingraben Turnover (Schlager and Schöllnberger, 1974) or Mid-Carnian Episode (Franz et al., 2019) were proposed in order to avoid preconditioning.

Various phenomena are considered to be associated to the Mid-Carnian Episode; and at least some of them were coupled. Pronounced sea-level fluctuations and related oceanographic responses were described from marine basins of the Boreal to Tethyan realms (e.g., Hornung et al. 2007b; Gattolin et al., 2015; Franz et al., 2014, 2019; Barrenechea et al., 2018). Shifts of marine habitats and input of terrigenous clastics triggered by these sea-level fluctuations contributed to turnovers of marine organisms on Tethyan shelves and beyond (e.g., Simms and Ruffell, 1989; Preto et al., 2013). Coeval perturbations of the carbon-cycle (e.g., Dal Corso et al., 2018a, b; Sun et al., 2016) further contributed to habitat shifts and turnovers in marine basins, and may have also affected some terrestrial groups (e.g., Bernardi et al., 2018). These perturbations of the carbon cycle and onset of a more humid climate during this Mid-Carnian episode are commonly proposed to have been triggered by substantial carbon dioxide exhalations from the Wrangellia Large Igneous Province (Greene et al., 2010) and other contemporaneous volcanic sources (e.g., Kohút et al., 2018; Dal Corso et al., 2018a, b).

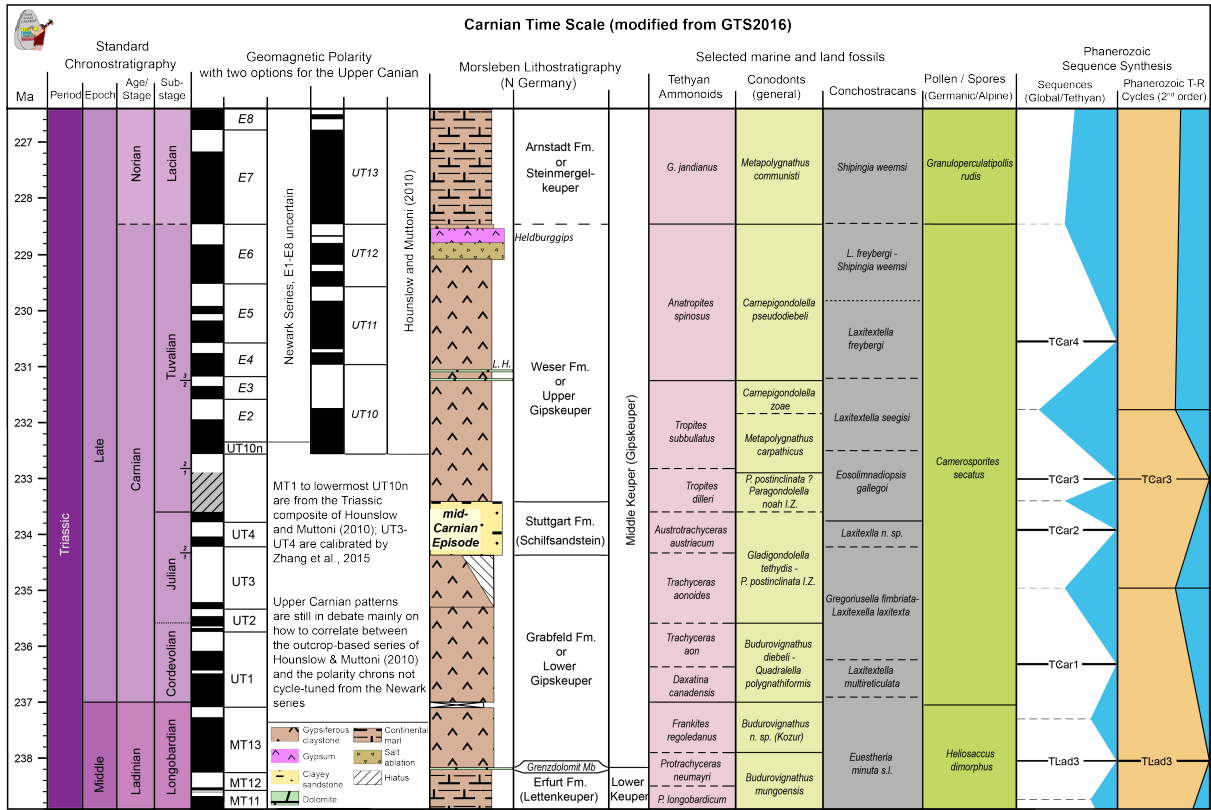


Figure 2.1. An example of previous Carnian stratigraphic scales from the GTS2012/2016 syntheses (Gradstein et al., 2012, using their "long Norian" option; Ogg et al., 2016). The early Carnian portion of the geomagnetic polarity column incorporates magnetostratigraphy scaled by astronomical cycles (Zhang et al., 2015) for magnetozones UT1 through UT4 of Hounslow and Muttoni (2010). The late Carnian to early Norian polarity patterns compares the magnetozones ages projected for the Newark Series (Kent and Olsen, 1999; Kent et al., 2017; although E1-E6 lack direct astronomical cycle calibration) to the "reference" synthesis of UT10-UT13 by Hounslow and Muttoni (2010) that had biostratigraphic age constraints. The grey-hatched interval above UT4 indicates the lack of magnetostratigraphic data in the Hounslow and Muttoni (2010) and GTS2016 compilations. Note that the base of the Norian had been placed erroneously at the base of E7n in that scale, but the current proposed marker of the lowest occurrence of conodont *Metapolygnathus parvus* (Mazza et al., 2018) occurs in latest E7n. The onset of the Carnian Pluvial Episode in the latest Julian is at the beginning of the sandy Stuttgart Formation (also called the Schilfsandstein). The salt ablation/residual bed in uppermost Weser Formation is according to the Morsleben borehole (e.g., Barnasch, 2010). Mb = Member. The Cordevolian substage of lowest Carnian is generally merged with the Julian substage into a single Julian substage by most Triassic stratigraphers. The diagram was generated using the databases in TSCreator v.7.4 (<https://timescalecreator.org>).

Even though the Mid-Carnian Episode is recorded worldwide in different depositional settings, the correlation among localities is challenging due to a lack of common fossil assemblages and the challenge to correlate between marine and terrestrial settings.

Magnetostratigraphy, especially when combined with cyclostratigraphy, has proved to be a robust way to build portions of the Triassic time scale (e.g., Hounslow and Muttoni, 2010) and to enable global correlation among various settings for the Induan-Olenekian-Anisian stages of the Early and Middle Triassic (e.g., Li et al., 2016; Szurlies, 2007) and for the Norian–Rhaetian stages of the Late Triassic (e.g., Kent and Olsen, 1999; Kent et al., 2017). This has not yet been achieved for the full Carnian Stage of Late Triassic, except for a ca. 2-myr interval in the Julian Substage (lower Carnian) that is dominated by a 1.3-myr reversed-polarity zone (Zhang et al., 2015) (Fig. 1). The biostratigraphic-constrained magnetostratigraphy from the Pignola-2 section of Italy displays a similar reverse-polarity-dominated pattern for the upper Julian substage (Maron et al., 2017); and the overlying Tuvolian portion of this section contains an ash bed dated by U-Pb as 230.91 ± 0.33 Ma (Furin et al., 2006). Analysis of the Mid-Carnian Episode in terrestrial successions in southwest England suggests an astronomical-cycle duration of 1.09 Myr (Miller et al., 2017), which is consistent with the earlier assumptions that it spanned two or three 405-kyr long-eccentricity cycles (Kozur and Bachmann, 2008; Roghi et al., 2010).

We conducted detailed magnetostratigraphic analyses of the upper Ladinian–Carnian–lower Norian strata from the centre of the Germanic Basin using three cored boreholes. The Stuttgart Formation, commonly considered as the type-example of the Mid-Carnian Episode (Simms and Ruffell, 1989), is well documented in these three boreholes (Barnasch, 2010; Franz et al., 2014). By verifying the magnetic polarity scale for the Mid-Carnian Episode and extending this scale from late Ladinian through the entire Carnian, this study investigated the global synchronicity of the Mid-Carnian Episode, correlated the basal portion of the Newark magnetic polarity pattern and its coeval signature in magnetostratigraphic sections in the western Tethys, and placed a numerical age model on this portion of the Late Triassic geomagnetic time scale.

2.2 Geologic Setting and Chronostratigraphic Control on the Keuper Group

During the Late Triassic, the epicontinental Germanic Basin (Central European Basin) was a large depocenter located at a paleolatitude of *ca.* 20°N that extended from England through northern and central Germany to eastern Poland and northern Switzerland (Fig. 2) (e.g., Stampfli and Kozur, 2006).

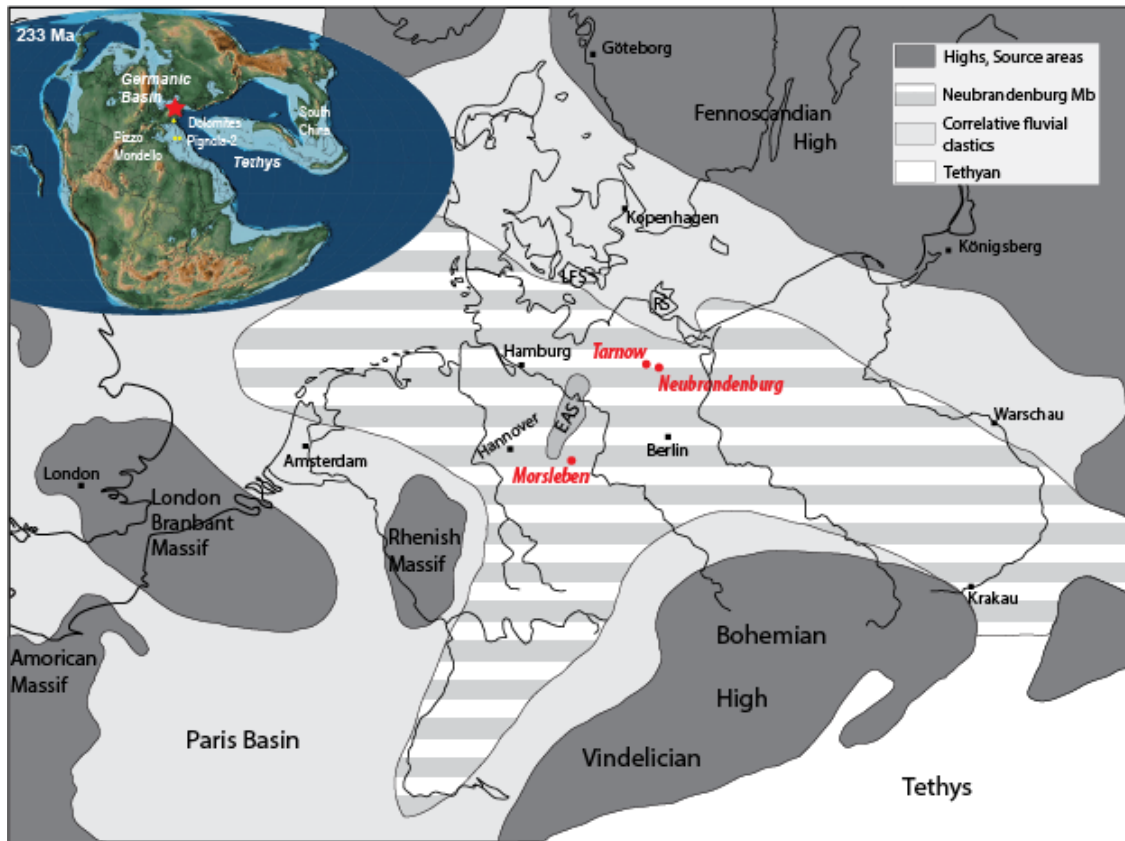


Figure 2.2. Paleogeography map of the Germanic Basin (Central European Basin) based on the Geological Atlas of Europe (Ziegler, 1990) and re-drawn from Franz et al. (2014). Red dots show the locations of the studied boreholes at Morsleben (Dp Morsleben 52A/95), Neubrandenburg (Gt Neubrandenburg 2/85) and Tarnow (Kb Tarnow 1/65). The hatched area is the extent of the brackish-marine Neubrandenburg Member of the Stuttgart Formation, and light grey is the correlative fluvial clastics. The massifs and highlands are in darker grey, and EAS is the central Eichsfeld–Altmark Swell. The Tethys ocean to the southeast of the basin is denoted in white.

The predominantly terrestrial Keuper Group spans most of the upper half of the Germanic Triassic. The biostratigraphic correlation of the Keuper with the international chronostratigraphic stages and sub-stages is well established using palynomorphs, conchostracans (now called spinicaudatans), ostracods and lamellibranchs (e.g., Kozur and Bachmann, 2008; Kozur and Weems, 2010; Franz et al., 2018a) (Fig. 1). Unfortunately, there is no radiometric dating directly on the Germanic Triassic stratigraphy. The Germanic Basin had been frequently influenced by marine Tethyan water advances and retreats from the south and southeast. Consequently, fossil-bearing horizons from these short-term marine transgressions are recorded in the Keuper Group and can be used as marker beds for basinal correlation.

The Lower, Middle, and Upper Keuper subgroups are further divided into formations. The Lower Keuper, also known as Erfurt Formation (or Lettenkeuper), is characterized by marine to lacustrine carbonate beds and fluvio-deltaic sandstones. In the southern part of the Germanic Basin, the palynomorph *Heliosaccus dimorphus* has its first appearance datum (FAD) at the base of the formation. In combination with a monospecific fauna of *Euestheria minuta*, a late Ladinian age (Longobardian) is indicated. The Erfurt Formation is capped by the “Grenzdolomit”, a widespread marker bed of predominantly marine dolomite (Franz et al., 2013) (Fig. 1). After the short but noticeable marine Grenzdolomit ingressions, the Grabfeld Formation (Lower Gipskeuper, upper Ladinian to lower Carnian) was deposited in playa- to sabkha-like conditions. The upper Ladinian index fossil *Myophoria kefersteini okeni* occurs in the thin marine Bleiglanzbank (“Galena Bed”) in the middle part of the Grabfeld Formation (Urlichs and Tichy, 2000). The basal Carnian (Cordevolian) is in the upper Grabfeld Formation at the base of the Estherienschichten (“Estheria Beds”) as indicated by the FAD of *Laxitextella multireticulata* (Geyer and Kelber, 2018). Higher up, the Estherienschichten contain the upper Cordevolian index form *Laxitextella laxitexta*. The early Carnian age is supported by palynomorphs such as *Triadispora verrucata*, *Ovalipollis pseudoalatus* and *Camerosporites secatus*.

The playa- to sabkha-like environment was interrupted by the pronounced change to the distinctive, predominantly fluvio-deltaic Stuttgart Formation (middle Carnian). Due to a pair of transgressions into basin center, the fluvio-deltaic Lower and Upper Schilfsandstein members occur sandwiched between the brackish-marine Neubrandenburg, Gaildorf and Beaumont members (Fig. 3). The brachyhaline to marine Neubrandenburg Member contains middle Carnian (Julian) ostracods like *Simeonella alpina* (e.g. Franz et al., 2014). The continuous succession of the Grabfeld and Stuttgart formations of the basin center, including localities of herein investigated wells, is in contrast to the discontinuous succession in the southern part of the basin. There, the Neubrandenburg Member and the upper part of the Estherienschichten were frequently eroded due to fluvial incision resulting in a substantial hiatus at the base of the Stuttgart Formation (e.g., Aigner and Bachmann, 1992). This is shown by the hatched area in Figure 2, suggesting a non-uniform disconformity between Grabfeld and Stuttgart Formations that usually occurs in southern Germany, but not central and north Germany (Fig. 1; e.g., Franz et al., 2014). Further details on the lithologic subdivisions and non-marine biostratigraphy of the Stuttgart Formation are given in Appendix A.

Predominantly playa- to sabkha-like reddish shales return with the Weser Formation (Upper Gipskeuper), whose base is late Carnian (Tuvalian) in age as indicated by the lamellibranch *Costatoria vestita* in brachyhaline-marine Beaumont Member of eastern France and Switzerland (Kozur and Bachmann, 2010). The lower part of the Weser Formation is partly marine and contains the ostracod *Simeonella nostorica*. The thin dolomitic layers (Lehrberg-Horizon) (denoted as L. H. in Fig. 1) of the boundary between the lower and middle members of the Weser Formation can be traced over the basin (e.g., Beutler et al., 2005). Conchostracans of the *Eosolimnadiopsis gallegoi* to *Laxitextella seegisi* zones indicate an early to middle Tuvalian age (Kozur and Weems, 2010; Geyer and Kelber, 2018). The upper Weser Formation is late Tuvalian in age as shown by conchostracans of the *Laxitextella freybergi* and *L. freybergi*-*Shipingia weemsi* zones (Kozur and Weems, 2010; Kozur et al., 2013; Geyer and Kelber, 2018). This is confirmed by palynomorphs of the *Corollina/Classopollis* group (Heunisch and Nitsch, 2011). The ‘Heldburggips’ gypsum layer (Heldburg Gypsum Member, Fig 1) in the uppermost Weser Formation is a regional lithologic marker bed that is traditionally assigned as latest Carnian (e.g., Barnasch, 2010). This horizon is roughly placed at the lower fifth of the conchostracan *L. seegisi* biozone (Franz et al., 2018a).

The Weser Formation is conformably overlain by the Arnstadt Formation (Steinmergelkeuper) consisting of playa-type shales and carbonates in the basin center and reddish to greyish shales with pedogenic dolcretes in marginal parts of the basin. The lower part of the basinal facies contains a single *Shipingia weemsi* conchostracan species of early Norian age (Lacian) (Kozur et al., 2013). Late Carnian (Tuvalian) index species like *Laxitextella freybergi* are not present.

In the marginal parts or on the Eichsfeld-Altmark Swell there exists a more or less pronounced hiatus that was referred to as the Early Kimmerian Unconformity (“Altkimmerische Hauptdiskordanz”; Beutler and Schüler, 1982). The unconformity is thought to be caused by the closure of the Paleotethys at the Carnian/Norian boundary (Stampfli and Kozur, 2006). If present, parts of the lower Arnstadt Formation are missing and the overlying succession may contain conchostracans of the *S. weemsi-Euestheria buravasi* to *S. hebaozhaiensis* zones indicating an early Norian (Lacian) to middle Norian (Alaunian) age (Kozur and Weems, 2010; Geyer and Kelber, 2018). In the upper Arnstadt Formation, conchostracans of the *Gregoriusella polonica*-*S. gerbachmanni* zone indicate a late Norian (Sevatian) age (Hauschke & Kozur, 2011).

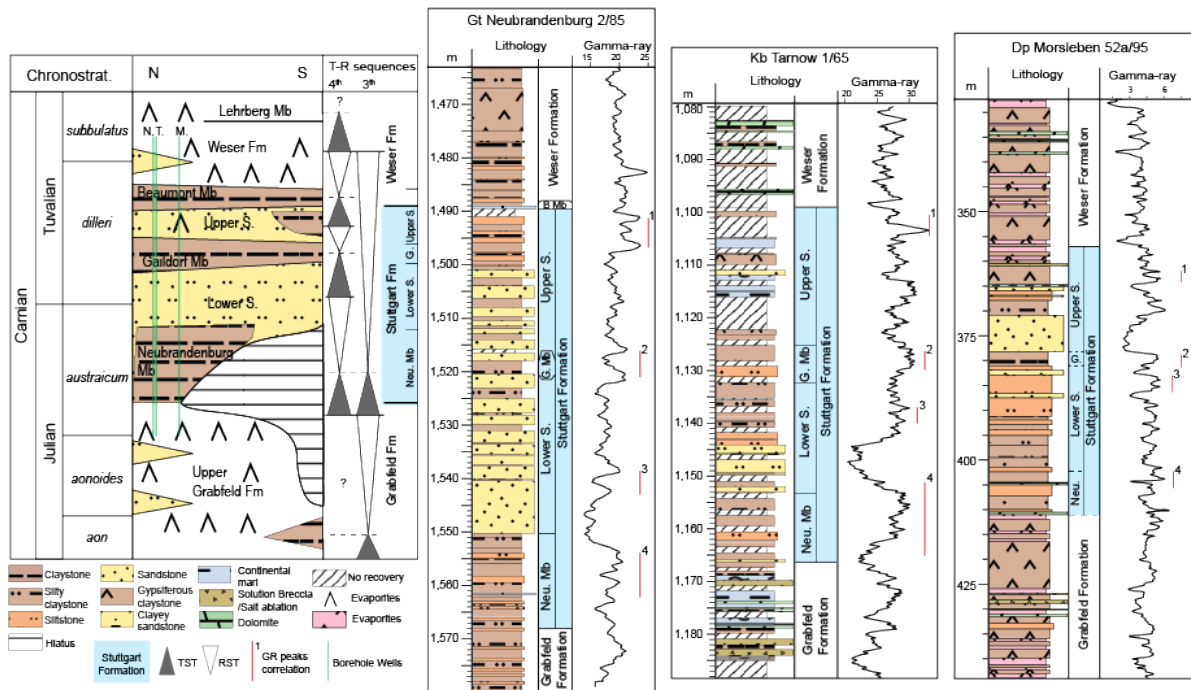


Figure 2.3. The Stuttgart Formation (Schilfsandstein) is highlighted in light blue within a general time frame provided by brief marine transgressions in the left panel (redrawn from Franz et al. (2014)). Vertical lines in green mark the approximate span of the three studied wells with abbreviated names: M.= Morsleben, N.= Neubrandenburg, and T.= Tarnow. The other three panels are the lithostratigraphy of these three studied wells. Gamma-ray logs of the Neubrandenburg and Tarnow boreholes are from LUNG M-V (under the copyright of Leibniz Institute for Applied Geophysics), and of the Morsleben borehole is digitized from Barnasch (2010) with artificial relative intensity scale of 1 to 8. Vertical red lines with numbers are possible correlation among the three wells as guided by lithology. Details on Stuttgart Formation lithologic subdivisions are given the Supplementary Material. Abbreviations: Chronostrat.= chronostratigraphy; Mb.= member; Neu. Mb= Neubrandenburg Member; Lower S.= Lower Schilfsandstein Member; G. Mb = Gaildorf Member; Upper S. = Upper Schilfsandstein Member; B Mb= Beaumont Member; N= north; S= south; TST= transgressive system tract; RS = regressive system tract.

2.3 Materials and Methods

2.3.1 Paleomagnetic sampling

Three boreholes (locations in Fig. 2) from the Germanic Basin were studied for magnetostratigraphy: Morsleben (Dp Morsleben 52a/95); Neubrandenburg (Gt Neubrandenburg 2/85); and Tarnow (Kb Tarnow/Altentreptow 1/65). The Morsleben cores from exploratory

investigations for a discontinued radioactive waste disposal facility are archived at the Grubenhagen core repository (managed by LBEG Hannover). The Neubrandenburg and Tarnow cores are stored in the core repository in Sternberg (managed by LUNG M-V). The Neubrandenburg cores are considered as a reference section of the Stuttgart Formation in northeastern Germany (Franz et al., 2014) because they record all three shaly marker horizons of the Neubrandenburg, Gaildorf and Beaumont members.

A total of ~200 minicores were collected from Morsleben cores using a drill press at the Grubenhagen lab, and 160 and 120 mini-cores were taken from Gt Neubrandenburg and Tarnow cores, respectively, using a gasoline-powered drill. The average sampling spacing was from 0.2 to 1.5 m. Sampling was guided by the lithology and the preservation status at all three boreholes; for example, gypsum intervals were skipped, and friable sediments were avoided.

2.3.2 Paleomagnetic analyses of Germanic Basin samples

Different suites of paleomagnetic minicores underwent low alternating-field (AF) demagnetization followed by progressive thermal demagnetization using facilities at three different paleomagnetic laboratories. The demagnetization steps continued to ca. 650°C for reddish-colored siltstones or to ca. 450°C for greyish ones. Details on the equipment and demagnetization procedures are provided in Appendix A.

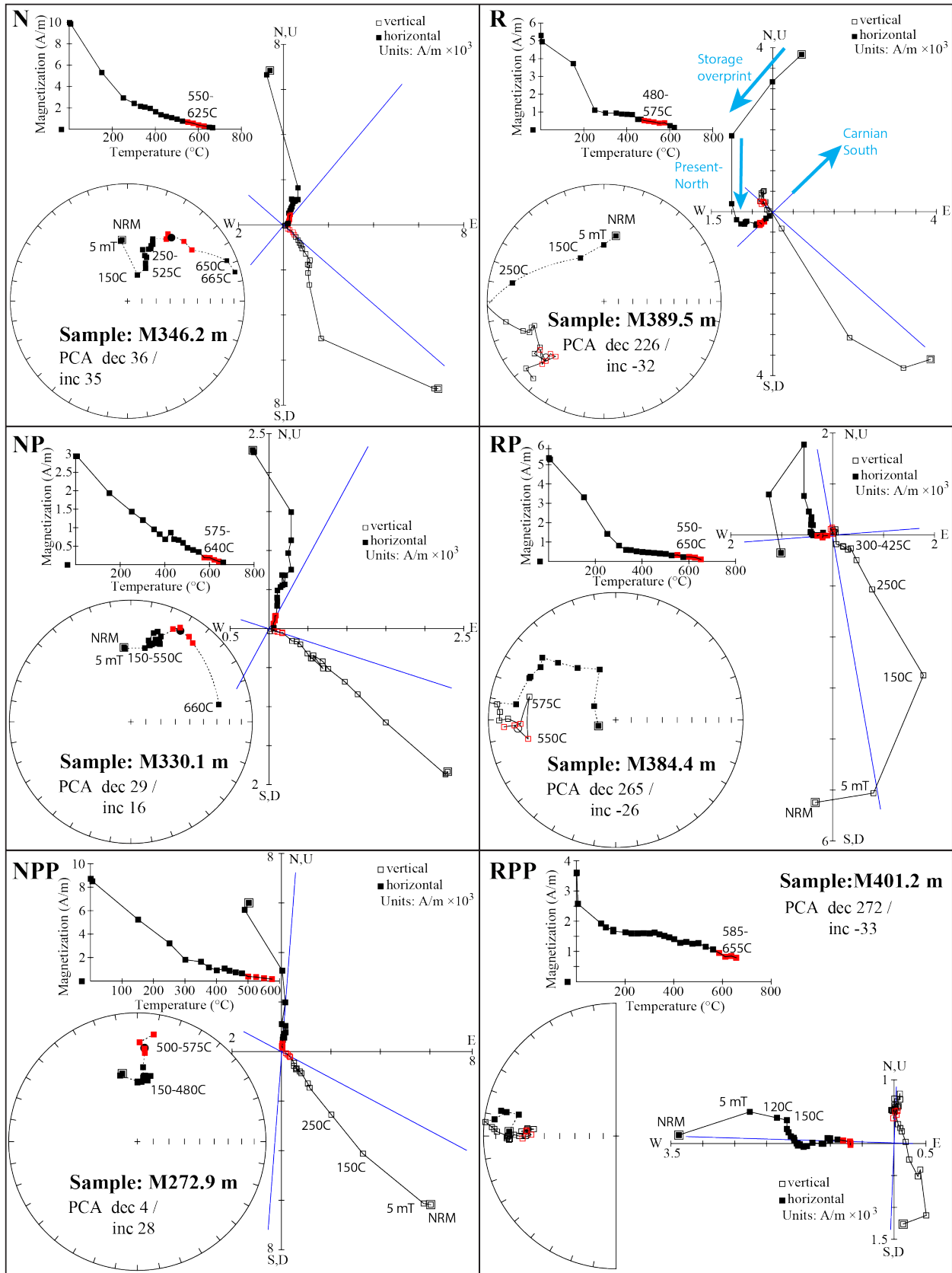
We applied a re-orienting of the samples using the vector removed during the initial demagnetization steps, which resulted in a partial statistical clustering of declinations during the low demagnetization steps toward an interpreted Brunhes-age North (details in Appendix A). This orientation-adjustment and the relative movement of the magnetic vectors upon the progressive higher demagnetization for those borehole samples helped to separate normal- versus reversed-polarity components.

The interpreted polarity and characteristic directions of the samples were given a quality rating of 'N(R)', 'NP(RP)', 'NPP(RPP)', 'N?(R?)' or 'INT' according to a semi-subjective judgment of the behaviors of the magnetic vectors during stepwise demagnetization. The 'N/R' ratings were generally reserved for those samples that attained a semi-stable characteristic remanent magnetization (ChRM) direction during progressive demagnetization. Mean directions for each polarity of each borehole were computed only using the ChRM vectors of the higher-quality-rated samples that had exhibited semi-stable declinations relative to the assumed

removed Brunhes overprint. Details of this procedure are in Appendices A and B. N/R-rated samples were given full weight in computing these mean directions and the 'NP/RP'-rated samples were given half-weight.

Polarity zones were assigned to stratigraphic clusters of ChRM vectors rated as N-NP-NPP or R-RP-RPP. Intervals with clusters of N?-INT-R? or significant gaps in sampling coverage are drawn as uncertain.

Figure 2.4. Typical examples of polarity ratings (N/R, NP/RP, and NPP/RPP) of samples from Morsleben. In each diagram, the lower-left subplot is the equal-area projection (solid/open squares are downward/upward vectors, respectively), the upper-left subplot is the magnetization intensity during progressive thermal (or AF) demagnetization steps, and the right subplot is the orthogonal projections of the vectors (Zijderveld, 1967) (solid squares are the projection onto the horizontal plane or declination, while open squares are projection onto a vertical plane or inclination). Steps used for ChRM are highlighted in red. The Principal Component Analysis (PCA) (Kirschvink, 1980) vectors are denoted in blue for N(P)/R(P) rated samples. The original declinations have been re-oriented based on the removed overprints at early demagnetization steps (see Methods section for details). Sample M346.2 – Polarity rating of “N” with ChRM direction assigned to the 550-575-600-625°C cluster. Sample M330.1 (330.1 m; pale reddish brown claystone; middle Weser Formation) – “NP” with ChRM computed from cluster of 4 steps between 575° and 640°C, with the P-quality rating because the ChRM inclination is anomalously shallow compared to the expected Carnian paleolatitude (Stampfli and Kozur, 2006). Sample M272.9 – “NPP” with ChRM calculated from the 4 steps, for which NPP is assigned due to being far (15°) from the expected Carnian normal-polarity declination; therefore, this sample was not used in computing the Carnian mean direction, although its normal-polarity is quite apparent. Sample M389.5 – “R” with ChRM calculated from a cluster of 5 steps during 480° to 575°C. For this sample, an interpreted storage overprint is removed at AF 5 mT and 150°C, followed by removal of a Brunhes north at 250°C; then a progressive great-circle movement toward the southwest with an upward inclination. Sample M384.4 – “RP” with ChRM computed from the cluster of 4 steps. Rated as RP due the counterclockwise rotation toward a Carnian-age reversed-polarity direction after removal of a downward drilling-induced overprint, but its ChRM declination was still significantly clockwise rotated from that expected Carnian reversed-polarity direction; therefore, it was not given full-weight in computing the mean paleomagnetic pole. Sample M401.2 – “RPP” with ChRM computed from 585°-655°C. The low-quality PP-rating was assigned due to having a trend toward an expected reversed-polarity direction, but not reaching an end point consistent with other re-oriented samples.



2.4 Results

2.4.1 Demagnetization behaviors

Magnetite and hematite appear to be the main magnetic remanence carriers for the ChRM of the grayish and of the reddish/brownish colored lithologies, respectively, according to the isothermal remanence magnetization (IRM) results (Fig. A.2) and to the progressive thermal demagnetization steps, similar to a previous paleomagnetic study by Hahn (1984). Most of reddish/brownish samples still retained partial magnetic remanence through 650–660°C, whereas the grayish ones often lost their remanence below instrumentation resolution or displayed anomalous viscous magnetizations above 500°C (or above 400°C for the Tarnow samples). Goethite may also be a contributor to the initial NRM based on the loss of nearly half of the NRM intensity upon heating at 100–250°C.

The initial NRM of most of the samples from the three studied boreholes have overprint components from drilling-induced and from an interpreted normal-polarity Brunhes (late Quaternary) field remanence that is progressively removed during demagnetization at low AF or low thermal demagnetization steps (e.g., Sample M389.5 in Fig. 4). Only half of our re-oriented samples displayed an acceptable resolution of primary magnetization (statistics summarized in Table 1), but this subset enabled computation of a mean paleomagnetic direction for the Carnian of the Germanic Basin (Table 1). Among the poor-quality-rated samples, those that displayed great-circle movement of their magnetic vectors toward either the expected normal-polarity or reversed-polarity hemispheres but did not attain a stable end-point were rated as N?/R?; while the rest were rated uncertain (INT). Typical examples from each well for samples with interpreted ChRM polarity ratings of N/R, NP/RP, and NPP/RPP are shown in Figs. 4, A.3 and A.4.

2.4.2 Mean characteristic directions

The high-quality N-rated samples generally display a gradual clockwise rotation away from the interpreted present-day North vector to stabilize at a northwest declination while shallowing from relatively steep-down to a positive inclination within 20°-40°. These directions are consistent with the apparent polar wander paths (APWPs) of northern Europe which places the Triassic-age north magnetic pole near present-day Siberia (Stampfli and Kozur, 2006), which

implies a total post-Carnian $\sim 40\text{-}45^\circ$ counterclockwise rotation of Germany. The R-rated samples rotate counterclockwise toward a southwest declination while progressively shallowing and then stabilizing at a negative inclination.

The mean ChRM directions of the re-oriented high-quality-rated normal-polarity and reversed polarity sample subsets are antipodal (Fig. 5, Table 1). The mean normal-polarity direction is centered at 37° declination, 30° inclination; and the mean reversed-polarity direction is 230° declination, -23° inclination. The apparent paleolatitude, even through there has been no adjustment for probable inclination flattening from later compaction, is about $15\text{-}20^\circ\text{N}$ for our Carnian subset, which also falls within the expected paleogeography reconstruction of the Central European Basin (Fig. 2). These means directions from the boreholes are consistent (within uncertainties) with the outcrop-derived mean paleomagnetic directions for the Stuttgart Formation by Hahn (1984).

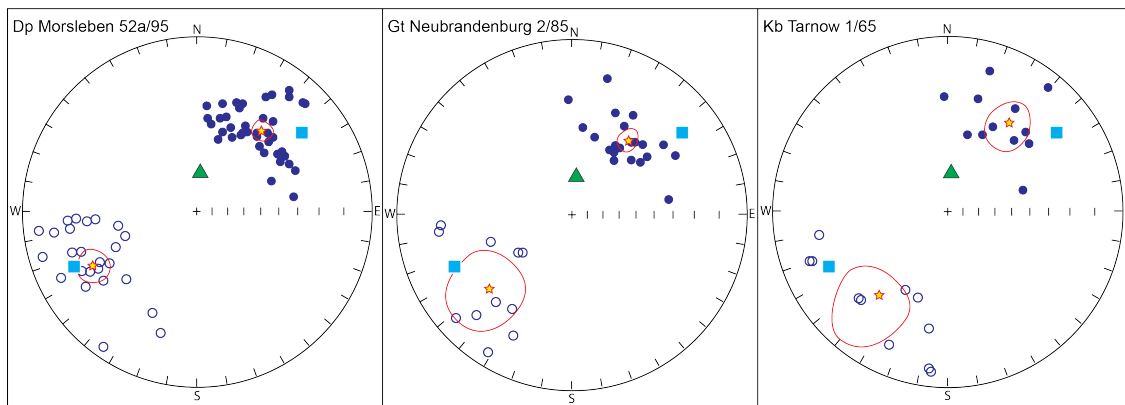


Figure 2.5. Equal-area projection of the characteristic directions (ChRM) for all re-oriented samples rated as N-NP- and R-RP-that were used for computation of mean directions (red star) and approximate 95% confidence (α_{95} , red circle) for each polarity cluster of the three boreholes (Table 1). Green triangle is the present-day geomagnetic field direction of modern Berlin (52.5°N , 13.4°E): 3.5° declination and 67.9° inclination computed from <https://www.ngdc.noaa.gov/geomag-web/#igrfwmm>. Cyan squares are the outcrop-derived mean paleomagnetic directions by Hahn (1984).

Table 2.1. Carnian paleomagnetic mean directions and virtual geomagnetic poles for the three boreholes (Fig. 5, this study) and results from outcrops by Hahn (1984). The statistics of samples from each borehole that yielded good-quality (N/NP and R/RP), poor (NPP/RPP) and very poor (N?/R?/INT) ratings are indicated. Hahn (1984) had interpreted that the deposition of Stuttgart Formation was diachronous as a delta advanced from North (outcrops dominated by N polarity recorded in Weserbergland) to Southwest Germany (outcrops dominated by R polarity in Swabia); but our results suggest that this may have been an artifact of the available exposures in each region.

Directions Locations			Mean site direction (°)					Virtual Geomagnetic Pole (VGP) (°)				
			Polarity	Decl.	Incl.	Num.	α_{95}	Lat.	Long.	δp	δm	Paleo-lat
Morsleben			N.	38.5	29.6	28.5	5.4	42.6N	136.6E	3.3	5.9	15.8
good	PP-	poor	R.	243.9	-22.4	18.5	8	-25.1	-65.1	4.5	8.5	-11.7
66	38	103	Com.	48.3	27.3	47	5.4	36.3N	127.3E	3.2	5.9	14.5
Neubrandenburg			N.	36.6	34.8	16	6.2	46.3N	138.9E	4.1	7.14	19.2
good	PP-	poor	R.	229.7	-26.0	7	18.8	-34.8	-51.0	11	20.4	-13.7
32	28	102	Com.	40.7	32.4	23	6.9	42.8N	135.5E	4.4	7.8	17.7
Tarnow			N.	34.2	28.7	8.5	11.8	44.1N	144.5E	7.2	13.0	15.3
good	PP-	poor	R.	219.6	-18.6	8.5	18.6	-36.5	-38.0	10.1	19.4	-9.6
22	11	38	Com.	36.9	23.8	17	10.4	40.3N	143.2E	5.9	11.1	12.5
Schilfsandstein (Hahn, 1984)				54	34	<i>Weserbergland</i>		33N	123E			
				244	-23	<i>N. Swabia</i>						

N.= Normal, R.= Reversed, and Com.= Combined polarity; Decl.= declination, Incl.= inclination. Num.= number of characteristic directions with quality ratings of N/NP and R/RP (with 'P'-rated given half-weight) that were used to compute mean directions for each polarity cluster; α_{95} is the confidence level at 95% level. Lat (Long) are the latitude (longitude) of the mean virtual geomagnetic pole; with uncertainties $\delta p/\delta m$ as the semi-axes (parallel/perpendicular, respectively) of the 95% confidence level ellipse on that paleomagnetic pole.

2.4.3 Magnetostratigraphy and inter-well correlation

The magnetostratigraphy of each borehole was constructed according to the clusters of interpreted normal- and reversed-polarity ChRMs. The magnetostratigraphy with polarity ratings for the lithology column of the Morsleben borehole is given in Figure 6; and those for the Neubrandenburg and Tarnow boreholes are in Suppl. Figures A.5 and A.6. Apparent polarity derived from ChRMs that had maximum angular deviations exceeding 15° were not incorporated in the magnetostratigraphy columns. Intervals in which the apparent polarity is based only on clusters of ChRMs with low NPP-N?/RPP-R? quality ratings were denoted by dark gray or light gray blocks to indicate that these are less reliable.

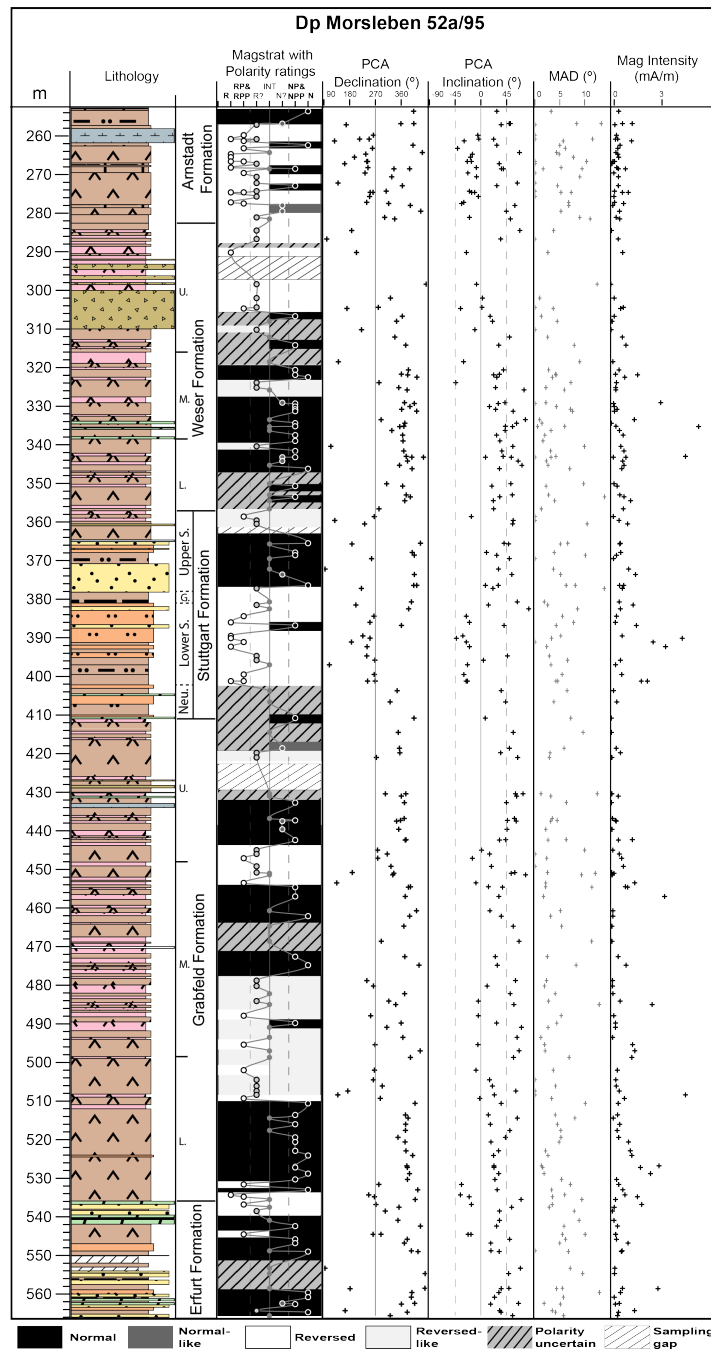


Figure 2.6. Magnetostratigraphy with polarity quality-ratings (open circles superimposed on the black-white polarity column) and lithology of the Morsleben borehole. Half-width bars indicate a single sample with an interpreted polarity opposite to the polarity of adjacent samples. Declinations, inclinations, maximum angle deviation (MAD, in degrees) and intensity (mA/m) are given for the ChRMs calculated by Principle Component Analysis (PCA) (Kirschvink, 1980). All MADs are less than 15°, thereby indicating a relatively good quality for these PCA directions. Declinations are after re-orientation to the early-removed overprint that was interpreted as the Brunhes North component. Gd.= Gaildorf Member; U.= Upper; M.= Middle; L.= Lower. See Figure 3 for the lithology legend.

We adapted a nomenclature modified after Kent et al. (1995) for the polarity magnetozones, in which the pairs of a lower predominantly normal-polarity "n" and an overlying reversed-polarity "r" magnetozones are numbered stratigraphically upward from the base of the section, and brief polarity subzones are indicated by a decimal (e.g., "r.1n"). Eight main magnetozones are identified in the Morsleben well, from M0 to M7 (M = Morsleben), of which the incomplete M0 and M7 have only a partial normal-polarity magnetozones. Five main zones are defined in the Neubrandenburg borehole (N1 to N5; with N = Neubrandenburg). The paleomagnetic results from the poorly preserved (and longer stored) sediments from the limited recovery in the Tarnow borehole are of relatively poorer reliability (Fig. A.6), therefore only 4 incomplete magnetozones of T1r, T2r, T3r and T4n (T= Tarnow) could be assigned.

2.5 Discussion

2.5.1 Composite magnetostratigraphy of the Germanic Basin

The magnetostratigraphic correlation among the three boreholes is guided by the rock formations (blue lines in Fig. 7B) followed by the relative dominance of polarity (red dashed lines in Fig. 7B). Correlations were also compared to potential regional gamma-ray (GR) markers (Fig. 3). This implies that magnetozones M5 in Morsleben correlates with N4 in Neubrandenburg in which M5r and N4r span the boundary between the Upper Stuttgart Formation and Weser Formation in each borehole (the two GR peaks numbered 1 in Fig. 3). Going downward, the upper part of magnetozones M4r is correlated with magneto-subzone N2r.2r that spans the boundary between the Upper and the Lower Stuttgart (GR peaks coded 2 in Fig. 3). The lower part of magneto-subzone N2r.1r in Neubrandenburg is coeval with Tarnow magnetozones T2r in the Neubrandenburg Member (characterized by a broad GR peak numbered 4 in Fig. 3). An uncertain magnetozones "M4?" due to lack of reliable data points in Morsleben is interpreted as a magnetozones dominated by reversed polarity based on the results from Neubrandenburg and Tarnow (N1r and T1r) (Fig. 7). Lower N1r in the upper Grabfeld Formation correlates with T1r (within a GR peak in both wells). M4n is presumably correlative with N1n, and both fall within a subtle trough in GR.

These correlations and the corresponding composite assume that there are intervals of relative condensations or surges of sedimentation (e.g., the expanded record of Neubrandenburg

Formation in its type borehole), but that there are no major gaps within the stratigraphy of these three wells. The completeness of the stratigraphy was based on comparison of these formations within arrays of boreholes and seismic regional mapping (e.g., Beutler et al., 2005; Franz et al., 2018a).

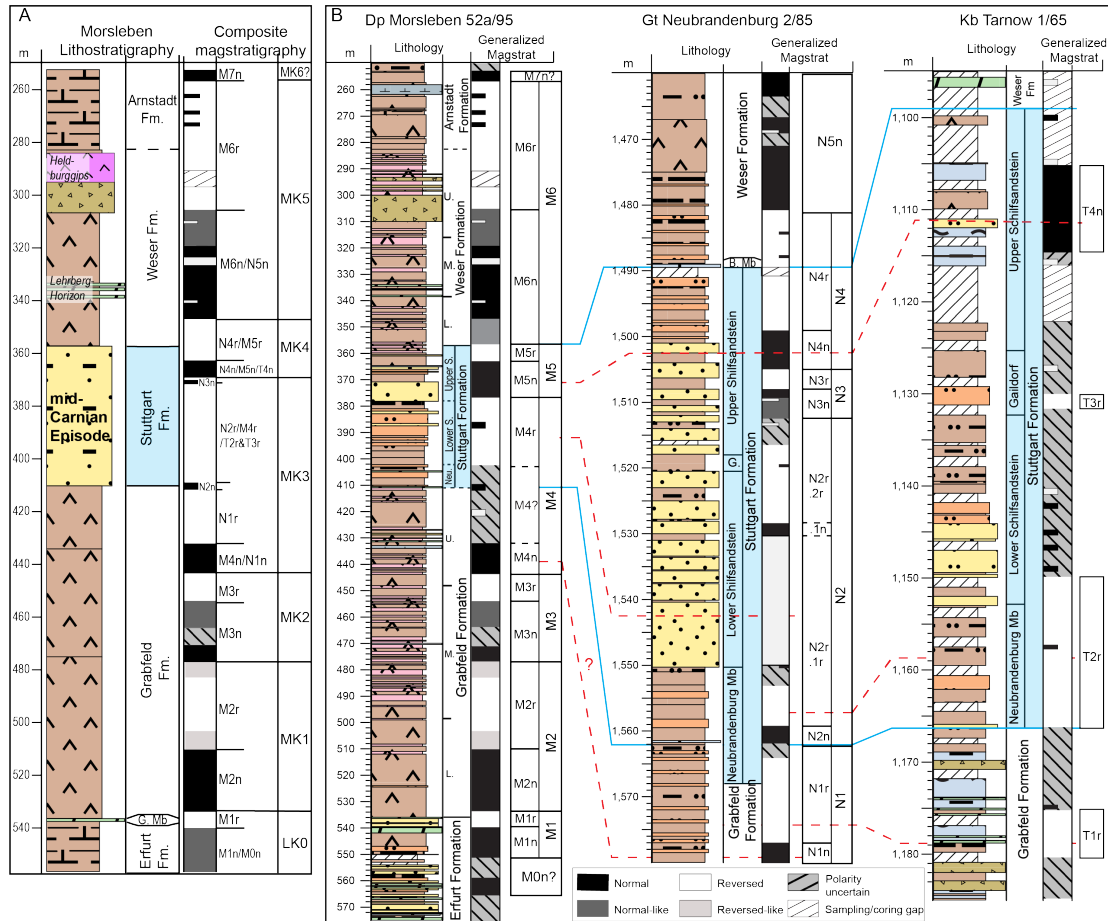


Figure 2.7. Inter-well correlation based on litho-magnetostratigraphy of the three boreholes in northern Germany (panel B) and the corresponding composite magnetostratigraphy for the generalized lithological units of Morsleben, northern Germany (panel A). The Lehrberg Horizon denotes the lower/middle Weser Formation by dolomitic-claystone variations (Barnasch, 2010). Note that the vertical scaling is enlarged for the Neubrandenburg and Tarnow boreholes. The Stuttgart Formation is highlighted in light blue with solid blue lines marking the formation base/top. In the composite polarity column, 7 main magnetic zones are denoted from LK0-MK6 (LK = Lower Keuper; MK = Middle Keuper) with the boreholes noted that were the sources for the relative widths of the polarity patterns. Red dashed lines indicate the interpreted correlation of the generalized polarity magnetozones of three boreholes; for example, the Morsleben normal-polarity magnetozones M5n in the upper Stuttgart Formation correlates to Neubrandenburg N4n and possibly to Tarnow T4n.

2.5.2 Correlation of the Germanic Basin magnetostratigraphy to the reference magnetic polarity scale

There are numerous magnetostratigraphy studies that span portions of the upper Ladinian, of the Carnian and of the lower Norian. The relative chronostratigraphic ages on these are partially constrained by a few biostratigraphic datums, by cyclostratigraphic scaling, or by interpreted correlations to a potential Mid-Carnian Episode (Fig. 8). Hounslow and Muttoni (2010) synthesized many of these studies into their "MT-UT" scale (Fig. 1), and we use their scale and nomenclature in the following discussions. An astronomically scaled "E" magnetostratigraphy from fluvial-lacustrine successions within the Newark rift basins of eastern North America tied to U-Pb-dated basalt flows capping the succession has been the standard for the Norian-Rhaetian polarity time scale (Kent and Olsen, 1999; Kent et al., 2017; Maron et al., 2019). This Newark polarity pattern extends into the upper Carnian, however, the projected ages and relative polarity-zone widths on that E1 to E7 portion were not derived from astronomical tuning, but on projecting the sediment accumulation rates of the overlying lacustrine cycles downward into this fluvial-dominated lower portion in the Newark borehole. The magnetic polarity zones from the terrestrial Newark basins have been verified in other Newark boreholes and have apparent correlations to the main magnetostratigraphic features observed in magnetostratigraphy studies of marine sediment outcrops (e.g., Hounslow et al., 2010; Kent et al., 2017), with the exception of the basal E1 to E4 portion.

A merger of the Hounslow-Muttoni MT-UT scale and the Newark "E" scale with an enhancement from a cycle-scaled lower Carnian polarity zonation from South China (Zhang et al., 2015) was presented as a reference polarity scale in GTS2016 (Ogg et al., 2016). That GTS2016 scale was similar to the one by Maron et al. (2019), who had corrected the placement for the Norian-Carnian stage boundary according to the position of the candidate GSSP within the Pizzo Mondello magnetostratigraphy and had utilized major reference sections for scaling instead of the composite by Hounslow and Muttoni (2010).

Our Germanic Basin composite magnetostratigraphy spans the entire Carnian stage. In this composite model, the major MK5 magnetozone of the Germanic Basin suite (Fig. 7) was divided into six sub-zones of MK5n.1n through MK5r.2r. (Fig. 8B). A gap in reliable data from the gypsum-rich interval at ca. 290–298 m in Morsleben is tentatively assigned as magnetochron MK5r.1n. The main polarity features in the Germanic Basin composite are consistent with the

main aspects of polarity patterns in other important magnetostratigraphic reference sections (Fig. 8). The upper portion of this interpretation and the projection of a normal polarity zone PM5n from Pizzo Mondello to the MK5r.1n data gap is based on the biostratigraphic evidences for continuous sedimentation in the upper Carnian–lower Norian interval of MK5n.2n to MK5r.1r without major hiatuses or abrupt sediment accumulation rate surges at the evaporite or paleosol horizons (Table A.2). In turn, the biostratigraphic and astronomical-cycle scaling of those other reference sections enable the Germanic Basin polarity pattern to be incorporated into an enhanced magnetic polarity time scale to span the entire Carnian.

We briefly summarize the logic behind the array of numbered correlation lines among these sections (Fig. 8).

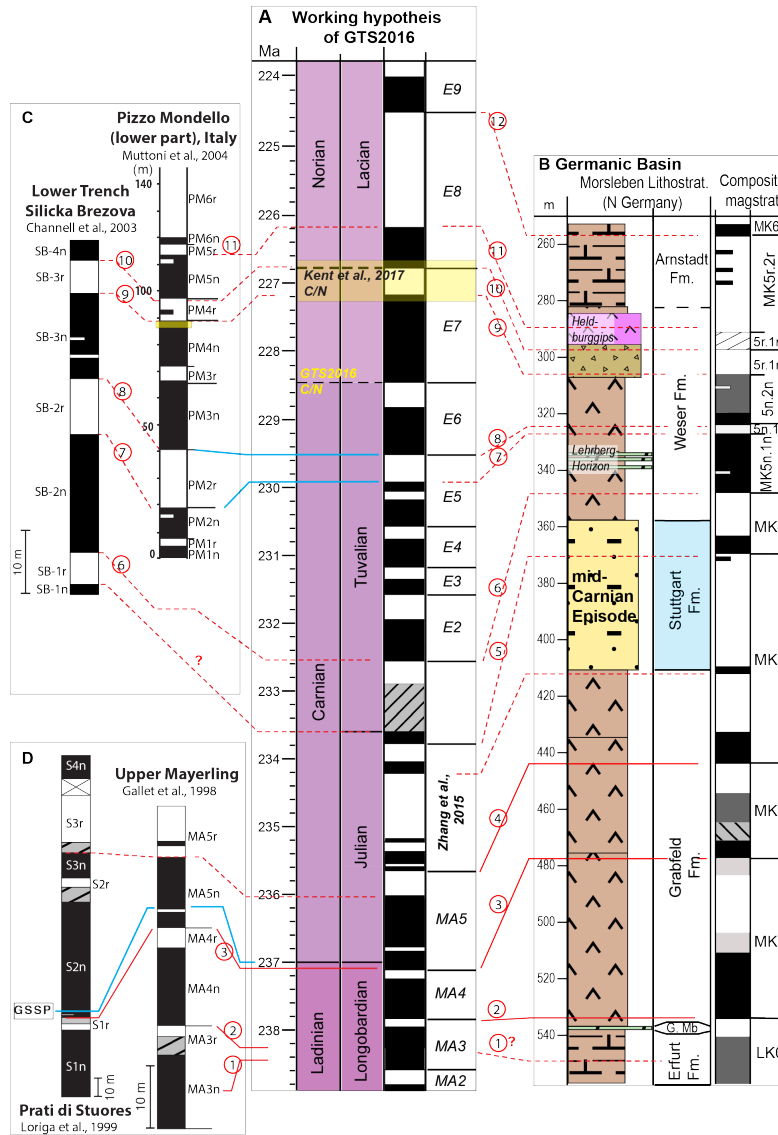


Figure 2.8. Proposed correlations of the main magnetostratigraphy features as guided by biostratigraphy and lithology of the Germanic Basin composite (B) of this study to other biostratigraphically-constrained magnetostratigraphy sections. Note that the originally defined MK5 in Fig. 7 is divided into six subchrons from lower to upper: MK5n.1n, MK5n.1r, MK5n.2n, MK5n.2n, MK5r.1r, MK5r.1n, and MK5r.2r. Circled numbers along with red lines (solid/dashed) denote the proposed correlations, with the solid lines of more confidence. (A) The reference polarity pattern used in GTS2016 (Ogg et al., 2016), which adopted the most recent synthesis in Maron et al. (2019). The Carnian/Norian (C/N) boundary is placed at the top of E7r according to Kent et al. (2017) and Maron et al. (2019) (translucent yellow box). (C) Upper Carnian sections including Lower Trench section at Silická Brezová (= SB) (Channell et al., 2003) and Pizzo Mondello (= PM), Sicily (Muttoni et al., 2004). The proposed C/N boundary GSSP is defined as the first occurrence of conodont *M. pavus* in the uppermost PM4n by Mazza et al. (2018) (narrow yellow bar). (D) Latest Ladinian to lower Carnian magnetostratigraphy in Prati di Stuores section (Italy) (= S) (Loriga et al., 1999) and upper Mayerling section (Austria) (= MA) (Gallet et al., 1998). The GSSP of base Carnian is marked at Lower Trench section.

Julian Substage; Correlation lines #1 to #5

Correlation lines #4 and #5 (middle through late Julian)

The magnetostratigraphic correlations in the mid-Carnian are constrained by the widespread Mid-Carnian Episode of latest Julian, which was originally recognized as the Stuttgart Formation in the Germanic Basin that was the focus of our study. The polarity pattern for the late Julian in the GTS2016 reference scale (Fig. 8A) is the astronomical-cycle-tuned magnetostratigraphy of the Wayao section in South China (Zhang et al., 2015), in which the upward transition from the relatively long-reversed-polarity-dominated light-gray limestone into dark clay-rich carbonates was followed by normal-polarity-dominated marls. This transition is considered to be equivalent to the early phases of the Mid-Carnian Episode (e.g., Sun et al., 2019) (Correlation line #6). Below the relatively long reversed-polarity zone at Wayao is a thin normal-polarity-dominated zone (Zhang et al., 2015). This polarity pattern of the middle through upper Julian is nearly identical to that in the upper Grabfeld through Stuttgart formations (magnetozones MK3-MK4n), as indicated by Lines #4 and #5.

Correlation lines #1, #2 and #3 (uppermost Ladinian to lower Julian)

Counting-downward with the polarity zones from the well-constrained MK3n correlations of mid-Julian, the Ladinian/Carnian stage boundary at the base of MA5 would be placed at the base of MK2 in the lower Grabfeld Formation (Fig. 8B). The uppermost Ladinian (Longobardian Substage), here including full magnetochrons MA4 to MA3, correlates to the polarity patterns of MK1 and LK0 in the middle-lower Grabfeld Formation and uppermost Erfurt Formation (Correlation lines #1 & 2). This correlation is in great consistency with the biostratigraphy constraints (detailed in Section 2) that middle Grabfeld Formation and uppermost Erfurt Formation belongs to upper Ladinian. It's worth to mention that the thick MK1r is composed of mostly R? samples with only three absolute R; in addition, there is a thick gypsum layer in upper middle MK1r. These could result in a shorter duration of the MK1 to match the brief MA4r.

Tuvalian Substage to lower Norian; Correlation lines #5 to #12

It is challenging to correlate the composite magnetostratigraphy to Newark series. For example, the middle Tuvalian reference scale with schematic polarity zones "E2" through "E8n" is uncertain. Nevertheless, there should be a general characteristic of relatively normal-polarity-dominated interval (E3n–E5n) with one or two brief reversed-polarity intervals for the middle

Tuvalian. This general pattern is consistent with the magnetostratigraphy from the Germanic Basin (MK5n.1n; Fig. 8B).

Correlation lines #5 to #9 (early to middle Tuvalian)

The Weser Formation begins in the lower Tuvalian according to biostratigraphic constraints (detailed in Section 2). The thin normal-polarity zone MK4n is thus correlated to the brief normal polarity zone of uppermost Julian from South China. The Julian/Tuvalian boundary is thus placed at the base of reversed-polarity zone MK4r in the uppermost Stuttgart Formation. Therefore, the data-gap spanning the lowermost Tuvalian in the schematic reference magnetic time scale of the GTS2016 composite, which Hounslow and Muttoni (2010) had labeled as uncertain arbitrary UT5–UT9 pending future magnetostratigraphy, is a single reversed-polarity zone MK4r of the lowermost Weser Formation (Correlation line #5).

The dominance by normal polarity of MK5n.1n through MK5n.2n in the middle Weser Formation contrasts with the relative abundance and thicknesses/durations that had been assigned to reversed-polarity zones within in the lowermost E-series of E2 to E6. We suggest that the temporal extent of some of the other reversed-polarity E-series magnetozones of E2r–E4r and E6r may have been overestimated or there may have been interpretations of reversed polarity that should be revisited (e.g., the relative span assigned to the E2r magnetozone).

Therefore, we assign the thick normal-polarity-dominated interval (MK5n.1n) of middle Tuvalian with indications of at least two thin reversed-polarity intervals (including the white half-width bar in Fig. 8B) to be equivalent to for the normal-polarity-dominated lower portion of the Newark sequence of E2n–E5n (delimited by Correlation lines #6 to #8). The relatively thick reversed-polarity zone MK5n.1r would then correlate to the relatively long-duration magnetozone E5r of the lowest Newark succession (Correlation lines #7 and #8), which has been correlated to the thick magnetozone PM2r of Upper Carnian at Pizzo Mondello (e.g., Kent et al., 2017) (Fig. 8C). The following normal-polarity interval of MK5n.2n is interpreted to be coeval with the normal-polarity-dominated intervals of E6–E7 and Pizzo Mondello PM3n–4n–5n–6n (Lines #8 and #9). The thin PM3r at Pizzo Mondello and the corresponding E6r of the Newark sequence were apparently not resolved in the relatively slower deposition systems of the Germanic Basin.

The higher correlation lines #9 to #11 are independently supported by cyclostratigraphy. Barnasch (2010) proposed that 3 repetitions of mudstone/breccia/gypsum followed by 3 cycles of

mudstone/gypsum within the upper Weser Formation, which is approximately the interval spanned by the uppermost MK5n.2n to lowermost MK5r.2r, were three 405-kyr long-eccentricity cycles followed by three ~100 kyr short-eccentricity or ~41 kyr obliquity orbital cycles, respectively. This interpretation would imply a duration of ~1.4-1.5 Myr for magnetozone MK5r, which is approximately the same as the projected duration of uppermost E7n to lowermost E8r.

Correlation lines #10, #11 and #12 (Carnian/Norian boundary interval)

The proposed Carnian/Norian boundary at the GSSP candidate of Pizzo Mondello is the first occurrence (FO) of conodont *Metapolygnathus parvus* within the uppermost magnetozone PM4n after a global conodont faunal turnover with the extinction of the typically Carnian genus *Carnepigondolella* (Mazza et al., 2018) (yellow bar in Fig. 8C). This is considered to be equivalent to a level in the uppermost Newark magnetozone E7n (Kent et al., 2017).

The uppermost Weser Formation and the basal Arnstadt Formation consists of a thick normal-polarity-dominated magnetozone MK5n.2n followed by a thick reversed-polarity-dominated (MK5r) in the Morsleben borehole that contains a ~8-m in a data gap. Based upon the relative spans of the polarity zones and assuming a semi-stable accumulation rate in this interval of the Morsleben borehole, we suggest that the ~8-m data gap projects to the span of Newark normal-polarity E8n and Pizzo Mondello PM5n, and therefore designate a tentative "MK5r.1n". This interpretation implies that the candidate placement for the Carnian/Norian boundary within the upper part of Pizzo Mondello PM4n and equivalent Newark E7n is in upper magnetozone MK5n.2n below the salt ablation interval (Correlation lines #9 and #10).

The basal Arnstadt formation has been commonly assigned to begin in the earliest Norian according to the occurrence of monospecific conchostracan *Shipingia weemsi* zone (see Section 2). Based on the gradual change of conchostracan faunas and on lithology investigations (e.g., Franz et al., 2018a), there does not appear to be any significant time gap between the Arnstadt and the underlying Weser formations. Therefore, if we assume that conchostracan-constrained age is accurate in its implied basal-Norian chronostratigraphic age, then the thick magnetozone MK5r.2r represents the relatively long-duration Newark chron E8r (Correlation lines #11 and #12). This correlation implies that the poorly documented normal-polarity zone MK6n of lowest Arnstadt Formation (Fig. 8B) would be correlative to E9n.

2.5.3 Correlation with Italian magnetostratigraphy sections

There are two magnetostratigraphy sections in Italy that span portions of the Upper Carnian (Pignola-2 and Dibona sections in Maron et al., 2017) that overlap with the upper portion of our Germanic Basin succession. Based on their stratigraphic constraints and using mainly the higher-quality paleomagnetic data published for those sections, we propose a correlation to the composite Germanic Basin and Wayao polarity pattern that differs slightly from that given in Maron et al. (2017), but would be consistent with a proposed episode of humid climate near the Tuvallian 1/2 boundary (Roghi et al., 2010; Dal Corso et al., 2018b).

The green radiolarian-rich clay horizon within the Calcari con Selce Formation of the Pignola-2 section had been interpreted as an influx of siliciclastics during the Mid-Carnian Episode (Maron et al., 2017). However, palynomorph *G. rudis* assemblage was found ~0.7 m below the ash bed in Pignola-2 with the co-occurrence of Tuvallian conodonts like *Metapolygnathus nodosus* (Furin et al., 2006). The age of the *G. rudis* assemblage has been calibrated by ammonoid biostratigraphy to the *T. subbullatus*-*A. spinosus* zones (e.g., Roghi, 2010; Dal Corso et al., 2018); therefore, the green clay horizon must post-date the main Mid-Carnian Episode of late Julian. The Aglianico ash bed (5-cm-thick) within the clay horizon yielded zircons dated by U-Pb methods as 230.91 ± 0.33 Ma (Furin et al., 2006). That 231 Ma radiometric age projects to the lower-middle of the *Tropites subbullatus* zone in our suggested Carnian age model (Fig. 9A) and implies that the normal-polarity dominance above that level in the Pignola-2 section would correspond to a portion of the extended MK5n.1n of the Germanic Basin. Interestingly, this correlation would suggest that the onset of the clay-rich interval might be correlative with the dolomitic layers of the Lehrberg Horizon, which records a short-term marine ingression into the Germanic Basin. Both of these events may correspond to a brief humid episode near the Tuvallian 1/Tuvallian 2 regional boundary and probably coincide with a fourth negative carbon isotope excursion (Roghi et al., 2010; Dal Corso et al., 2018a) (Column C in Fig. 9). A typical Julian conodont association has been interpreted from the Calcari con Selce Formation below the clay-rich horizon (e.g., Furin et al., 2006; Maron et al., 2017). Therefore, the reversed polarity of the lower Calcari con Selce Formation is correlated by us to reversed-polarity zone WYr, and implying a hiatus or condensation of ca. 2.5 myr at the facies boundary in the Lagonegro Basin.

The Dibona section in the Dolomites includes three siliciclastic pulses, which were coded as B-C-D by Roghi et al. (2010). The lower B and C episodes in the Heiligkreuz Formation were correlated to the Mid-Carnian Episode, and the Julian/Tuvalian substage boundary (J/T) was assigned to the top of the C episode (Dal Corso et al., 2018b). The base of the Travenanzes Formation is an unconformable contact onto the underlying Dibona sandstone member and contains a siliciclastic D pulse in its middle part. The D pulse contains an association of the palynomorph *Granuloperculatipollis rudis* and *Riccisporites cf. R. tuberculatus* and was interpreted being Tuvalian 2 in age (Fig. 9). Therefore, the D pulse might correspond approximately to the clay horizon of Pignola-2 section and thus the Lehrberg Horizon. The lowermost Travenanzes Formation yielded an indication of a reversed-polarity base overlain by a normal-polarity interval, and we suggest that this might correlate with the brief reversed-polarity horizon within the MK5n.1n near Tuvalian 1/Tuvalian 2 boundary (Fig. 9). The co-occurrence of conodonts *Paragondolella noah* and *Metapolygnathus praecommunisi* in the underlying Lagazuoi Member of Heiligkreuz Formation has been interpreted as Tuvalian 1 in age. Therefore, we tentatively place a ca. 0.4 myr hiatus at the top of Heiligkreuz Formation (Fig. 9), consistent with the projection in Bernardi et al. (2018). Even though only a few of the paleomagnetic samples from the Dibona section yielded unambiguous polarity interpretations (Maron et al., 2017), the upward change from normal-polarity-dominated to the suggested reversed polarity at the interpreted J/T boundary is consistent with the polarity change at the approximately equivalent stratigraphic level in the Stuttgart Formation in the Germanic Basin (Fig. 9).

2.5.4 Correlation with Qingyangou section, South China

Multiple efforts have been done to correlate the stratigraphy of Qingyangou section in Hanwang (HWQ; previously called the Hanwang magnetostratigraphy section in Zhang et al., 2015), Sichuan Basin of South China to other global events within the Carnian. The demise of shallow-water carbonates at the sharp lithological change from oolitic-bioclastic limestone and sponge reef mounds to dark grey terrigenous clastics had been interpreted to be a local manifestation of the Mid-Carnian Episode according to the magnetic polarity correlation in Zhang et al. (2015) and Shi et al. (2017). However, detailed biostratigraphic and carbon stable isotope data from HWQ by Jin et al. (2018a, b) suggested that this carbonate crisis in HWQ may not have occurred until the end of the Carnian with the magnetostratigraphy of the section

spanning latest Tuvalian to early Norian. We adopted the age assignment of Jin et al. (2018a) to suggest a polarity match based upon the two thick intervals of reversed polarity (Fig. 9).

2.5.5 The Carnian polarity time scale and implied chronostratigraphy of the Germanic Basin formations

By correlating the composite magnetostratigraphy from the Germanic Basin to other reference sections, we compile a polarity scale spanning the entire Carnian Stage (Fig. 9). The polarity chrons MA3 and MA4 of latest Ladinian (Maron et al., 2019) are also verified by the Germanic composite (Fig. 8). This Carnian polarity time scale implies that the former "uncertain" gap of a provisional "UT5-UT9" (Hounslow and Muttoni, 2010) in the early Tuvalian substage (Fig. 1) consists of a single reversed-polarity-dominated magnetozone MK4r.

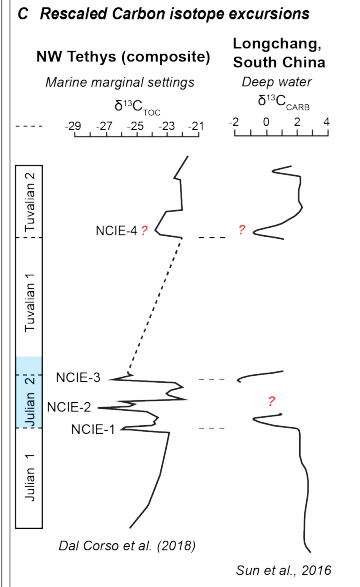
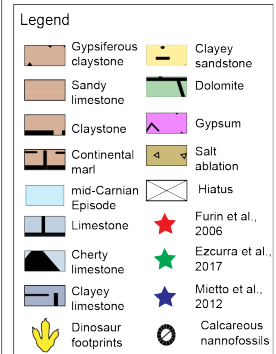
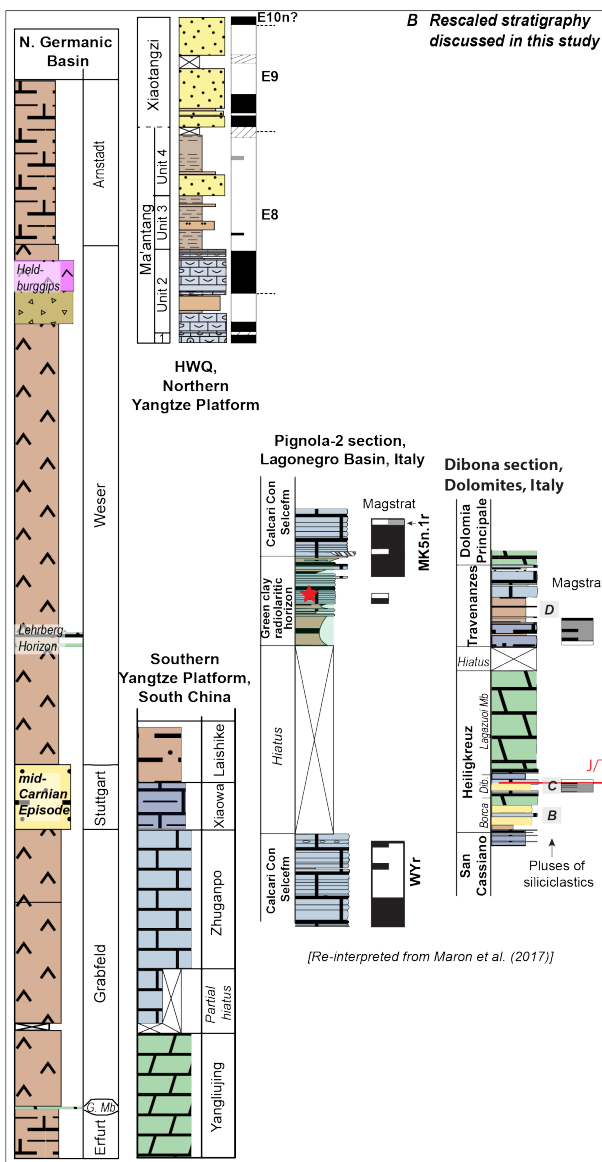
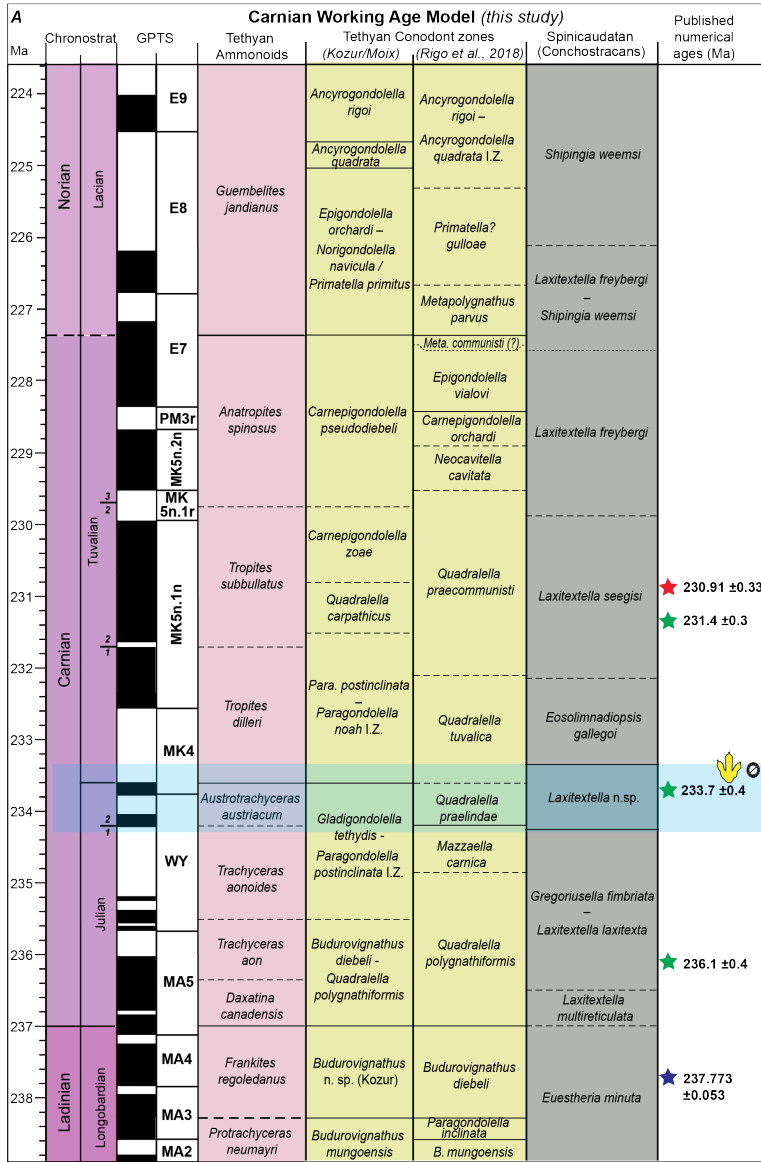
We are aware of the inherent uncertainty in merely trying to match magnetic polarity patterns among this array of sections, especially where two (Germanic Basin and the fluvial facies of the lower Newark) lack reliable correlation to marine-based biostratigraphic zones and undoubtedly have variable accumulation rates. For example, by using different assumptions, it is possible to propose alternate correlations and thus scaling of the polarity patterns in the upper Weser Formation in which the major polarity zone MK5n is regarded as an expanded record of Newark polarity zones E2n-E5n (elaborated in Appendix A, Section 3).

In the composite of our preferred interpretation, the base of the Arnstadt Formation lies in the upper portion of magnetochron E8r, therefore has a projected age of earliest Norian. The brief reversed-polarity pattern within MK5n.1n (Fig. 8B) is correlative with the thin reversed-polarity zone at Pizzo Mondello (PM1r), and perhaps to the single reversed sample just above the green clay horizon in Pignola-2; and all of these levels may be near a proposed humid-climate excursion at the Tuvalian 1 to 2 boundary (Roghi et al., 2010). The brief MK5n.1r is equivalent with the E5r of Newark, PM2r of Pizzo Mondello, SB-3r of Lower Trench at Silická Brezová, and potentially the single reversed polarity sample in the uppermost Pignola-2 magnetostratigraphy.

Applying this composite polarity time scale to the rock units of the Middle Keuper within the Germanic Basin yields a ~3.5 Myr span for the Grabfeld Formation, ~1 Myr for the Stuttgart Formation (the Mid-Carnian Episode), and ~7.2 Myr for the Weser Formation (Fig. 9). The implied sediment accumulation rates in the Morsleben 52a/95 are ca. 37 m/Myr for the Grabfeld

Formation, increasing to 50 m/Myr for the increased influx of sands in the Stuttgart Formation during the Mid-Carnian Episode, slowing to an average of 11 m/Myr for the evaporite-claystone and paleosols of the Weser Formation playa, then increasing to ~21 m/Myr in the uppermost Weser Formation and the transition to the Arnstadt Formation.

Figure 2.9. (A) Age model for the Carnian Stage with the magnetic polarity scale developed in this study, selected biostratigraphic zones, published radiometric dates and the projected first occurrences of dinosaur footprints and nannoplankton. The nomenclature for the main magnetochrons in indicate the main reference compilations: MA from Mayerling in Austria (Maron et al., 2018), WY from Wayao in South China (Zhang et al., 2015), MK4 and MK5 from the composite Germanic Basin magnetostratigraphy (Fig. 8), PM3r from Pizzo Modello in Italy (Muttoni et al., 2004), and E7-E9 from the Newark series (Kent et al., 2017). Tethyan conodont zonations are rescaled from Rigo et al. (2018) with the Carnian-Norian boundary correlations from Mazza et al. (2018) and with nomenclature of genera as recommended by Michael Orchard (pers. commun., Nov 2019). Spinicaudata (formerly called conchostracans) zones are from Geyer and Kelber (2018) using correlations to Germanic basin stratigraphy from Franz et al. (2018). Radiometric dates are from Furin et al. (2006), Ezcurra et al. (2017) and Mietto et al. (2012). (B) Rescaled composite lithostratigraphy of the northern Germanic Basin, and of magnetostratigraphy reference sections from South China, from a portion of the Pignola-2 section in the Lagonegro Basin and from the Dibona section in the Italian Dolomites (Maron et al., 2017). The scaling for the HWQ section of South China is based on the biostratigraphy and carbon isotope interpretation of Jin et al. (2018a, b) as detailed in Section 5.3. The “B, C & D” labels in the Dibona section are siliciclastic pulses (Roghi et al., 2010) and the red line marks the Julian/Tuvalian (J/T) boundary based on conodonts (Maron et al., 2017). (C) Composite of negative carbon isotope excursions from NW Tethys (Dal Corso et al., 2018b) and from the Longchang section in South China (Sun et al., 2016, 2019) rescaled to this age model.



2.6 Conclusions

Three boreholes through the Middle Keuper formations of the Germanic Basin yielded overlapping records of magnetic polarity successions spanning the entire Carnian, including the Mid-Carnian Episode. The composite Carnian magnetostratigraphy from the Germanic Basin has 7 main magnetozones. The main features can be correlated with Newark series of eastern North American, and enhance the main polarity patterns obtained from Carnian reference sections like Pizzo Mondello (Fig. 8). The former gap in coverage that had been indicated as an uncertain 'UT5-9' of early Late Carnian (Hounslow and Muttoni, 2010; Maron et al., 2019) is represented by ca. 1-myrs reversed-polarity zone MK4r (Fig. 9A), where "MK" denotes Middle Keuper.

The Mid-Carnian Episode as represented by the sand-rich Stuttgart Formation (Schilfsandstein) in the Germanic Basin is coeval with the termination of the Yangtze carbonate platform of South China, according to the magnetostratigraphy of the Wayao (or Xiaowa) Formation. The magnetostratigraphic correlations imply that the greenish radiolarian-rich claystone of the Pignola-2 section, which contains a volcanic ash that yielded a U-Pb date of 230.9 ± 0.3 Ma, is within magnetozone MK5n.1n; thereby serving as an age constraint for the middle Tuvalian portion of the Carnian magnetic polarity time scale. This green clay horizon in Pignola-2 is correlative to the D pulse of siliciclastics in Dibona section, which may correspond to the Lehrberg Horizon and marine incursion in the Germanic Basin and to a negative carbon isotope excursion (NCIE-4 in Fig. 9) in the northwest Tethys.

The magnetic polarity correlations imply that the non-cyclic fluvial facies of the lower Newark series begin in the early Late Carnian (early Tuvalian). This interval is dominated by normal polarity in the Germanic basin boreholes; therefore it suggests that the published polarity pattern for this lowermost Newark succession may have over-emphasized the relative durations of some of its reversed-polarity intervals.

In the future, this magnetic polarity model can be applied and tested at other sections to enhance global correlation, especially to deposits interpreted as regional signatures of the Mid-Carnian Episode and to formations hosting the earliest dinosaur records in South America.

Acknowledgements

Dr. Gabi Ogg is greatly thanked for arranging and aiding the paleomagnetic sample drilling in Germany, and she also provided numerous enhancements to the manuscript. Lena Wallbrecht and Dr. Jochen Erbacher enabled the sampling of the Morsleben core and pilot measurements at the Grubenhagen lab. Dr. Ken Kodama and John Geissman graciously allowed use of their paleomagnetic labs at Lehigh University and at University of Texas at Dallas, respectively. Funding for fieldwork, graduate-student support, and international travel costs for Yang Zhang and Mingsong Li is mostly from the Geologic TimeScale Foundation (USA).

2.7 References

- Aigner, T., and Bachmann, G. H., 1992, Sequence-stratigraphic framework of the German Triassic: *Sedimentary Geology*, v. 80, no. 1-2, p. 115-135.
- Barnasch, J., 2010. Der Keuper im Westteil des Zentraleuropäischen Beckens (Deutschland, Niederlande, England, Dänemark): diskontinuierliche Sedimentation, Litho-, Zyklo- und Sequenzstratigraphie. *Schriftenreihe der Deutschen Gesellschaft für Geowissenschaften* 71, 1-169. <http://digital.bibliothek.uni-halle.de/hs/urn/urn:nbn:de:gbv:3:4-1137>
- Barrenechea, J. F., López-Gómez, J., and De La Horra, R., 2018, Sedimentology, clay mineralogy and palaeosols of the Mid-Carnian Pluvial Episode in eastern Spain: insights into humidity and sea-level variations: *Journal of the Geological Society*.
- Bernardi, M., Gianolla, P., Petti, F. M., Mietto, P., and Benton, M. J., 2018. Dinosaur diversification linked with the Carnian Pluvial Episode. *Nature Communications* 9, article no. 1499, 1-10. <https://doi.org/10.1038/s41467-018-03996-1>
- Beutler, G., and Häusser, I., 1982, Über den Schilfsandstein der DDR: *Zeitschrift für Geologische Wissenschaften*, v. 10, no. 4, p. 511-525.
- Beutler, G., Hauschke, N., Nitsch, E., and Vath, U., 2005. *Stratigraphie von Deutschland, IV - Keuper*. Courier Forschungs-Institut Senckenberg 253, 1-296.
- Channell, J., Kozur, H. W., Sievers, T., Mock, R., Aubrecht, R., and Sykora, M., 2003, Carnian–Norian biomagnetostratigraphy at Silická Brezová (Slovakia): correlation to other Tethyan sections and to the Newark Basin: *Palaeogeography, Palaeoclimatology, Palaeoecology*, v. 191, no. 2, p. 65-109.

- Dal Corso, J., Benton, M.J., Bernardi, M., Franz, M., Gianolla, P., Hohn, S., Kustatscher, E., Merico, A., Roghi, G., Ruffell, A., Ogg, J.G., Preto, N., Schmidt, A., Seyfullah, L., Simms, M., Shi, Z., and Zhang, Y., 2018a. First workshop on the Carnian Pluvial Episode (Late Triassic): A report. *Albertiana* 44, 49-57. https://albertiana-sts.org/wp-content/uploads/2018/02/44-4-Corso_etal.pdf
- Dal Corso, J., Gianolla, P., Rigo, M., Franceschi, M., Roghi, G., Mietto, P., Manfrin, S., Raucsik, B., Budai, T., Jenkyns, H. C., Reymond, C. E., Caggiati, M., Gattolin, G., Breda, A., Merico, A., and Preto, N., 2018b. Multiple negative carbon-isotope excursions during the Carnian Pluvial Episode (Late Triassic). *Earth-Science Reviews* 185, 732-750. <https://doi.org/10.1016/j.earscirev.2018.07.004>
- Ezcurra, M. D., Fiorelli, L. E., Martinelli, A. G., Rocher, S., von Baczko, M. B., Ezpeleta, M., Taborda, J. R., Hechenleitner, E. M., Trotteyn, M. J., and Desojo, J. B., 2017. Deep faunistic turnovers preceded the rise of dinosaurs in southwestern Pangaea. *Nature Ecology & Evolution* 1 (10), 1477-1483. <https://doi.org/10.1038/s41559-017-0305-5>
- Franz, M., Henniger, M., and Barnasch, J., 2013. The strong diachronous Muschelkalk/Keuper facies shift in the Central European Basin: implications from the type-section of the Erfurt Formation (Lower Keuper, Triassic) and basin-wide correlations. *International Journal of Earth Sciences* 102 (3), 761–780. <https://doi.org/10.1007/s00531-012-0823-y>
- Franz, M., Nowak, K., Berner, U., Heunisch, C., Bandel, K., Röhling, H.G., and Wolfgramm, M., 2014. Eustatic control on epicontinental basins: The example of the Stuttgart Formation in the Central European Basin (Middle Keuper, Late Triassic). *Global and Planetary Change* 122, 305–329. <http://dx.doi.org/10.1016/j.gloplacha.2014.07.010>
- Franz, M., Bachmann, G.H., Barnasch, J., Heunisch, C., and Röhling, H.-G., 2018. Der Keuper in der Stratigraphischen Tabelle von Deutschland 2016 – kontinuierliche Sedimentation in der norddeutschen Beckenfazies (Variante B) / The Keuper Group in the Stratigraphic Table of Germany 2016 – continuous sedimentation in the North German Basin (variant B). *Zeitschrift der Deutschen Gesellschaft für Geowissenschaften (German Journal of Geology)*, 169 (2), 203–224. <https://doi.org/10.1127/zdgg/2018/0114>
- Franz, M., Kustatscher, E., Heunisch, C., Niegel, S., and Röhling, H.G., 2019. The Schilfsandstein and its flora - arguments for a humid mid-Carnian episode? *Journal of the Geological Society* 176, 133–148. <https://doi.org/10.1144/jgs2018-053>

- Furin, S., Preto, N., Rigo, M., Roghi, G., Gianolla, P., Crowley, J.L., and Bowring, S.A., 2006. High-precision U-Pb zircon age from the Triassic of Italy: Implications for the Triassic time scale and the Carnian origin of calcareous nannoplankton and dinosaurs. *Geology* 34 (12), 1009-1012. <http://doi.org/10.1130/g22967a.1>
- Gallet, Y., Krystyn, L., and Besse, J., 1998, Upper Anisian to Lower Carnian magnetostratigraphy from the northern calcareous Alps (Austria): *Journal of Geophysical Research: Solid Earth* (1978–2012), v. 103, no. B1, p. 605-621.
- Gattolin, G., Preto, N., Breda, A., Franceschi, M., Isotton, M., and Gianolla, P., 2015, Sequence stratigraphy after the demise of a high-relief carbonate platform (Carnian of the Dolomites): Sea-level and climate disentangled: *Palaeogeography, Palaeoclimatology, Palaeoecology*, v. 423, p. 1-17.
- Geyer, G., and Kelber, K.-P., 2018. Spinicaudata (“Conchostraca,” Crustacea) from the Middle Keuper (Upper Triassic) of the southern Germanic Basin, with a review of Carnian–Norian taxa and suggested biozones. *PalZ (Paläontologische Zeitschrift)* 92 (1), 1-34. <https://doi.org/10.1007/s12542-017-0363-7>
- Gradstein, F.M., Ogg, J.G., Schmitz, M.D., and Ogg, G.M. (coordinators), 2012. *The Geologic Time Scale 2012*. Elsevier, 1-1144.
- Greene, A.R., Scoates, J.S., Weis, D., Nixon, G.T., and Kieffer, B., 2009. Melting history and magmatic evolution of basalts and picrites from the accreted Wrangellia oceanic plateau, Vancouver Island, Canada. *Journal of Petrology* 50 (3), 467-505. <https://doi.org/10.1093/petrology/egp008>
- Hauschke, N., and Kozur, H. W., 2011, Two new conchostracan species from the Late Triassic of the Fuchsberg, northern foreland of the Harz Mountains northeast of Seinstedt (lower Saxony, Germany). *Fossil Record 3*. New Mexico Museum of Natural History and Science: Bulletin, v. 53, p. 187-194.
- Hahn, G.G., 1984. Paläomagnetische Untersuchungen im Schilfsandstein (Trias, Km²) Westeuropas. *Geologische Rundschau* 73 (2), 499-516.
- Heunisch, C., and Nitsch, E., 2011, Eine seltene Mikroflora aus der Mainhardt-Formation (Keuper, Trias) von Baden-Württemberg (Süddeutschland): *Jahresberichte und Mitteilungen des Oberrheinischen Geologischen Vereins*, p. 55-76.

- Hornung, T., Krystyn, L., and Brandner, R., 2007a, A Tethys-wide mid-Carnian (Upper Triassic) carbonate productivity crisis: Evidence for the Alpine Reingraben Event from Spiti (Indian Himalaya)?: *Journal of Asian Earth Sciences*, v. 30, no. 2, p. 285-302.
- Hornung, T., Brandner, R., Krystyn, L., Joachimski, M.M., and Lorenz, K., 2007b. Multistratigraphic constraints on the NW Tethyan "Carnian Crisis". In: Lucas, S.G. and Spielmann, J.A., (Eds.), *The Global Triassic*. New Mexico Museum of Natural History and Science Bulletin 41, 59-67.
- Hounslow, M.W., and Muttoni, G., 2010. The geomagnetic polarity timescale for the Triassic: linkage to stage boundary definitions. In: Lucas, S.G. (Ed.), *The Triassic Timescale*. Geological Society, London, Special Publication 334, 61-102. <http://dx.doi.org/10.1144/sp334.4>
- Jin, X., McRoberts, C. A., Shi, Z., Mietto, P., Rigo, M., Roghi, G., Manfrin, S., Franceschi, M., and Preto, N., 2018a, The aftermath of the CPE and the Carnian–Norian transition in northwestern Sichuan Basin, South China: *Journal of the Geological Society* 176 (1), 179-196.
- Jin, X., Shi, Z., Rigo, M., Franceschi, M., and Preto, N., 2018b, Carbonate platform crisis in the Carnian (Late Triassic) of Hanwang (Sichuan Basin, South China): Insights from conodonts and stable isotope data: *Journal of Asian Earth Sciences* 164, 104-124.
- Kent, D. V., and Olsen, E., 1999. Astronomically tuned geomagnetic polarity timescale for the Late Triassic. *Journal of Geophysical Research: Solid Earth* 104, no. B6, 12831-12841. <http://dx.doi.org/10.1029/1999JB900076>
- Kent, D. V., Olsen, E., and Muttoni, G., 2017. Astrochronostratigraphic polarity time scale (APTS) for the Late Triassic and Early Jurassic from continental sediments and correlation with standard marine stages. *Earth-Science Reviews* 166, no. Supplement C, 153-180. <https://doi.org/10.1016/j.epsl.2017.06.014>
- Kirschvink, J., 1980. The least-squares line and plane and the analysis of palaeomagnetic data. *Geophysical Journal International* 62 (3), 699-718.
- Kohút, M., Hofmann, M., Havrila, M., Linnemann, U., and Havrila, J., 2018, Tracking an upper limit of the “Carnian Crisis” and/or Carnian stage in the Western Carpathians (Slovakia): *International Journal of Earth Sciences*, v. 107, no. 1, p. 321-335.

- Kozur, H.W., and Bachmann, G.H., 2008. Updated correlation of the Germanic Triassic with the Tethyan scale and assigned numeric ages. In: L. Krystyn and G.W. Mandl, (Eds.), Upper Triassic Subdivisions, Zonations and Events. *Berichte Geologische Bundesanstalt* 76, 53-58.
- Kozur, H. W., and Bachmann, G. H., 2010, The Middle Carnian Wet Intermezzo of the Stuttgart Formation (Schilfsandstein), Germanic Basin: Palaeogeography, Palaeoclimatology, Palaeoecology, v. 290, no. 1-4, p. 107-119.
- Kozur, H.W., and Weems, R. E., 2010. The biostratigraphic importance of conchostracans in the continental Triassic of the northern hemisphere. In: Lucas, S.G. (Ed.), *The Triassic Timescale*. Geological Society, London, Special Publications 334, 315-417. <https://doi.org/10.1144/SP334.13>
- Kozur, H.W., Franz, M., and Bachmann, G.H., 2013. *Shipingia weemsi* n. sp., a biostratigraphically important conchostracan species from the uppermost Carnian and lowermost Norian of Central Europe. In Lucas, S.G. (Ed.), *The Triassic System*. New Mexico Museum of Natural History and Science Bulletin 61, 325-330.
- Li, M.S., Ogg, J.G., Zhang, Y., Huang, C., Hinnov, L.A., Chen, Z.-Q., and Zou, Z., 2016. Astronomical tuning of the end-Permian extinction and the Early Triassic Epoch of South China and Germany. *Earth and Planetary Science Letters* 441, 10-25. <http://dx.doi.org/10.1016/j.epsl.2016.02.017>
- Loriga, C., Cirilli, S., De Zanche, V., Di Bari, D., Gianolla, P., Laghi, G. F., Lowrie, W., Manfrin, S., Mastandrea, A., and Mietto, P., 1999, The Prati di Stuares/Stuares Wiesen section (Dolomites, Italy): a candidate global stratotype section and point for the base of the Carnian stage.
- Maron, M., Muttoni, G., Dekkers, M.J., Mazza, M., Roghi, G., Breda, A., Krijgsman, W., and Rigo, M., 2017. Contribution to the magnetostratigraphy of the Carnian: new magneto-biostratigraphic constraints from Pignola-2 and Dibona marine sections, Italy. *Newsletters on Stratigraphy* 50 (2), 187-203. <https://doi.org/10.1127/nos/2017/0291>
- Maron, M., Muttoni, G., Rigo, M., Gianolla, P., and Kent, D.V., 2019. New magnetobiostratigraphic results from the Ladinian of the Dolomites and implications for the Triassic geomagnetic polarity timescale. *Palaeogeography, Palaeoclimatology, Palaeoecology* 517, 52-73. <https://doi.org/10.1016/j.palaeo.2018.11.024>

- Mazza, M., Nicora, A. and Rigo, M., 2018. *Metapolygnathus parvus* Kozur, 1972 (Conodonta): a potential primary marker for the Norian GSSP (Upper Triassic). *Bollettino della Società Paleontologica Italiana* 57 (2), 81–101. doi:10.4435/BSPI.2018.06
- Mietto, P., Manfrin, S., Preto, N., Rigo, M., Roghi, G., Furin, S., Gianolla, P., Posenato, R., Muttoni, G., and Nicora, A., 2012. The global boundary stratotype section and point (GSSP) of the Carnian stage (Late Triassic) at Prati di Stuores/Stuores Wiesen section (Southern Alps, NE Italy). *Episodes* 35 (3), 414.
- Miller, C.S., Peterse, F., da Silva, A.-C., Baranyi, V., Reichart, G.J., and Kürschner, W.M., 2017. Astronomical age constraints and extinction mechanisms of the Late Triassic Carnian crisis. *Scientific Reports* 7 (1), 2557. <https://doi.org/10.1038/s41598-017-02817-7>
- Muttoni, G., Kent, D. V., Olsen, E., Di Stefano, P., Lowrie, W., Bernasconi, S. M., and Hernández, F. M., 2004. Tethyan magnetostratigraphy from Pizzo Mondello (Sicily) and correlation to the Late Triassic Newark astrochronological polarity time scale. *Geological Society of America Bulletin* 116 (9), 1043-1058. <https://doi.org/10.1130/B25326.1>
- Ogg, J.G., 2015. The Mysterious Mid-Carnian “Wet Intermezzo” Global Event. *Journal of Earth Science* 26 (2), 181-191. doi:10.1007/s12583-015-0527-x
- Ogg, J.G., Ogg, G.M., and Gradstein, F.M., 2016. *A Concise Geologic Time Scale 2016*. Elsevier Publ., 1-234.
- Preto, N., Agnini, C., Rigo, M., Sprovieri, M., and Westphal, H., 2013. The calcareous nannofossil *Prinsiosphaera* achieved rock-forming abundances in the latest Triassic of western Tethys: consequences for the $\delta^{13}\text{C}$ of bulk carbonate. *Biogeosciences* 10 (9), 6053-6068. <https://doi.org/10.5194/bg-10-6053-2013>
- Rigo, M., Mazza, M., Karádi, V., Nicora, A., 2018. New Upper Triassic conodont biozonation of the Tethyan Realm. In: Tanner, L.H. (Ed.) *The Late Triassic World: Earth in a Time of Transition*, *Topics in Geobiology*, 46, Springer Publ., p. 189-235. https://doi.org/10.1007/978-3-319-68009-5_6
- Roghi, G., Gianolla, P., Minarelli, L., Pilati, C., and Preto, N., 2010. Palynological correlation of Carnian humid pulses throughout western Tethys: Palaeogeography Palaeoclimatology Palaeoecology 290 (1-4), 89-106.

- Ruffell, A., Simms, M.J., and Wignall, B., 2016. The Carnian Humid Episode of the late Triassic: a review. *Geological Magazine* 153 (2), 271-284. <https://doi.org/10.1017/S0016756815000424>
- Schlager, W., and Schöllnberger, W., 1974, Das Prinzip stratigraphischer Wenden in der Schichtfolge der Nördlichen Kalkalpen: *Mitt. Geol. Ges. Wien*, v. 66, no. 67, p. 165-193.
- Shi, Z., Preto, N., Jiang, H., Krystyn, L., Zhang, Y., Ogg, J. G., Jin, X., Yuan, J., Yang, X., and Du, Y., 2017, Demise of Late Triassic sponge mounds along the northwestern margin of the Yangtze Block, South China: Related to the Carnian Pluvial Phase?: *Palaeogeography, Palaeoclimatology, Palaeoecology*, v. 474, p. 247-263.
- Simms, M. J., and Ruffell, A. H., 1989, Synchronicity of climatic change and extinctions in the Late Triassic: *Geology*, v. 17, no. 3, p. 265.
- Stampfli, G.M., and Kozur, H.W., 2006. Europe from the Variscan to the Alpine cycles. In: Gee, D.G., and Stephenson, R.A. (Eds.), *European Lithospheric Dynamics*. Geological Society of London, *Memoirs* 32, 57-82.
- Sun, Y.D., Wignall, P.B., Joachimski, M.M., Bond, D.P.G., Grasby, S.E., Lai, X.L., Wang, L.N., Zhang, Z.T., and Sun, S., 2016. Climate warming, euxinia and carbon isotope perturbations during the Carnian (Triassic) Crisis in South China. *Earth and Planetary Science Letters* 444, 88–100. <https://doi.org/10.1016/j.epsl.2016.03.037>
- Sun, Y.D., Richo, S., Krystyn, L., Zhang, Z.T., and Joachimski, M.M., 2019. Perturbations in carbon cycle during the Carnian Humid Episode: Carbonate carbon isotope records from southwestern China and northern Oman. *Journal of the Geological Society* 176, 167-177. <https://doi.org/10.1144/jgs2017-170>
- Szurliés, M., 2007. Latest Permian to Middle Triassic cyclo-magnetostratigraphy from the Central European Basin, Germany: Implications for the geomagnetic polarity timescale. *Earth and Planetary Science Letters* 261 (3-4), 602-619. <https://doi.org/10.1016/j.epsl.2007.07.018>
- Urlichs, M., and Tichy, G., 2000, Correlation of the Bleiglanzbank (Gipskeuper, Grabfeld Formation) of Germany with Upper Ladinian beds of the Dolomites (Italy): *Zentralblatt der Geologie und Paläontologie, Teil II*, v. 1998, p. 997-1007.

- Zhang, Y., Li, M.S., Ogg, J.G., Montgomery, P., Huang, C.J., Chen, Z.-Q., Shi, Z.Q., Enos, P., and Lehrmann, D.J., 2015. Cycle-calibrated magnetostratigraphy of middle Carnian from South China: Implications for Late Triassic time scale and termination of the Yangtze Platform. *Palaeogeography, Palaeoclimatology, Palaeoecology* 436, 135-166. <https://doi.org/10.1016/j.palaeo.2015.05.033>
- Zijderveld, J.D.A., 1967. A.C. Demagnetisation of rocks: Analysis of results. In: Collinson, D.W., Creer, K.M., and Runcorn, S.K. (Eds.), *Methods in Palaeomagnetism*. *Developments in Solid Earth Geophysics* 3, 254-286.

Appendix A Additional stratigraphic and paleomagnetic information

Additional stratigraphic information

There is a continuous depositional succession between the Grabfeld Formation and the overlying Stuttgart Formation in central and northern Germany (this study); whereas a major unconformity exists between these units in southern Germany (Franz et al., 2018a). The Stuttgart Formation is mainly characterized by clayey to sandy sediments that are commonly interpreted as fluvio-deltaic system in northern Germany (Franz et al., 2014, 2018b) and meandering channel-floodplain system in central and southern Germany (Shukla et al., 2010). It is subdivided into two main Lower and Upper Schilfsandstein members, but three transgressions form marker-horizon members: the Neubrandenburg Member (below the Lower Schilfsandstein), the Gaildorf Member between Lower and Upper Schilfsandstein, and the Beaumont Member (lowermost Weser Formation; above the Upper Schilfsandstein) (Franz et al., 2014) (Fig. 3). The Neubrandenburg Member, in northern Germany partly more than 20 m thick, is missing or is very thinned in southern Germany as part of the major disconformity between the Grabfeld and Stuttgart Formations (schematically shown in Figs. 1 and 3). Sediment color varies from dark grey to grey in the transgressions horizons and in the Lower Schilfsandstein to predominantly reddish in the Upper Schilfsandstein and is variegated to reddish in the uppermost Stuttgart Formation and Weser Formation.

The paleomagnetic sampling of Morsleben 52a/95 spans the interval from 253 m to 570 m and encompasses the Arnstadt (Norian), Weser (Carnian), Stuttgart (Schilfsandstein, Carnian), Grabfeld (Carnian-Ladinian) and Erfurt (Ladinian) formations. The paleomagnetic sampling interval of the Neubrandenburg 2 and Tarnow 1 wells includes Weser, Stuttgart, and Grabfeld formations; however, Tarnow is poorly preserved given the fact of being drilled half-a-century ago. These borehole cores provide relatively complete successions of the Stuttgart Formation spanning ~50 m in Morsleben 52a/95, ~72 m in Neubrandenburg and ~68 m in Tarnow. The Gaildorf Member appears as a ~5-m thick horizon of dark clay/shale and silty sediments, but is not well recorded in Tarnow and Morsleben. The Neubrandenburg Member, ~12 m thick in the Neubrandenburg core, is typically a dark colored laminated claystone-siltstone. The Lower Stuttgart Formation is grayish in color while Upper Stuttgart Formation is predominantly reddish/brownish (see lithology descriptions of all samples in the Excel file of Appendix C).

Additional paleomagnetic information

Paleomagnetic instrumentation and demagnetization procedures

An initial pilot set of 30 samples from Morsleben was measured at the paleomagnetic lab in Grubenhagen immediately after the sampling. Bulk susceptibility was measured at 300°C and higher temperature steps to monitor changes in magnetic mineral composition. However, the lack of magnetic-shielded room at that facility required that the rest of the Morsleben specimens were analyzed in the Paleomagnetic lab at the University of Texas at Dallas, hosted by Dr. John Geissman. Neubrandenburg and Tarnow samples were demagnetized in the magnetic-shielded paleomagnetic lab in Lehigh University, hosted by Dr. Ken Kodama. In both labs, the remanent magnetization was measured using a 2G-760R cryogenic magnetometer.

The demagnetization procedure depended on the color of the samples. Most of the reddish/brownish samples, which generally had a stronger natural remanent magnetization (NRM) intensity, underwent a low alternating-field (AF) demagnetization treatment (5 mT) followed by progressive thermal demagnetization in an ASC Scientific TD-48 oven using 50°C steps until 400-450°C and then 25°C steps until 625-650°C. The greyish samples, which had generally weaker NRMs, underwent progressive thermal demagnetization at close-spaced 15-25°C steps after the same initial low field AF treatment. Magnetic susceptibility of Neubrandenburg and Tarnow samples was measured from 250°C onward using a BartingtonMS2 magnetic susceptibility meter to monitor changes in magnetic mineral composition. The progressive thermal demagnetization of a sample was generally terminated when the remanent magnetization displayed either anomalous surge in magnetic susceptibility, was too weak ($<ca. 5 \times 10^{-8}$ A/m) for statistically valid mean directions, or exhibited irregular magnetic directions/intensities for two or three consecutive steps.

The characteristic remanent magnetization (ChRM) of the suite of demagnetization data from each sample was computed by a three-dimensional “least-squares fitting” technique (Kirschvink, 1980) using the public software Paleomagnetic Analysis Program v.4.0 (Zhang and Ogg, 2003).

Orientation of paleomagnetic samples from unoriented boreholes using vectors of removed magnetic components

Generally, there was no declination orientation for these cored/drilled sediments. Therefore, the directions of Natural Remnant Magnetization (NRM) and at thermal demagnetization steps of all samples from the Neubrandenburg and Tarnow boreholes display a

random distribution in their declination (Fig. A.1-A). However, an approximate orientation relative to the present-day magnetic north was often possible by using the initial removed vector during these lowest steps of demagnetization if one assumes that a significant component of this overprint was from the present north-directed magnetic field prior to the borehole drillings. Therefore, we applied a re-orienting of the samples using the vector removed during the initial demagnetization steps of 120°-150°C for weaker specimens and steps of 150°-250°C for stronger ones.

The re-oriented declinations of samples mostly show the removal of northward direction (either northeast or northwest) before reaching the expected present-day North. For example, sample M389.5 m (quality-rated as 'R', Fig. 4) from Morsleben core removed an overprint with a vector of a northeastern direction at 5 mT-150°C, followed by removal of a component that we had interpreted as a present-day North overprint (150°-250°C), and followed by great-circle rotation toward a Carnian southward reversed-polarity direction that was stabilized at thermal demagnetization steps of 480°-575°C. [NOTE: We interpret the first overprint (5 mT-150°C) to be caused by the long-term storage in the Earth's field for the past two decades; and was particularly noticeable for the Morsleben cores which were uniformly drill-pressed "down" into the holding boxes, therefore this first overprint had a common "declination" orientation artifact. Such a long-term storage overprint was not as significant in the samples from the Neubrandenburg and Tarnow boreholes.] This re-orientation transformation resulted in a partial statistical clustering in declination at the low demagnetization steps (Fig. A.1) and helped to separate normal- versus reversed-polarity components upon progressive higher demagnetization for those borehole samples. This also enabled an estimate of the amount of total rotation of this part of the Germanic Basin since the Carnian.

In some cases, it appeared from the NRM magnetizations that some core pieces had been inadvertently inverted upside-down due to handling over the years. We assume the inclination of the NRMs should be positive (pointing downward), and therefore any samples displaying an initial negative (upward) inclination of NRM should have the paleomagnetic measurement array inverted (rotated 180° around minicore-axis) to be positive. In addition, the removed vector or the Brunhes component of those samples is often pointing up indicating upside down. In total, 34 samples were treated upside down, 3 from Morsleben, 19 from Neubrandenburg, and 12 from Tarnow (Appendix B).

Paleogeographic reconstructions imply that the Germanic Basin region has rotated counterclockwise by approximately 40° since the middle Triassic (e.g., Stampfli and Kozur, 2006; Torsvik et al., 2012; Scotese, 2014). The paleo-North magnetic pole was located in present-day easternmost Siberia (Fig. 1). Therefore, if one assumed that the NRM was dominated by a significant overprint from the late Pleistocene north-directed field, then the progressive removal of this overprint to unblock a normal-polarity Carnian direction would be seen in the demagnetization plot as a clockwise drift in declination and then stabilization at approximately 40° relative to the NRM declination, plus a slight shallowing in the inclination. In contrast, the progressive unblocking of a reversed-polarity Carnian direction may be exhibited as a significant counter-clockwise rotation as the vector shifts toward the opposite hemisphere. These trends in great-circle rotation played an important role in making the polarity interpretations of these declination-unoriented core samples that failed to reach a stable endpoint before the onset of spurious magnetizations or loss of magnetization. The ChRMs from these two types of great circle drift that did not attain a semi-stable endpoint were generally assigned 'NP/RP' or 'NPP/RPP' rating, depending upon the subjective judgment if the associated inclination of the highest useful steps was also an indication of the normal/reversed polarity. ChRMs rated as 'NPP/RPP' and were not used for computing the mean directions. Samples with questionable indications of polarity or with spurious behavior were rated as 'N?/R?' or 'INT', and were generally not used for assigning polarity zones.

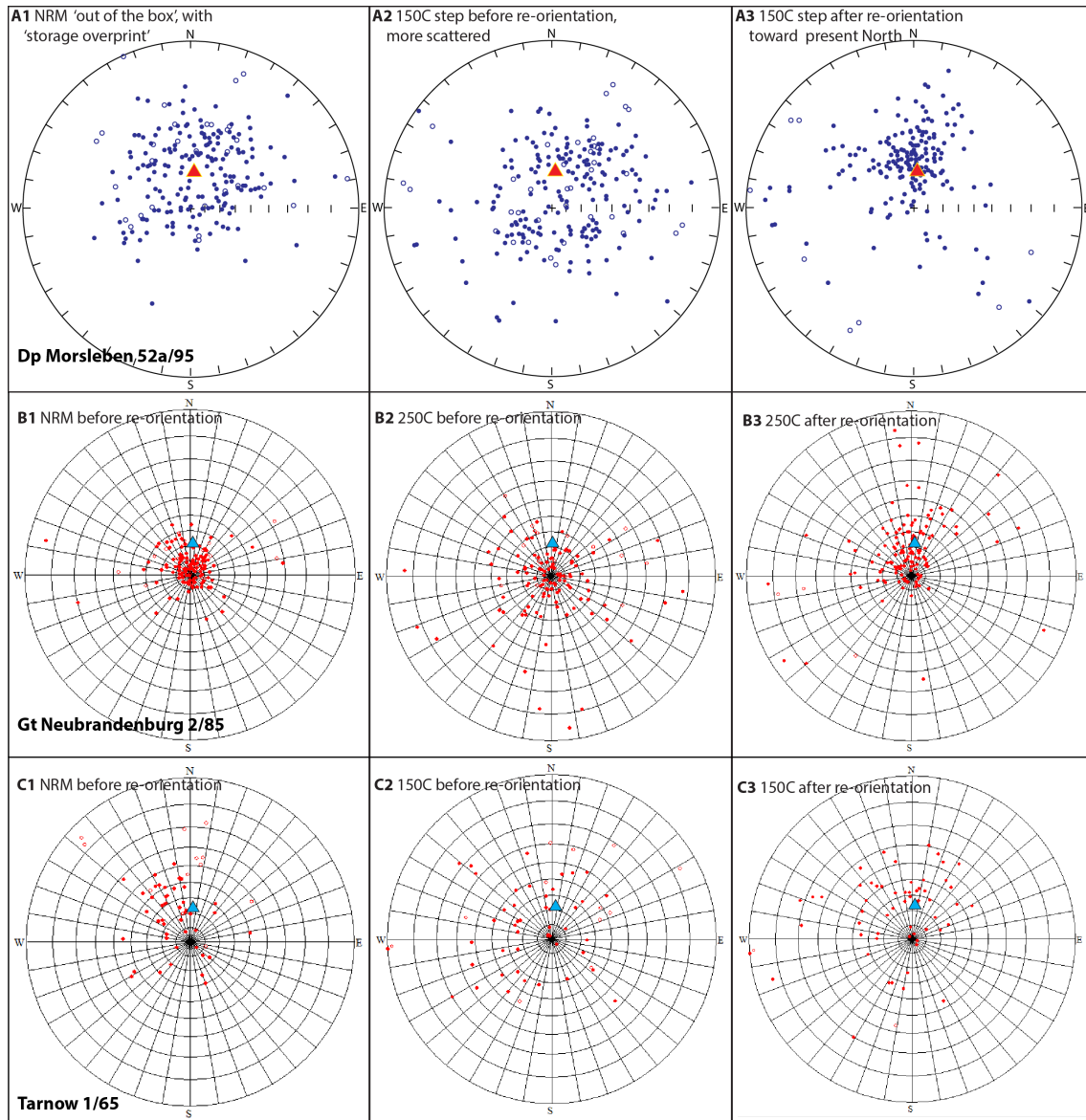


Figure A.1. Stereoplots showing the clustering toward present-day North after removing the initial storage overprints from Dp Morsleben 52a/95 (A1/B1/C1), Gt Neubrandenburg 2/85 (A2/B2/C2) and Tarnow 1/65 (A3/B3/C3), respectively. The stereoplots are vectors of (1) NRMs before re-orientation, (2) 150°C/250°C demagnetization step before re-orientation, and (3) 150°C/250°C step after re-orientation based on the removed interpreted "present-day North" vectors. Closed/open circles in red indicate the stereo projection of the remanence magnetization vectors onto the lower/upper hemisphere. The triangles in red or light blue denotes the present-day magnetic field at Berlin (calculated from <https://www.ngdc.noaa.gov/geomag-web/#igrfwmm> for 52.5° N, 13.4°E).

Isothermal Remanent Magnetization (IRM)

Two representative samples (greenish and reddish, respectively; Fig. A. 2) were subjected to Isothermal Remanent Magnetization (IRM) experiments to help unravel the nature of the

remanent magnetization carriers and assist in interpretation of demagnetization behaviors. The tests were conducted at the paleomagnetic lab in Grubenhagen.

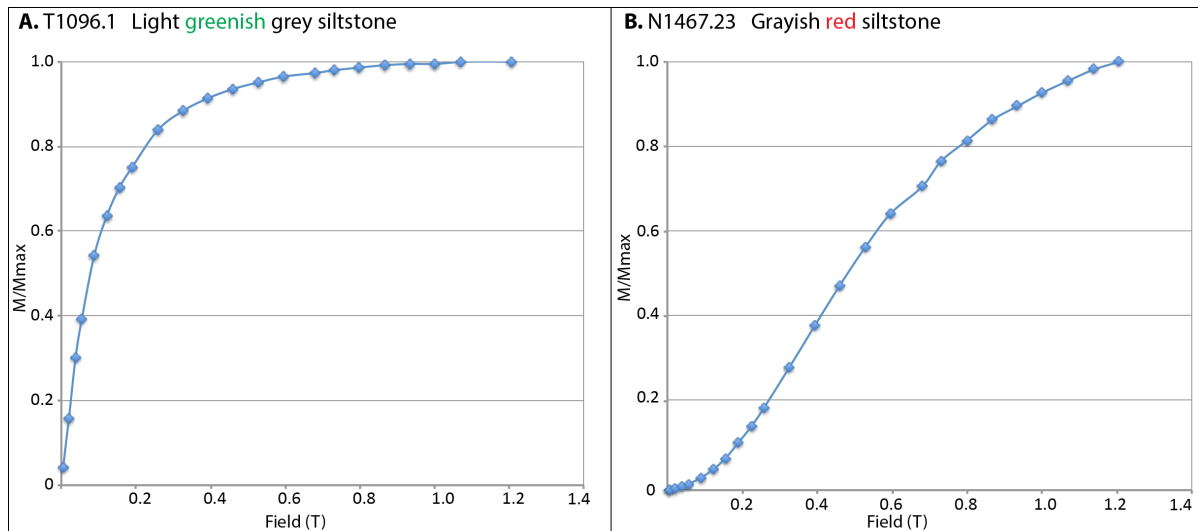


Figure A.2. Stereoplots showing the clustering toward present-day North after removing the initial storage overprints from Dp Morsleben 52a/95 (A1/B1/C1), Gt Neubrandenburg 2/85 (A2/B2/C2) and Tarnow 1/65 (A3/B3/C3), respectively. The stereoplots are vectors of (1) NRM's before re-orientation, (2) 150°C/250°C demagnetization step before re-orientation, and (3) 150°C/250°C step after re-orientation based on the removed interpreted "present-day North" vectors. Closed/open circles in red indicate the stereo projection of the remanence magnetization vectors onto the lower/upper hemisphere. The triangles in red or light blue denotes the present-day magnetic field at Berlin (calculated from <https://www.ngdc.noaa.gov/geomag-web/#igrfwmm> for 52.5° N, 13.4°E).

Typical demagnetization behaviors (Neubrandenburg and Tarnow borehole samples)

Magnetic susceptibility of the reddish/brownish-colored samples from the Neubrandenburg and Tarnow wells starts to increase at around 500°C and often doubles/triples at 525°C. In contrast, the grayish-colored samples display a susceptibility surge beginning at 325°-350°C. However, the intensity and directions of the remanent magnetization did not change significantly at the initial onset of this increase in susceptibility; therefore, some of these demagnetization steps were included in the computation of the ChRM vectors.

Figure A.3. Typical examples of polarity ratings (N/R, NP/RP, and NPP/RPP) of samples from Neubrandenburg. In each composite diagram, the (1) lower-left subplot is the equal-area projection (solid squares indicate downward inclinations while open squares are upward); (2) the upper-left subplot is the magnetization intensity change along thermal (or AF) demagnetization steps; and (3) the right subplot is the orthogonal projections (Zijderveld, 1967) (solid squares are the horizontal projection of declination and the open squares are vertical projections or inclination). Steps used for ChRM are highlighted in red. These orthogonal-projection plots also displays the direction of the 3-dimensional Principal Component Analysis (PCA) line-fit vector in blue for N(P)/R(P) rated samples. Note that all the declinations shown are after re-orienting the sample orientations based on the removed overprints at early demagnetization steps (see Appendix A, Section 2.2 for details).

Polarity rating of “N” – Sample N1477.65 (1477.65 m; Pale reddish-brown siltstone of lower Weser Formation): A southwesterly steep-downward vector (interpreted as a mixture of storage and sampling/handling magnetization disturbance) was removed during initial steps of AF 5 mT and 80°C; followed by gradual removal of present-day North overprint with a semi-clustering from 120°C to 625°C; then clockwise rotation and slight shallowing to reach end points. The computed ChRM from the cluster of 3 steps between 650°C and 675°C is 25° declination and 20° inclination.

Polarity rating of “NP” – Sample N1500.1 (1500.1 m; Pale reddish-brown siltstone of upper Stuttgart Formation): Similar to Sample G1477.65, with initial removal of a southwesterly steep-down vector, then gradually becoming shallower. The computed ChRM from the cluster of 4 steps between 500°C and 650°C is 356° declination and 23° inclination. NP-rating assigned due to not reaching the expected normal-polarity Carnian declination with our re-orientation adjustment but was almost due-North.

Polarity rating of “NPP” – Sample N1484.53 (1484.53 m; light-greenish-grey mudstone in the Beaumont Mud Member of Weser Formation): Initial removal of southwesterly steep-down vector, then clustering at ca. 55° inclination towards due North. The ChRM is 358° declination and 57° inclination from the cluster of 10 steps between 150°C and 325°C. Note that this greyish mudstone is one order of magnitude weaker intensity compared to the reddish/brownish samples.

Polarity rating of “R” – Sample N1491.75 (1491.75 m; pinkish siltstone of uppermost Stuttgart Formation): Similar initial behavior as the normal-polarity samples with removal of a southwesterly steep-down vector at AF 5 mT and then gradual removal of present-day North overprint. Flips direction upon heating at 120°C with a cluster of upward vectors towards southwest. The ChRM computed from cluster of 4 steps between 225°C and 300°C is 213° declination and -25° inclination.

Polarity rating of “RP” – Sample N1493.1b (1493.1 m; grayish-red siltstone with gypsum clasts of uppermost Stuttgart Formation): Gradually rotates clockwise from due North to a southwesterly declination with a nice trend toward reversed; but inclinations did not become negative until the last two steps of 650-670°C. A close-up of the vectors at 350-670°C steps is also shown. Rating of 'RP' assigned because of not reaching the expected end point, having a relatively shallow inclination and intensities did not decay 'back' toward the origin. The vectors of 650-670°C are used for ChRM with 224° declination and -14° inclination.

Polarity rating of “RPP” – Sample N1554.8 (1554.8 m; light-gray sandy siltstone of Neubrandenburg Member of Stuttgart Formation): Gradual removal of the storage, drilling and present-day north overprints until flipping over at 300°C. Nice 'R-trend' but becoming too weak to measure at 390°C. The computed ChRM from the cluster of 3 steps between 330°-390°C is 266° declination and -16° inclination. RPP-rating due to declination of nearly due west, and thus not falling into the expected R declination range for Carnian.

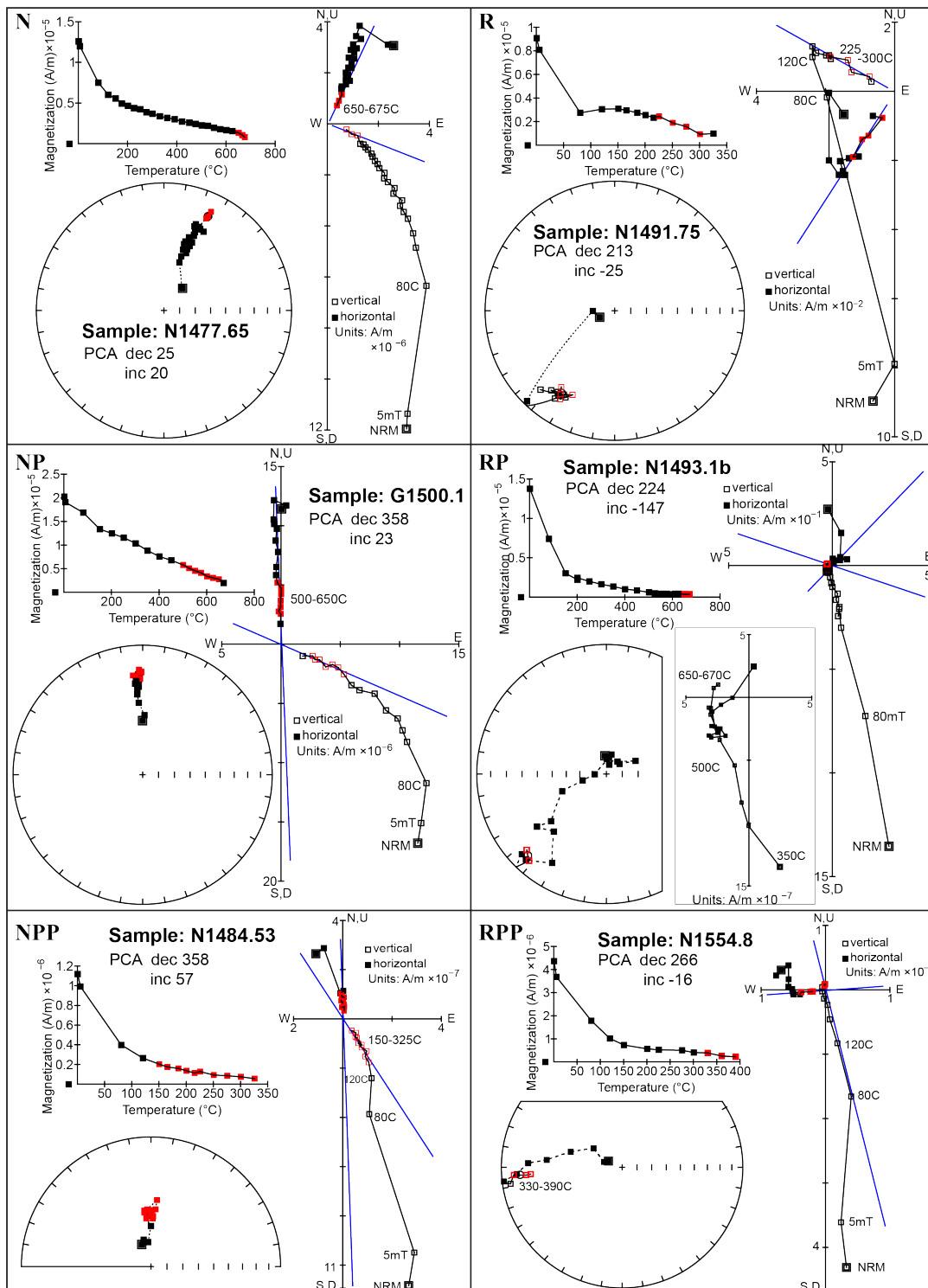
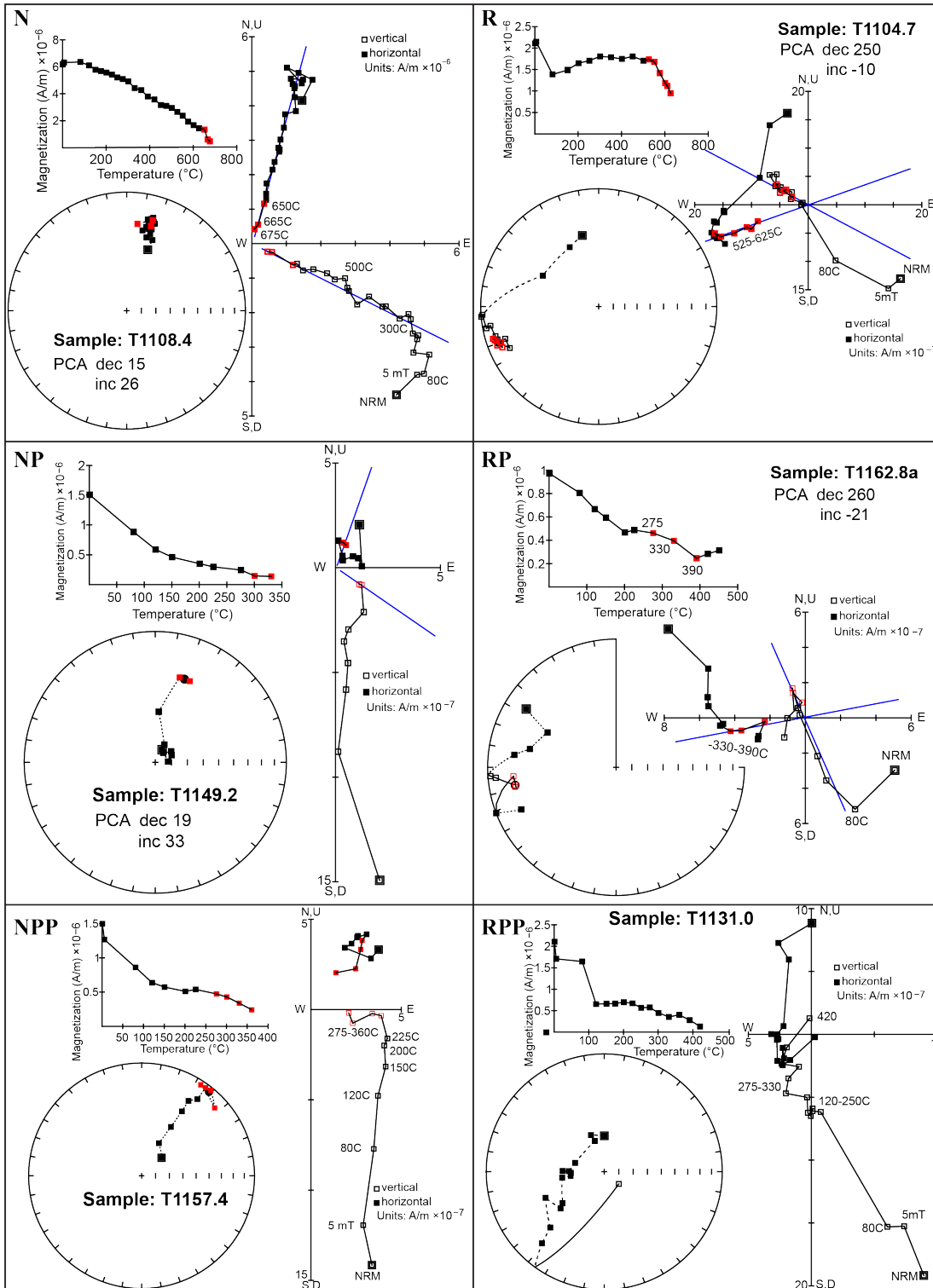


Figure A.4. Typical examples of polarity ratings (N/R, NP/RP, and NPP/RPP) of samples from Tarnow. Same types of plots as in Fig. A.3. **Polarity rating of “N” – Sample T1108.4 (1108.4 m pale-red siltstone of Upper Schilfsandstein):** Initial removal of a southwesterly downward vector (a mixture of storage, drilling overprint and sampling/handling magnetization disturbance), followed by a cluster of vectors downward toward northeast until the final steps. The ChRM computed from the cluster of 3 steps between 650° and 675°C is 15° declination and 26° inclination. **Polarity rating of “NP” – Sample T1149.2 (1149.2 m; light-greenish-grey fine-grained sandstone of lowermost lower Schilfsandstein):** Progressively removal present-day north and drilling overprints until moving out of the cluster and shallowing. The ChRM computed from two steps of 300-350C is 19° declination and 33° inclination. Rated 'NP' due to a lack of stable end points with intensities progressively decaying toward origin before becoming too weak to measure. **Polarity rating of “NPP” – Sample T1157.4 (1157.4 m; light-grey fine-grained sandstone of Neubrandenburg Member):** Gradually clockwise rotation and shallowing until 225°C, then becoming near-horizontal. NPP-rating assigned because vectors are from the expected Normal-polarity range for Carnian. The ChRM calculated from a cluster of 4 steps between 275°-360°C is 39° declination and 5° inclination. **Polarity rating of “R” – Sample T1104.7 (1104.7 m; moderate-reddish-orange siltstone of upper Schilfsandstein):** Gradually rotates counterclockwise from due north to the southwest, and changing to negative inclination at 150°C. The ChRM computed from a cluster of steps between 550°C and 625°C is 250° declination and -11° inclination. **Polarity rating of “RP” – Sample T1162.8a (1162.8 m; light-grey fine-grained sandstone with plant debris):** Rotates counterclockwise from northwest to a southwesterly declination while inclinations turn negative at 200°C. Intensity increased after 400°C while directions became unstable. RP-rating given due to still having a westward declination and not reaching a stable end point. **Polarity rating of “RPP” – Sample T1131 (1131 m; light-grey fine-grained sandstone of Gaildorf Member of Stuttgart Formation):** Removal of storage and present-day north overprints at low demagnetization steps; then a counterclockwise rotation to a southwesterly declination, but never reached a R-range end point. Vectors over 420°C are unstable and thus are not shown here. RPP-rating was assigned and no ChRM was computed.



Magnetostratigraphy with polarity interpretations and ChRM (Neubrandenburg and Tarnow borehole samples)

Summary plots of the lithology of three boreholes with the interpreted polarity patterns were generated with the public TSCreator visualization software (<https://timescalecreator.org>).

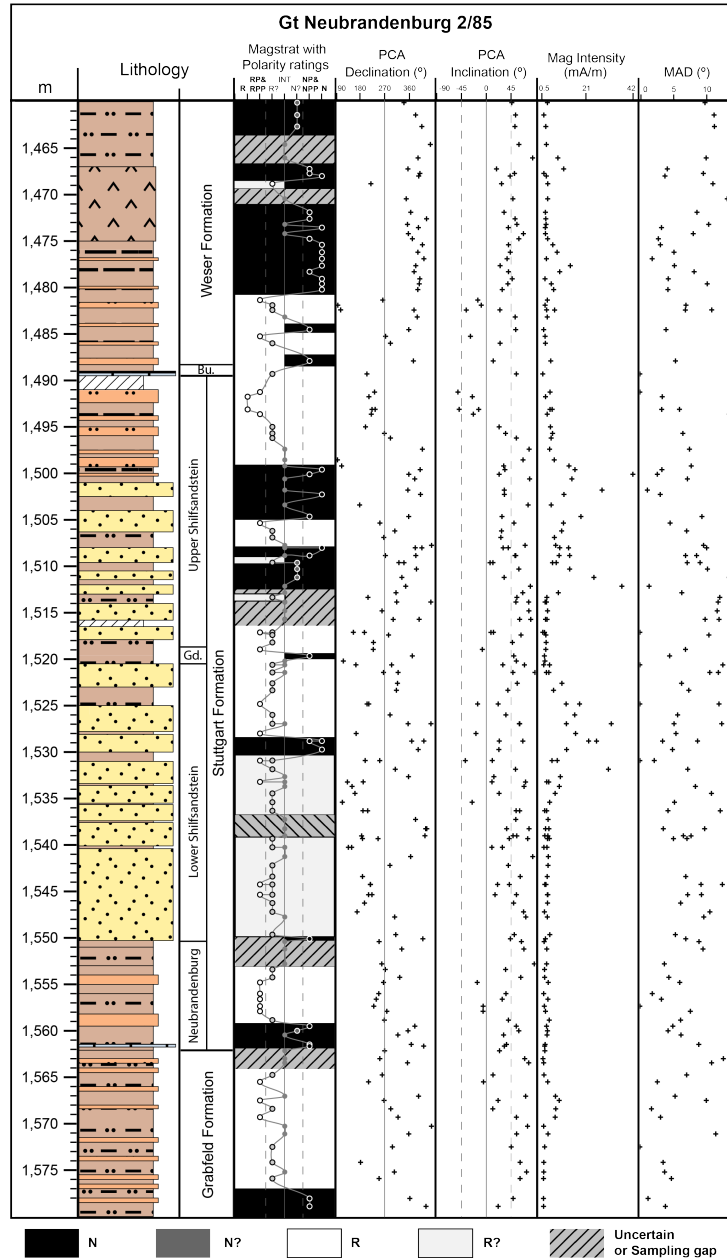


Figure A.5. Magnetostratigraphy with polarity ratings of Neubrandenburg well with lithology column. See Figure 3 in the main text for the lithology legend. Bu. = Beaumont Member, Gd. = Gaidorf Member.

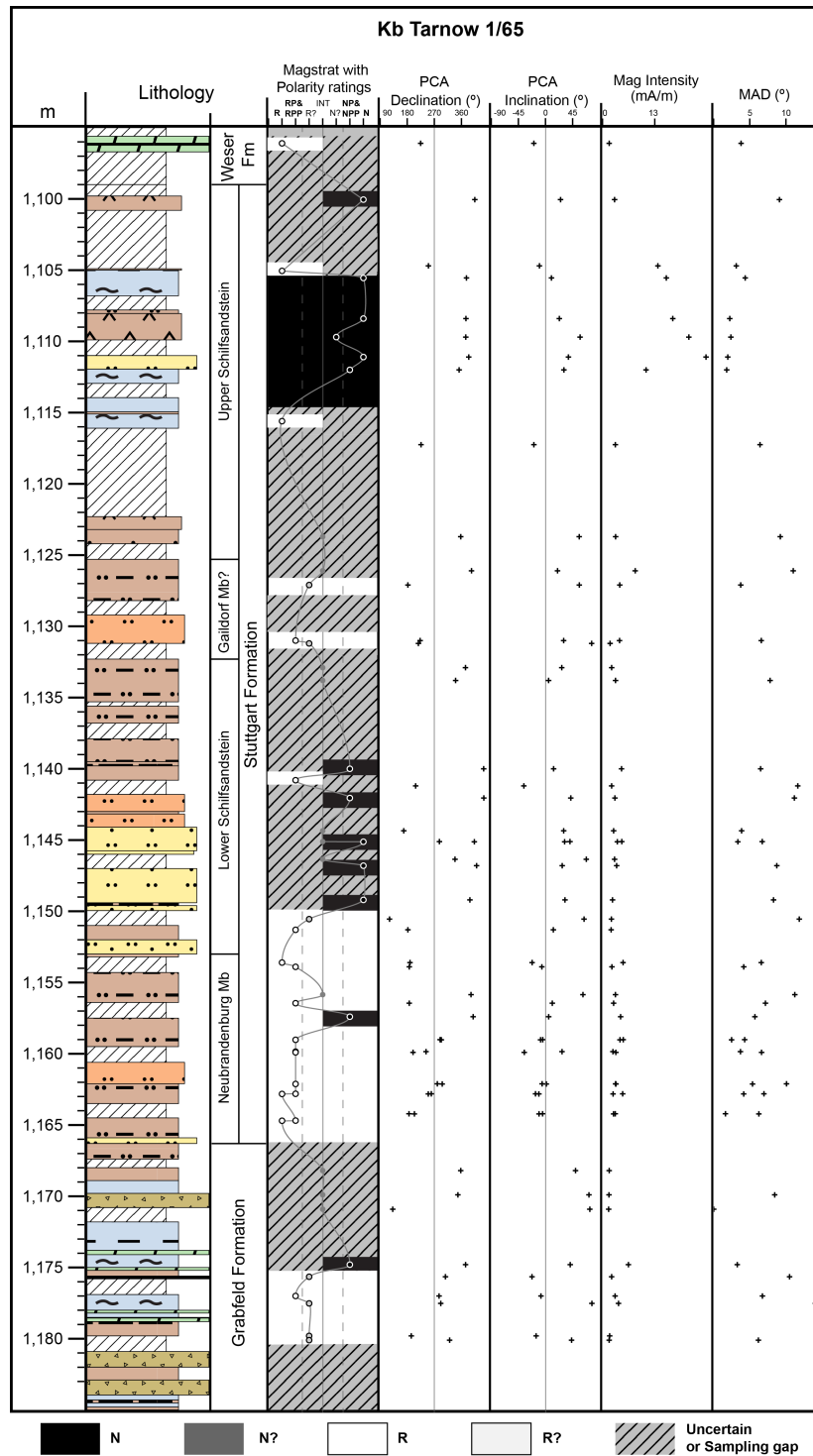


Figure A.6. Magnetostatigraphy with polarity ratings of Tarnow well with lithology column. See Figure 3 in the main text for the lithology legend.

Alternate correlation options for the uppermost Carnian polarity patterns

Traditionally, due to the lack of means to reliably correlate to marine facies, a tentative Carnian-Norian boundary within the Germanic Basin had been commonly assigned as the boundary between the Weser and the Arnstadt formations. This approximate placement was partially supported by the occurrence within the lowermost Arnstadt Formation of a monospecific conchostracan *Shipingia weemsi* zone (Kozur et al., 2013). Unfortunately, there are no reliable guide fossils; in part because of disagreements on the correlation of the terrestrial conchostracan assemblages in this interval of the Germanic Basin to marine biostratigraphy and to the uncertain taxonomy and ranges of Carnian and early Norian conodonts (e.g., Kozur and Weems, 2007).

Therefore, two alternate correlation options exist if we compare the Germanic composite to other coeval magnetic polarity scale by pattern match. In Option 1 (Section 4.1 Fig. A. 7), the base of the Arnstadt Formation is not necessarily constrained by the conchostracan "Norian" assignment and the data-gap in upper Weser Formation is allowed to be reversed polarity, similar to the polarity below and above that interval. In Option 2 (Section 4.2 Fig. A. 9), the base of Arnstadt Formation is assigned to be the Carnian/Norian boundary. The resultant durations and generalized sediment accumulation rates of each rock formation according to the preferred model (main text) and these two alternate models are summarized in Table A. 2.

Alternate option 1 -- basal Arnstadt Formation is late Carnian in age

Below and just above the mid-Carnian Episode, the correlation suites of the Lower Carnian (Julian Substage) and of lowermost portion of the Upper Carnian (lower Tuvalian Substage) remain the same as the option in the main text (Correlation lines #1 to #6). This alternate option assumes that the MK5n correlates to the suite of E2 to E5n while MK5r correlates to E5r of Newark Supergroup, and the SB-2n of Lower Trench at Silická Brezová. In this option, the Weser Formation spans nearly 3 myr shorter. The description of this option for the early and middle Tuvalian repeats some of the material from the main text in order to provide the context.

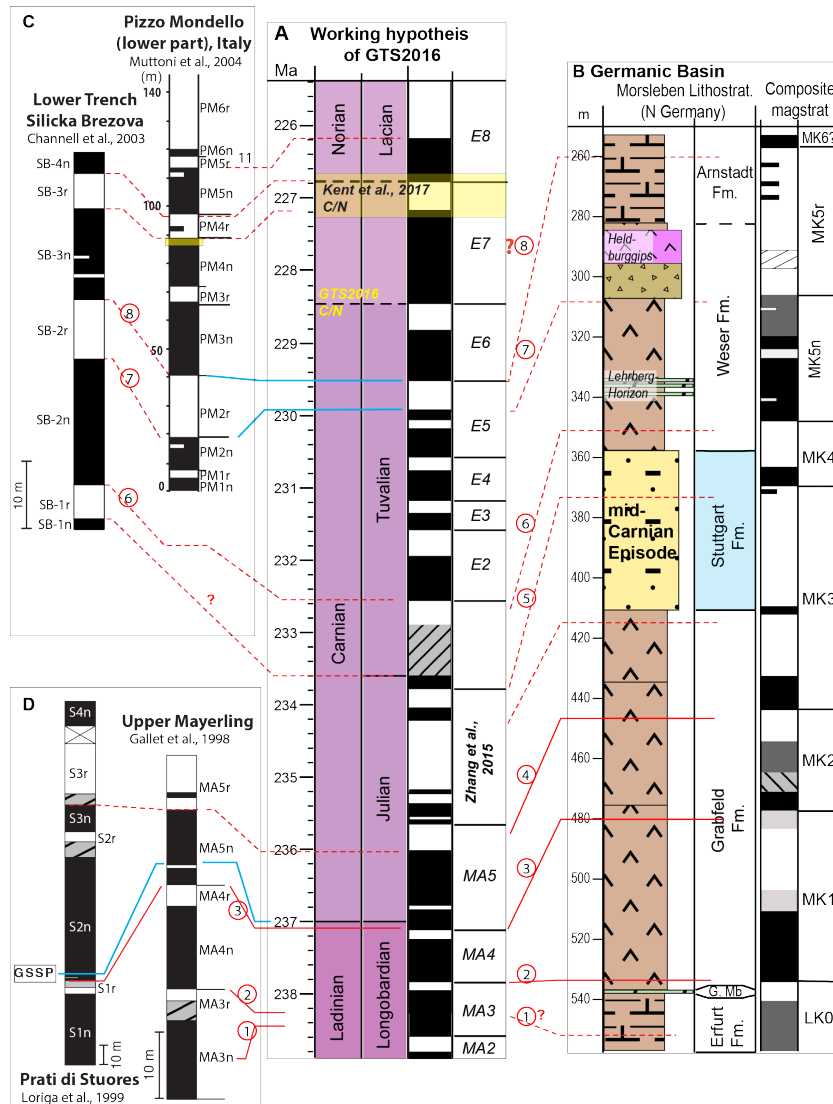


Figure A.7. Alternate correlations of the main magnetostratigraphy features as guided by biostratigraphy and lithology of the Germanic Basin composite (B) of this study to other magnetostratigraphy sections by pattern match. The correlation lines of #1 - #6 are of the same logic as the Fig. 8 in the main text, except that in this alternative option, we tentatively correlate (1) MK5n to E2-to-E5n, and SB-2n, (2) the base MK6 to base E6 of Newark series (Line #8 from column B to A), (3) the brief reversed zone in middle of the MK5n to PM1r (within Lines #6 and #7). Note that this alternate working age model assumes a late Carnian age of basal Arnstadt Formation, instead of it being Norian as suggested by conchostracan assembly. See Fig. 8 in the main text for the detailed caption.

1) *Correlation lines #6, #7 and #8 (early to middle Tuvalian)*

An interval of reversed polarity overlies the Stuttgart Formation in the Germanic Basin (lowermost Weser Formation; MK4r). This is followed by a thick normal-polarity zone (MK5n) with indications of three thin reversed-polarity intervals (half white bars in Fig. A. 7B). The

thick MK5n is considered to be middle Tuvanian in geologic age (details available in Section 2 of main text), therefore is consistent with the projected age and provides a partial verification for the normal-polarity-dominated lower portion of the Newark sequence of E2n-E5n (delimited by Correlation Lines #6 to #7). Therefore, the earlier uncertain interval in the GTS2016 reference scale appears to consist entirely of reversed polarity. The dominance by normal-polarity MK5n in the middle Weser Formation contrasts with the relative thicknesses/durations that had been assigned the E-series reversed-polarity magnetozones in this time interval. We suggest that the extent of some of these E-series magnetozones may have been overestimated or there may have been interpretations of reversed-polarity that should be revisited (e.g., the relatively thickness assigned to the E2r magnetozones).

2) Correlation Lines #7 and #8 (late Tuvanian)

The upper half of the Weser Formation into the basal Arnstadt Formation is a reversed-polarity magnetozones (MK5r) in the Morsleben borehole. A poorly documented normal-polarity zone (MK6n) begins in the lowest Arnstadt Formation (Fig. A. 7B). According to Kozur et al. (2013), there was no significant time gap between these two formations based on the gradual change of conchostracan faunas and on lithology investigations. Palynology of the lower Arnstadt Formation, such as the occurrence of *Granuloperculatipollis rudis* does not shed light on its geologic age, because *G. rudis* is also found within upper Carnian in the Tethyan region (e.g., Kürschner and Herengreen, 2010).

Therefore, if there is no major hiatus, then we tentatively assign the main reversed-polarity magnetozones MK5r, delimited by Correlation Lines #7 and #8 of the upper Weser Formation, to be equivalent to the magnetozones E5r of the lower Newark succession. The E5r has been correlated to magnetozones PM2r in upper Carnian at Pizzo Mondello and SB-2r in Lower Trench (Fig. A. 7C). This assignment of MK5r would imply that the normal-polarity-dominated interval of Newark magnetozones E6n-7n and its corresponding normal-polarity-dominated interval of PM3n-4n-5n at Pizzo Mondello were only sampled in its lowermost portion (MK6n) in our Germanic Basin study (Correlation Line #8). Therefore, this proposed magnetostratigraphy correlation to other reference sections with marine biostratigraphy (e.g., Pizzo Mondello, a candidate for the Carnian/Norian boundary GSSP; Fig. A. 7C) and to the astronomical-scaled Newark magnetic polarity time scale (Fig. A. 7A) implies that the onset of the Arnstadt Formation begins in the late Carnian, not at the base of the Norian (Fig. A.8). This

calibration hypothesis can be tested when a detailed magnetostratigraphy is obtained from the entire lower Arnstadt Formation.

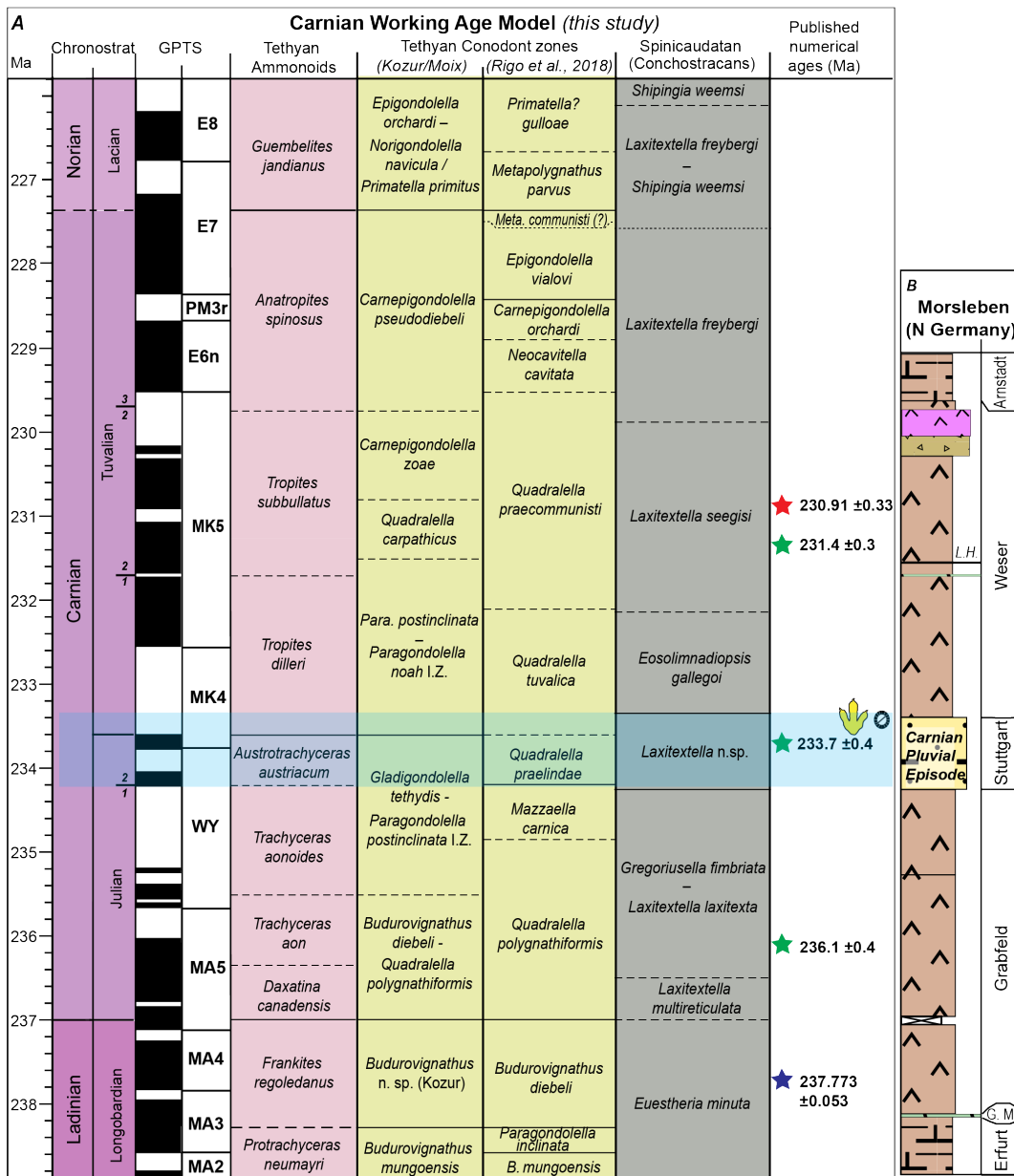


Figure A.8. Alternate correlations of the main magnetostratigraphy features as guided by biostratigraphy and lithology of the Germanic Basin composite (B) of this study to other magnetostratigraphy sections by pattern match. The correlation lines of #1 - #6 are of the same logic as the Fig. 8 in the main text, except that in this alternative option, we tentatively correlate (1) MK5n to E2-to-E5n, (2) the base MK6 to base E7 of Newark series (Line #9 from column B to A), (3) the brief reversed zone in middle of the MK5n to PM1r, and GZ3r (bounded by Lines #7 and #8). Note that this alternate working age model assumes a late Carnian age of basal Arnstadt Formation, instead of it being Norian as suggested by conchostracan assembly. See Fig. 8 in the main text for the detailed caption.

However, due to the presence of thick gypsum and salt ablation/residual layers of uppermost Weser Formation, reliable paleomagnetic signatures could have not been preserved. The normal-polarity-dominated interval of PM3n-4n in Pizzo Mondello and the SB-3n in Lower Trench at Silická Brezová, and its presumed equivalent of E6n-E7n in the Newark succession may have not been resolved in the Germanic composite.

Alternate option 2 -- basal Arnstadt Formation falls within Carnian/Norian boundary

If the current interpretations of the calibration of conchostracan zones to chronostratigraphic stages and substages are considered to be accurate, then one must propose an alternate correlation model for the uppermost Carnian. Again, Correlation lines #1 to #6 are the same as the first two options.

1) Correlation Lines #8 and #9 - #10 (late Tuvanian)

Correlation lines #8 and #9 are the same as the preferred option in the main text. However, in this alternate option, the base MK6 of basal Arnstadt Formation (now fixed to be earliest Norian) is correlated to the base of E8 (Correlation Line #10) that is of early Norian according to the Pizzo Mondello section (Mazza et al., 2018).

The data-gap within the Heldburggips Horizon is no longer regarded as a separate normal-polarity, but belongs to the MK5r. This reversed polarity is correlated to the E7r of Newark series, to the PM4r of Pizzo Mondello, and the SB-3r of Lower Trench (bracketed by Correlation lines #9 and #10).

The underlying MK5n.2n is thus correlated to the normal-polarity-dominating E6–E7 in the Newark Series, to PM3–PM4 in Pizzo Mondello, and to SB-3n of Lower Trench (Fig. A.9 column B correlated to columns A to C). However, the reversed-polarity zone E6r that in Pizzo Mondello (PM3r) is not recovered in the composite Germanic Basin magnetostratigraphy.

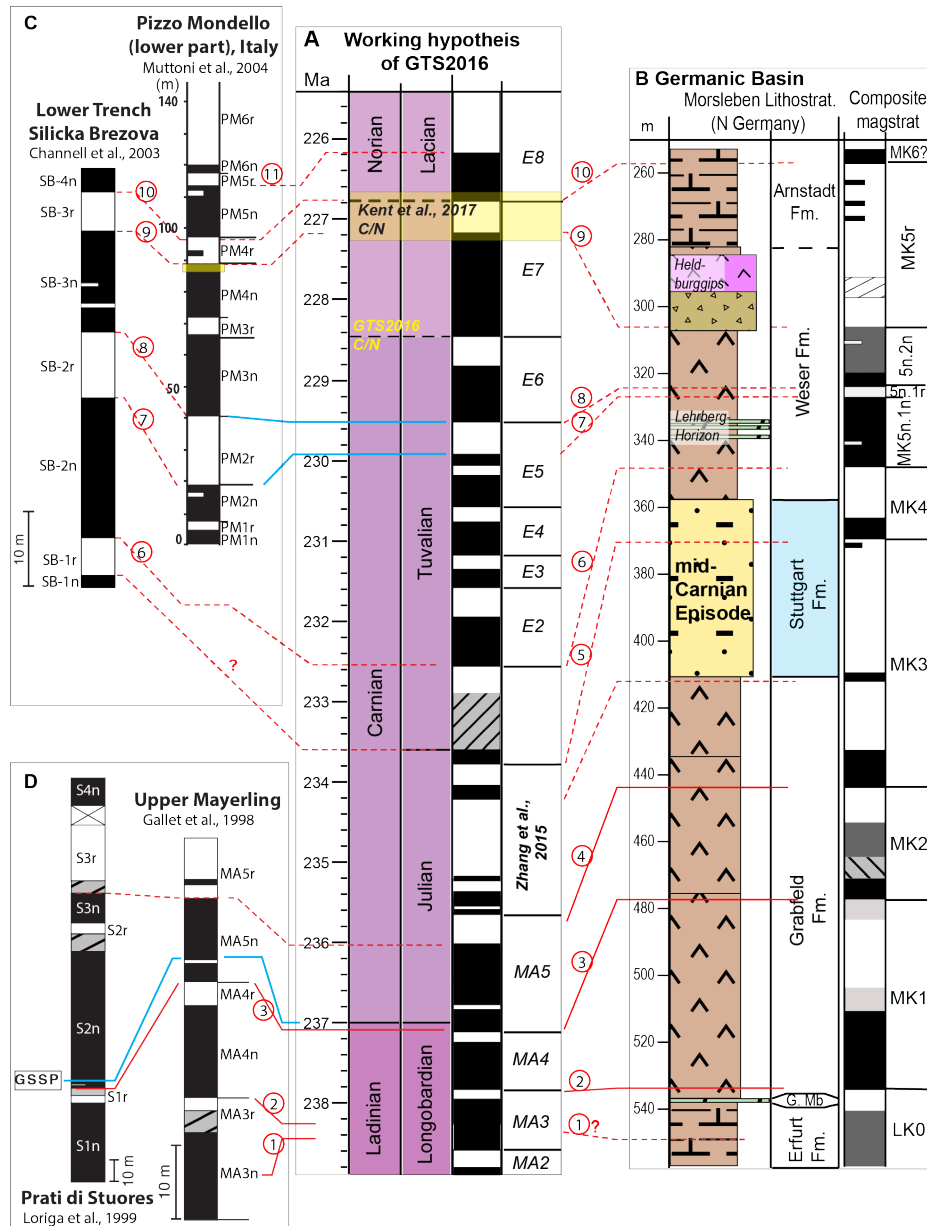


Figure A.9. Alternate working hypothesis on the Carnian geomagnetic time scale assuming that the basal Arnstadt Formation must have an age of earliest Norian. This assumption is based on the currently assigned chronostratigraphic age to the conchostracan assemblages of *Laxitextella freybergi*-*Shipingia weemsi* found in the uppermost ‘Heldburggips’ (Heldburg Gypsum Member) and of the monospecific *S. weemsi* Zone in the basal Arnstadt Formation. A relatively short time-gap was suggested by the transitional shift of these two conchostracan zones (Kozur et al., 2015). The correlation lines of #1 - #9 are of the same logic as the Fig. 8 in the main text, except that in this alternative option 2, we tentatively by not considering the data gap as a distinguishable polarity, and correlate the base MK6 to base E8 of Newark series (Line #10 from column A to B). See Fig. 8 in the main text for the detailed explanation of figure columns.

2) *Implications for latest Carnian polarity time scale*

In this alternative magnetic polarity time scale (Fig. A.8), the Julian through early Tuvalian are the same as in the preferred option (Fig. 9 in main text). The middle and upper Tuvalian is still dominated by normal polarity.

Consequently, the Weser Formation would span ca. 6 myr, which is ~1myr shorter than the preferred option in the main text. The durations of the underlying Stuttgart and the Grabfeld Formation have not changed (ca. 1 myr and 3.5 myr, respectively. Barnasch (2010) observed 18 large cyclothem of the Weser Formation, if we assume these cyclothem represent Milankovitch cycles, then an average of ~333 ky is expected for each cyclothem. This is close to but shorter than the 405-ky long eccentricity periodicity, probably indicating a mixing/alternating of short and long eccentricities to the large cyclothem. Similarly, the 8 cyclothem and 29 cyclothem recognized in the Stuttgart and Grabfeld Formations respectively would be possibly more related to the short eccentricity cycles, with an average duration of 125 kyr and 120 kyr for the cyclothem in each formation.

In the Morsleben borehole, the sediment accumulation rates for the Grabfeld (120 m) and Stuttgart (50 m) Formations would be 3.4 cm/kyr and 5 cm/kyr, respectively. But the average accumulation rate for the Weser Formation (80 m) would be reduced to ca. 1.3 cm/kyr, compared to the 1.8 cm/kyr in the preferred option. The Weser Formation was deposited in a similar arid/semi-arid environment as the Grabfeld Formation, but has more playa-environment evaporative gypsum and salt-deposit residues that might indicate occasional saline water intrusions (Barnasch, 2010). These evaporites and the additional arid paleosols may explain the slower net accumulation rate.

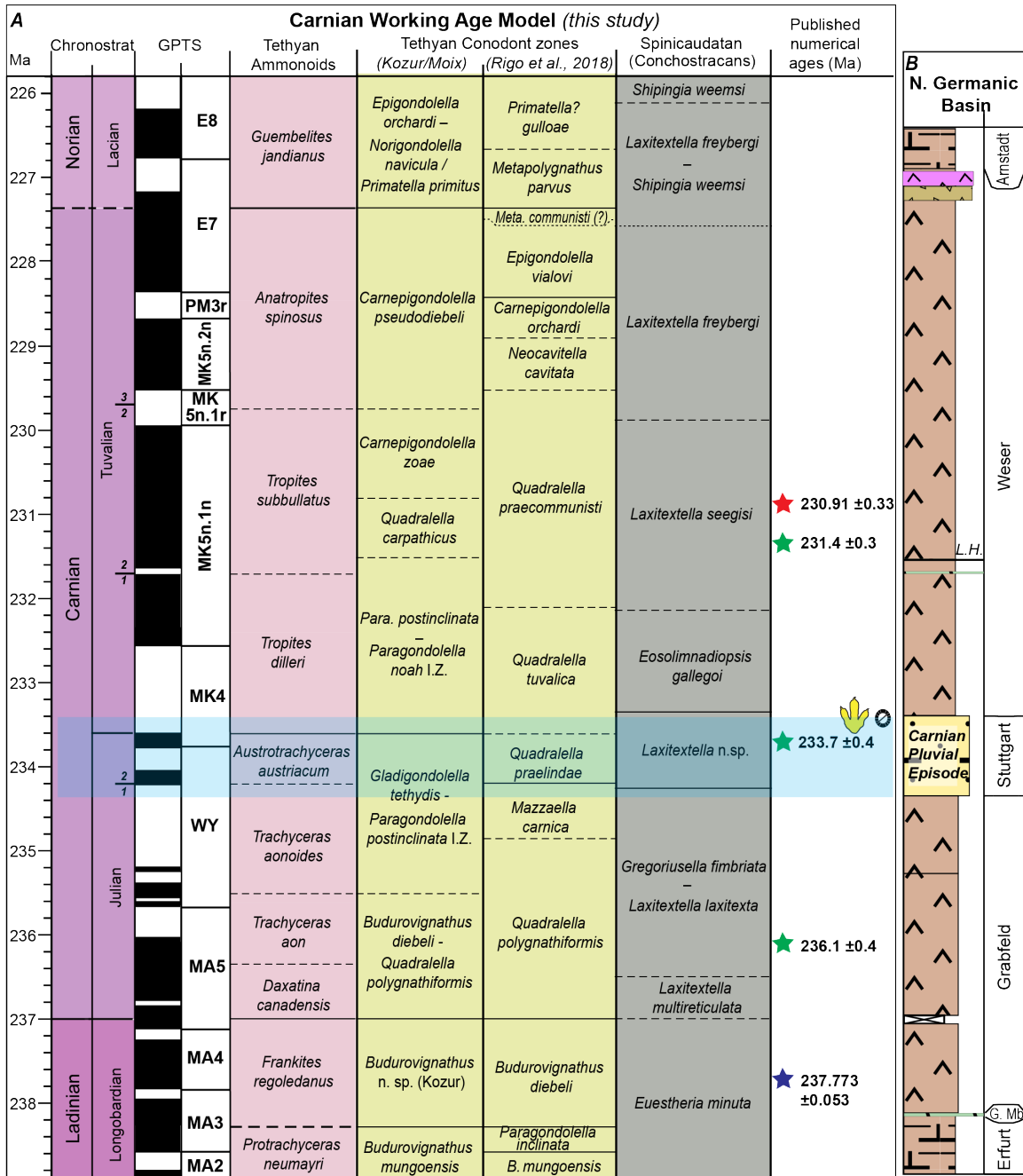


Figure A.10. The resulting magnetic polarity time scale for the Carnian Stage based on the alternate Option 2 that requires that the base of the Arnstadt Formation must be at the Carnian/Norian boundary (Fig. A.16). In this option, the Weser Formation spans a nearly 2.5 myr longer interval and the magnetic polarity patterns of middle and upper Tuvalian are dominated by normal polarity compared to the preferred option presented in the main text. See Fig. 9 in the main text for the detailed explanation of figure columns.

Comparison of sediment accumulation rates under different options

Table A.1. The resultant durations and sediment accumulation rates of each rock formation of the Morsleben core according to the three options (main text, and the 2 alternate options) for correlating the magnetostratigraphy of the Weser Formation. Fm = Formation. Sed. rate = sedimentation rate.

	Thickness (m)	Cyclothem in Barnasch (2010)	Thickness (m) of each cyclothem	Comments
Weser Fm	80	18	4.4	
Stuttgart	50	8	6.25	
Grabfeld	130	29	4.5	
Preferred age model (main text)	Duration (myr)	Average duration (kyr) of each cyclothem	Sed. rate (cm/kyr)	
basal				Carnian/Norian = Weser/Arnstadt.
Arnstadt (~28m)	~1.4		1.8	MK5-3r = E8r = 1.7 myr. This ~36m long interval ends up with a sedimentation rate of 36 m/ 1.7 myr=
Weser Fm	7	389	1.1	~ 1.4 cm/kyr ; while the remaining
Stuttgart Fm	1	125	5.0	Weser Fm at ~70 m/7.2 myr = 0.8 cm/kyr .
Grabfeld Fm	3.5	121	3.7	The cyclothem of Weser Fm lie within the 405-kyr long eccentricity
Alternate Option 1				
Weser Fm	3.5	195	2.3	late Carnian = Weser/Arnstadt. The
Stuttgart Fm	1	125	5.0	MK5r = E5r = ~400 kyr. ~50m long. Then a high sedimentation rate of
Grabfeld Fm	3.5	121	3.7	~ 12.5 cm/kyr is obtained while the lower Weser Fm at ~50 m/3.4 myr =
				1.6 cm/kyr , which is quite a surge compared to the Stuttgart formation. Thus, those facies cyclothem of Weser Fm represent a mixing of 100 kyr or 405 kyr.
Alternate Option 2				
Weser Fm	6.0	333	1.3	Carnian/Norian = Weser/Arnstadt. The
Stuttgart Fm	1	125	5.0	MK5r = E7r = ~400 kyr. Similarly, a high sedimentation rate of
Grabfeld Fm	3.5	121	3.7	~ 12.5 cm/kyr is obtained while the lower Weser Fm at ~50 m/6 myr =
				0.8 cm/kyr . Thus, those facies cyclothem of Weser Fm represent a mixing of 100 kyr or 405 kyr

Among the three models, the two alternate options in the Appendix both require an abrupt surge of sedimentation rates across the Weser/Arnstadt Fm, from 1.6 or 0.8 cm/kyr to

12.5 cm/kyr; while the preferred model suggests a more gradual increase from 0.8 to 1.4 cm/kyr. The implications for the durations of rock cyclothem based on visual facies analysis by Barnasch (2010) are also listed. The cyclothem of the Grabfeld and Stuttgart Fm appear to be consistent with a short-eccentricity periodicity, while those in the Weser Fm seem to consist of a mix of short- and long-eccentricity cycles (Table A.1).

Unfortunately, it is difficult to apply the usual methods of cyclostratigraphy in this terrestrial setting, such as astronomical tuning of physical logs of gamma-ray, given that there may be condensation at evaporite or paleosol levels and/or changes in sediment accumulation rates. Barnasch (2010) (Table A.1) interpreted 29 cyclothem bundled into 6 main cycles in Grabfeld Formation. These were 9 claystone-gypsum cycles in lower Grabfeld Fm, 12 dolomite-claystone-gypsum cycles in middle Grabfeld Fm, and 8 cyclothem of variable combinations (claystone-gypsum, dolomite-claystone-gypsum, and claystone-gypsum-salt) in upper Grabfeld Fm. For the Weser Formation, he identified 18 cyclothem bundled into 3 main cycles: 5 claystone-gypsum-salt cycles in lower Weser, 7 dolomite-claystone-gypsum/claystone-gypsum-salt cycles in middle Weser, and 6 claystone-breccia-gypsum/claystone-gypsum/claystone-gypsum-salt cycles in upper Weser. Whether such sedimentary cycles have any relationship to long-term climate changes caused by long-eccentricity cycles or the ca. 1.2-myrs long-modulation of eccentricity is an intriguing topic for future investigations.

Additional references

- Lurcock, C., and Wilson, G.S., 2012. PuffinPlot: A versatile, user-friendly program for paleomagnetic analysis. *Geochemistry, Geophysics, Geosystems* 13 (6), Q06Z45, doi:10.1029/2012GC004098.
- Shukla, U. K., Bachmann, G. H., and Singh, I. B., 2010. Facies architecture of the Stuttgart Formation (Schilfsandstein, Upper Triassic), central Germany, and its comparison with modern Ganga system, India. *Palaeogeography, Palaeoclimatology, Palaeoecology*, 297 (1), 110-128.
- Scotese, C., 2014. Atlas of Middle & Late Permian and Triassic Paleogeographic maps, maps 43 - 48 from volume 3 of the PALEOMAP Atlas for ArcGIS (Jurassic and Triassic) and maps 49–52 from volume 4 of the PALEOMAP PaleoAtlas for ArcGIS (Late Paleozoic): Mollweide Projection. PALEOMAP Project, Evanston.

- Torsvik, T. H., Van der Voo, R., Preeden, U., Mac Niocaill, C., Steinberger, B., Doubrovine, P. V., Cocks, L. R. M., 2012. Phanerozoic polar wander, palaeogeography and dynamics. *Earth-Science Reviews*, 114 (3), 325-368.
[doi:https://doi.org/10.1016/j.earscirev.2012.06.007](https://doi.org/10.1016/j.earscirev.2012.06.007)
- Zhang, C. F., and Ogg, J. G., 2003. An integrated paleomagnetic analysis program for stratigraphy labs and research projects. *Computers & Geosciences*, 29 (5), 613-625.
[public version 4.2 at: <http://www.eaps.purdue.edu/paleomag/>]

CHAPTER 3. MAGNETOSTRATIGRAPHY OF U/PB-DATED BOREHOLES IN SVALBARD, NORWAY, IMPLIES THAT THE BARREMIAN–APTIAN BOUNDARY (BEGINNING OF CHRON M0R) IS 121.2 ±0.4 MA

Yang Zhang¹, James G. Ogg^{2,1*}, Daniel Minguetz³, Mark W. Hounslow⁴, Snorre Olausen⁵, Felix M. Gradstein⁶, and Selen Esmeray-Senlet³

¹*Department of Earth, Atmospheric and Planetary Sciences, Purdue University, 550 Stadium Mall Drive, West Lafayette, IN 47907-2051, USA*

²*State Key Laboratory of Oil and Gas Reservoir Geology and Exploitation, Institute of Sedimentary Geology, Chengdu University of Technology, Chengdu, Sichuan 610059, China*

³*Chevron Energy Technology Company, 1500 Louisiana, St., Houston, TX 77002*

⁴*Lancaster Environment Centre, Lancaster University, Lancaster LA1 4YB, UK*

⁵*Department of Arctic Geology, University Centre in Svalbard, PO Box 156, 9171 Longyearbyen, Norway*

⁶*Geology Museum, University of Oslo, N-0318 Oslo, Norway*

* Corresponding author: jogg@purdue.edu

Abstract: The marker for the base of the Aptian Stage is the base of magnetic polarity Chron M0r. The age of M0r is disputed due to divergence of published radiometric dates and ambiguities in stratigraphic correlation of sections. Our magnetostratigraphy of cores from Svalbard places a bentonite bed, previously dated by U/Pb methods as 123.1 ±0.3 Ma, approximately 80% into Chron M1r, which is 1.9 myr before the beginning of Chron M0r. The implied 121.2 ±0.4 Ma age for the Aptian base, which is significantly younger than the estimated age in current time scales, agrees with a revised cyclostratigraphic duration of 8.0 myr for the Stage relative to the Aptian-Albian boundary previously dated as 113.1 ±0.3 Ma. This new age model is applied to the Aptian microfossil and $\delta^{13}\text{C}$ stratigraphy.

3.1 Introduction

The high-resolution timescale for the Late Jurassic through Early Cretaceous is mainly compiled from the correlation of biostratigraphy to the M-sequence of magnetic polarity chrons (e.g., Channell et al., 1995). The durations of M-sequence polarity chrons and correlated

biozones have been derived from cyclostratigraphy on reference sections (e.g., Sprovieri et al., 2006; Martinez et al., 2015).

The age model for this "floating" scale had been derived from the consistency of $^{40}\text{Ar}/^{39}\text{Ar}$ and U/Pb radiometric dating of oceanic basalts and volcanic ash beds from Ocean Drilling Program (ODP) sites, Argentina and the Great Valley Group in California (Fig. 1). These implied an age of ca. 126 Ma for the beginning of Chron M0r, which is the proposed marker for the base of the Aptian Stage. That 126 Ma age was consistent with a duration of 13 myr for the Aptian according to high-resolution cyclostratigraphic interpretation of the Piobbico core of central Italy (Huang et al., 2010) relative to a U-Pb date of 113.1 ± 0.3 Ma near the Aptian/Albian boundary (Selby et al., 2009).

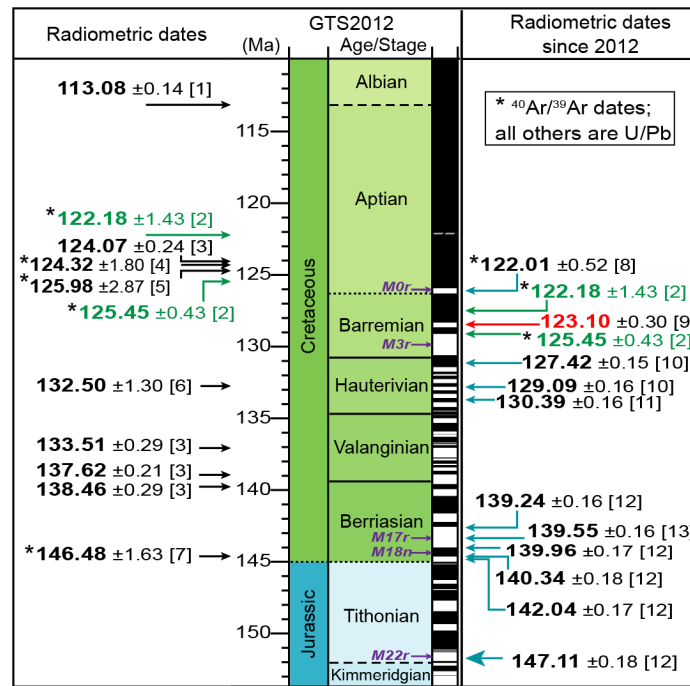


Figure 3.1. Radiometric dates used in Geologic Time Scale 2012 (GTS2012; Gradstein et al., 2012) (left panel) compared to selected radiometric dates published since 2012 that imply a systematic offset to younger ages (right panel). Dates are positioned according to their constraints from biostratigraphy or magnetic polarity. Two dates from MIT Guyot ([2], in green) were re-positioned in the right column to align with a reinterpreted correlation to polarity chrons. [1] Germany, Selby et al., 2009; [2] MIT Guyot, Pacific; [3] Great Valley, California; [4] and [5] Ontong Java Plateau, Pacific; [6] Argentina; [7] Shatsky Rise, Pacific; [8] Reversed-polarity basalt in North China; [9] Svalbard (in red), Midtkandal et al., 2016; and [10 through 13] Argentina. All $^{40}\text{Ar}/^{39}\text{Ar}$ dates are calibrated to a Fish Canyon Tuff monitor standard of 28.20 Ma (Kuiper et al., 2008). [Full references are given in GSA Data Repository Table DR1.]

However, U-Pb dates published after 2012, which used an isotope dilution thermal ionization mass spectrometry (ID-TIMS) method coupled with new techniques for processing of zircons and EARTHTIME standards, seem to suggest that nearly all of the $^{40}\text{Ar}/^{39}\text{Ar}$ dates derived from ODP basalt sites and the pre-2012 U-Pb dating of volcanic ashes were systematically too old by an average of ca. 4 myr (Fig. 1). For example, a volcanic ash bed in the uppermost Hauterivian of Argentina that has yielded a U/Pb date of 132.5 ± 1.3 Ma was re-dated by ID-TIMS as 129.09 ± 0.16 Ma (Aguirre-Urreta et al., 2015).

The $^{40}\text{Ar}/^{39}\text{Ar}$ dates of ca. 124 Ma from ODP sites in the mid-early Aptian basalts of Ontong Java Plateau (Fig. 1), which had supported the 13-myr duration for the Aptian derived from cyclostratigraphy (Huang et al., 2010), were challenged by an averaged U-Pb date of 123.1 ± 0.3 Ma on a bentonite layer in Svalbard (Corfu et al., 2013; Midtkandal et al., 2016). The bentonite in the Helvetiafjellet Formation was interpreted as within the mid-late Barremian based upon regional palynology and a negative carbon-isotopic ($\delta^{13}\text{C}_{\text{org}}$) excursion in the overlying Carlinefjellet Formation. That $\delta^{13}\text{C}_{\text{org}}$ excursion was proposed as equivalent to the $\delta^{13}\text{C}$ excursion accompanying Oceanic Anoxic Event 1a (OAE1a) of mid-Early Aptian (Midtkandal et al., 2016), which, in turn, has been considered to initiated by the eruption of the Ontong Java Plateau large igneous province (e.g., Erba et al., 2015). Meanwhile, in contrast to the Ontong Java Plateau dating, $^{40}\text{Ar}/^{39}\text{Ar}$ dates on basalt flows of reversed polarity in northeast China had produced an age of 122.0 ± 0.5 that was interpreted as M0r (He et al., 2008), but these flows lacked biostratigraphic constraints.

Two ways to help resolve the disputed age model in Barremian-Aptian are (1) to obtain a magnetostratigraphy of the Helvetiafjellet Formation in the Svalbard borehole to accurately place the U/Pb-dated 123.1 Ma bentonite into the Barremian through earliest Aptian magnetic polarity time scale, and (2) to revisit the cyclostratigraphic interpretation of the Aptian portion of the Piobbico core that had implied a duration of 13 myr (Huang et al., 2010).

3.2 Materials and methods

The DH boreholes (Fig. 2D) stored in the University Centre in Svalbard (UNIS) had been continuously cored to investigate CO_2 sequestration (Braathen et al., 2012). The cored lower Cretaceous succession in the boreholes consist of a 75-m-thick paralic sandstone-dominated Helvetiafjellet Formation which is sandwiched between two formations of open-marine facies;

the lower Valanginian to lowest Barremian Rurikfjellet Formation and the Aptian to Albian Carolinefjellet Formation (Grundvåg et al., 2019). The base of Helvetiafjellet Formation is on a subaerial unconformity surface (Fig. 2B). A 20-cm-thick volcanic ash layer occurs in both borehole DH3 and DH7 (Corfu et al., 2013; Midtkandal et al., 2016) and projects to just below a sandstone layer at about 180 m in borehole DH1. The volcanic ashes are considered to be a product of the regional High Arctic Large Igneous Province. The transgressive base of the overlying clay-rich Carolinefjellet Formation is a reworked deposit marking the flooding of the coastal plain.

Paleomagnetic minicores were drill-pressed at approximately 1-m spacing from 130 m to 215 m from core DH1, which has a detailed lithostratigraphy and had yielded the negative $\delta^{13}\text{C}_{\text{org}}$ excursion of potential mid-early Aptian age (Midtkandal et al., 2016). We sampled DH1 for magnetostratigraphy, rather than DH3, because the upper part of the Helvetiafjellet Formation and Carolinefjellet Formation overlying the dated volcanic ash bed in DH3 had been distorted by permafrost, whereas the cored sediments in DH1 were intact. The 110 minicores were analyzed using both alternating field (AF) and thermal demagnetization treatments. Quality ratings were assigned to the characteristic remanent magnetization (ChRM) directions and polarity interpretations (see Tables DR2 and DR3 for paleomagnetic details).

The previous interpretation of the cyclostratigraphy of the Aptian stage had used a grayscale of images of the Piobbico cores of Italy (Huang et al., 2010). The source data is proprietary and not available, therefore a digitization was made of the published diagram (Fig. 1 in Huang et al., 2010) (Table DR4). A newly developed program *Acycle* v.0.2.4 (Li et al., 2019) was utilized for the time series analysis of this digitized signal, including applying eCOCO to guide traditional 405-kyr tuning (see the GSA Data Repository for cyclostratigraphy details).

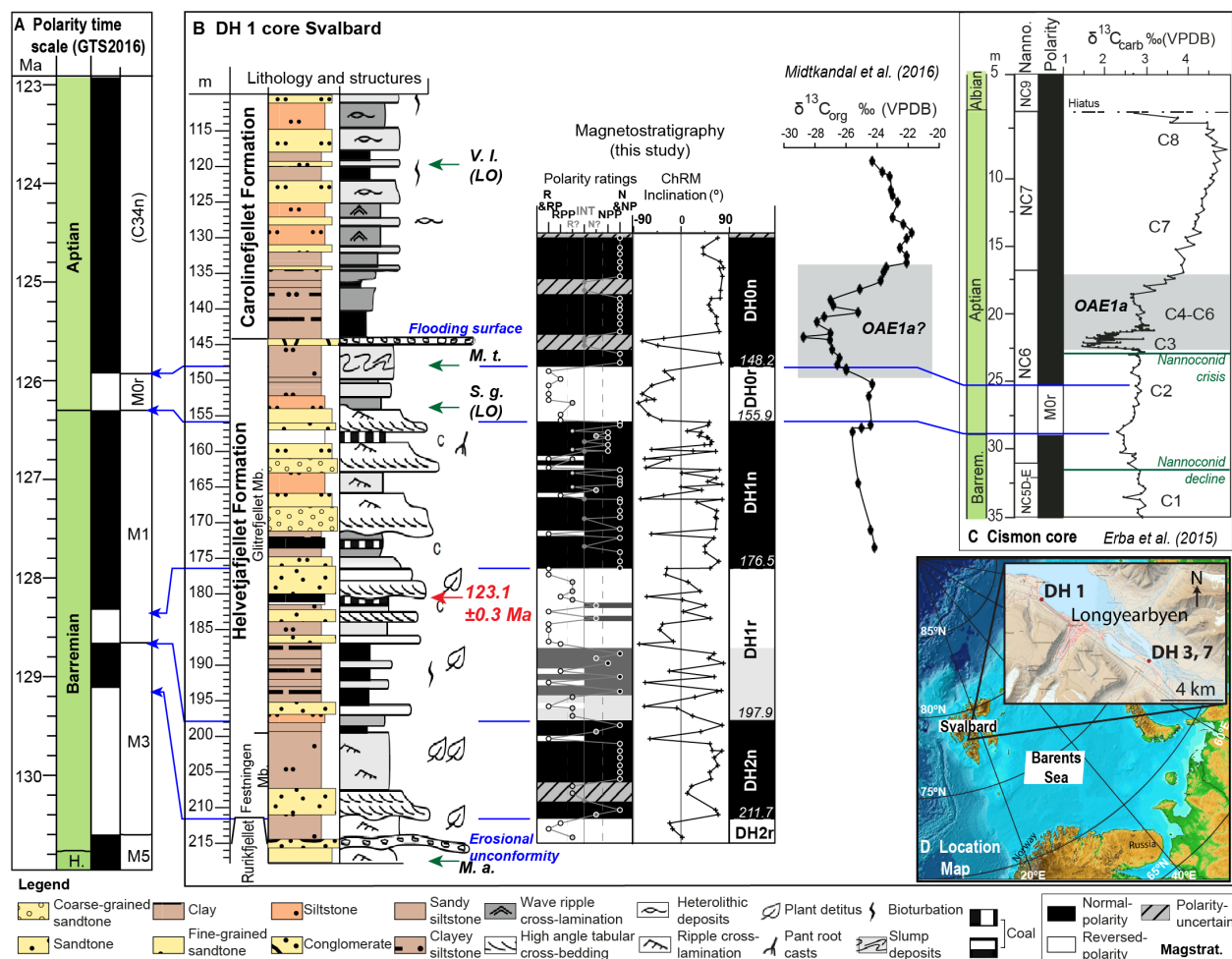


Figure 3.2. Magnetostratigraphy across the U/Pb-dated horizons in Svalbard borehole DH1 (B), and correlation (blue lines) to (A) the GTS2012/2016 magnetic polarity scale (Ogg et al., 2016) in which the base Aptian was 126.3 Ma. Biostratigraphic constraints on DH1 core are palynomorphs of Barremian (*M. t.* = *Muderongia tetracantha*, *S. g.* = *Sirmiodinium grossii*) and Hauterivian (*M. a.* = *Muderongia australis*) and a dinoflagellate cyst of Aptian (*V. l.* = *Vesperopsis longicornis*). Carbon isotope curve from DH1 (Midtkandal et al., 2016) is compared to (C) the Cison core of Italy that has carbon isotope trends, OAE1a (gray shaded interval) and magnetostratigraphy. The level of the U/Pb date (in red) in the DH1 core is projected from the two nearby volcanic ashes-bearing cores (DH3 and DH7). (D) Locations of the DH cores (modified from Midtkandal et al., 2016).

3.3 Results and discussion

The magnetostratigraphy of DH1 yielded three pairs of reversed and normal-polarity magnetozones (DH0 to DH2) (Fig. 2). Magnetozone DH0r in the uppermost Helvetiafjellet Formation is just below the negative $\delta^{13}\text{C}_{\text{org}}$ excursion; therefore, it is in the same stratigraphic position as magnetochron M0r below the OAE1a $\delta^{13}\text{C}_{\text{carb}}$ excursion at Aptian reference sections

in central Italy (Fig. 1). Even through the instantaneous sediment accumulation rates in the deltaic facies of the upper Helvetiafjellet Formation are expected to be irregular, the base of magnetozone DH0r has the same alignment with a positive $\delta^{13}\text{C}_{\text{org}}$ trend, as the placement of the base of M0r within the C2 segment of $\delta^{13}\text{C}_{\text{carb}}$ in the Cismon core of Italy (Fig. 2C).

Guided by correlation of DH0r and constraints from palynology suggesting that the base of the Helvetiafjellet Formation is no older than mid-early Barremian, then the underlying magnetozones DH1 and DH2 are correlated to magnetochrons M1n, M1r, M3n and uppermost M3r, respectively (blue guide lines in Fig. 2). This implies that the volcanic ash dated by U-Pb as 123.1 ± 0.3 Ma is approximately 80% up through magnetozone M1r. Cyclostratigraphy of magnetostratigraphic sections in Italy yield durations for magnetochrons M1r and M1n of 0.25 myr and 1.85 myr, respectively (Sprovieri et al., 2006). Therefore, the base of DH0r and thus the base of the Aptian is calculated to be 1.9 myr (± 0.1 myr) younger, i.e., 121.2 ± 0.4 Ma (combining the uncertainties on both the U-Pb date and its relative placement within magnetozone DH1r).

How can one accommodate this projected 121.2 Ma age with both the 113.1 Ma date on the Aptian-Albian boundary (Selby et al., 2009) and the cyclostratigraphy of the Piobbico core through the majority of the Aptian stage which implied a duration of 13 myr for the Aptian? The eCOCO methods and our revised cyclostratigraphy of the Piobbico core (detailed in GSA Data Repository Table DR5) indicated a fairly constant accumulation rate for some intervals that had previously been interpreted (Huang et al., 2010) as condensed. Guided by the eCOCO analysis, the tuning of the dominance of light or dark intervals to 405-kyr long-eccentricity cyclicity yielded 15 cycles of 405-kyr long-eccentricity above the OAE1a, a duration of 1.3 myr through the OAE1a, and ca. 0.7 cycle to the top of magnetozone M0r. Adding the ca. 0.4 myr duration of Chron M0r (Herbert et al., 1995) to this 7.7 myr total implies that the Aptian spans 8.1 myr; which is ca. 5 myr shorter than what Huang et al. (2010) had interpreted. Therefore, relative to the 113.1 ± 0.3 Ma age of the Aptian-Albian boundary, the basal age for the Aptian is 121.2 ± 0.4 Ma, which agrees with the magnetostratigraphic placement of the U/Pb-dated volcanic ash bed from Svalbard.

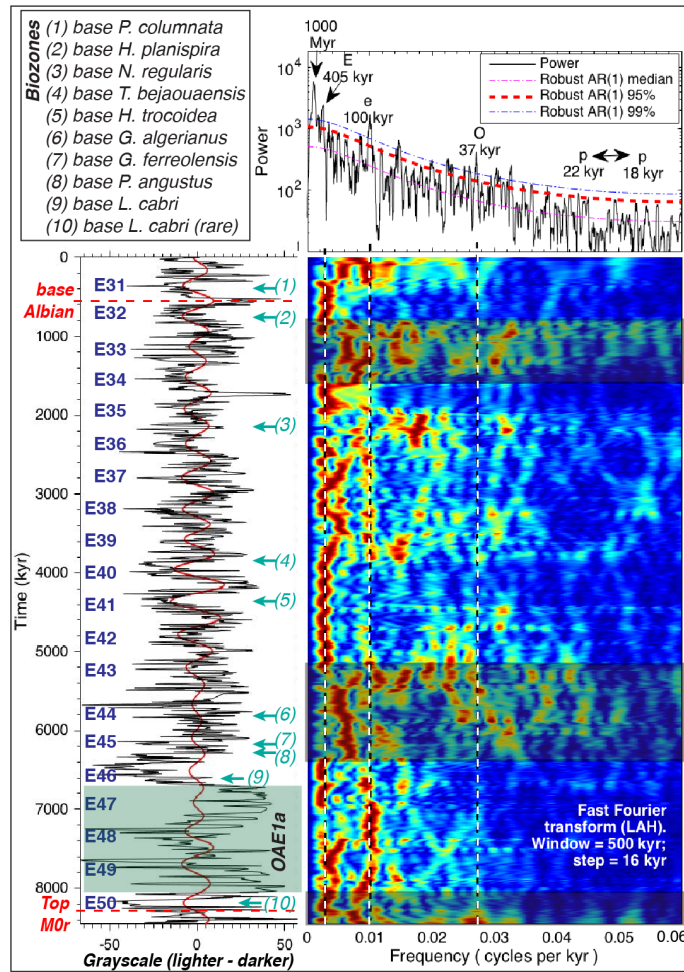


Figure 3.3. The astronomically tuned grayscale data with the 405-kyr cycles (Gauss filter; passband: 0.00245 ± 0.00052), and with multitaper and evolutionary spectral analysis with significant frequencies/cycles marked. Bases of planktonic foraminifer zones (and *P. columnata* nannofossil) are from Larson et al. (1993) for this Piobbico core. The top E31 is the same long-eccentricity number as Huang et al. (2010), but underlying E's are different. The three shaded intervals were not directly tuned due to ambiguous/distorted signals (see GSA Data Repository).

3.4 Implications and conclusions

The revised stratigraphic levels from the cyclostratigraphic analysis of the Piobbico reference core also yields an age model for Aptian planktonic foraminifera zones (Fig. 3; Table DR5). Other biostratigraphic zones, geochemical trends and major sea-level changes are partly calibrated to those foraminifera zones (Gradstein et al., 2012; Erba et al., 2015; Ogg et al., 2016); therefore, an integrated time scale can be compiled for the entire Aptian (Fig. 4). The durations of zones in this Aptian scale are fixed according to the cyclostratigraphy, but a ± 0.4 myr uncertainty in the numerical ages is inherited from the radiometric dates.

The implied ca. 5-myr shortening of the Aptian Stage relative to the GTS2012 scale does not imply that the underlying Barremian Stage becomes longer. Instead, it appears that the array of new U/Pb dates (Fig. 1) requires that the age model for the entire Early Cretaceous through Late Jurassic needs to be shifted younger by ca. 4 myr compared to the array of pre-2012 published dates. The numerous consistent studies of the cycle-calibrated-durations of Early Cretaceous biozones, stages and magnetic polarity zones also imply that these will maintain approximately the same durations as compiled in GTS2012. This suggests that the required expansion of the age model would be for the Middle Jurassic stages, which are relatively brief in GTS2012 owing to the $^{40}\text{Ar}/^{39}\text{Ar}$ date of 168.7 ± 1.7 Ma on ODP Site 801c on Pacific magnetic anomaly M42n.4r (Koppers et al., 2003). This hypothesis requires testing by acquiring radiometric dates from Middle Jurassic sediments and future cycle scaling of those geologic stages.

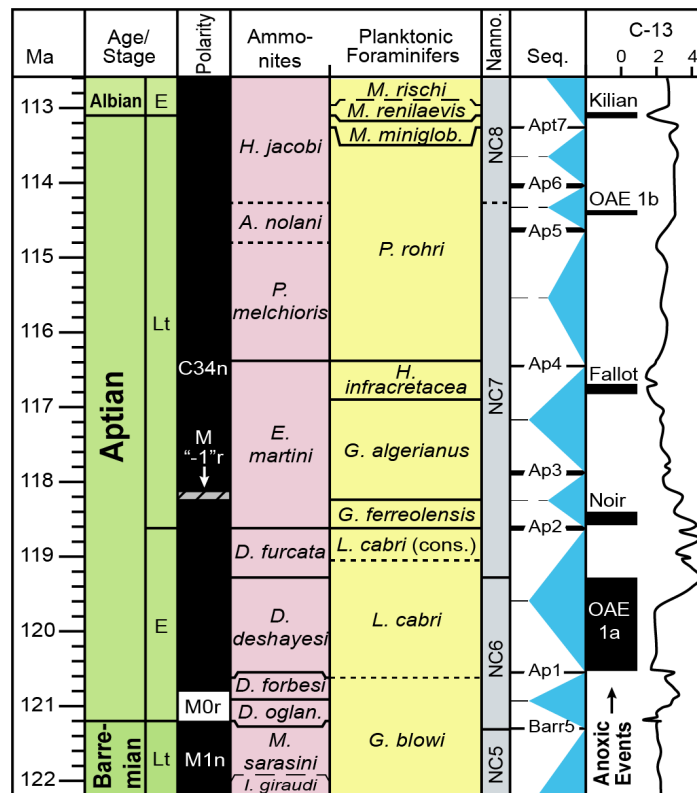


Figure 3.4. New Aptian time scale based on the cyclostratigraphy of the Piobbico core (Fig. 3) with ages of selected zones of Sub-Mediterranean ammonites (modified from Reboulet et al., 2014), planktonic foraminifers (Huber and Petrizzo, 2014; and pers. commun.), calcareous nannoplankton, major sea-level sequences (Haq, 2014) and generalized trends of $\delta^{13}\text{C}$ with widespread organic-rich shale events (compiled from Föllmi et al., 2006; Kennedy et al., 2014; and other sources).

Why are all the radiometric dates published before 2012 for the Early Cretaceous (especially those for the early Aptian) significantly older relative to U/Pb dates measured after 2012? Some possible factors include: (1) $^{40}\text{Ar}/^{39}\text{Ar}$ dates on Mesozoic oceanic and seamount basalts (Ontong Java Plateau, Shatsky Rise, MIT Guyot) have been affected by subtle alteration, and (2) pre-2012 published U/Pb dates from California and Argentina were not derived using the ID-TIMS methods with EARTHTIME standards. These problems do not affect the $^{40}\text{Ar}/^{39}\text{Ar}$ dates that constrain the Late Cretaceous time scale, because those were produced from sanidine feldspar crystal separated from bentonites interbedded with cyclic carbonate sediments.

Our 121.2 ± 0.4 Ma date for the base of the Aptian can be calibrated further in the future by applying ID-TIMS/EARTHTIME methods to the California volcanic ash layers, by acquiring correlative cyclostratigraphy through the Aptian from ODP cores or other borehole/outcrop studies, and/or by acquiring additional radiometric dates from the Barremian-Aptian-Albian interval. In particular, the implied ca. 4-myr upward shifting of the majority of the Late Jurassic through Early Cretaceous time scale needs further verification through additional radiometric dating of sediments that have precise biostratigraphy, magnetostratigraphy and cyclostratigraphy.

Acknowledgments

We thank Geology Editor XX and the reviewers for their constructive suggestions. This magnetostratigraphy and cyclostratigraphy program was inspired by numerous discussions with Elisabetta Erba, Beatriz Aguirre-Urreta, Víctor A. Ramos and Elizabeth Johnson. We thank UNIS CO₂ LABcore for access to core material and logistics, and Julian Janocha for his careful drill-pressing, and sponsorship from the LoCrA consortium (Lower Cretaceous basin studies in the Arctic) consortium managed by the University of Stavanger and The University Center in Svalbard (UNIS). Dr. Anita Di Chiara and Cassil Karloukovski helped with the paleomagnetic measurements in Lancaster. Funding was provided by research grants from the Geologic TimeScale Foundation, Chevron Energy Technology Company, Chengdu University of Technology, and the Research Council of Norway.

3.5 References cited

- Aguirre-Urreta, B., Lescano, M., Schmitz, M.D., Tunik, M., Concheyro, A., Rawson, P.F., and Ramos, V.A., 2015, Filling the gap: new precise Early Cretaceous radioisotopic ages from the Andes: *Geological Magazine*, v. 152, p. 557–564. <http://dx.doi.org/10.1017/S001675681400082X>.
- Braathen, A. et al., 2012, The Longyearbyen CO₂ Lab of Svalbard, Norway - initial assessment of the geological conditions for CO₂ sequestration: *Norwegian Journal of Geology*, v. 92, p. 353–376.
- Channell, J. E. T., Cecca, F., and Erba, E., 1995, Correlations of Hauterivian and Barremian (early Cretaceous) stage boundaries to polarity chrons: *Earth Planetary Science Letters*, v. 134, p. 125–140. [https://doi.org/10.1016/0012-821X\(95\)00111-O](https://doi.org/10.1016/0012-821X(95)00111-O).
- Corfu, F., Polteau, S., Planke, S., Faleide, J. I., Svensen, H., Zayoncheck, A., and Stolbov, N., 2013, U–Pb geochronology of Cretaceous magmatism on Svalbard and Franz Josef Land, Barents Sea large igneous province: *Geological Magazine*, v. 150, p. 1127–1135. <https://doi.org/10.1017/S0016756813000162>.
- Erba, E., Duncan, R.A., Bottini, C., Daniele, T., Weissert, H., Jenkyns, H.C., and Malinverno, A., 2015, Environmental consequences of Ontong Java Plateau and Kerguelen Plateau volcanism. in: Neel, C.R., Sager, W.W., Sano, T., and Erba, E., eds., *The Origin, Evolution and Environmental Impact of Oceanic Large Igneous Provinces*: Geological Society of America Special Paper, v. 511, p. 271–303. [http://dx.doi.org/10.1130/2015.2511\(15\)](http://dx.doi.org/10.1130/2015.2511(15)).
- Föllmi, K.B., Godet, A., Bodin, S., and Linder, P., 2006, Interactions between environmental change and shallow water carbonate buildup along the northern Tethyan margin and their impact on the Early Cretaceous carbon isotope record: *Paleoceanography*, v. 21, p. 97–128, PA4211. <http://dx.doi.org/10.1029/2006PA001313>.
- Gradstein, F.M., Ogg, J.G., Schmitz, M.D., and Ogg, G.M., (coordinators), 2012, *The Geologic Time Scale 2012*: Elsevier, Boston, USA. 1174 p. (2-volume book).
- Grundvåg, S.A., Jelby, M.E., Śliwińska, K.K., Nøhr-Hansen, H., Aadland, T., Sandvik, S.E., Tennvassås, I., Engen, T. & Olaussen, S. 2019, Sedimentology and palynology of the Lower Cretaceous succession of central Spitsbergen: integration of subsurface and outcrop data: *Norwegian Journal of Geology*, v. 99, p. 1–32.

- Haq, B.U., 2014, Cretaceous eustasy revisited: Global and Planetary Change, v. 113, p. 44–58.
- Herbert, T.D., D'Hondt, S.L., Premoli Silva, I., Erba, E., and Fischer, A.G., 1995, Orbital chronology of Cretaceous-Early Palaeocene marine sediments, in: Berggren, W.A., Kent, D.V., Aubry, M.-P., and Hardenbol, J., eds., Geochronology, Time Scales, and Global Stratigraphic Correlation: SEPM Special Publication, v. 54, p. 81-94.
- Huang, C.J., Hinnov, L.A., Fischer, A.G., Grippo, A., and Herbert, T., 2010, Astronomical tuning of the Aptian Stage from Italian reference sections: *Geology*, v. 38, p. 899–902. <https://doi.org/10.1130/G31177.1>.
- Huber, B.T., and Petrizzo, M.R., 2014, Evolution and taxonomic study of the Cretaceous planktonic foraminifer genus *Helvetoglobotruncana* Reiss 1957: *Journal of Foraminiferal Research*, v. 44, p. 40–57.
- Kennedy, W.J., Gale, A.S., Huber, B.T., Petrizzo, M.R., Bown, P., Barchetta, A., and Jenkyns, H.C., 2014, Integrated stratigraphy across the Aptian/Albian boundary at Col de Pré-Guittard (southeast France): a candidate Global Boundary Stratotype Section: *Cretaceous Research*, v. 51, p. 248–259.
- Koppers, A.A.P., Staudigel, H., and Duncan, R.A., 2003, High-resolution $^{40}\text{Ar}/^{39}\text{Ar}$ dating of the oldest oceanic basement basalts in the western Pacific Basin: *Geochemistry Geophysics Geosystems*, v. 4, p. 1-20. <https://doi.org/10.1029/2003GC000574>.
- Larson, R.L., Fischer, A.G., Erba, E., and Premoli Silva, I., eds., 1993, APTICORE ALBICORE: A workshop report on global events and rhythms of the mid Cretaceous, 4–9 October, 1992, Perugia, Italy, 56 p. <https://usoceandiscovery.org/past-workshops-old/apticore-albicore-global-events-and-rhythms-of-the-mid-cretaceous/>
- Li, M.S., Hinnov, L.A., and Kump, L., 2019, Acycle: Time-series analysis software for paleoclimate research and education: *Computers and Geosciences*, v. 127, p. 12-22. <https://doi.org/10.1016/j.cageo.2019.02.011>.
- Martinez, M., Deconinck, J.F., Pellenard, P., Riquier, L., Company, M., Reboulet, S., and Moiroud, M., 2015, Astrochronology of the Valanginian–Hauterivian stages (Early Cretaceous): Chronological relationships between the Paraná–Etendeka large igneous province and the Weissert and the Faraoni events: *Cretaceous Research*, v. 131, p. 158–173. <https://doi.org/10.1016/j.gloplacha.2015.06.001>.

- Midtkandal, I. et al., 2016, The Aptian (Early Cretaceous) oceanic anoxic event (OAE1a) in Svalbard, Barents Sea, and the absolute age of the Barremian-Aptian boundary: *Palaeogeography, Palaeoclimatology, Palaeoecology*, v. 463, p. 126-135. <https://doi.org/10.1016/j.palaeo.2016.09.023>.
- Ogg, J.G., Ogg, G.M., and Gradstein, F.M., 2016, *A Concise Geologic Time Scale 2016*: Amsterdam, Netherlands, Elsevier, 234 p., <https://doi.org/10.1016/B978-0-444-59467-9.00001-7>.
- Reboulet, S., et al., 2014, Report on the 5th international meeting of the IUGS Lower Cretaceous Working Group, the Kilian Group (Ankara, Turkey, 31st August 2013): *Cretaceous Research*, v. 50, p. 126–137.
- Selby, D., Mutterlose, J., and Condon, D.J., 2009, U/Pb and Re/Os geochronology of the Aptian/Albian and Cenomanian/Turonian stage boundaries; implications for timescale calibration, osmium isotope sea water composition and Re-Os systematics in organic-rich sediments: *Chemical Geology*: v. 265, p. 394–409. <https://doi.org/10.1016/j.chemgeo.2009.05.005>.
- Sprovieri, M., Coccioni, R., Lirer, F., Pelosi, N., and Lozar, F., 2006, Orbital tuning of a lower Cretaceous composite record (Maiolica Formation, central Italy): *Paleoceanography*, v. 21, PA4212, p. 1-19. <http://dx.doi.org/10.1029/2005PA001224>.

Appendix B GSA data repository

Paleomagnetic and magnetostratigraphy methods and results, with Supplementary Figures DR1-DR4 (paleomagnetism)

Rock magnetism

Magnetic mineral compositions are determined along with sets from demagnetization treatments. Figures DR1-1, 1-2, and 1-3 illustrate the orthogonal isothermal remanent magnetization (IRM) results. The IRM acquisition curves are similar for most of the samples, with fast acquisition before 100 mT and then near saturation be at 300-500 mT, with limited acquisition afterwards, indicating the remanence properties are dominated by a large low coercivity and small high coercivity component, inferring minerals like magnetite (or a magnetic sulfide) and hematite. The three-component IRM data often show consistently loss of remanence in all three coercivity fractions, implying a wide range of particle sizes. Specifically, the uppermost and lowermost levels show a dominance of hematite while the upper- middle section suggests an apparent contribution from magnetite, and the lower middle section depicts some surge after 400-450 °C. This behavior may be attributable to greigite (or pyrrhotite) oxidation during demagnetization (e.g., Dekkers et al., 2000). In summary, the carriers of magnetic remanence for the lowermost Carlinefjellet Formation includes hematite and probably magnetite, and in the Helvetiafjellet Formation magnetite, except meter levels of ~185-196 m that may contain greigite, which oxidizes at treatment temperatures above 350-400 °C.

Paleomagnetism

A total of 110 mini-cores were collected from borehole DH1, of which 11 were selected as “pairs” to run comparative thermal/alternating AF field demagnetization before productive measurements. The thermal-only runs were performed using a Magnetic Measurements Ltd. (Aughton, Lancashire, UK) thermal demagnetizer, at increments ranging from 25-50 °C until the magnetization was either too weak to measure or displayed unstable behavior (up to 450 °C). While the AF-only measurements were demagnetized using a Molspin tumbling alternating field demagnetizer (Molspin Ltd, Newcastle on Tyne, UK) at steps of 5 mT until 20 mT and then transitioned to 10 mT until 50-80 mT according to the demagnetization behaviors.

After examining the rock magnetic property and pilot sets data, a composite demagnetization scheme using thermal demagnetization to 200-300 °C (dictated by lithology) followed by AF was found to be most effective. Large changes in rock color (mineralogy)

accompanied by surges in susceptibility and magnetic intensity were often seen above this critical range of thermal steps. The specimens were measured on a RAPID 2G magnetometer with noise level of ca. $1 \times 10^{-12} \text{ Am}^2$ (ca $1 \text{ } \mu\text{A/m}$). Details on polarity interpretation are included in Supplementary Table DR2.

The characteristic remanent magnetization (ChRM) for each sample was computed by a three-dimensional “least-squares fitting” technique (Kirschvink, 1980) using the public software PaleoMagX (Jones, 2002). A quality rating of ‘N(R)’, ‘NP(RP)’, ‘NPP(RPP)’, ‘N?(R?)’ or ‘INT’ were assigned to the characteristic remanent magnetization (ChRM) directions and polarity interpretation according to a semi-subjective judgment of the behaviors of the magnetic vectors during the progressive demagnetization. Examples of the quality-rated demagnetization are shown in Figs. DR2 and DR3.

The obtained magnetostratigraphy (Fig. 2) allows a consistent match with the reference scale in GTS2016. Even though the fluvial-deltaic facies of the Helvetiafjellet Formation has a very irregular sediment accumulation punctuated by soil horizons and scour at bases of fluvial-deltaic channels and though there is a low quality rating for many of the paleomagnetic samples, the combination of the subset of the higher-quality ChRMs and the other stratigraphic constraints do not allow another option to this main correlation to the magnetic polarity reference scale.

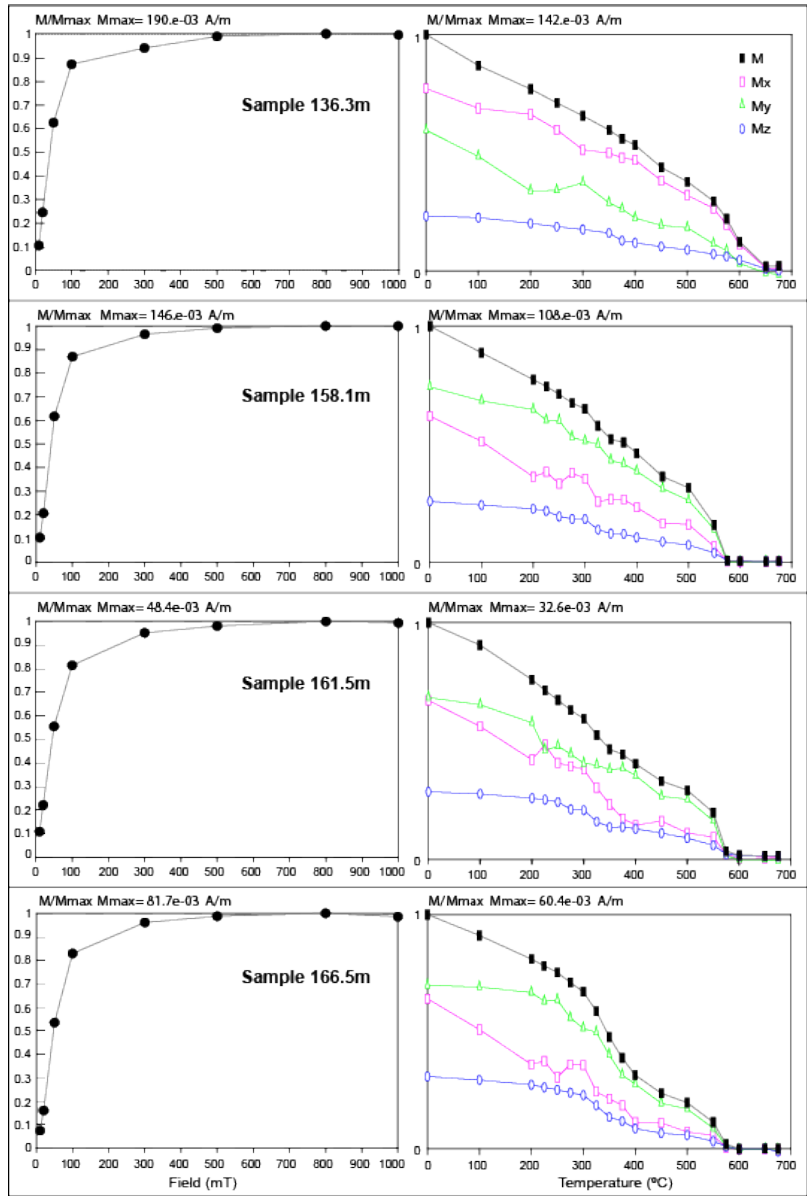


Figure DR1-1. (Left panels) The Isothermal Remanent Magnetization (IRM) acquisitions and (Right panels) the thermal demagnetization of orthogonal isothermal remanent magnetization (Lowrie, 1990): Thermal demagnetization of IRMs applied along x (30 mT, pink squares), y (100 mT, green triangles), and z (1000 mT, blue circles) axes of induced magnetization. Total magnetization is shown as black diamonds.

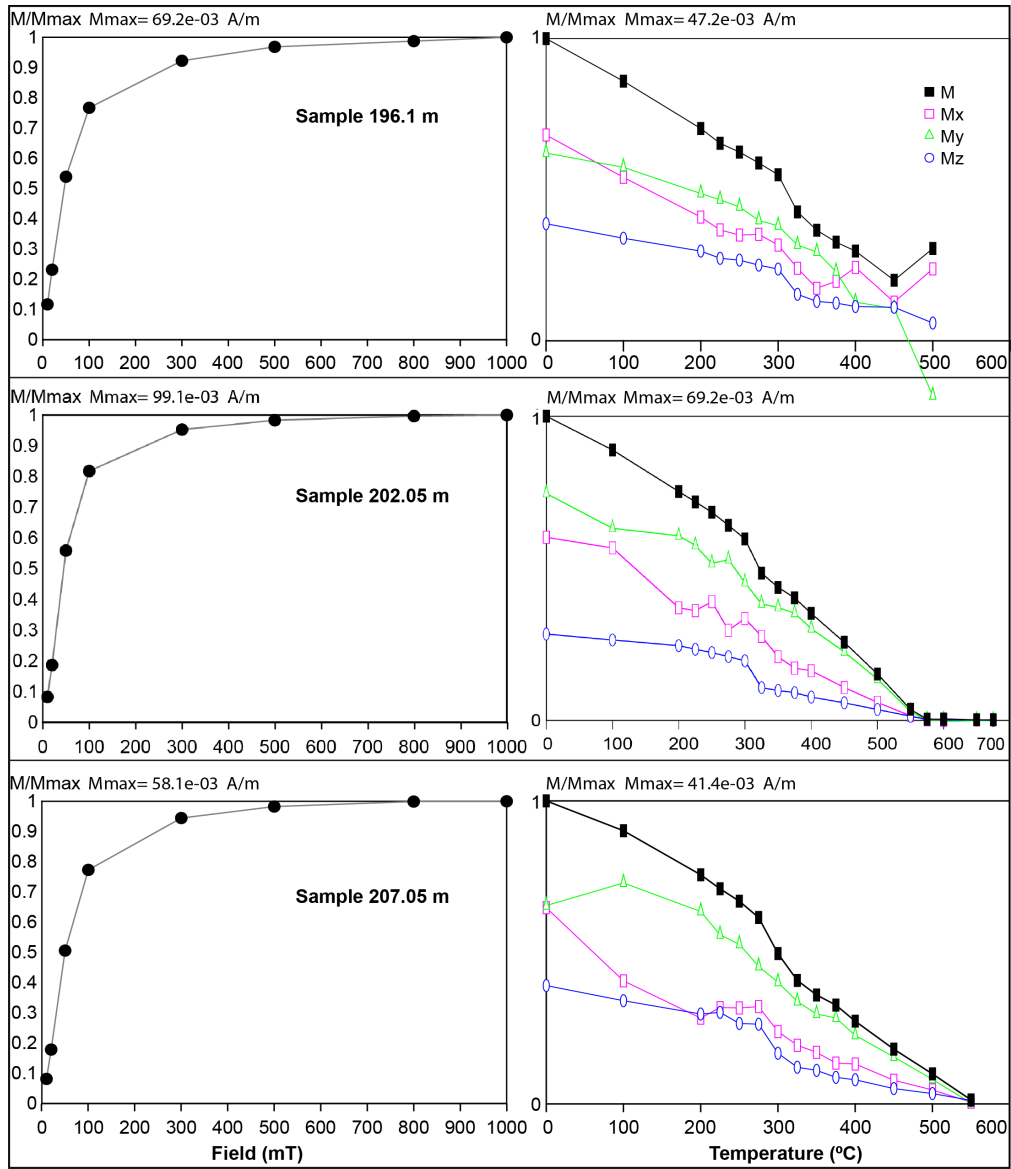


Figure DR1-2. Additional (orthogonal) IRM tests (see Fig. DR2-1 for details).

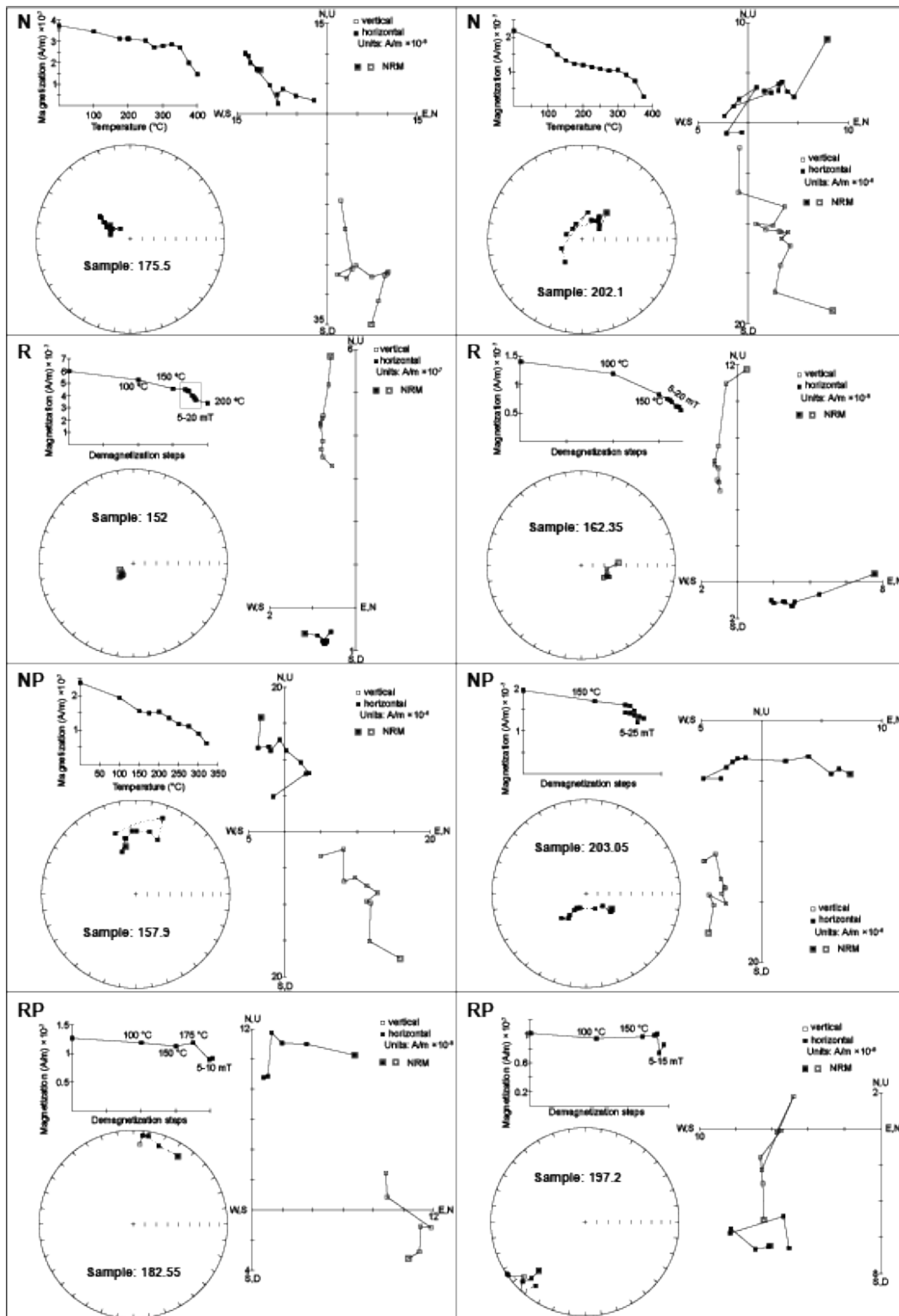


Figure DR2. Examples of relatively good quality-rated (N/R for the upper two panels and NP/RP for the lower two panels) vector end-point diagrams of typical demagnetization behaviors. For lithologies and brief notes on polarity interpretation of each sample, see Table DR2. Complete demagnetization data for each sample is in Table DR3.

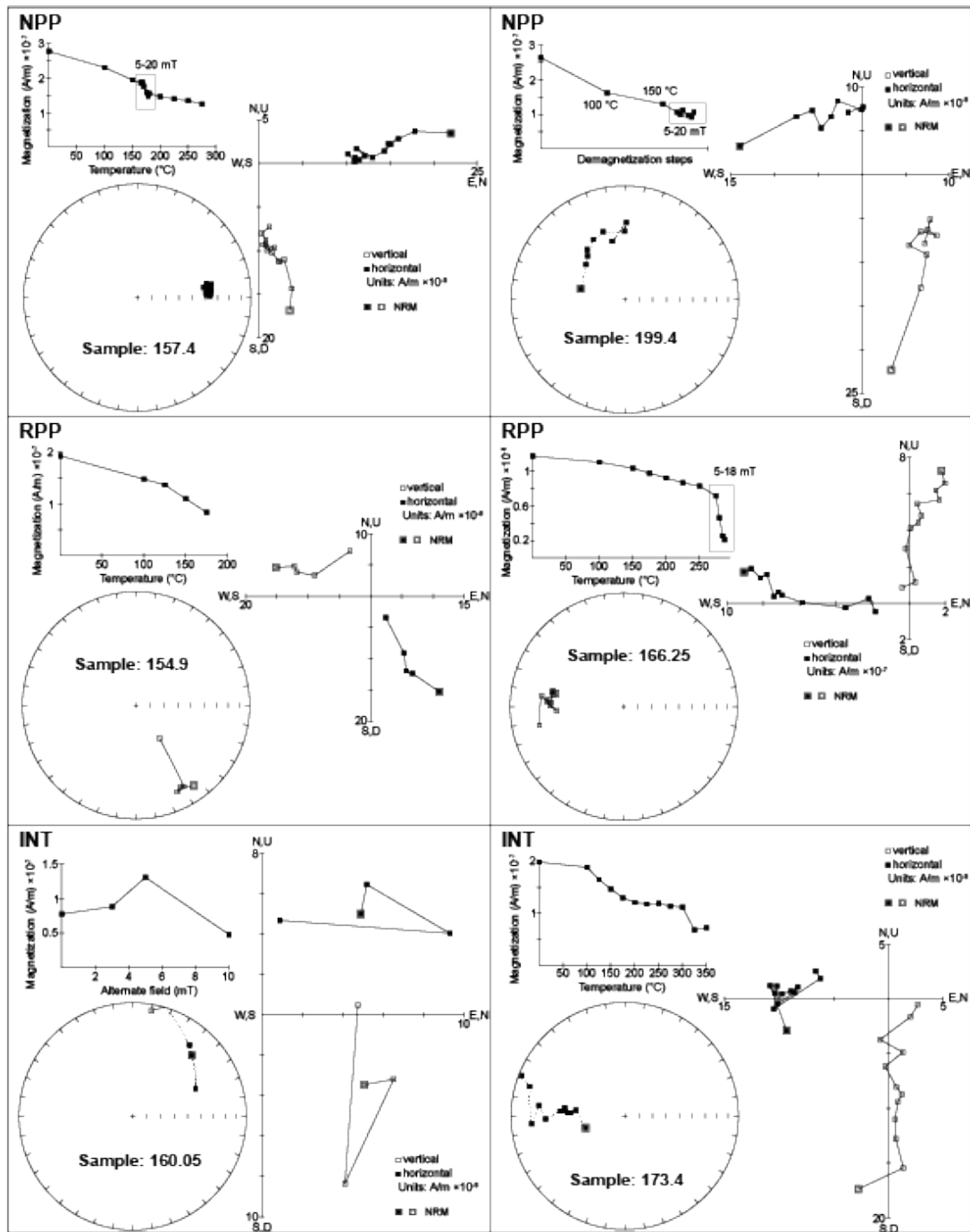


Figure DR3. Examples of poor quality-rated (NPP/RPP for the upper two panels and INT for the lowest panel) vector end-point diagrams of typical demagnetization behaviors. For lithologies and brief notes on polarity interpretation of each sample, see Table DR2. Complete demagnetization data for each sample is in Table DR3.

Cyclostratigraphy methods and results, with Supplementary Figures DR4-DR13 (cyclostratigraphy)

Facies trends and natural gamma ray log of DH1 – no clear cyclic climate signals recorded

The Helvetiafjellet Formation has a discontinuity onto the underlying Rurikfjellet Formation at a major erosion surface, known as the Barremian subaerial unconformity (e.g. Grundvåg et al., 2019; Fig. 2B). The lower Cretaceous basin fill in Svalbard is a response to crustal updoming with uplift in the north caused by the opening of the Amerasian Basin and the onset of the High Arctic Large Igneous Province (HALIP) to the northwest (e.g., Gjelberg and Steel, 1995; Maher, 2001, Midtkandal and Nystuen, 2009; Grundvåg et al., 2019). The Festningen Member of the lowermost Helvetiafjellet Formation is dominated by coarse-grained quartz sandstones that are interpreted as braidplain deposits. The overlying Glitrefjellet Member is a more heterolithic paralic facies, that is transitional between fluvial and a very flat deltaic coastal plain facies. The Glitrefjellet Member represents a type of very low-angle clinof orm; and tidal dunes between crevasse splays and soil profiles with coal suggest a very flat terrain. The detailed facies analysis in Engen (2018) concluded that the depositional environments of DH1 changed upward into an interdistributary bay facies in the uppermost part; thereby representing an overall increase in relative sea level. This Glitrefjellet Member also shows an upwards increase in volcanoclastic fragments (Maher et al., 2004), including the 20-cm thick volcanic ash layer in wells DH3 and DH7 (Corfu et al., 2013; Midtkandal et al., 2017). Well correlation between DH3-DH7 and DH1 place the same surface just below a thick sandstone bed at about 180 m in borehole DH1. These bentonites are direct evidence of the HALIP (Polteau et al., 2016). The base of the overlying Carolinefjellet Formation is defined by a flooding surface, and the uppermost beds of the Helvetiafjellet Formation consist of wave-reworked mouth-bar sands followed by a conglomeratic lag deposit containing lithic and siderite clasts (Engen, 2018; Grundvåg et al., 2019). Both the transgressive base and the transgressive surface at the top of the Helvetiafjellet Formation are probably close to chronostratigraphic horizons, at least among the cluster of DH cores. The lower ca. 10 m of the overlying Carolinefjellet Formation is an organic-rich shale as a regional flooding transformed the Helvetiafjellet Formation coastal plain into a shallow shelf depositional setting (Grundvåg et al., 2019).

The coastal plain during the deposition of the Helvetiafjellet Formation was subject to several relative sea level oscillations and/or shifting depocenters of sediment inputs (Midtkandal

et al., 2007) that were unrelated to Milankovitch-type climate cycles. As a result, the Helvetiafjellet Formation in the boreholes contains thin coal beds and soil horizons, in addition to scouring at the bases of some sandstone-filled channels (e.g., Grundvåg and Olausen, 2017; Engen, 2018). Therefore, even though there is an apparent correlation of the major fining-upward sand-rich episodes among the DH boreholes (Engen, 2018) that suggested a potential response to long-term climatic oscillations, this type of facies precluded resolving any unambiguous cyclic-climate signals from the natural gamma ray (NGR) logs of borehole DH1.

Filtering of ca. 7.3-m cycles were shown in comparison with the expected durations of each magnetic chron according to the reference time scale (GTS2016; green numbers in Fig. DR4). As is shown, these wavelengths' climate implications are challenged; for example, if assuming a 405-kyr (long eccentricity) to each of the 7.3-m wavelength, then the DH2n would represent at least 2 or 3 of 405-kyr, which is overly too long compared to the expected duration of ~450 kyr. If assuming a 100-kyr (short eccentricity), then the DH1n would be much shorter (< 400 kyr) compared to the expected 2 myr. Besides, sedimentation gaps, by erosion or non-deposition, are commonly seen from the detailed sedimentology (e.g., Engen, 2018), which make it a less than ideal core for extraction of cyclostratigraphy.

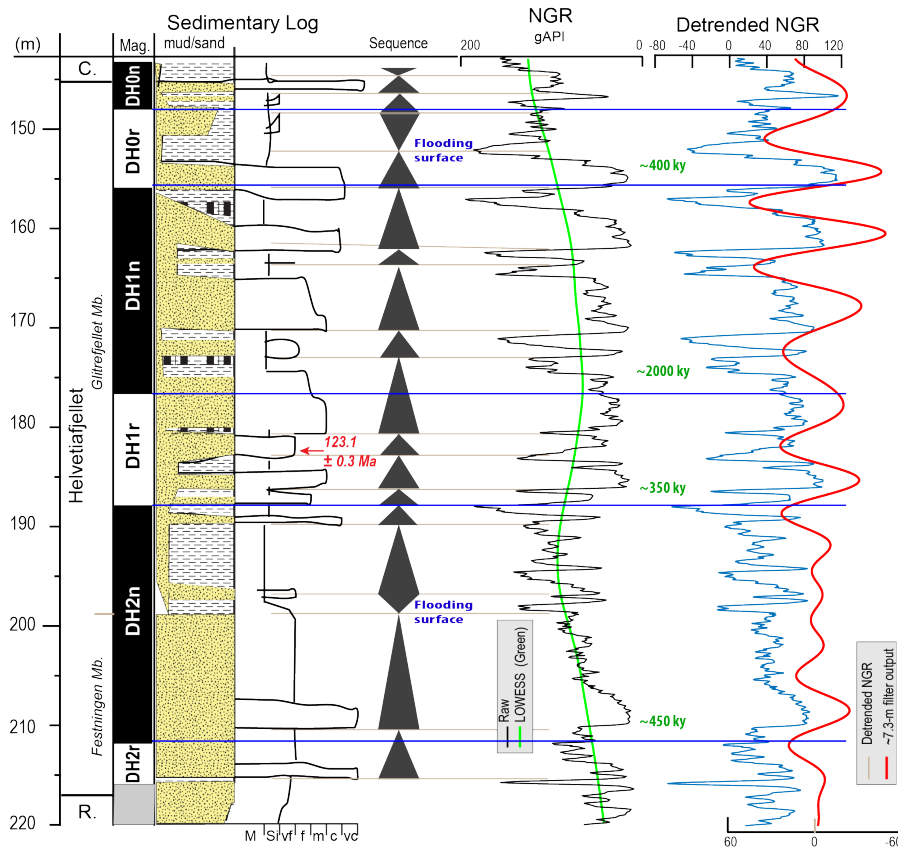


Figure DR4. Sequence stratigraphy and the downhole natural gamma ray log with ~ 7.3 m filter output. From left to right: (1) The magnetostratigraphy obtained from borehole DH1. (2) Generalized lithostratigraphy showing the mud/sand ratio. The radiometric age (denoted in red) is projected to the DH1 core from the other two nearby bentonite-bearing cores (DH3&7). The blue lines denote the reversal boundaries; and the numbers in green (between NGR and Detrended NGR curves) are the durations for the corresponding magnetic polarity chrons as derived from the astronomically-calibrated geomagnetic time scale in GTS2012/2016 (Ogg et al., 2016). (3) Schematic fining- or coarsening-upward sequences (triangles in gray) are based on the mud/sand variations and the detailed facies analysis in Engen (2016). (4) The natural gamma ray data (NGR, raw data in black) depicts a ~ 30 m long-term trend (green line) towards higher values, i.e., higher mud contents or more marine-influenced in this case. (5) After removing this trend, the NGR (detrended, navy blue) was filtered by ca. 7.3-m wavelengths (red, ranging from ~ 5.5 to 11.1 m). Note that the filters could not match the durations of polarity chrons, no matter which orbital parameter(s) are assigned.

Re-interpreting the greyscale data of the Piobbico core, northern Italy

We utilized a newly developed program *Acycle* (www.mingsongli.com/acycle), which applies a correlation coefficient (COCO) technique to obtain the best fit of sediment accumulation rates. Based on an assumption of astronomical forcing for the suite of identified filtered cycles, this *Acycle* estimation computes the correlation coefficient between the frequency

spectra of target astronomical solutions and the presence of different cycles within studied data to achieve the numerical estimation of the depositional rates (higher correlation coefficient corresponds to the most ‘real’ rate) (Li et al., 2018, 2019). Monte Carlo simulations (or probability simulations) are embedded in the COCO method to test the significant level of astronomical forcing assumption, with the null hypothesis (H_0) indicating no orbital forcing. In addition, number of contributing astronomical cycles at each possible sediment accumulation rate is also evaluated. For example, a sediment accumulation rate that has the low (<1%) null hypothesis significant level (H_0 -SL), high correlation coefficient (>0.5) and a greater number of orbital cycles (maximum of 7) involved are interpreted to be most possible. To track the variation of the sediment accumulation rates throughout the data series, a sliding window technique, termed Evolutionary COCO (eCOCO) is applied.

1) Sedimentation rate-based time calibration of the entire greyscale data

Initially, the greyscale data were analyzed as a whole series (Figs DR5, DR6 and DR7). The 2π MTM power spectrum shows that the dominant cycles have wavelengths of ~ 2 , 0.5, 0.2-0.26 and ~ 0.13 -0.17 m. The ~ 2 m filtering (Gauss filter, passband: 0.45 ± 0.21) indicates at least 17 cycles, which is only half of the 405-kyr long eccentricity cycles recognized by Huang et al. (2010). COCO analysis extracts four peaks of sediment accumulation rates (Fig. DR6) at 0.35, 0.59, 0.71 and ~ 0.98 cm/kyr, respectively. All 7 astronomical cycles tested in the COCO analysis are involved, and the null hypothesis significance level is <0.01. Based on these COCO and eCOCO results, we tracked the sediment-accumulation rate solutions that had the higher correlation coefficient ($\rho > 0.3$), lower H_0 significance level (<0.01), and more astronomical terms (≥ 6) through the succession (marked in Fig. DR7; detailed data in Table DR4).

The resulting duration of the entire series from the eCOCO analysis method spans about 8.3 myr (Fig. DR7). The base Albian was placed at ~ 0.58 myr and the top of magnetozone M0r at ~ 8.19 myr, revealing a duration of 7.6 myr for the portion of Aptian except the M0r. Therefore, taking the 370 kyr of M0r, the entire Aptian would last ~ 8.0 myr ($= \sim 7.6 + 0.37$). The base Aptian is then placed at ~ 121.1 Ma ($= 113.1 + \sim 8.0$) with an uncertainty of ± 0.3 Ma based on the base Albian dating. However, compared to the better recognized duration of the OAE1a (~ 1 -1.4 myr), this age model yields only 390 kyr (Fig. DR7), which raises concern on the viability of this result. As discussed in the next section (Section 2.2.2), this short-duration of OAE1a in this age model, could be due to the still-imprinted-long-term-trend, given the fact that the condensed low-

carbonate OAE1a interval hindered the recognition of sedimentation rates (e.g., Herbert, 1992). The lack of significant carbonate within the OAE1a interval was caused by the "nannoconid crisis" and global reduction in calcification (Erba, 1994; Erba et al., 2015).

2) Removing intervals distorted by core recovery or condensation

Except for the carbonate-poor OAE1a interval that was analyzed separately, the Aptian portion of the Piobbico core has two other short intervals that had been distorted by non-recovery and uncertain placement of the recovered pieces. Therefore, these were excluded from the high-precision tuning, and then were re-inserted into the final time scale by applying a similar sediment accumulation rate to that obtained from the adjacent segments.

Therefore, four intervals – 45.77-49.94 m; 65.67-71.96 m, OAE1a interval (73.15-75.47 m), and the short segment from 75.47 m to base of record at ca. 77 m – were isolated from the main spectra analysis. In addition, the evolutive spectra of these distorted intervals seem to involve more frequencies/cycles other than the “cleaner” levels above and below (Fig. DR5). These distorted intervals were "cut out" using the previous band-pass results to have an integer number of component main cycles.

3) Tuning the undistorted series

The spliced (after removing the distorted intervals) grayscale series (Fig. DR8) produces a “cleaner” 2π MTM power spectrum with four main wavelengths of ~1.4-2.6 m, ~0.4 m, 0.2 m and 0.12 m, which is similar to that of the entire series (Fig. DR6). Those frequencies are trackable throughout the series as depicted in the FFT spectrum. Therefore, by tuning the most significant 1.4-2.6-m cycle, we obtained a duration of ca. 4.67 myr (Fig. DR9). The resultant spectra correlate very well to the astronomical parameters in La2004.

4) Compensating for the distorted intervals

It was assumed that the removed intervals that were distorted by core recovery encompassed an integer number of long-eccentricity cycles, based upon the pre-cut band-pass signal. The number of cycles were assumed to fit the sediment accumulation rates of the adjacent tuned cycles. Therefore, for the lower distorted segment at 65.67-71.96 m, three long-eccentricity cycles were assigned to the interval, which assumes a 0.57 cm/kyr of sediment accumulation rate (Supplementary Table DR5), which is intermediate to the 0.37 cm/kyr below (just above the very slow accumulation rate of 0.28 cm/kyr during OAE1a) and 0.64 cm/kyr above (after the full recovery from carbonate crisis). This trend toward lighter thus less clay

sediments could be seen from the grayscale data (Fig. DR5). Similarly, for the upper distorted segment at 45.77-49.94 m, two long-eccentricity cycles were assigned to the interval. The implied ca. 0.47 cm/kyr sediment accumulation rate is slightly faster than the 0.39 cm/kyr below and 0.35 cm/kyr above. A slightly higher clastic influx is suggested by the greater amplitude oscillations of light/dark in the grayscale data (Fig. DR6).

5) Tuning the condensed OAE1a carbonate-poor interval

Following the lead of other cyclostratigraphic interpretations of the OAE1a interval in Italy (e.g., Herbert et al., 1995; Sprovieri et al., 2006; Li et al., 2008; Huang et al., 2010), this OAE1a interval in the Piobbico core was tuned to the 100-kyr short-eccentricity cycle. The 2π MTM power spectrum (Fig. DR10) shows significant wavelengths of ~ 47 cm, ~ 12 cm and 6.3 cm. By assigning 100-kyr to the ca. 12-cm cycles, we obtained a duration of ca. 1.33 myr for the OAE1a (Supplementary Table DR5), which is equivalent to ca. 3.3 E cycles and similar to the estimate by Li et al. (2008). The power spectra of the tuned series (Fig. DR11) also has additional peaks at ca. 40 kyr (obliquity) and at 270 kyr, but no higher frequencies corresponding to the precessional bands. The lack of resolving precession signal is probably due to the spacing of the data points as digitized from the Fig. 1 of Huang et al. (2010).

6) The combined Piobbico core cyclostratigraphy in the time domain

The five separately tuned intervals are spliced into a complete tuned time series (Fig. 3 in the main text), which spans 8.46 myr. For consistency, we numbered the identified E cycles downward from #31 at the base of the Albian in this Piobbico core (Grippio et al., 1994; Huang et al., 2010) (Fig. DR12). To the 15 cycles above the OAE1a (Fig. DR13), we add the tuned duration of 1.3 myr of OAE1a, and the ca. 0.7 E cycle to the top of magnetozone M0r. Therefore, the time span from the base of the Albian (cycle E31) to the top of magnetochron M0r (cycle ca. E50) is 7.72 myr (Supplementary Table DR5). The duration of magnetochron M0r is estimated as ca. 0.4 myr (Herbert et al., 1995); for a total duration of the Aptian (using base of M0r as the base-Aptian) of 8.1 myr.

The durations of other regional organic-rich levels (positions on the Piobbico in Fig. DR12), of which some may correspond to global oceanic anoxic events, are calculated from their span within the Piobbico core relative to the tuned cyclostratigraphy. The Kilian event in that core has an implied duration of 100 kyr for the Kilian event, the Jacob event as ca. 60 kyr, and ca. 190 kyr for the Fallot event.

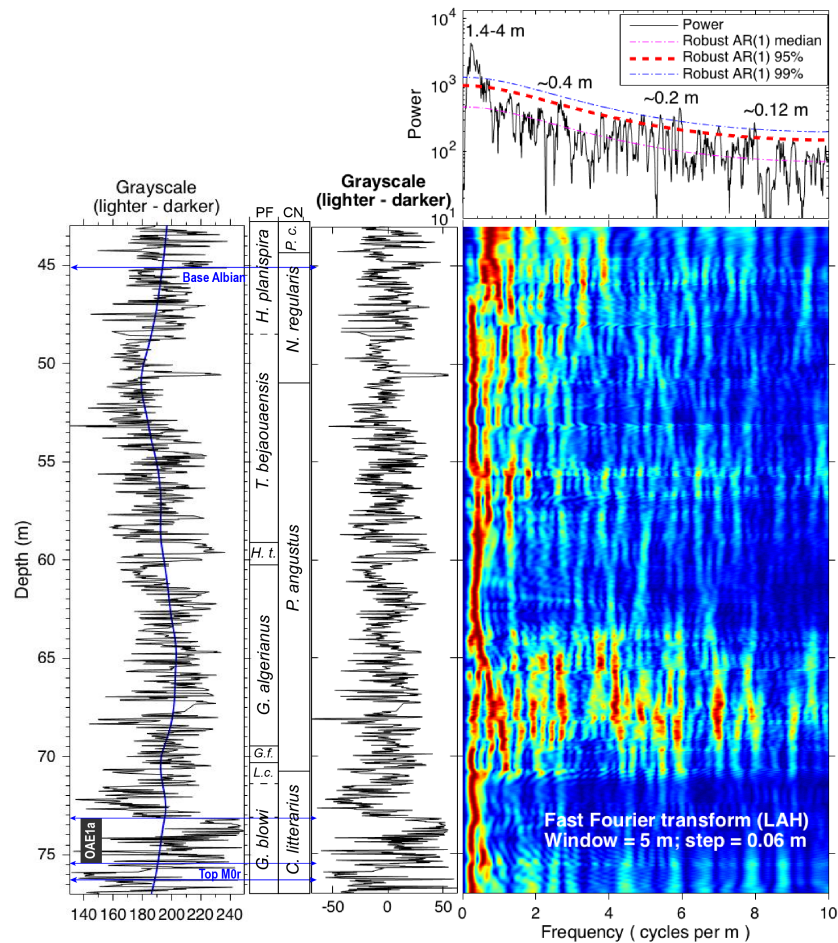


Figure DR5. Spectral analysis of the detrended greyscale data of Piobbico core. From left to right shows, the ‘raw’ greyscale data (solid black line) and the ca. 8.5-m LOWESS trend (blue line), the plankton foraminiferal (PF) and calcareous nannofossil (CN) zonation, the detrended data. The proposed positions of the base Albian, OAE1a, and Top of magnetochron M0r are also labeled. A 5-point-smoothing and an interpolation of 0.02 m is applied to the digitized data before the spectral analysis. Evolutionary power spectrum (Fast Fourier transform, FFT, Kodama and Hinnov, 2015) uses a 5-m window. The 2π MTM power spectrum shows that the dominant cycles have wavelengths of ~ 1.5 -4 m, ~ 0.4 m, 0.18 m, and 0.12 m, respectively. *P.c.* = *P. columnata*. *H.t.* = *H. trocoidea*. *G.f.* = *G. ferreolensis*. *L.c.* = *L. cabri*.

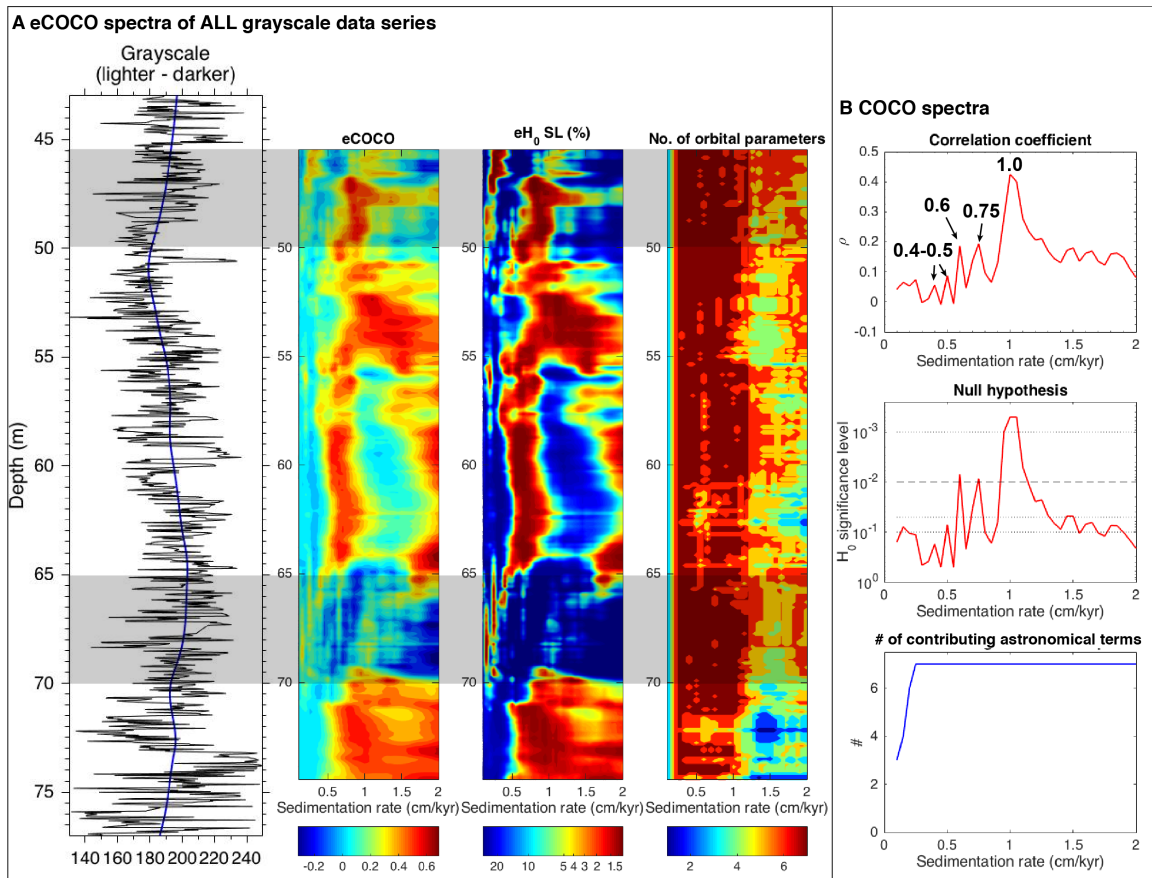


Figure DR6. COCO and eCOCO analysis of the greyscale data from Piobbico core. (A) Columns from left to right are the digitized data with trend, the evolutionary correlation coefficient, the evolutionary H_0 significance level, and the evolutionary map of the number of astronomical terms identified in the NGR data series. The sliding window is 5 m using 0.12-m steps. All periodograms were analyzed with the AR(1) red noise model removed. The number of Monte Carlo simulations is 2000. The tested sedimentation rates range from 0.1 to 2 cm/kyr with a step of 0.05 cm/kyr. The shaded intervals indicated vague sedimentation rates. (B) The upper to lower panels are the *Correlation coefficient* ρ with higher- ρ sediment accumulation rates (in cm/kyr) labeled, the *Null hypothesis* (H_0 = no astronomical forcing) results showing that all the high- ρ sediment accumulation rates are less than 0.01 with the 0.59 and 0.71 cm/kyr range less than 0.001, and the *Number of astronomical terms* (#) identified in the tested sediment accumulation range from 0.01 to 2 cm/kyr. The step used for the COCO analysis is 0.01 cm/kyr. The target series is the La2004 astronomical solution for the early Cretaceous (111 to 126 Ma; Laskar, 2004).

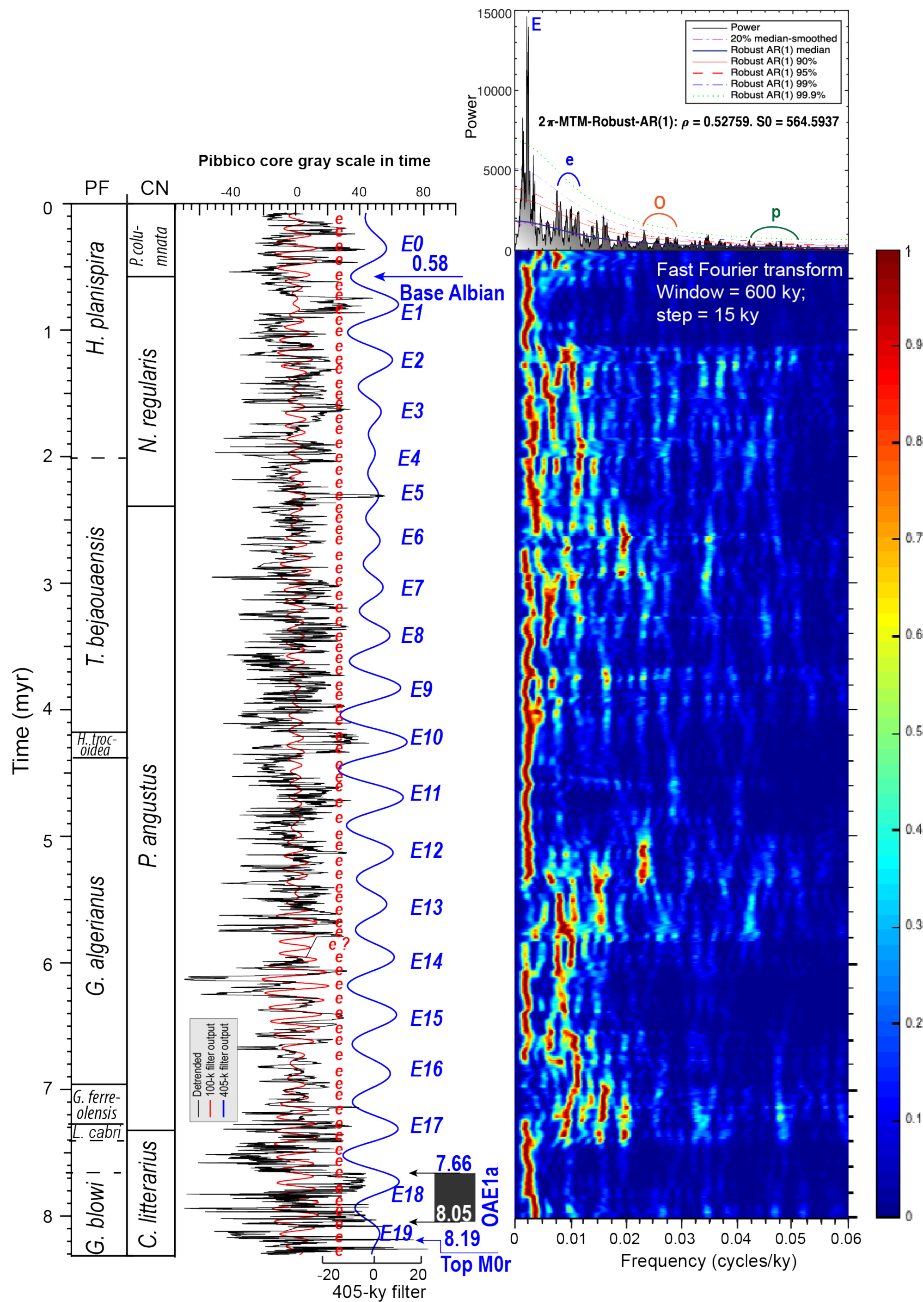


Figure DR7. The greyscale series converted into time domain with its power spectra showing the dominating cyclicality that matches the Milankovitch cycles (La2004 solution; Laskar, 2004). The biozones and events are also shown. The numbers above arrows of events are in myr. The filtered long (blue line) and short (red) eccentricity are at passband of 0.0023083 ± 0.0004617 and 0.0095 ± 0.0011 , respectively. Note that the OAE1a interval here has a duration of ~ 390 kyr, far shorter compared to the well-recognized 1-1.4 myr (e.g., Huang et al., 2010; Li et al., 2008).

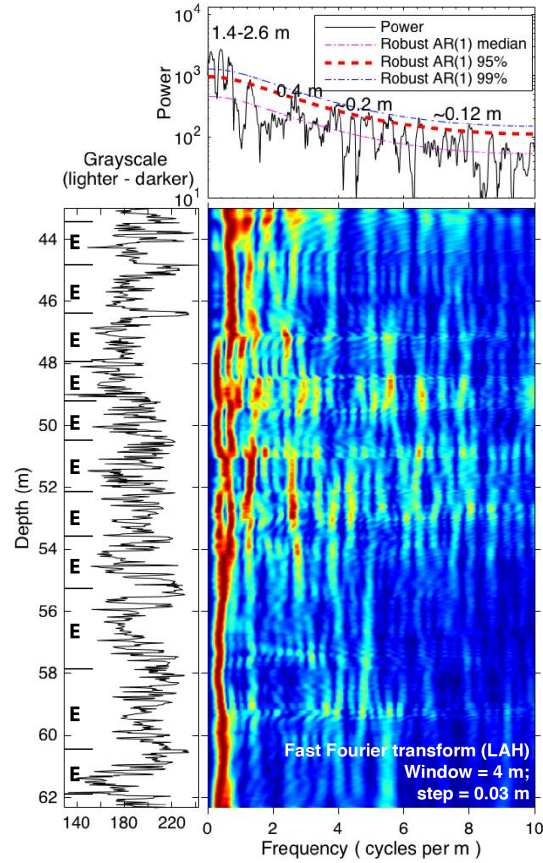


Figure DR8. Spectral analysis of the 4.8-m LOWESS detrended greyscale data of Piobbico core excluding 45.77-49.94 m, 65.67-71.96 m, and 73.17-end (including the OAE1a interval, i.e., 73.17-75.47 m). The “E”s denotes the picks of long eccentricity cycles.

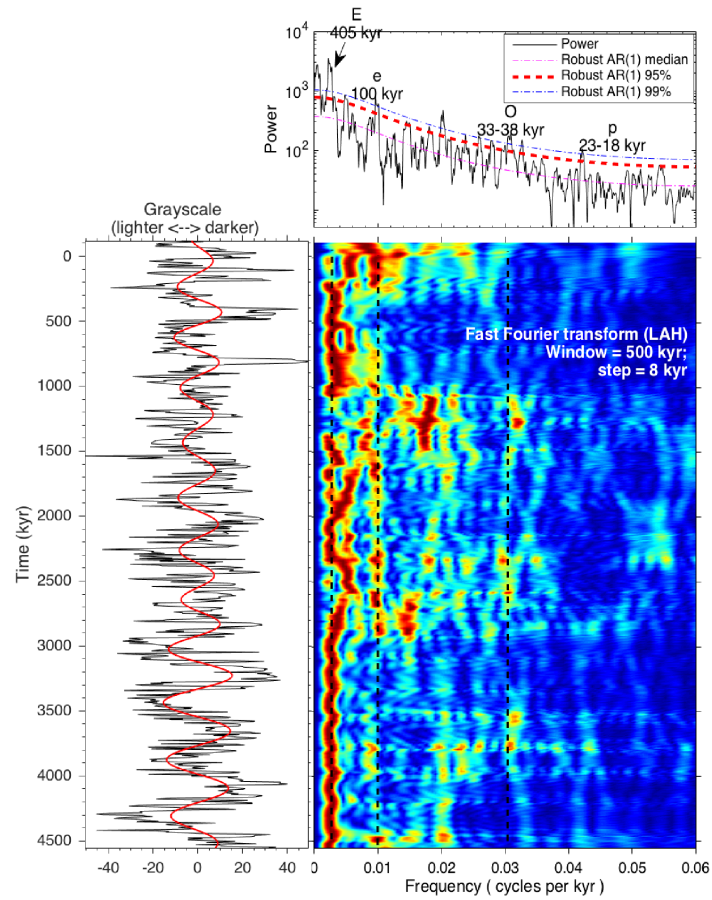


Figure DR9. Spectral analysis of the 405-kyr tuned grayscale data excluding the four intervals that distorted the astronomical signal. The multitaper spectrum shows nicely all the astronomical parameters in La2004, which are found throughout the tuned series according to the Fast Fourier transform.

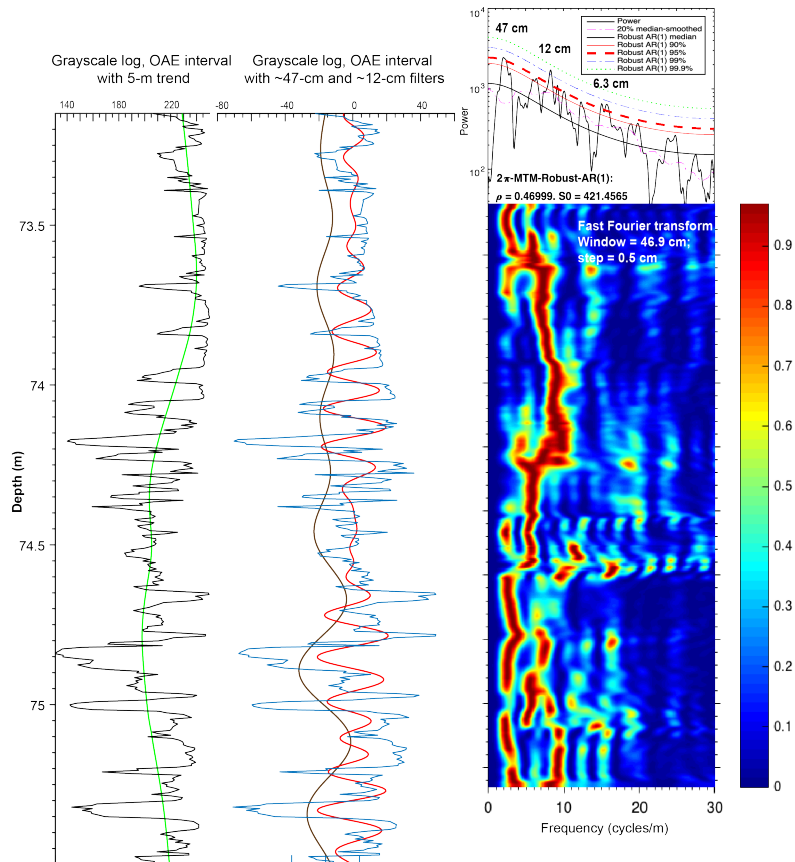


Figure DR10. Spectral analysis of the OAE1a interval of the greyscale data from the Piobbico core. From left to right shows, the ‘raw’ greyscale data (solid black line) and the 1.2-m LOWESS trend (green line), the detrended data (navy blue line), the ~47-cm filter output (Gauss filter, passband: 2.128 ± 0.478 ; brown line), and the ~12-cm filter output (Gauss filter, passband: 7.8 ± 1.7 ; red line).

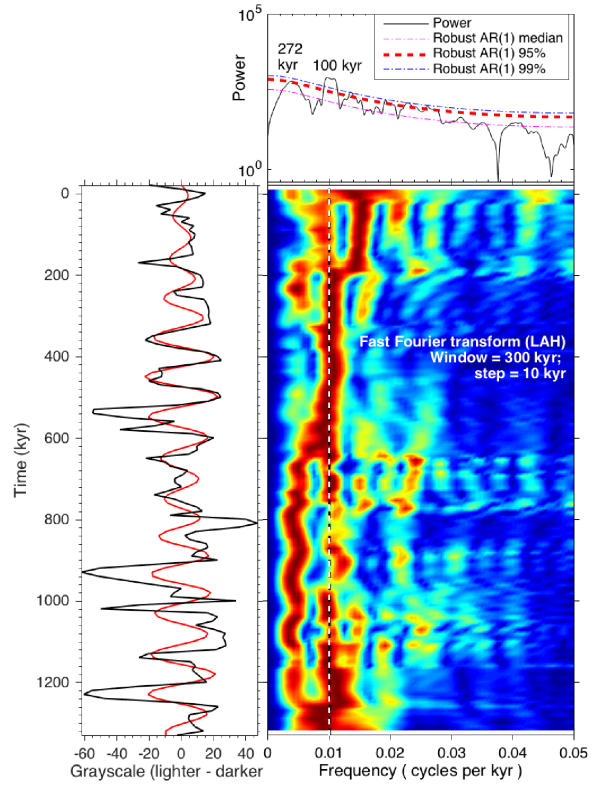


Figure DR11. Spectral analysis of the 100-kyr tuned grayscale data from the OAE1a interval. Passband 0.010294 ± 0.002059 is used for the Gaussian filter of 100-kyr.

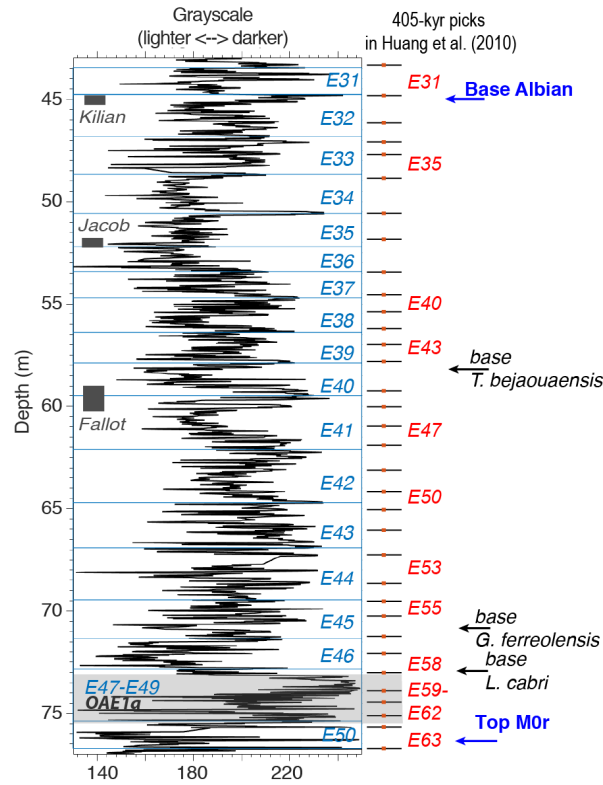


Figure DR12. The astronomical tuning age model in this study (blue lines and "E" long-eccentricity cycle numbers) compared to the model from Huang et al. (2010) (their E-levels indicated by light-gray line-segments with an orange-colored dot in the middle; with selected "E" numbers in red). For consistency with the overlying Albian cyclostratigraphy (downward numbering of E1 through E30; Grippo et al., 2004), the E cycles interpreted in our study use the same (top) number of E31 as in Huang et al. (2010). Biostratigraphic zones and positions of oceanic anoxic events (OAE1a) or regional organic-rich levels are adopted from Huang et al. (2010) and references therein, except the base Albian GSSP, which was placed in the middle of the Kilian organic-rich bed according to Kennedy et al. (2017).

Supplementary references cited

- Braathen, A., Balum, K., Christensen, H.H., Dahl, T., Eiken, O., Elvebakk, H., Hansen, F., Hanssen, T.H., Jochmann, M., Lie, T., Johansen, T.A., Johnsen, H., Larsen, L., Mertes, J. Mork, A., Mork, M.B., Nemec, W.J., Olaussen, S., Oye, V, Roed, K., Titlestad, G.O., Tveranger, J., and Vagle, K., 2012, The Longyearbyen CO₂ Lab of Svalbard, Norway - initial assessment of the geological conditions for CO₂ sequestration: *Norwegian Journal of Geology*, v. 92, p. 353–376.
- Dekkers, M.J., Passier, H.F., and Schoonen, M.A.A., 2000, Magnetic properties of hydrothermally synthesized greigite (Fe₃S₄)—II. High- and low-temperature characteristics: *Geophysical Journal International*, v. 141, p. 809-819. <https://doi.org/10.1046/j.1365-246x.2000.00129.x>.
- Erba, E., 1994, Nannofossils and superplumes: The Early Aptian “nannoconid crisis”: *Paleoceanography*, v. 9, p. 483-501.
- Gjelberg, J., and Steel, R.J., 1995, Helvetiafjellet formation (Barremian-Aptian), Spitsbergen: characteristics of a transgressive succession: *Norwegian Petroleum Society Special Publications*, v. 5, p. 571–593. [http://dx.doi.org/10.1016/S0928-8937\(06\)80087-1](http://dx.doi.org/10.1016/S0928-8937(06)80087-1)
- Grundvåg, S.A., and Olaussen, S., 2017, Sedimentology of the Lower Cretaceous at Kikutodden and Keilhaufjellet, southern Spitsbergen: implications for an onshore–offshore link: *Polar Research*, v. 36, p. 1302124. <https://doi.org/10.1080/17518369.2017.1302124>.
- Grundvåg, S.A., Jelby, M.E., Śliwińska, K.K., Nøhr-Hansen, H., Aadland, T., Sandvik, S.E., Tennvassås, I., Engen, T. & Olaussen, S. 2019: Sedimentology and palynology of the Lower Cretaceous succession of central Spitsbergen: integration of subsurface and outcrop data. *Norwegian Journal of Geology* 99. <https://dx.doi.org/10.17850/njg006>.
- Herbert, T.D., 1992, Paleomagnetic calibration of Milankovitch cyclicity in lower Cretaceous sediments: *Earth and Planetary Science Letters*, v. 112, p. 15–28. [https://doi.org/10.1016/0012-821X\(92\)90003-E](https://doi.org/10.1016/0012-821X(92)90003-E).
- Kennedy, W.J., Gale, A.S., Huber, B.T., Petrizzo, M.R., Bown, P., Barchetta, A., and Jenkyns, H.C., 2014, Integrated stratigraphy across the Aptian/Albian boundary at Col de Pré-Guittard (southeast France): a candidate Global Boundary Stratotype Section: *Cretaceous Research*, v. 51, p. 248–259.

- Kirschvink, J., 1980, The least-squares line and plane and the analysis of palaeomagnetic data: *Geophysical Journal International*, v. 62, p. 699-718.
- Kodama, K.P., and Hinnov, L., 2015, *Rock Magnetic Cyclostratigraphy*: John Wiley & Sons, v. 5, 165 p. doi:10.1002/9781118561294.
- Laskar, J., 2004, A long-term numerical solution for the insolation quantities of the Earth: *Astronomy & Astrophysics*, v. 428, no. 1, p. 261-285.
- Li, M.S., Hinnov, L.A., and Kump, L., 2019, Acycle: Time-series analysis software for paleoclimate research and education: *Computers & Geosciences*, v. 127, p. 12-22.
- Li, M.S., Kump, L., Hinnov, L. A., and Mann, M. E., 2018, Tracking variable sedimentation rates and astronomical forcing in Phanerozoic paleoclimate proxy series with evolutionary correlation coefficients and hypothesis testing: *Earth and Planetary Science Letters*, v. 501, p. 165-179.
- Li, Y.-X., Bralower, T.J., Montañez, I.P., Osleger, D.A., Arthur, M.A., Bice, D.M., Herbert, T.D., Erba, E., and Premoli S., 2008, Toward an orbital chronology for the early Aptian Oceanic Anoxic Event (OAE1a, ~120 Ma): *Earth and Planetary Science Letters*, v. 271, p. 88-100. <https://doi.org/10.1016/j.epsl.2008.03.055>.
- Lowrie, W., 1990, Identification of ferromagnetic minerals in a rock by coercivity and unblocking temperature properties: *Geophysical research letters*, v. 17, p. 159-162.
- Maher Jr., H.D., 2001, Manifestations of the Cretaceous High Arctic Large Igneous Province in Svalbard: *The Journal of Geology*, v. 109, p. 91–104. <https://doi.org/10.1086/317960>.
- Maher, H.D., Hays, T., Shuster, R., and Mutrux, J. 2004, Petrography of the Lower Cretaceous sandstones of Spitsbergen: *Polar Research*, v. 23, p. 147–165. <https://doi.org/10.1111/j.1751-8369.2004.tb00005.x>
- Midtkandal, I., and Nystuen, J.P., 2009, Depositional architecture of a low-gradient ramp shelf in an epicontinental sea: the lower Cretaceous of Svalbard: *Basin Research*, v. 21, p. 655–675. <http://dx.doi.org/10.1111/j.1365-2117.2009.00399.x>.
- Midtkandal, I., Nystuen, J. P., and Nagy, J., 2007, Paralic sedimentation on an epicontinental ramp shelf during a full cycle of relative sea-level fluctuation; the Helvetiafjellet Formation in Nordenskiöld land, Spitsbergen: *Norsk Geologisk Tidsskrift*, v. 87, p. 343-359.

CHAPTER 4. PLIOCENE-PLEISTOCENE MAGNETO-CYCLOSTRATIGRAPHY OF IODP SITE U1499 AND IMPLICATIONS FOR CLIMATE-DRIVEN SEDIMENTATION IN THE NORTHERN SOUTH CHINA SEA

Yang Zhang¹, Liang Yi², James G. Ogg^{3,1,*}

¹*Department of Earth, Atmospheric and Planetary Sciences, Purdue University, 550 Stadium Mall Drive, West Lafayette, IN 47907-2051, USA*

²*State Key Laboratory of Marine Geology, Tongji University, Shanghai 200092, PR China*

³*State Key Laboratory of Oil and Gas Reservoir Geology and Exploitation, Chengdu University of Technology, Chengdu, Sichuan 610059, PR China*

* Corresponding author: jogg@purdue.edu

Abstract: A high-resolution astronomical-tuned magnetostratigraphy was obtained from a continuous 333-m succession recovered at International Ocean Discovery Program (IODP) Hole U1499A in the north margin of the South China Sea (SCS) during joint Legs 367 & 368. A total of 12 magnetic reversals are identified through the Pliocene and Pleistocene. The cycle analysis of natural gamma ray (NGR) data shows an average suite of ca. 33 m and 8 m wavelengths with lesser 1.5-m cycles, which are consistent with the ratios of Milankovitch orbital-climate oscillations caused by long eccentricity (405 kyr), short eccentricity (~100 kyr), and precession (~20 kyr). The astronomical-tuned magnetostratigraphy correlates with nearly all features of the Pliocene-Pleistocene geomagnetic polarity time scale. There was a significant shift to ~100-kyr-dominated cyclicity at ca. 1.3 Ma, which marks the onset of the Mid-Pleistocene Transition, during which the influx of the clay component decreased. A general enrichment in silt-sand influx during the past 0.4 Myr was punctuated by surges in coarser-grained components (lowest NGR) during or at the end of each major global glacial event. Comparison to a high-resolution sediment record spanning the Pliocene-Pleistocene on the southern margin of the SCS (ODP Site 1143) indicates common intervals of changing rates of sediment accumulation. In both regions, there are relatively lower rates of sediment accumulation during the late Zanclean (mid-Pliocene; ca. 4.1 to 3.6 Ma), early Gelasian (ca. 2.5 to 2.0 Ma), early Calabrian (ca. 1.6 to 1.4 Ma) and the earliest Middle Pleistocene (ca. 0.6 Ma). The merger of magnetostratigraphy, cyclostratigraphy

and the NGR record to produce a high-resolution profile of bulk sediment accumulation rates and relative clay to sand-silt components is a powerful tool and climate proxy to reconstruct the general history of sediment input into the SCS and its relationships to East Asia monsoon and tectonic evolution.

Keywords: Plio-Pleistocene; magnetostratigraphy; Milankovitch; East Asia monsoon; Mid-Pleistocene Transition

4.1 Introduction

The South China Sea (SCS), the largest marginal sea along the western Pacific, receives the discharge of many major rivers draining southeastern Asia, Taiwan, Luzon and Borneo (Liu et al., 2016) (Fig. 1). These fluvial influxes, plus the products of marine productivity, accumulated in thick Neogene deposits that provide excellent records of land-sea interaction and paleoclimate changes (e.g., Ao et al., 2011; Li et al., 2008; Tian et al., 2002; Wang et al., 2003).

The Pliocene-Pleistocene generally had a high seasonality with relatively cooler temperatures during northern hemisphere glaciations (Clemens et al., 1996; Zachos et al., 2001; Molnar, 2004). The East Asian monsoon system is characterized during the Summer Monsoon phase by heavy rainfall and by warm winds from the south, and during the Winter Monsoon phase by strong dry winds from the north/northeast (Jian et al., 2009). There was an apparent general enhancement of the East Asia Winter Monsoon during the cooling trend after the mid-Pliocene (~3 Ma) (e.g., Wan et al., 2007). Its variation during the Quaternary was heavily influenced by high-latitude glaciations (e.g., An, 2014; An et al., 2001), which are believed to be orbitally forced (Holbourn et al., 2007; Sun et al., 2006). In addition, the East Asian monsoon was significantly affected by uplift phases of the Himalaya-Tibetan Plateau (e.g., Li et al., 2014; Tada et al., 2016) and atmospheric CO₂ levels (e.g., Huber and Goldner, 2012).

Additional major regional climate shifts during the Quaternary include the Mid-Pleistocene Transition (MPT) (e.g., Li et al., 2008), the Mid-Brunhes Event at an insolation minima (e.g., Kemp et al., 2010), and the sea-level lowstands during glacials which exposed large portions of the shelf, thereby leading to surges of terrestrial input into the deeper parts of the SCS basins (Wang and Li, 2009; Liu et al., 2007). These main trends and superimposed smaller regional oscillations are recorded by the SCS marine sediments (Wang et al., 2005).

A continuous ~333-m succession recovered at Site U1499 during IODP Expeditions 367 & 368 (Fig 1; Sun et al., 2018) was estimated to span the early Pliocene through Pleistocene according to the few microfossil events and the shipboard magnetostratigraphy. This provides a good opportunity to investigate the regional Plio-Pleistocene sedimentation history that is significantly affected by the trends in the East Asian monsoon system and major Quaternary paleoclimate changes. However, such investigations require a robust high-resolution time scale to determine changes in sediment influx rates and climate shifts. Astronomical calibrated magnetostratigraphy has been proven to be a powerful tool to construct high-resolution age models for Cenozoic deposits (e.g., Hilgen et al., 2003; Hüsing et al., 2010).

Climate oscillations produced by astronomical-controlled Milankovitch cycles have pronounced impacts on seasonal precipitation into fluvial watersheds, on sediment load and types delivered to the margins and on marine productivity. These cycles are often reflected in variable relative clay content within the accumulating offshore sediments. The natural gamma radiation (NGR) signal is commonly used as an indicator of relative clay content, in which high NGR values are associated with clay-rich sediments and lower NGR values with coarser-grained or carbonate-rich sediments (e.g., Schnyder et al., 2006; Hesselbo et al., 2009). Therefore, a NGR log provides a useful proxy to analyze paleoclimatic variations and cycles in both marine and non-marine sediment successions (e.g., Li et al., 2017; Wu et al., 2013; Zhang et al., 2015).

Our goal is to establish a continuous Plio-Pleistocene cycle-calibrated magnetostratigraphy of Site U1499 that is consistent with the limited shipboard biostratigraphy. The inclusion of Milankovitch cycle records within each polarity zone enables (1) calculations of the implied rates of sediment accumulation for the past 4.5 Myr, (2) identification of general patterns among northern/southern margins by high-resolution correlation with other SCS sites that have comparable cyclostratigraphy (IODP Sites 1148 and 1143); (3) exploration of the implications of the astronomical-tuned clastic input proxy (NGR data) on the East Asia monsoon intensity history during the Pliocene-Pleistocene by comparing to other published monsoon proxies in SCS; and (4) identify the Middle Pleistocene Transition and the Mid-Brunhes Event at this locality and their regional significance.

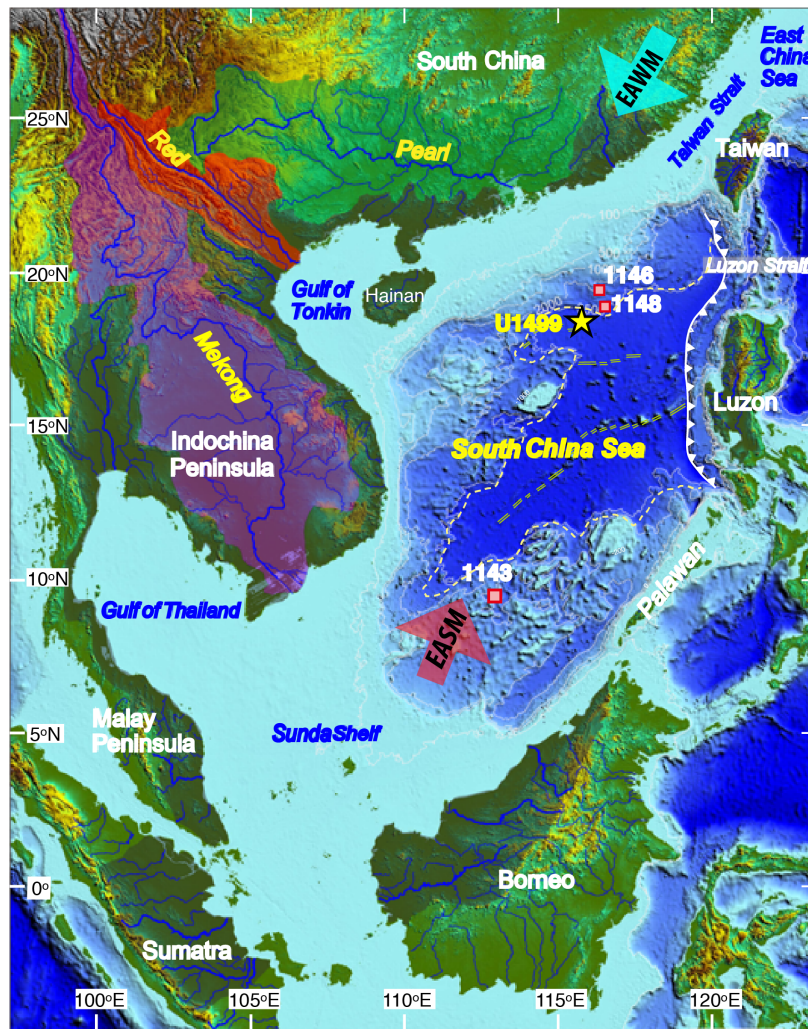


Figure 4.1. Location of Site U1499 (star in yellow) in the South China Sea (SCS) (modified from Liu et al, 2016). Sites 1148, 1146 and 1143 of ODP Leg 184 are marked by pinkish squares. Major river systems discharging into the SCS are shown. The cyan and the red arrows indicate the dominant directions of the East Asian Winter Monsoon (EAWM) and of the East Asian Summer Monsoon (EASM), respectively.

4.2 Materials and methods

4.2.1 Lithology, paleomagnetic sampling and NGR logging

Site U1499 (18° 24.57' N, 115° 51.59' E; water depth of 3760 m) is in the northern part of the SCS within the continent-ocean transition (Fig. 1). A very generalized chronostratigraphy was established from the few microfossils and interpretation of the initial shipboard paleomagnetism (Sun et al., 2018). The APC/XCB coring at Hole U1499A (0-333 m) had a high

recovery of Pliocene-Pleistocene sediments that were divided into three lithological units (Fig. 3A). Unit I (middle-late Pleistocene; 0-48.85 m, U1499A-1H-1 to 6H-3) is composed of dark greenish gray bioclastic clay interbedded with thin clayey silt and foraminiferal sand layers and with which a moderate to poor preservation of nannofossils and foraminifers. Unit II (48.85–100.04 m, U1499A-6H-3 to 11H-5) contains well-developed syn-sedimentary deformations and unusually old (Pliocene) dated microfossils; therefore, it is interpreted as a slump deposit with distinctive erosive upper and lower contacts; Unit III (early Pliocene to early Pleistocene; 100.04–333.65 m, U1499A-11H-5 to 36X-CC) is dominated by dark greenish gray clay with very thin to thin clayey silt and calcareous sand layers. This Unit III was subdivided into two subunits (IIIA and IIIB, with boundary at 181.8 m), of which Subunit IIIB contains more nannofossils and foraminifers. Unit III has several microfossil datums, including the last appearance datum (LAD) of *Discoaster brouweri* (1.93 Ma) and the first appearance datum (FAD) of *Globorotalia tosaensis* (3.35 Ma), which constrained the Pleistocene/Pliocene boundary (2.58 Ma) to be between levels U1499A-20X-CC (181.7 m) and 27X-CC (242.25 m). The FAD of *Sphaeroidinellopsis seminulina* (3.59 Ma) within U1499A-29X (269.2 m) was considered to mark the Zanclean/Piacenzian stage boundary (Late/Early Pliocene boundary).

In order to establish a high-resolution paleomagnetic and cycle analysis, we collected a total of 220 discrete samples for magnetostratigraphic and rock magnetic studies from the upper 333 m of Hole U1499A at the IODP Gulf Coast Repository at Texas A&M University, College Station, Texas, USA. The sampling resolution was guided by the preliminary shipboard paleomagnetic results in order to have a higher sampling density across the main magnetic polarity zone boundaries. Before applying spectral analysis to the NGR data (10-cm spacing) for cyclostratigraphy, we removed all suspicious or spurious values – these are often associated with ash layers of higher heavy mineral concentrations and from some false signals from edge effects (e.g., De Vleeschouwer et al., 2017).

4.2.2 Methods

Time series analysis

We applied a newly developed program *Acycle* v.0.2.4 (Li et al., 2019) for the time series analysis. This analysis program uses a correlation coefficient (COCO, ρ) method for an objective statistic technique to provide the most likely estimates of sediment accumulation rates within a

sedimentary record. Based on an assumption of astronomical forcing for the suite of identified filtered cycles, this *Acycle* estimation computes the correlation coefficient between the frequency spectra of target astronomical solutions and the presence of different cycles within sediment data to achieve the numerical estimation of the depositional rates (higher correlation coefficient corresponds to the most 'real' rate) (Li et al., 2018, 2019). Monte Carlo simulations (or probability simulations) are embedded in the COCO method to test the significant level of astronomical forcing assumption, with the null hypothesis (H_0) indicating no orbital forcing. In addition, number of contributing astronomical cycles at each possible sediment accumulation rate is also evaluated. For example, a sediment accumulation rate that has the low (<1%) null hypothesis significant level (H_0 -SL), high correlation coefficient (>0.5) and a greater number of orbital cycles (maximum of 7) involved are interpreted to be most possible. To track the variation of the sediment accumulation rates throughout the data series, a sliding window technique, termed Evolutionary COCO (eCOCO) is applied. Detailed explanations and a user manual are available at www.mingsongli.com/acycle.

The slump deposit interval (Unit II, 48.85–100.04 m) was removed from the NGR data series. Anomalously high/low data points that usually correspond to core/section edges or ash layers were also deleted, followed by an interpolation of 20 cm before removing the long-term background trend using a 70.4-m LOWESS filter. The AR(1) red noise was removed from the detrended NGR series for spectral analysis. Target astronomical cycles periodicities of 405, 125, 95, 41, 24, 22 and 19 kyr for both COCO and eCOCO analysis were generated from the Laskar 2004 astronomical solutions for 0 to 3 Ma (Laskar et al., 2004). The tested sediment accumulation rates using *Acycle* ranged from 1 to 20 cm/kyr with a step of 0.1 cm/kyr by 2000 Monte Carlo simulations.

Rock magnetism and paleomagnetism

In order to verify and enhance the shipboard paleomagnetic analysis (detailed in Supplement 2), rock magnetic analyses and remanence measurements were conducted on the extensive suite of discrete samples in the Paleomagnetic Laboratory (KIRSCHVINK LABORATORY) at the California Institute of Technology.

Four samples were subjected to rock magnetic experiments to unravel the nature of the remanent magnetization carriers and assist in interpretation of demagnetization behaviors. These studies included anhysteretic remanent magnetization (ARM), isothermal remanent

magnetization (IRM) to assess inter-grain interaction effects (Cisowski, 1981), and AF demagnetization derived tests like Lowrie-Fuller and Fuller NRM (natural remanent magnetization) tests (Fuller et al., 2002; Johnson et al., 1975). The tests were conducted in a mu-metal-shielded clean room. MatLab Scripts (Kopp, 2007) are employed to analyze and plot these rock magnetic results.

A total of 165 discrete samples underwent a progressive combination of AF (a set of 2.3-4.6-6.9 mT) and thermal demagnetization (up to 660 °C) steps. The remanent magnetization were measured on a 2GTM Enterprises model 755 superconducting rock magnetometer with 3-axis DC SQUID system (named the Eugene M. Shoemaker Memorial Magnetometer) in a double-layer, mu-metal shielded room. Baseline noise level, including that for the quartz-glass vacuum sample holder, usually yields a moment sensitivity of $<2 \times 10^{-9}$ emu, whereas the remanent magnetization of the samples were usually at levels of 10^{-5} to 10^{-4} emu. Due to the magnetometer settings, magnetic moment (in emu) rather than magnetization (moment per volume) is used here to discuss sensitivity. Progressive thermal demagnetization was performed in the same shielded room using a modified computer-controlled oven under a gentle flow of N₂ gas starting at 75°C to avoid oxidation of ferrimagnetic minerals, such as greigite (Roberts and Weaver, 2005), and at increments ranging from 25-50 °C until the magnetization was either too weak to measure or displayed unstable behavior. The specimens in plastic cubes were first extruded and dried naturally before thermal demagnetization treatment. Details of the automated paleomagnetic and rock magnetic measurements are in Kirschvink et al. (2008). Principle component analysis (PCA) (Kirschvink, 1980) was used to determine the ChRM using PuffinPlot software (Lurcock and Wilson, 2012).

4.3 Results

4.3.1 Rock magnetic properties

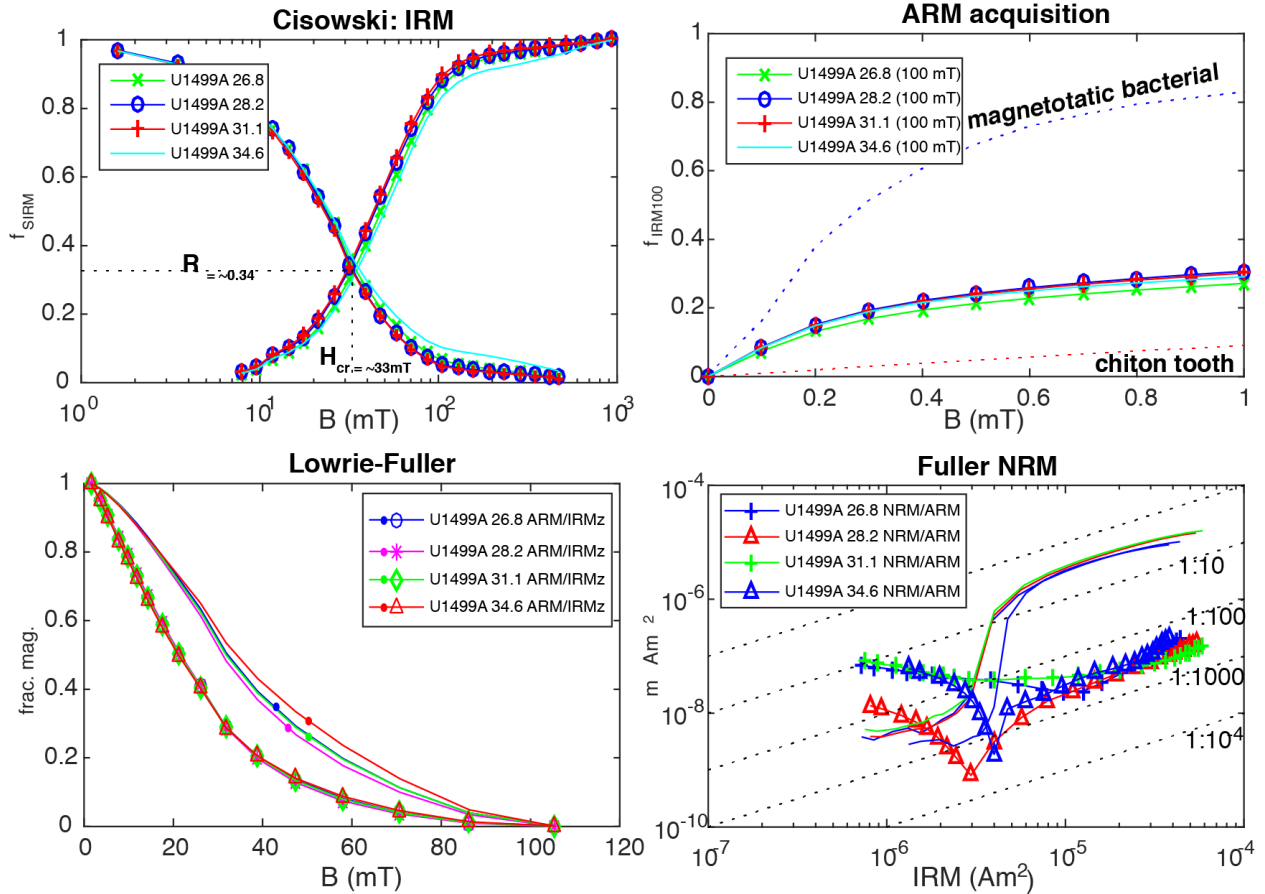


Figure 4.2. Rock magnetic properties of 4 samples from U1499A: Sample 26.8 (Core 26X, core catcher), Sample 28.2 (Core 28X, Section 2), Sample 31.1 (Core 31X, Section 1), and Sample 34.6 (Core 34X, Section 6). R is the ratio of saturation remanence, demagnetized to the remanent coercive force value, to undemagnetized saturation remanence. Values equal to and above 0.5 are characteristic of non-interacting single domain (SD) grains (Dunlop, 1972; Wohlfarth, 1958). H_{cr} is intersection of acquisition and AF demagnetization of IRM that approximates the remanent coercive force field, at which the magnetization re-aligned by the reversed field should equal the magnetization unaffected by the reversed field. NRM: Natural remanent magnetization; IRM: isothermal remanent magnetization; ARM: anhysteretic remanence magnetization.

The four representative samples chosen for rock-magnetic studies displayed reproducible coercivity spectra, which indicate similar remanence magnetization carriers (Fig. 2). The IRM/ARM coercivity spectral analysis (Cisowski, 1981) obtained a remanent coercive force $H_{cr} = 33$ mT (approximates the medium destructive field) with saturation approached before 300 mT,

suggesting that the main component is low-coercivity ferromagnetic phase such as magnetite. The ARM acquisition curve sits between the highly interacting chiton tooth ($R = 0.26$) and non-interacting magnetotactic bacterial ($R \geq 5$) reference curves, indicating a mixed composition (with R value 0.34). The sample is predominately composed of (pseudo-) single-domain grains according to the ARM version of the Lowrie-Fuller test (Johnson et al., 1975) with the stepwise demagnetization of ARM all lying on top of that IRM. The Fuller NRM test, which compares the remanent NRM during the AF demagnetization of IRM (Fuller et al., 1988), shows that the NRM values are nearly 3 orders of magnitude less than the corresponding IRM. This Fuller test strongly supports the interpretation that the NRM signal is a depositional or post-depositional remanent magnetization (DRM/pDRM), rather than chemical remanent magnetization (CRM) or thermal remanent magnetization (TRM) (Hart and Fuller, 1988). Samples 26.8 and 31.1 show a different trajectory compared to 28.2 and 34.6, which may indicate a grain-size effect of coarser versus finer. Overall, the carriers of the remanent magnetization in these four samples are interpreted to be fine-grained, magnetite-dominating particles.

4.3.2 Paleomagnetic results (Post-expedition)

The present-day magnetic inclination at the Site U1499 is estimated to be 25.6° (<https://www.ngdc.noaa.gov/geomag/calculators/magcalc.shtml#igrfwmm>). There has been no significant paleolatitude motion after the termination of SCS seafloor spreading in the middle Miocene (e.g., Li et al., 2014); therefore, we interpreted the normal polarity versus reversed polarity according to whether the demagnetized samples from Hole U1499A displayed positive (downward-pointing) or negative (upward-pointing) inclinations of ca. 25° . The shipboard magnetostratigraphy (Fig. A.1) are included in Supplement 2.

The stepwise demagnetization suggests three components in the initial NRM: a steep-downward drilling-induced overprint as had been already observed in the shipboard data, followed by the removal of a transitional vector before unblocking the stable ChRM direction. Rock magnetic measurements suggest that single domain magnetite is the primary carrier of characteristic remanence magnetization. The ChRM directions from the demagnetization of shore-based discrete samples were generally computed using the relatively stable vector directions during thermal steps of 475 - 575°C (Figs. 4C and 4D).

The post-cruise magnetostratigraphy verified and enhanced the main shipboard patterns (Fig. 3B; detailed interpretations are in Supplements 1 and 2); and implied revision of the magnetozone boundaries and addition of magneto-subzones (Fig. A.6). The two sets were merged into a composite magnetostratigraphy with four main pairs of reversed- and normal-polarity magnetozones (S1r/n to S4r/n; where 'S' denotes a magnetozone from this South China Sea site) (Fig. 3A).

For magnetozone S3n, we used the polarity interpretations (S3r.2n and S3r.3n) from the post-cruise results, but assigned the placement of the reversed-polarity subzone boundaries (S3n.1r and S3n.2r) based on shipboard results. The only minor uncertainty was in Cores 29X and 30X for which shipboard results indicated a R-dominated pattern with only a brief normal at the bottom of Core 30X; whereas the post-cruise discrete-sample results are ambiguous due to unstable demagnetization behaviors. There is a data gap at Core 25X which recovered only 2 cm of silty sediments owing to the cored sediments falling out of the core barrel while being retrieved (Sun et al., 2018). We initially assumed a reversed polarity for this Core 25X interval based on the adjacent polarity of the portions of the cores immediately above and below and on an initial pattern match to the reference geomagnetic polarity time scale (Fig. 7A; Table 1).

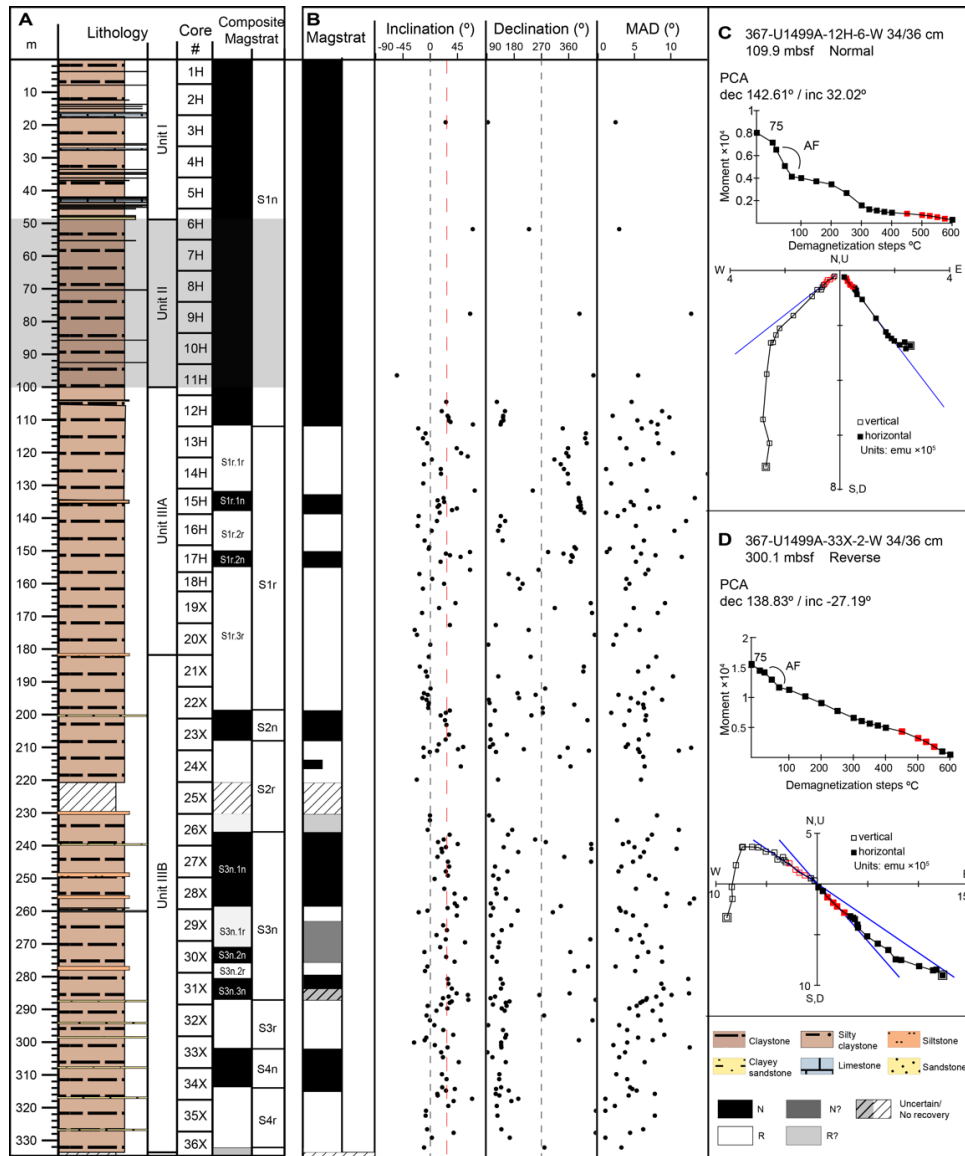


Figure 4.3. Merger of shore-based and shipboard paleomagnetic results. (A) Composite magnetostratigraphy of Hole U1499A (0-333 m) combining both shipboard and post-cruise results (detailed correlation is shown in Fig s6 in the Supplement 2). Divisions of magnetochrons/subchrons are named from S4 to S1 using a nomenclature style similar to that recommended by Kent et al. (1995). (B) Shore-based post-cruise magnetostratigraphy of the ChRM directions against lithostratigraphic units and cored intervals. Magstrat = magnetostratigraphy. MAD = maximum angular deviation. The dashed red line in the Inclination column indicates the present-day magnetic inclination at this location. “S” of the magnetozones S4r to S1n is for South China Sea. (C & D) Representative examples of demagnetization behaviors (intensity and magnetic vectors) of samples interpreted as high-quality-rated normal- and reversed-polarity. In the orthogonal projection of the magnetic vectors (Zijderveld, 1967), the open/solid squares are the projections of the vectors on the vertical/horizontal planes. The blue line indicates the ChRM direction computed in the PuffinPlot program based on the subset of steps shown in red. PCA = Principal component analysis. Dec = declination. Inc = inclination.

The upper long normal-polarity S1n correlates to the late Pleistocene normal-polarity magnetochron (Brunhes, magnetochron C1n). Therefore, the underlying reversed-polarity-dominated S1r is magnetochron C1r (upper part of the Matuyama). However, the assignment of the underlying polarity zones/subzones required additional constraints from the biostratigraphy and an astronomical tuning of the relative time spans for each interval.

4.3.3 Astrochronology and the time-calibrated magnetostratigraphy

There is a striking variation between darker and lighter gray beds in the core images (e.g., Fig. 4). This generally reflects an alternation between clay-rich and silt/sand-rich layers, which is mirrored in the NGR log. There is an abrupt decrease in the NGR that starts from Core 12H followed by pronounced high-amplitude variations (Fig. 4).

The Unit II slump deposit has been removed from the signal; but the entire NGR record is displayed in Fig. A.6 together with physical properties of reflectance parameter lightness L^* and magnetic susceptibility. However, there is an erosive top and bottom observed for this slump interval that suggests that some time must be missing.

The 2π MTM power spectral analysis of the detrended NGR shows significant wavelengths of 25-43, 6-10, ~ 2.5 and ~ 1.5 m (Fig. 4). The ratios of these wavelengths have approximately the 20:5:1 ratio predicted for the Milankovitch periodicities of long eccentricity (E; 405 kyr), short eccentricity (e; ~ 100 kyr) and precession (p; ~ 20 kyr) during the Quaternary. This fit implies an average sediment accumulation rate of ~ 8 cm/kyr. The evolutionary spectral analysis (Fig. 4) indicates that the low-frequency band (correlates to long-eccentricity E) stays significant throughout the NGR series, except in the interval of 120-145 m where the short-eccentricity 'e' is dominant. This estimation of sediment accumulation rate implies that the obliquity band have a wavelength of 0.18-0.3 cycles/m. This signal is prominent in the lower part (~ 260 -300 m) and in the upper 200 meters. The short-eccentricity 'e' band becomes stronger and focused in the upper ~ 170 m. In addition, the sediment accumulation rate is increasing upward according to the shifting of the wavelength of the short 'e' band in the evolutionary power spectrum.

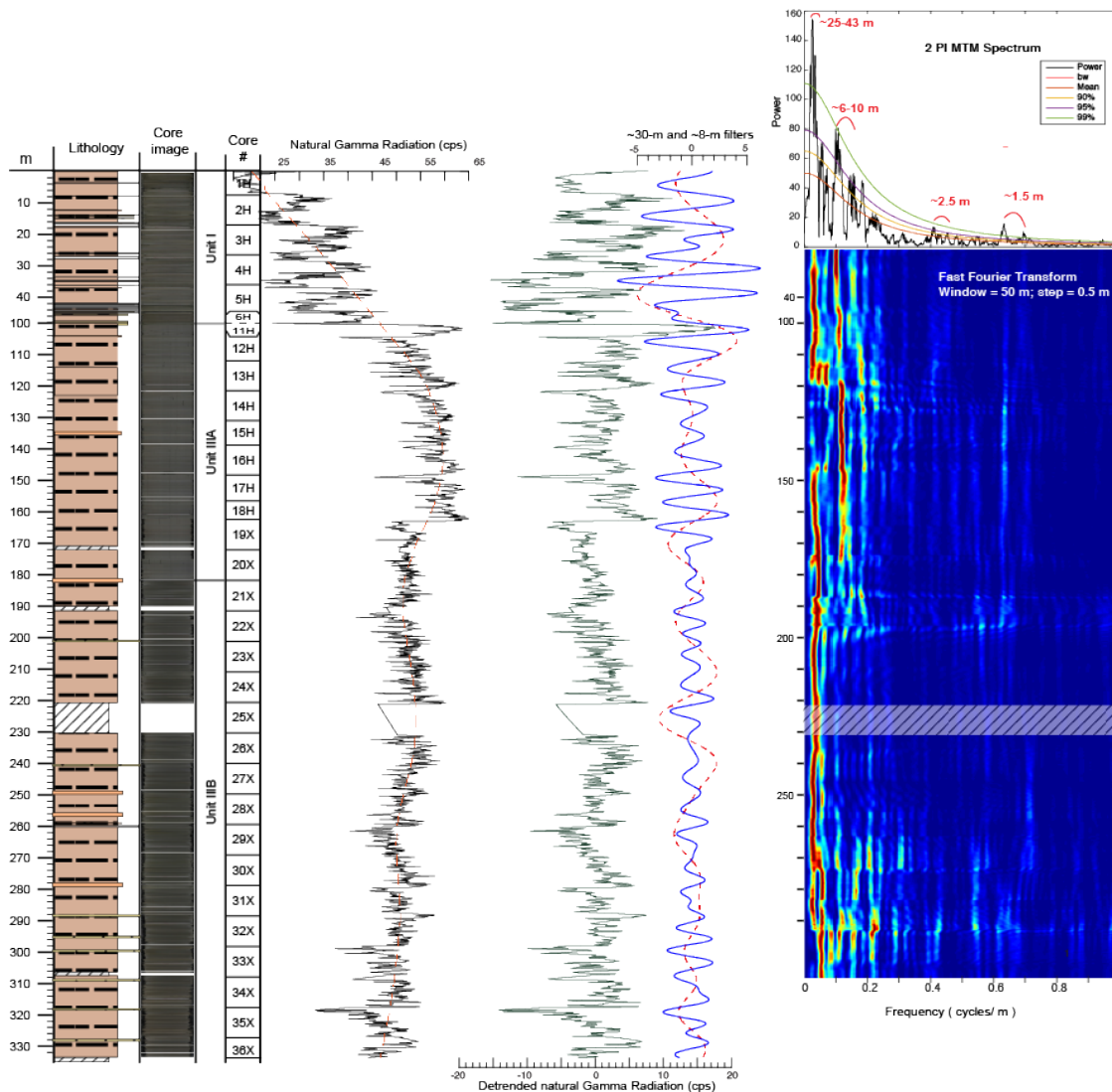


Figure 4.4. Spectral analysis of the detrended natural gamma radiation (NGR) data (dark green) after removal of the slumped interval of lithologic Unit II. The dashed red line and solid blue line represent the two dominating cycles at $\sim 30\text{-m}$ and 8-m , respectively (Gauss filter, passband: 0.033 ± 0.015 and 0.125 ± 0.04 , respectively). The ‘raw’ NGR data (solid black line; with the fake high/low values deleted) and the 74-m LOWESS trend (dashed line in orange) are shown against the lithology units, core images and core numbers. An interpolation of 0.2 m is applied before the spectral analysis. Evolutionary power spectrum uses a 50-m window. The 2π MTM power spectrum shows that the dominant cycles have wavelengths of 25-43, 5-10, ~ 2.5 and ~ 1.5 m.

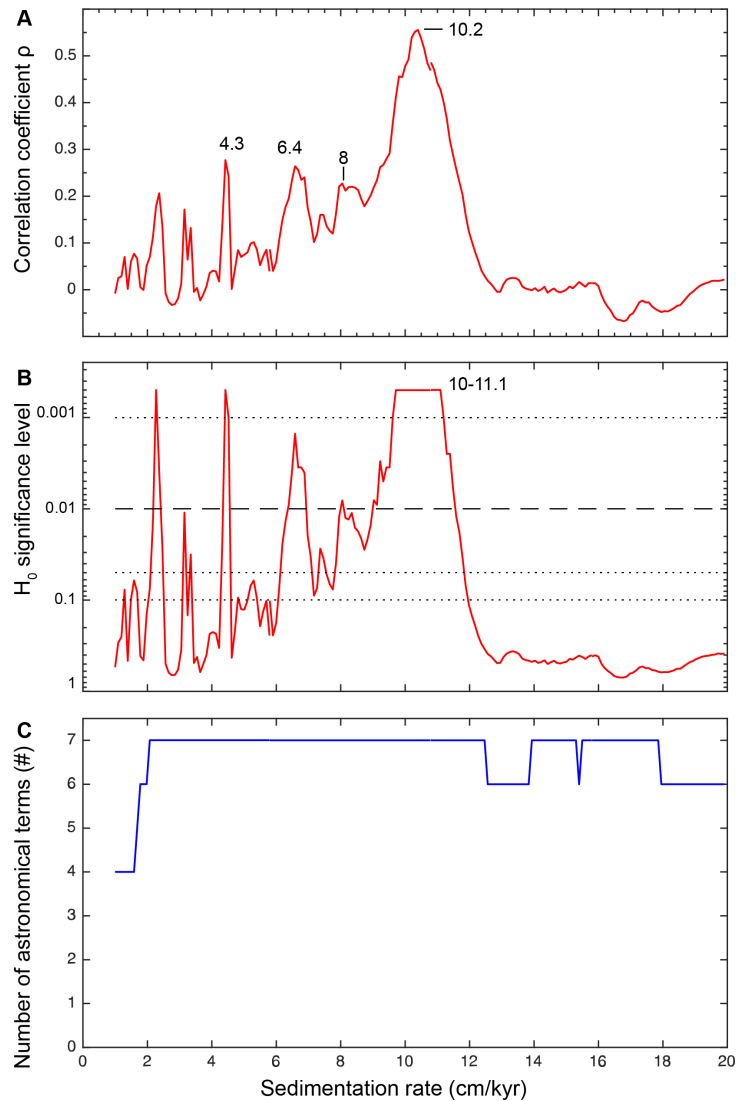


Figure 4.5. COCO analysis of NGR of Hole U1499A (0-333 m). The upper to lower panels are (A) the *Correlation coefficient* ρ with higher- ρ sediment accumulation rates (in cm/kyr) labeled, (B) the *Null hypothesis* (H_0 = no astronomical forcing) results showing that all the high- ρ sediment accumulation rates are less than 0.01 but only the 4.3 and ~10-11.1 cm/kyr range less than 0.001, and (C) the *Number of astronomical terms* (#) identified in the tested sediment accumulation range from 1 to 20 cm/kyr. The step used for the COCO analysis is 0.2 cm/kyr. The target series is the La2004 astronomical solution for the late Pliocene (0 to 3 Ma).

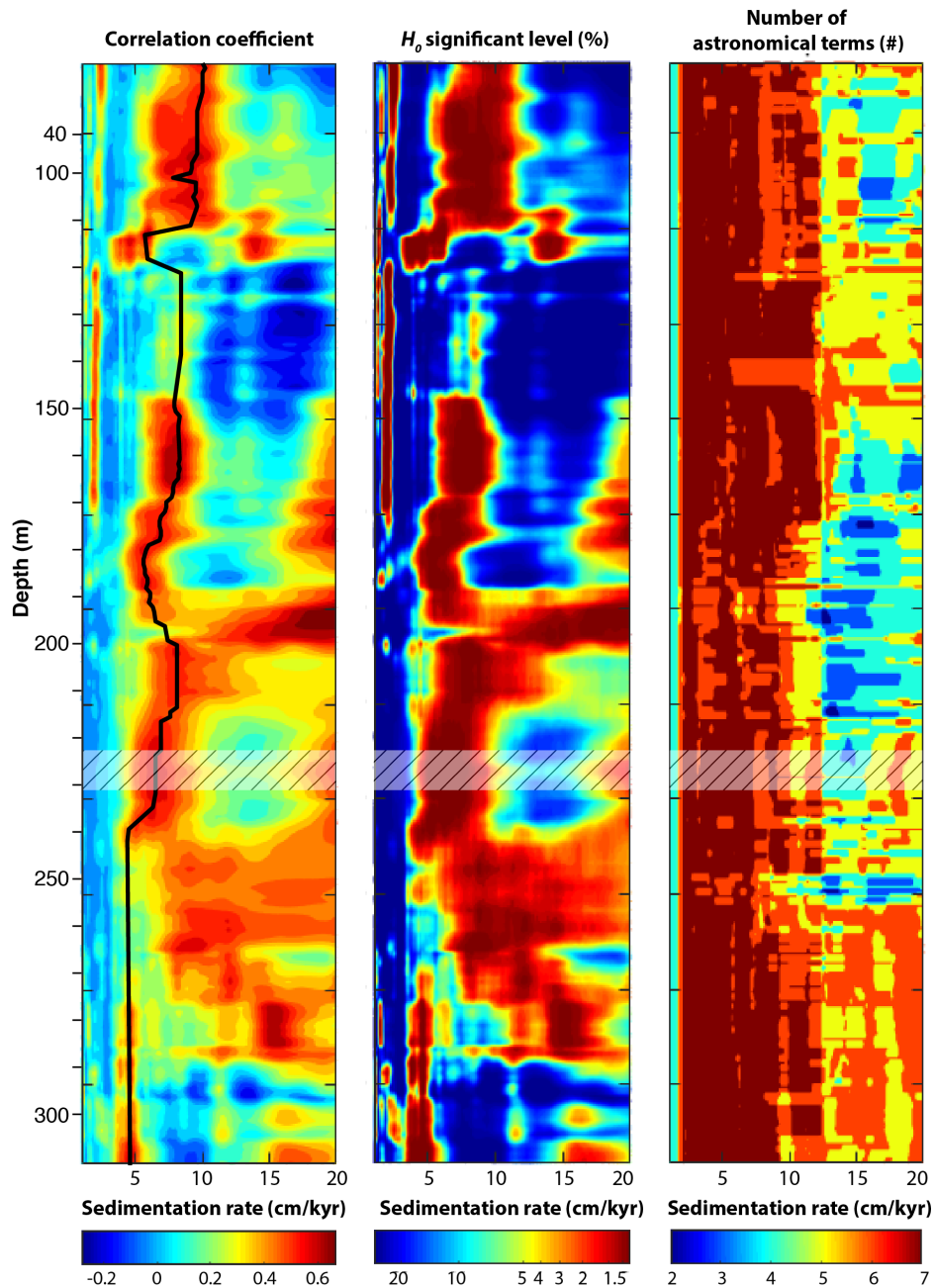


Figure 4.6. The eCOCO sediment-accumulation rate mapping of NGR of Hole U1499A (0-333 m) after removing slumped interval of Lithologic Unit II. Columns from left to right are the evolutionary correlation coefficient, the evolutionary H_0 significance level, and the evolutionary map of the number of astronomical terms identified in the NGR data series. The sliding window is 50 m using 5-m steps. All periodograms were analyzed with the AR(1) red noise model removed. The number of Monte Carlo simulations is 2000. The tested sedimentation rates range from 1 to 20 cm/kyr with a step of 0.2 cm/kyr. The tracked sediment accumulation rates shown by the black line in the Correlation coefficient map (leftmost column) were used to generate the age model in this study. The translucent hatched areas point is the non-recovery interval of Core 25X, for which the eCOCO results spanning that window might not be valid.

Changes in sediment accumulation rate are confirmed by the COCO and eCOCO analysis. COCO analysis extracts four peaks of sediment accumulation rates (Fig. 5) at 4.3, 6.4, 8 and ~10.2 cm/kyr. A lesser peak at ~2.1 cm/kyr seems to be of very low significance. All 7 astronomical cycles tested in the COCO analysis are involved, and the null hypothesis significance level is <0.01 for the 4.3 cm/kyr and less than 0.001 for the ~10.2 cm/kyr. According to the from the eCOCO spectra, this potential 4.3 cm/kyr solution co-exists with the ~10.2 cm/kyr solution only in the upper 170 m (Fig. 6). However, the lithologic features and the age model from both shipboard microfossil and magnetostratigraphy do not support this potential eCOCO solution of an upward decrease of sediment accumulation rate. An interval at ~110-120 m with a slightly reduced sediment accumulation rate is adopted here, rather than a surge up to ~14 cm/kyr, because this high rate is not detected by the COCO analysis. An independent age model based on the limited shipboard biostratigraphy (Sun et al., 2018) had implied an average sediment accumulation rate of 5 cm/kyr from ~100-300 m, followed by a surge to 13 cm/kyr for the uppermost 50 m, but our COCO and eCOCO evaluations imply that the accumulation rates were slightly more rapid in the lowermost interval and had a generally more gradual upward increase.

Based on these COCO and eCOCO results, we tracked the sediment-accumulation rate solutions that had the higher correlation coefficient ($\rho > 0.25$), lower H_0 significance level (<0.01), and more astronomical terms (≥ 6) through the succession (the thick black line in Fig. 6). Similar to the evolutionary spectra results (Fig. 4), these sediment accumulation rates have an overall upward increase from ~5 cm/kyr to ~10 cm/kyr, but indicate that there were two intervals with slightly slower rates at ~180-200 m and ~110-120 m. We applied these sediment accumulation rates to convert both the magnetostratigraphy and the NGR series in depth to the time domain spanning ~4.5 Myr (Fig. A.8). This thus yielded the duration of each magnetozone. An approximate age for the beginning of each magnetozone from S1n down to S4r was projected relative to a "0 Ma" assigned to the top of the hole (Table 1).

Table 4.1. Correlation of the magnetostratigraphy of IODP Hole U1499A (0-333 mbsf) to the Plio-Pleistocene geomagnetic polarity time scale (from GTS2016; Ogg et al., 2016). The uncertainties in depth for the placement of magnetozone boundaries are given (e.g. ± 1.2 (m)). The two right columns are the apparent offsets in the age and in the time-span between the reference magnetochron ages from GTS2016 and astronomical-tuned age model for the magnetozones in this study. Offsets to a younger age or to shorter durations are indicated by red-colored negative numbers.

Polarity Chron/Subchron	Base age (Ma)	Duratio n (Myr)	Magne tozone (U149 9A)	Base (mbsf)	Base age (Ma)	Dura -tion (Myr)	Age offset (Ma)	Duratio n offset (Myr)
Present	0							
C1n (Brunhes)	0.773	0.773	S1n	111.76 ± 1.20	0.62	0.62	-0.153	-0.153
C1r.1r	1.008	0.235	S1r.1r	132.50 ± 2.28	0.91	0.29	-0.098	0.055
C1r.1n (Jaramillo)	1.076	0.068	S1r.1n	138.64 ± 1.04	0.98	0.07	-0.096	0.002
C1r.2r	1.189	0.113	S1r.2r	149.89 ± 0.99	1.12	0.14	-0.069	0.027
C1r.2n (Cobb Mountain)	1.221	0.032	S1r.2n	154.99 ± 3.75	1.18	0.06	-0.041	0.028
C1r.3r	1.775	0.554	S1r	198.54 ± 1.50	1.82	0.64	0.045	0.086
C2n (Olduvai)	1.934	0.159	S2n	211.05 ± 0.40	1.98	0.16	0.046	0.001
C2r.1r	2.12	0.186	–	–	–	–	–	–
C2r.1n (Feni)	2.155	0.035	–	–	–	–	–	–
C2r.2r (base Matuyama)	2.61	0.455	S2r	235.80 ± 1.47	2.34	0.36	-0.270	-0.316
<i>(C2r in total)</i>		<i>0.676</i>						
C2An.1n	3.032	0.422	S3n.1n	258.00 ± 0.80	2.83	0.49	-0.202	0.068
C2An.1r (Keana)	3.116	0.084	S3n.1r	270.4 ± 1.47	3.12	0.29	0.004	0.206
C2An.2n	3.207	0.091	S3n.2n	276.0 ± 1.48	3.25	0.13	0.043	0.039
C2An.2r (Mammoth)	3.33	0.123	S3n.2r	280.0 ± 2.41	3.34	0.09	0.010	-0.033
C2An.3n (base Gauss)	3.596	0.266	S3n.3n	286.5 ± 0.49	3.48	0.14	-0.116	-0.126
C2Ar (Topmost Gilbert)	4.187	0.591	S3r	302.0 ± 1.50	3.84	0.36	-0.347	-0.231
C3n.1n (Cochiti)	4.3	0.113	S4n	315.26 ± 1.00	4.1	0.26	-0.200	0.147

4.4 Discussion

4.4.1 Accuracy of the astronomically-tuned magnetostratigraphy

The upper magnetozones of S2n to S1n of the astronomically-tuned magnetostratigraphy have a fairly good match to the middle and upper Pleistocene portion of the reference geomagnetic polarity time scale of GTS2016 (Fig. 7B and Table 1). There are inevitable minor discrepancies caused by microfossil preservation, sampling resolution, drilling-induced biscuit effect, and non-recovery gaps, etc. The Brunhes/Matuyama boundary at 0.77 Ma (Singer, 2014) projects to an astronomically-tuned polarity boundary at 0.62 Ma in this study; which indicates that the major slumped interval with erosive top and bottom contacts in Cores 6H to 10H that had been removed from this analysis probably encompassed or scoured about 0.15 Myr in time.

There is also an offset in the astronomical-tuned age model that is apparently caused by the recovery gap at Core 25X. Prior to ~2 Ma (magnetozones S2r to S4r), this offset is *ca.* 200-300 kyr. For example, the base of magnetozone S2r is projected as 2.34 Ma, which is about 270 kyr younger than the base of the corresponding magnetochron C2r.2r (base Matuyama) in GTS2016. The apparent hiatus within the Core 25X recovery gap would also account for the offset in magnetozone ages from the shipboard microfossil datums. For instance, the base of S3n.1r (at 3.12 Ma in this astronomical-tuned age model) is slightly below the top occurrences (LAD) of nannofossil *Sphenolithus spp.* and foraminifer *Sphaeroidinellopsis seminulina*, which have ages of 3.55 Ma and 3.59 Ma, respectively, in GTS2016. [Note, however, such shipboard microfossil datums are mostly from core catchers and therefore an inherent uncertainty of at least 10 m, which corresponds to ~200 kyr using the sediment accumulation rates (~5 cm/kyr in this interval).] Therefore, we included a ~ 200-kyr adjustment at Core 25X in the age model (Table A.1).

With those adjustments, then the time-calibrated magnetostratigraphy (Fig. 7B) agrees well with the Pliocene-Pleistocene geomagnetic polarity time scale. The placements of the major magnetochron boundaries from sample spacing are within 0.4-1.5 m (Table 1); therefore, the sediment accumulate rates implies that this uncertainty in depth is generally less than 30 kyr in time.

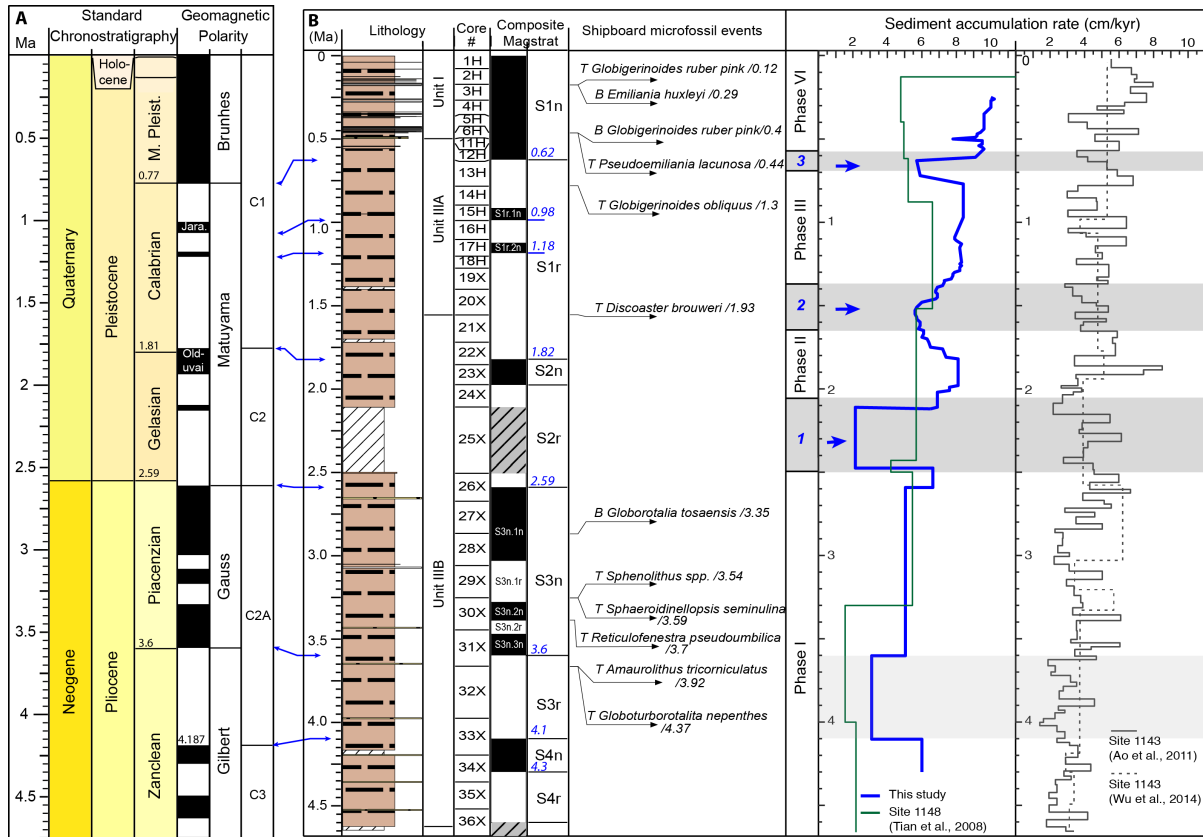


Figure 4.7. Time calibrated magnetostratigraphy of Hole U1499A and its correlation with other geologic events. (A) The chronostratigraphy of the past 4.7 Myr from GTS2016 (Ogg et al., 2016) with magnetochrons and ages of stage boundaries. (B) The time-calibrated composite magnetostratigraphy of U1499. Blue-colored double-headed lines are the correlation of the composite magnetostratigraphy to the GTS2016 geomagnetic polarity time scale. This scale assumes that ~200-300 kyr is missing from magnetozone S2r (the recovery gap of Core 25X) (Table A.1). The shipboard microfossil datums (Sun et al., 2018) have ages according to GTS2016; B = Bottom of range (FAD), and T = Top of range (LAD). The columns on the right are sediment accumulation rates, with the thick blue line of Hole U1499A being the same as the thick black line of its sediment-accumulation rates in Fig. 6 but converted to the time domain. These U1499A sediment accumulation rates are averaged over 50-m windows with the values centered on the corresponding projected age; which is why the curve does not extend to the base and top of the studied interval. Published sediment accumulation rates for other Ocean Drilling sites in the SCS (locations in Fig. 1) are included for comparison: ODP Site 1148 in green based on intervals between benthic oxygen-isotope excursions correlated to major MIS events (modified from Tian et al., 2008; Table A.2), ODP Site 1143 in solid line is from a detailed visual correlation of benthic oxygen-isotope excursions record to the LR04 benthic stack (Lisiecki and Raymo, 2005) (from Ao et al., 2011; Table A.3) and Site 1143 dashed line are average rates within each polarity zone (modified from Wu et al., 2017; Table A.4). The numbered blue arrows and shaded areas highlight the major intervals of lower sediment accumulation rates in Hole U1499A during the Quaternary and their possible equivalents at Site 1143, which separated the sedimentation into four main phases (Phase I to Phase VI discussed in the main text).

4.4.2 Regional sedimentation responses to the East Asia climate evolution during the Pliocene-Pleistocene

There were several overlapping climatic, tectonic and sea-level processes that influenced the sediment accumulation during the Pliocene-Pleistocene at Site U1499. These include (1) a series of tectonic uplift phases for the Tibetan and other hinterland source regions (e.g., Li et al., 2014; Tada et al., 2016), (2) the incision of major rivers through coastal or other ranges, such as the Yangtze River establishing a direct Three Gorges outlet to the sea at ca. 0.8 Ma in contrast to its former sediment ponding in a large lake system in Sichuan Basin (e.g., Xiang et al., 2007), (3) Taiwan Island to the northeast has experienced rapid uplift and erosion, and consequently becomes the major provenance of sediments onto the northern margin (e.g., Wan et al., 2006; Li et al., 2015), (4) deep-water currents that altered the delivery paths of fine-grained sediment to the site (Shao et al., 2007), (5) major cold or glacial episodes during the Quaternary were associated with increased physical weathering of hinterlands, increased downstream delivery of coarse-grained clastics and formation of river terraces within all major Chinese river systems and elsewhere (e.g., Bridgland and Westway, 2014; He et al., 2015), (6) global lowstands during glacial maximums that caused Chinese rivers to discharge further out into the SCS basins and also triggered partial seaward redeposition of sediments from the emergent shelves (e.g., Molnar, 2000), (7) enhanced East Asia summer monsoon conditions, especially during warm intervals, that increased chemical weathering, seasonal river discharge and prograding of deltas across the continental margins (e.g. Clift et al., 2014), and (8) other regional and global climatic trends, such as the Mid-Pleistocene Transition (e.g., Li et al., 2008). This makes it a challenge to evaluate which were the main processes influencing the depositional history at any specific site within the SCS.

In addition, as at all sites, these processes are superimposed on natural burial compaction, which produces a background artifact of an apparent linear upward increase in accumulation rates. None of the comparison studies at SCS sites (Fig. 7) have attempted to remove this burial-compaction factor; and the trends in sediment lithology and NGR within Site U1499 suggests that the main variations are caused by changes in terrestrial clastic influx, rather than differential compaction overprints.

Our astronomically tuned sediment-accumulation rate profile at Site U1499 (Fig. 7), which is 500-kyr averages within a sliding window at 5-kyr increments, has some features in

common with the rates estimated at nearby Site 1148 (Fig. 7); therefore, one can extract some general trends for this portion of the northern SCS. Both sites display a long-term upward increase spanning the past 4 Myr; but our Site U1499A, even after compensating for the 50-m thick re-deposited slump of lithologic Unit II, has an overall thicker Plio-Pleistocene succession preserved. There are several main oscillations of the sediment accumulation rate, of which most are synchronous between the northern SCS (our site) and the southern SCS (Site 1143); for example, both margins recorded an increase stage at ~2.5 Ma. Except that the northern margin overall has a faster depositional process compared to the southern margin. Furthermore, four phases of sedimentation roughly separated by three major ‘Anomalies’ (1, 2, and 3 as noted in Fig. 7B) are recognized at Site U1499 for the past 4.5 Myr (discussed as follows).

4.4.3 Pliocene and Early Pleistocene

Phase I (4.5 to ca. 2.5 Ma) is the middle and late Pliocene. Both our site and nearby Site 1148 suggest a significant upward increase in average sediment accumulation rates from the Zanclean Stage (Gilbert reversed-polarity Chron C3r) to the Piacenzian Stage (Gauss normal-polarity Chron C2n). This upward increase is also present, but relatively subdued, in the southern SCS Site 1143 (Fig. 7B, rightmost column). The NGR signal at our Site U1499 has moderate intensity (ca. 50 cps; Fig. 4) with no significant excursions.

At both our Site U1499 and at the southern Site 1143, there is an apparent slower rate of sediment accumulation during the late Zanclean (ca. 4.1 to 3.6 Ma) (Fig. 7). This relatively slower rate is also indicated by magnetostratigraphy-scaled rates at nearby Site 1148 (Wu et al., 2014) (Fig. 7).

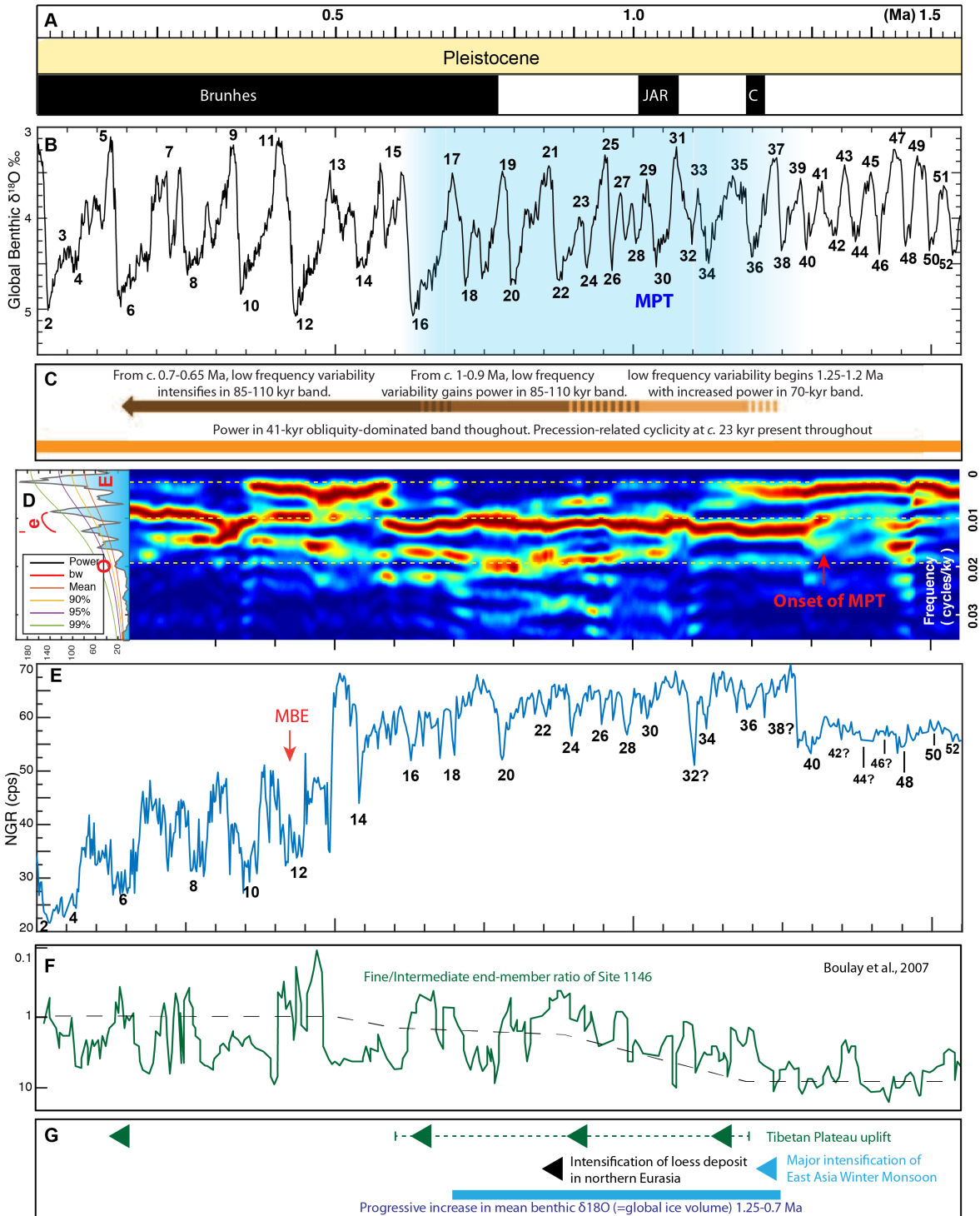
Low-accumulation-rate Interval #1 (ca. 2.5-2.1 Ma) of earliest Pleistocene at our Site U1499 was a gap in recovery, but the magnetostratigraphy correlations imply that this Core 25X interval must contain either condensed deposition or an erosional hiatus. This is immediately after the first major Quaternary glacial event (ca. 2.6 Ma; base of Matuyama reversed-polarity Chron C2r), which is preserved in upper Core 26X according to the magnetostratigraphy and is represented by a low-NGR signal (Fig. 4), which is interpreted a greater concentration of coarser-grained clastics. Therefore, a contributing factor to this anomalous low-accumulation rate might have been the ponding of terrigenous influx during the following early-Gelasian transgression and highstand. The record in nearby Site 1148 lacks the resolution to resolve such a

feature; but the southern SCS Site 1143 also displays a significant slowing of accumulation rates relative to the preceding late Pliocene-earliest Gelasian and the following late-Gelasian (Fig. 7; right column).

Phase II (ca. 2.1 to 1.7 Ma) of increased accumulation rates during the late Gelasian and earliest Calabrian of early Pleistocene. This interval of Cores U1499A-24X through 22X includes the Oldovai normal-polarity Chron C2n. There are coeval surges in the sediment accumulation rate recorded in the southern SCS Site 1143 at 1.9-1.7 Ma, especially during the interval encompassing MIS 74-68 (ca. 1.9 Ma).

Low-accumulation-rate Interval #2 (ca. 1.7 to 1.4 Ma) is a relatively slower accumulation interval during the early Calabrian. There is a coeval slowing in the average accumulation rates at the southern SCS Site 1143 between 1.7 to 1.4 Ma. No major change of the monsoon intensity has been reported during this time interval, but the climate oscillations were dominated by relatively low-amplitude 40-kyr obliquity cycles (Lisiecki and Raymo, 2005) (Fig. 8B), which might lead to weakened average seasonality and thus less precipitation to erode and transport clastics into the marginal seas. Another possible contributing factor for this ~500-kyr interval of lowered clastic influx might be a re-distribution of drainage systems which reduced sediment transportation into the SCS.

Figure 4.8. The Mid-Pleistocene Transition (MPT) and Mid-Brunhes Event (MBE) recorded in the NGR series of Hole U1499A (A) Geomagnetic polarity time scale of GTS2016 (Ogg et al., 2016); JAR = Jaramillo Subchron, C = Cobb Mountain Event. (B) Benthic foraminifer $\delta^{18}\text{O}$ records (LR04 stack; Lisiecki and Raymo, 2005) for the past 1.55 Myr with even-numbered marine isotope stages (MIS) corresponding to the cold events. The Early-Middle Pleistocene Transition (from 1.25-0.7 Ma, (Head and Gibbard, 2015)) is shaded in light blue. (C) The shift of dominating periodicity interpreted from the wavelet spectrum of LR04 stack by Head et al. (2008). (D) Evolutive spectra of the astronomically tuned NGR series of Hole U1499A (right), with its 2π MTM power spectrum (left) showing peaks at 405-kyr long-eccentricity 'E', \sim 100-kyr short-eccentricity 'e', \sim 40-kyr obliquity 'O' and \sim 20-kyr precession 'p' frequencies. The evolutionary power spectrum (right) displays the distribution of these orbital cycles. The sliding window applied here is 300 kyr with 4 kyr steps. (E) The astronomical-tuned NGR of the past 1.55 Myr. After compensating for the slump in lithologic Unit II, then the peaks and troughs of the time-calibrated NGR series show a reasonably good consistency with the benthic foraminifer $\delta^{18}\text{O}$ curve. The numbers denote the possible correlations to the MIS cold intervals. (F) Ratio of fine to intermediate grain-sizes in the sediments of ODP Site 1146 (location in Fig. 1) (modified from Figure 7 in Boulay et al., 2007) with the dashed line indicating the long-term trend. Note that the scale is inverted, so that relatively clay-rich compositions are below the dashed line. (G) Contemporary geologic events in Asia, i.e., the global ice expansion interval (Clark et al., 2006), stepwise uplifting stages of the northeast Tibetan Plateau (green triangles with uncertainties in dashed line) estimated by stratigraphic and paleomagnetic evidences in Yellow River drainage basins (e.g. Li et al., 1997, 2014; Liu et al., 2010) and the major intensification of East Asia Winter Monsoon supported by a Chinese loess records (Heslop et al., 2002).



4.4.4 Mid-Pleistocene Transition

Phase III, spanning ca. 1.4 to 0.7 Ma, correlates to the Mid-Pleistocene Transition. Beginning at ~1.3 Ma (Core U1499A-18H) there is a sharp increase in the average NGR values which remain at their highest sustained levels (ca. 65 cps) of the entire Plio-Pleistocene interval to Core 12H (Figs. 4, 8). This high-NGR represents enrichment in clay content; which implies a surge in the influx of clay rather than a reduction in coarser clastics or carbonate, because sediment accumulation rates remain high (Fig. 7). Site 1143 in the southern SCS also has relatively high rates of sediment accumulation from 1.3 to 1.0 Ma, although this was followed by a relative low rate from 1.0 to 0.75 Ma.

This interval of a high influx of clay-rich sediment to Site U1499 corresponds to the global Mid-Pleistocene Transition (MPT, also known as the Mid-Pleistocene Revolution or the Early-Middle Pleistocene transition), which represents a major episode in Earth history (e.g., Berger et al., 1993; Clark et al., 2006; Head and Gibbard, 2005, 2015). The MPT is the shift of the dominant climate periodicity from 41-kyr to ~100-kyr accompanied by prominent global climate and environmental changes (Fig. 8). An onset at ca. 1.3 Ma in the dominance of 100-kyr cycles is also seen in the evolutive spectra of the astronomically tuned NGR data (Fig. 8D), and it appears that the relative spikes in low-NGR (which generally correspond to silt-rich layers in the cores) represent episodes of influx of coarser-grained clastics during the cold MIS events. A similar change in cyclicity is observed at ODP Site 1143 in the southern SCS (Wang et al., 2003). The cause of the shift to the ca. 100-kyr cyclicity during the MPT is uncertain (reviewed in Head and Gibbard, 2015), including whether this is caused by a dominance of short-eccentricity 'e' of ca. 100-kyr, or is partly the statistical artifact of skipping 1-2 obliquity cycles (Huybers, 2007) rather than an orbital re-configuration. Other proposed factors for the MPT and the shift to 100-kyr climate cycles also invoked feedbacks by delayed CO₂ emissions from mid-ocean volcanism (Huybers and Langmuir, 2017) or a tectonic-climate interplay from an uplift phase of NE Tibetan Plateau (the Laojunmiao Movement of Liu et al., 2010; the Kunhuang or Huanghe Movement of Li et al., 2014).

In central Asia, the MPT cycles produced prominent signals in the Chinese Loess record superimposed on an enhancement of the East Asian monsoon. For example, Han et al. (2012, 2014) proposed from records of Asian aridity that there was a remarkable two-step shift of the

100-kyr cyclicality with onset at ~0.9 Ma and stabilization at ~0.64 Ma; and they suggest a driving force for the MPT was the last stage of the Kunhuang Movement uplift phase of the Tibetan Plateau. Indeed, a stronger East Asia summer monsoon through the MPT with its influence on chemical weathering and fluvial discharge of clay-rich sediments into the SCS current system would be a potential explanation for the increased accumulation rate of clay-rich sediment at Site U1499.

A low-accumulation-rate Interval #3 (ca. 0.7 to 0.55 Ma) in Hole U1499A (upper Core 13H through 12H) corresponds to the beginning of the Middle Pleistocene (earliest part of Brunhes normal-polarity Chron C1n) (Fig. 7). The NGR record suggests that this encompasses the equivalent of MIS 20 to MIS 16 (Figs. 4 and 8E). This low-accumulation interval is terminated by the arrival of a 50-m slump deposit (lithologic Unit II) at ca. 0.6 Ma which has an erosional base; therefore, it is probably that the low-accumulation interpretation is partly an artifact of the disrupted sedimentary record.

4.4.5 Mid-Brunhes Event and Middle Pleistocene Glacial Cycles

Phase IV (ca. 0.5 Ma to present) of Middle Pleistocene has a greatly reduced NGR signal (ca. 35 cps average) with superimposed high oscillations (Fig. 8B). However, this low-NGR interval also has a ca. 50% increase in average sediment accumulation rates relative to any of the previous high-accumulation rates (Fig. 7). According to the core lithologies, this lowering of the NGR as sediment accumulation rates increases was caused by a major increase in the average amount of coarse-grained silt and sand. The lowest NGR values (coarse-grain-rich layers) correlate with the maximum cold MIS glacial events (Fig. 8).

A similar increase in average sediment accumulation rates is also seen in the southern SCS Site 1143, where that detailed isotope-to-MIS and monsoon-to-insolation correlation suite enables the resolution that this Phase IV consists of several surges of very-high accumulation episodes. A rapid surge of sediment accumulation rate is documented at nearby Site 1148 from ~4.5 to nearly 14 cm/kyr (Fig. 7B); however, due to low-resolution tie points (Table A.2), no detailed variation could be recovered. The onset of this Phase IV is documented in Site 1146 as nearly a 10-fold surge in the ratio of silt-sand relative to clay-sized particles (Fig. 8F).

Shortly after the beginning of this Phase IV features the Mid-Brunhes Event (MBE), which is a major cold event that occurred at an insolation amplitude minima (Tzedakis et al.,

2009). Following the MBE, large-amplitude glacial-interglacial cycles of 100-kyr periodicity dominated the past 400 kyr (EPICA community members, 2004). The MBE is the largest amplitude oscillation in the Quaternary benthic foraminifer $\delta^{18}\text{O}$ records (the major glacial MIS 12) (Fig. 8B) and within ice-core CO_2 records (Lüthi et al., 2008), thereby indicating a fundamental re-organization of the Earth system (Kemp et al., 2010). There was a simultaneous intensification of both the summer and winter monsoon after ~ 0.5 Ma (An, 2014; Sun et al., 2006) with increased summer monsoon precipitation during interglacials (Clift et al., 2014). The climate of the interior of China was also influenced by the last stage of the "Kunhuang Movement" uplift phase of the Tibetan Plateau at about 0.7-0.6 Ma (Li et al., 2014), which was believed to have significantly enhanced the Asian desiccation (Han et al., 2014), although this trend may not have contributed substantially to the sediment history recorded at the location of Site U1499A.

Therefore, the major increase in coarse-grained sediment flux to Site U1499A and the other sites was probably a combined result of the generally cooler regional climate with increased physical weathering, the tectonic uplift of the hinterland provenance areas, and the episodes of glacial erosion at higher altitudes. The general enrichment in silt-sand influx was punctuated by coarser-grained intervals (lowest NGR) during each cold MIS glacial event (Fig. 8), although we suggest that the timing of these coarse-grained events might correspond to the increased flushing of coarse-grained material into the SCS basin upon the onset of each humid interglacial. This lag in delivery of coarser-grained sediment is seen in the history of river terraces in this region and elsewhere, where the coarser-grained material accumulates in river beds and banks during cold climatic episodes, and is then incised and partly eroded during the beginning of each warm interglacial (e.g., Bridgland and Westway, 2014).

4.4.6 Synchronicity of northern SCS and southern SCS sedimentation history

The main relative changes in the sediment-accumulation record of Site U1499 in the northern SCS appear to be synchronous with those in the detailed record of Site 1143 in the southern SCS. In both regions, there are relatively lower rates of sediment accumulation during the late Zanclean (mid-Pliocene; ca. 4.0 to 3.6 Ma), early Gelasian (ca. 2.5 to 2.0 Ma), early Calabrian (ca. 1.6 to 1.4 Ma) and the earliest Middle Pleistocene (ca. 0.6 Ma) (Fig. 7).

However, there are only two high-resolution records from either astronomical tuning (our study) or from detailed oxygen-18 curve matching (Ao et al., 2011) that are currently available for the majority of the Pliocene-Pleistocene of the SCS. Therefore, even though some of these changes, such as the Mid-Pleistocene Transition (MPT; ca. 1.4 to 0.7 Ma), are also global climatic trends, there needs to be a larger synthesis and mapping of the regional sedimentation patterns through the SCS region and separation of depositional rates for different components with this high-resolution time framework before making further interpretations. For example, the deep-water circulation probably played a role in the sedimentation patterns (Wang et al., 2005). Therefore, the apparent correlations and trends are thought provoking, and await further confirmation and correlation.

4.5 Conclusions

A 4.6-Myr cycle-calibrated magnetostratigraphy was constructed for the upper 333 m of IODP Site U1499. After adjustment for recovery gaps, the resulting time scale is consistent with the Plio-Pleistocene geomagnetic polarity time scale and the constraints from the preliminary shipboard microfossil datums. This enabled the calculation of sediment accumulation rate history through the past 4.6 myr at this site.

At Site U1499, there were four main phases of relatively higher rates of sediment accumulation. The first two phases of higher sediment accumulation rates (early Zanclean, and Piacenzian Stage) did not affect the average natural gamma-ray (NGR) intensity, but the third interval (late Gelasian) was caused by an increase in the influx of clay (higher intensity in natural-gamma ray, NGR). In contrast, the fourth high-rate interval (the past 0.5 Myr) was caused by a surge in the influx of silt-sand components.

These four high-rate intervals were separated by slower rates during the late Zanclean (mid-Pliocene; ca. 4.1 to 3.6 Ma), early Gelasian (ca. 2.5 to 2.0 Ma), early Calabrian (ca. 1.6 to 1.4 Ma) and the earliest Middle Pleistocene (ca. 0.6 Ma). Even though two of the low-accumulation rate intervals in Hole U1499A might have been influenced by distortions in core recovery (early Gelasian) and adjustments for a slumped interval (earliest Pleistocene), it is intriguing that all of the phases of increased or decreased sediment accumulation rates at this site on the northern margin of the SCS seem to be present within the high-resolution record of its southern margin at Site 1143. Some of these apparent synchronous trends in accumulation rate

on both the northern and southern margins of the SCS might be a combination of global trends (e.g., the Northern Hemisphere cooling and glacial episodes during late Quaternary), but others might be associated with the uplift phases of the NE Tibetan Plateau during the Pliocene-Pleistocene.

Both the Mid-Pleistocene Transition (MPT; ca. 1.3 to 0.7 Ma) and the Mid-Brunhes Event (MBE; 0.4 Ma) are identified at Site U1499. The onset of the MPT in the evolutive spectra analysis is indicated by an increase in the significance of the ~100-kyr band followed by its dominance. The MBE, which is equivalent to the major global cold-stage marine-isotope stage (MIS) 12 in the benthic foraminifer oxygen-18 record, is recorded as the beginning of a series of major amplitude shifts in the NGR. Each minimum in those high-amplitude NGR oscillations is interpreted as a surge in coarser-grained silt-sand component; and each of these coarse-grained pulses can be matched to a maximum in the cold-stage MIS of the benthic foraminifer oxygen-18 record. We suggest that these surges in silt-sand influxes represent the onset of flushing of river channel accumulations of coarser-grained components during the glacial intervals as the intensity of the East Asian summer monsoon increased at the beginning of each interglacial episode.

The merger of magnetostratigraphy, cyclostratigraphy, and the NGR record to produce a high-resolution profile of bulk sediment accumulation rates and relative clay to sand-silt components is a powerful tool and climate proxy to reconstruct the general history of sediment input into the South China Sea and its relationships to East Asia monsoon and tectonic evolution through the Pliocene-Pleistocene.

Acknowledgements

The International Ocean Discovery Program (IODP) provided the samples and data used in this study. All our research was entirely dependent upon the careful observations and thought-provoking ideas by shipboard scientists and staff on IODP Expedition 367. Dr. Steven Skinner, as a partner shipboard paleomagnetist, is especially thanked for his participation on analyzing the shipboard data. Thanks are given to those that participated at the Sample Party in College Station. Dr. Joe Kirschvink and Dr. Isaac Hilburn provided invaluable assistance and access to their paleomagnetic KIRSCHVINK LAB at Caltech and aided in the data analysis. Dr. Mingsong Li provided a preliminary version and training in his Acycle program, which was vital to the analysis of sediment accumulation rates. Dr. Matthew Huber, as one of Y.Z.'s advisors, provided

valuable insights to the initial manuscript. Y.Z. ("Wendy") wishes to thank Ting Hao for providing a quiet working place and enlightening discussions. This research is funded by a Post Expedition Award granted to Y.Z., a subaward from the National Science Foundation (NSF) sponsored Ocean Drilling Project, and by a grant to the State Key Laboratory of Marine Geology, Tongji University (No. MG201907).

4.6 References

- Allerton, S., Pariso, J., Stokking, L., and McClelland, E., 1995, 23. Origin of the natural remanent magnetization of sheeted dikes in Hole 504B cored during Legs 137 and 140., in *Proceedings of the Ocean Drilling Program, Scientific Results*, v. 137/140, p. 263-270.
- An, Z. S., 2014 (ed.), *Late Cenozoic Climate Change in Asia: Loess, Monsoon and Monsoon-arid Environment Evolution*: Springer Science, Dordrecht, Netherlands: Springer, 587 pp.
- An, Z. S., Kutzbach, J. E., Prell, W. L., and Porter, S. C., 2001, Evolution of Asian monsoons and phased uplift of the Himalaya–Tibetan plateau since Late Miocene times: *Nature*, v. 411, p. 62. <https://doi.org/10.1038/35075035>
- Ao, H., Dekkers, M. J., Qin, L., and Xiao, G. Q, 2011, An updated astronomical timescale for the Plio-Pleistocene deposits from South China Sea and new insights into Asian monsoon evolution: *Quaternary Science Reviews*, v. 30, no. 13–14, p. 1560-1575. <https://doi.org/10.1016/j.quascirev.2011.04.009>
- Berger, W., Bickert, T., Jansen, E., Wefer, G., and Yasuda, M., 1993, The central mystery of the Quaternary ice age: a view from the South Pacific: *Oceanus*, v. 36, no. 4, p. 53-57.
- Boulay, S., Colin, C., Trentesaux, A., Clain, S., Liu, Z., and Lauer-Leredde, C., 2007, Sedimentary responses to the Pleistocene climatic variations recorded in the South China Sea: *Quaternary Research*, v. 68, no. 1, p. 162-172. <http://dx.doi.org/10.1016/j.yqres.2007.03.004>
- Bridgland, D. R., and Westway, R., 2014, Quaternary fluvial archives and landscape evolution: a global synthesis: *Proceedings of the Geologists' Association*, v. 125, p. 600–629. <http://dx.doi.org/10.1016/j.pgeola.2014.10.009>
- Cisowski, S., 1981, Interacting vs. non-interacting single domain behavior in natural and synthetic samples: *Physics of the Earth and Planetary Interiors*, v. 26, no. 1, p. 56-62.

- Clark, P. U., Archer, D., Pollard, D., Blum, J. D., Rial, J. A., Brovkin, V., Mix, A. C., Pisias, N. G., and Roy, M., 2006, The middle Pleistocene transition: characteristics, mechanisms, and implications for long-term changes in atmospheric pCO₂: *Quaternary Science Reviews*, v. 25, no. 23, p. 3150-3184. <https://doi.org/10.1016/j.quascirev.2006.07.008>
- Clift, P. D., 2006, Controls on the erosion of Cenozoic Asia and the flux of clastic sediment to the ocean: *Earth and Planetary Science Letters*, v. 241, no. 3, p. 571-580. <https://doi.org/10.1016/j.epsl.2005.11.028>
- Clift, P. D., Wan, S., and Blusztajn, J., 2014, Reconstructing chemical weathering, physical erosion and monsoon intensity since 25Ma in the northern South China Sea: A review of competing proxies: *Earth-Science Reviews*, v. 130, p. 86-102. <http://dx.doi.org/10.1016/j.marpetgeo.2014.07.001>
- De Vleeschouwer, D., Dunlea, A. G., Auer, G., Anderson, C. H., Brumsack, H., de Loach, A., Gurnis, M., Huh, Y., Ishiwa, T., Jang, K., Kominz, M. A., März, C., Schnetger, B., Murray, R. W., and Pälike, H., 2017, Quantifying K, U, and Th contents of marine sediments using shipboard natural gamma radiation spectra measured on DV JOIDES Resolution: *Geochemistry, Geophysics, Geosystems*, v. 18, no. 3, p. 1053-1064. doi: 10.1002/2016GC006715
- Dunlop, D., 1972, Magnetic mineralogy of unheated and heated red sediments by coercivity spectrum analysis: *Geophysical Journal International*, v. 27, no. 1, p. 37-55.
- EPICA community members (Augustin, L., Barbante, C., Barnes, P. R. F., Marc Barnola, J., Bigler, M., Castellano, E., Cattani, O., Chappellaz, J., Dahl-Jensen, D., Delmonte, B., Dreyfus, G., Durand, G., Falourd, S., Fischer, H., Flückiger, J., Hansson, M. E., Huybrechts, P., Jugie, G., Johnsen, S. J., Jouzel, J., Kaufmann, P., Kipfstuhl, J., Lambert, F., Lipenkov, V. Y., Littot, G. C., Longinelli, A., Lorrain, R., Maggi, V., Masson-Delmotte, V., Miller, H., Mulvaney, R., Oerlemans, J., Oerter, H., Orombelli, G., Parrenin, F., Peel, D. A., Petit, J.-R., Raynaud, D., Ritz, C., Ruth, U., Schwander, J., Siegenthaler, U., Souchez, R., Stauffer, B., Peder Steffensen, J., Stenni, B., Stocker, T. F., Tabacco, I. E., Udisti, R., van de Wal, R. S. W., van den Broeke, M., Weiss, J., Wilhelms, F., Winther, J.-G., Wolff, E. W., and Zucchelli, M.), 2004, Eight glacial cycles from an Antarctic ice core: *Nature*, v. 429, p. 623. <https://doi.org/10.1038/nature02599>

- Fuller, M., Cisowski, S., Hart, M., Haston, R., Schmidtke, E., and Jarrard, R., 1988, NRM: IRM (s) demagnetization plots; an aid to the interpretation of natural remanent magnetization: *Geophysical Research Letters*, v. 15, no. 5, p. 518-521.
- Fuller, M., Kidane, T., and Ali, J., 2002, AF demagnetization characteristics of NRM, compared with anhysteretic and saturation isothermal remanence: an aid in the interpretation of NRM: *Physics and Chemistry of the Earth, Parts A/B/C*, v. 27, no. 25-31, p. 1169-1177.
- Han, W. X., Fang, X. M., and Berger, A., 2012, Tibet forcing of mid-Pleistocene synchronous enhancement of East Asian winter and summer monsoons revealed by Chinese loess record: *Quaternary Research*, v. 78, no. 2, p. 174-184. <https://doi.org/10.1016/j.yqres.2012.05.001>
- Han, W. X., Fang, X. M., Ye, C. C., Teng, X. H., and Zhang, T., 2014, Tibet forcing Quaternary stepwise enhancement of westerly jet and central Asian aridification: Carbonate isotope records from deep drilling in the Qaidam salt playa, NE Tibet: *Global and Planetary Change*, v. 116, p. 68-75. <https://doi.org/10.1016/j.gloplacha.2014.02.006>
- Hart, M., and Fuller, M., 1988, Magnetization of a dolomite bed in the Monterey Formation: Implications for diagenesis: *Geophysical research letters*, v. 15, no. 5, p. 491-494.
- He, Z.X., Zhang, X. J., Bao, S. Y., Qiao, Y. S., Sheng, Y. Y., Liu, X. T., He, X. G., Yang, X. C., Zhao, J. X., Liu, R., and Lu, C. Y., 2015, Multiple climatic cycles imprinted on regional uplift-controlled fluvial terraces in the lower Yalong River and Anning River, SE Tibetan Plateau: *Geomorphology*, v. 250, p. 95-112. <http://dx.doi.org/10.1016/j.geomorph.2015.08.010>
- Head, M. J., and Gibbard, P. L., 2005, Early-Middle Pleistocene transitions: an overview and recommendation for the defining boundary: *Geological Society, London, Special Publications*, v. 247, no. 1, p. 1-18. doi: 10.1144/gsl.sp.2005.247.01.01
- Head, M. J., and Gibbard, P. L., 2015, Early–Middle Pleistocene transitions: linking terrestrial and marine realms: *Quaternary International*, v. 389, p. 7-46. <https://doi.org/10.1016/j.quaint.2015.09.042>
- Head, M. J., Pillans, B., and Farquhar, S. A., 2008, The Early-Middle Pleistocene transition: characterization and proposed guide for the defining boundary: *Episodes*, v. 31, no. 2, p. 255-259.

- Hesselbo, S. P., Deconinck, J.-F., Huggett, J. M., and Morgans-Bell, H. S., 2009, Late Jurassic palaeoclimatic change from clay mineralogy and gamma-ray spectrometry of the Kimmeridge Clay, Dorset, UK: *Journal of the Geological Society*, v. 166, p. 1123-1133. <https://doi.org/10.1144/0016-76492009-070>
- Heslop, D., Dekkers, M., and Langereis, C., 2002, Timing and structure of the mid-Pleistocene transition: records from the loess deposits of northern China: *Palaeogeography, Palaeoclimatology, Palaeoecology*, v. 185, no. 1, p. 133-143. [https://doi.org/10.1016/S0031-0182\(02\)00282-1](https://doi.org/10.1016/S0031-0182(02)00282-1)
- Hilgen, F. J., Abdul Aziz, H., Krijgsman, W., Raffi, I., and Turco, E., 2003, Integrated stratigraphy and astronomical tuning of the Serravallian and lower Tortonian at Monte dei Corvi (Middle–Upper Miocene, northern Italy): *Palaeogeography, Palaeoclimatology, Palaeoecology*, v. 199, no. 3–4, p. 229-264. [http://dx.doi.org/10.1016/S0031-0182\(03\)00505-4](http://dx.doi.org/10.1016/S0031-0182(03)00505-4)
- Holbourn, A., Kuhnt, W., Schulz, M., Flores, J.-A., and Andersen, N., 2007, Orbitally-paced climate evolution during the middle Miocene “Monterey” carbon-isotope excursion: *Earth and Planetary Science Letters*, v. 261, no. 3-4, p. 534-550. doi: 10.1016/j.epsl.2007.07.026
- Huber, M., and Goldner, A., 2012, Eocene monsoons: *Journal of Asian Earth Sciences*, v. 44, p. 3-23. <https://doi.org/10.1016/j.jseaes.2011.09.014>
- Hüsing, S. K., Cascella, A., Hilgen, F. J., Krijgsman, W., Kuiper, K. F., Turco, E., and Wilson, D., 2010, Astrochronology of the Mediterranean Langhian between 15.29 and 14.17Ma: *Earth and Planetary Science Letters*, v. 290, no. 3-4, p. 254-269. doi: 10.1016/j.epsl.2009.12.002
- Huybers, P., 2007, Glacial variability over the last two million years: an extended depth-derived age model, continuous obliquity pacing, and the Pleistocene progression: *Quaternary Science Reviews*, v. 26, no. 1-2, p. 37-55. doi: 10.1016/j.quascirev.2006.07.013
- Huybers, P., and Langmuir, C. H., 2017, Delayed CO₂ emissions from mid-ocean ridge volcanism as a possible cause of late-Pleistocene glacial cycles: *Earth and Planetary Science Letters*, v. 457, p. 238-249. <https://doi.org/10.1016/j.epsl.2016.09.021>

- Johnson, H., Lowrie, W., and Kent, D. V., 1975, Stability of anhysteretic remanent magnetization in fine and coarse magnetite and maghemite particles: *Geophysical Journal International*, v. 41, no. 1, p. 1-10.
- Kemp, A. E. S., Grigorov, I., Pearce, R. B., and Naveira Garabato, A. C., 2010, Migration of the Antarctic Polar Front through the mid-Pleistocene transition: evidence and climatic implications: *Quaternary Science Reviews*, v. 29, no. 17, p. 1993-2009. <https://doi.org/10.1016/j.quascirev.2010.04.027>
- Kent, D. V., Olsen, P. E., and Witte, W. K., 1995, Late Triassic-earliest Jurassic Geomagnetic Polarity Sequence and Paleolatitudes: *Journal of Geophysical Research*, v. 100, no. B8, p. 14965-14998.
- Kirschvink, J., 1980, The least-squares line and plane and the analysis of palaeomagnetic data: *Geophysical Journal International*, v. 62, no. 3, p. 699-718.
- Kirschvink, J. L., Kopp, R. E., Raub, T. D., Baumgartner, C. T., and Holt, J. W., 2008, Rapid, precise, and high-sensitivity acquisition of paleomagnetic and rock-magnetic data: Development of a low-noise automatic sample changing system for superconducting rock magnetometers: *Geochemistry, Geophysics, Geosystems*, v. 9, no. 5. doi: 10.1029/2007GC001856
- Kopp, R. E., 2007, The identification and interpretation of microbial biogeomagnetism, Dissertation (Ph.D.), California Institute of Technology. <http://resolver.caltech.edu/CaltechETD:etd-04122007-135320>
- Laskar, J., Robutel, P., Joutel, F., Gastineau, M., Correia, A. C. M., and Levrard, B., 2004, A long-term numerical solution for the insolation quantities of the Earth: *Astronomy & Astrophysics*, v. 428, no. 1, p. 261-285. <https://doi.org/10.1051/0004-6361:20041335>
- Li, C., Lin, J., Kulhanek, D., Williams, T., Bao, R., Briaies, A., Brown, E., Chen, Y., Clift, P., and Colwell, F., the Expedition 349 Scientists, 2015. Expedition 349 summary: Proceedings of the International Ocean Discovery Program, v. 349, p. 1-43. <http://dx.doi.org/10.14379/iodp.proc.349.2015>

- Li, C. F., Xu, X., Lin, J., Sun, Z., Zhu, J., Yao, Y., Zhao, X., Liu, Q., Kulhanek, D. K., Wang, J., Song, T., Zhao, J., Qiu, N., Guan, Y., Zhou, Z., Williams, T., Bao, R., Briais, A., Brown, E. A., Chen, Y., Clift, P. D., Colwell, F. S., Dadd, K. A., Ding, W., Almeida, I. H., Huang, X.-L., Hyun, S., Jiang, T., Koppers, A. A. P., Li, Q., Liu, C., Liu, Z., Nagai, R. H., Peleo-Alampay, A., Su, X., Tejada, M. L. G., Trinh, H. S., Yeh, Y.-C., Zhang, C., Zhang, F., and Zhang, G.-L., 2014, Ages and magnetic structures of the South China Sea constrained by deep tow magnetic surveys and IODP Expedition 349: *Geochemistry, Geophysics, Geosystems*, v. 15, no. 12, p. 4958-4983. doi: 10.1002/2014GC005567
- Li, C. F., Li, J., Ding, W., Franke, D., Yao, Y., Shi, H., Pang, X., Cao, Y., Lin, J., and Kulhanek, D. K., 2015, Seismic stratigraphy of the central South China Sea basin and implications for neotectonics: *Journal of Geophysical Research: Solid Earth*, v. 120, no. 3, p. 1377-1399. doi: 10.1002/2014JB011686.
- Li, J. J., Fang, X. M., Van der Voo, R., Zhu, J. J., Niocail, C. M., Ono, Y., Pan, B. T., Zhong, W., Wang, J. L., and Sasaki, T., 1997, Magnetostratigraphic dating of river terraces: Rapid and intermittent incision by the Yellow River of the northeastern margin of the Tibetan Plateau during the Quaternary: *Journal of Geophysical Research: Solid Earth*, v. 102, no. B5, p. 10121-10132.
- Li, J. J., Fang, X. M., Song, C. H., Pan, B. T., Ma, Y. Z., and Yan, M. D., 2014. Late Miocene–Quaternary rapid stepwise uplift of the NE Tibetan Plateau and its effects on climatic and environmental changes: *Quaternary Research*, v. 81: p. 400-423. <http://dx.doi.org/10.1016/j.yqres.2014.01.002>
- Li, M. S., Zhang, Y., Huang, C. J., Ogg, J., Hinnov, L., Wang, Y. D., Zou, Z. Z., and Li, L. Q., 2017, Astronomical tuning and magnetostratigraphy of the Upper Triassic Xujiahe Formation of South China and Newark Supergroup of North America: Implications for the Late Triassic time scale: *Earth and Planetary Science Letters*, v. 475, p. 207-223. <https://doi.org/10.1016/j.epsl.2017.07.015>
- Li, M. S., Kump, L. R., Hinnov, L. A., and Mann, M. E., 2018, Tracking variable sedimentation rates and astronomical forcing in Phanerozoic paleoclimate proxy series with evolutionary correlation coefficients and hypothesis testing: *Earth and Planetary Science Letters*, v. 501, p. 165-179. <https://doi.org/10.1016/j.epsl.2018.08.041>

- Li, M. S., Hinnov, L. A., and Kump, L. R., 2019, Acycle: Time-series analysis software for paleoclimate research and education: *Computers & Geosciences*, v. 127, p. 12-22. <https://doi.org/10.1016/j.cageo.2019.02.011>
- Li, Q. Y., Wang, P. X., Zhao, Q. H., Tian, J., Cheng, X. r., Jian, Z. M., Zhong, G. F., and Chen, M. H., 2008, Paleoceanography of the mid-Pleistocene South China Sea: *Quaternary Science Reviews*, v. 27, no. 11, p. 1217-1233. <https://doi.org/10.1016/j.quascirev.2008.02.007>
- Lisiecki, L. E., and Raymo, M. E., 2005, A Pliocene-Pleistocene stack of 57 globally distributed benthic $\delta^{18}\text{O}$ records: *Paleoceanography*, v. 20, no. 1. <https://doi.org/10.1029/2004PA001071>
- Liu, D. L., Fang, X. M., Song, C. H., Dai, S., Zhang, T., Zhang, W. L., Miao, Y. F., Liu, Y. Q., and Wang, J. Y., 2010, Stratigraphic and paleomagnetic evidence of mid-Pleistocene rapid deformation and uplift of the NE Tibetan Plateau: *Tectonophysics*, v. 486, no. 1, p. 108-119. <https://doi.org/10.1016/j.tecto.2010.01.014>
- Liu, Z., Colin, C., Huang, W., Le, K. P., Tong, S., Chen, Z., and Trentesaux, A., 2007, Climatic and tectonic controls on weathering in south China and Indochina Peninsula: Clay mineralogical and geochemical investigations from the Pearl, Red, and Mekong drainage basins: *Geochemistry, Geophysics, Geosystems*, v. 8, no. 5. <https://doi.org/10.1029/2006GC001490>
- Liu, Z., Zhao, Y., Colin, C., Statterger, K., Wiesner, M. G., Huh, C.-A., Zhang, Y., Li, X., Sompongchaiyakul, P., You, C.-F., Huang, C.-Y., Liu, J. T., Siringan, F. P., Le, K. P., Sathiamurthy, E., Hantoro, W. S., Liu, J., Tuo, S., Zhao, S., Zhou, S., He, Z., Wang, Y., Bunsomboonsakul, S., and Li, Y., 2016, Source-to-sink transport processes of fluvial sediments in the South China Sea: *Earth-Science Reviews*, v. 153, p. 238-273. <https://doi.org/10.1016/j.earscirev.2015.08.005>
- Lurcock, P. C., and Wilson, G. S., 2012, PuffinPlot: A versatile, user-friendly program for paleomagnetic analysis: *Geochemistry, Geophysics, Geosystems*, v. 13, no. 6. <https://doi.org/10.1029/2012GC004098>

- Lüthi, D., Le Floch, M., Bereiter, B., Blunier, T., Barnola, J.-M., Siegenthaler, U., Raynaud, D., Jouzel, J., Fischer, H., Kawamura, K., and Stocker, T. F., 2008, High-resolution carbon dioxide concentration record 650,000–800,000 years before present: *Nature*, v. 453, p. 379. <https://doi.org/10.1038/nature06949>
- Molnar, P., 2004, Late Cenozoic Increase in Accumulation Rates of Terrestrial Sediment: How Might Climate Change Have Affected Erosion Rates? p. 67-89. <https://doi.org/10.1146/annurev.earth.32.091003.143456>
- Ogg, J. G., Ogg, G., and Gradstein, F. M., 2016, *A Concise Geologic Time Scale: 2016*, Elsevier.
- Rego, J. L., Meselhe, E., Stronach, J., and Habib, E., 2010, Numerical modeling of the Mississippi-Atchafalaya Rivers' sediment transport and fate: Considerations for diversion scenarios: *Journal of Coastal Research*, v. 26, no. 2, p. 212-229. <https://doi.org/10.2112/08-1072.1>
- Roberts, A. P., and Weaver, R., 2005, Multiple mechanisms of remagnetization involving sedimentary greigite (Fe₃S₄): *Earth and Planetary Science Letters*, v. 231, no. 3-4, p. 263-277. <https://doi.org/10.1016/j.epsl.2004.11.024>
- Schnyder, J., Ruffell, A., Deconinck, J.-F., and Baudin, F., 2006, Conjunctive use of spectral gamma-ray logs and clay mineralogy in defining late Jurassic–early Cretaceous palaeoclimate change (Dorset, UK): *Palaeogeography, Palaeoclimatology, Palaeoecology*, v. 229, no. 4, p. 303-320. <https://doi.org/10.1016/j.palaeo.2005.06.027>
- Shao, L., Li, X., Geng, J., Pang, X., Lei, Y., Qiao, P., Wang, L., and Wang, H., 2007, Deep water bottom current deposition in the northern South China Sea: *Science in China Series D: Earth Sciences*, v. 50, no. 7, p. 1060-1066.
- Singer, B. S., 2014, A Quaternary geomagnetic instability time scale: *Quaternary Geochronology*, v. 21, p. 29-52. <https://doi.org/10.1016/j.quageo.2013.10.003>
- Sun, Y., Clemens, S. C., An, Z., and Yu, Z., 2006, Astronomical timescale and palaeoclimatic implication of stacked 3.6-Myr monsoon records from the Chinese Loess Plateau: *Quaternary Science Reviews*, v. 25, no. 1, p. 33-48. <https://doi.org/10.1016/j.quascirev.2005.07.005>

- Sun, Z., Jian, Z., Stock, J.M., Larsen, H.C., Klaus, A., Alvarez Zarikian, C.A., and the Expedition 367/368 Scientists, 2018. South China Sea Rifted Margin. Proceedings of the International Ocean Discovery Program, 367/368: College Station, TX (International Ocean Discovery Program). <https://doi.org/10.14379/iodp.proc.367368.2018>
- Sun, Z., Stock, J., Jian, Z., McIntosh, K., Alvarez-Zarikian, C.A., and Klaus, A., 2016. Expedition 367/368 Scientific Prospectus: South China Sea Rifted Margin. International Ocean Discovery Program. <https://doi.org/10.14379/iodp.sp.367368.2016>
- Tada, R., Zheng, H., and Clift, P. D., 2016, Evolution and variability of the Asian monsoon and its potential linkage with uplift of the Himalaya and Tibetan Plateau: Progress in Earth and Planetary Science, v. 3, no. 1, p. 4. <https://doi.org/10.1186/s40645-016-0080-y>
- Tian, J., Wang, P., Cheng, X., and Li, Q., 2002, Astronomically tuned Plio–Pleistocene benthic $\delta^{18}\text{O}$ record from South China Sea and Atlantic–Pacific comparison: Earth and Planetary Science Letters, v. 203, no. 3, p. 1015-1029. [https://doi.org/10.1016/S0012-821X\(02\)00923-8](https://doi.org/10.1016/S0012-821X(02)00923-8)
- Tian, J., Zhao, Q., Wang, P., Li, Q., and Cheng, X., 2008, Astronomically modulated Neogene sediment records from the South China Sea: Paleooceanography, v. 23, no. 3. <https://doi.org/10.1029/2007PA001552>
- Tzedakis, P. C., Raynaud, D., McManus, J. F., Berger, A., Brovkin, V., and Kiefer, T., 2009, Interglacial diversity: Nature Geoscience, v. 2, p. 751.
- Wan, S., Li, A., Clift, P. D., and Jiang, H., 2006, Development of the East Asian summer monsoon: Evidence from the sediment record in the South China Sea since 8.5 Ma: Palaeogeography, Palaeoclimatology, Palaeoecology, v. 241, no. 1, p. 139-159. <https://doi.org/10.1016/j.palaeo.2006.06.013>
- Wan, S., Li, A., Jan-Berend, W. S., and Xu, F., 2007, Grain-size records at ODP site 1146 from the northern South China Sea: Implications on the East Asian monsoon evolution since 20 Ma: Science in China Series D: Earth Sciences, v. 50, no. 10, p. 1536-1547. <https://doi.org/10.1007/s11430-007-0082-0>
- Wang, P., Clemens, S., Beaufort, L., Braconnot, P., Ganssen, G., Jian, Z., Kershaw, P., and Sarnthein, M., 2005, Evolution and variability of the Asian monsoon system: state of the art and outstanding issues: Quaternary Science Reviews, v. 24, no. 5-6, p. 595-629. <https://doi.org/10.1016/j.quascirev.2004.10.002>

- Wang, P., and Li, Q., 2009, Oceanographical and geological background, The South China Sea, Springer, p. 25-73. https://doi.org/10.1007/978-1-4020-9745-4_2
- Wang, P., Prell, W., and Blum, P. e. a., 2000, Proceedings of Ocean Drilling Program, Initial Reports, Volume 184, College Station: Ocean Drilling Program. doi:10.2973/odp.proc.ir.184.2000
- Wang, P., Zhao, Q., Jian, Z., Cheng, X., Huang, W., Tian, J., Wang, J., Li, Q., Li, B., and Su, X., 2003, Thirty million year deep sea records in the South China Sea: Chinese Science Bulletin, v. 48, no. 23, p. 2524-2535. <https://doi.org/10.1007/BF03037016>
- Wohlfarth, E., 1958, Relations between different modes of acquisition of the remanent magnetization of ferromagnetic particles: Journal of Applied Physics, v. 29, no. 3, p. 595-596.
- Wu, H., Shi, M., Zhao, X., Huang, B., Zhang, S., Li, H., Yang, T., and Lin, C., 2017, Magnetostratigraphy of ODP Site 1143 in the South China Sea since the Early Pliocene: Marine Geology, v. 394, p. 133-142. <https://doi.org/10.1016/j.margeo.2017.08.010>
- Wu, H., Zhang, S., Jiang, G., Hinnov, L., Yang, T., Li, H., Wan, X., and Wang, C., 2013, Astrochronology of the Early Turonian–Early Campanian terrestrial succession in the Songliao Basin, northeastern China and its implication for long-period behavior of the Solar System: Palaeogeography, Palaeoclimatology, Palaeoecology, v. 385, p. 55-70. <https://doi.org/10.1016/j.palaeo.2012.09.004>
- Wu, H., Zhao, X., Shi, M., Zhang, S., Li, H., and Yang, T., 2014, A 23 Myr magnetostratigraphic time framework for Site 1148, ODP Leg 184 in South China Sea and its geological implications: Marine and Petroleum Geology, v. 58, Part B, p. 749-759. <http://dx.doi.org/10.1016/j.marpetgeo.2014.01.003>
- Xiang, F., Zhu, L. D., Wang, C. S., Zhao, X. X., Chen H. D., and Yang, W. G., 2007, Quaternary sediment in the Yichang area: implications for the formation of the Three Gorges of the Yangtze River: Geomorphology, v. 85, p. 249–258. <https://doi.org/10.1016/j.geomorph.2006.03.027>

- Zhang, Y., Li, M., Ogg, J. G., Montgomery, P., Huang, C., Chen, Z.-Q., Shi, Z., Enos, P., and Lehrmann, D. J., 2015, Cycle-calibrated magnetostratigraphy of middle Carnian from South China: Implications for Late Triassic time scale and termination of the Yangtze Platform: *Palaeogeography, Palaeoclimatology, Palaeoecology*, v. 436, p. 135-166. <https://doi.org/10.1016/j.palaeo.2015.05.033>
- Zijderveld, J. D. A., 1967, A.C. Demagnetisation of rocks: Analysis of results: In: Collinson, D.W., Creer, K.M., and Runcorn, S.K., (Editors), *Methods in Paleomagnetism*. Elsevier, Amsterdam,, p. 254-286.

Appendix C Additional rock magnetic studies and data

Paleomagnetic sampling strategies

Upward arrows were marked on the sampled sediments before sampling. Measurements by an Icefield MI-5 core orientation tool mounted on the core barrel partly enabled orientation relative to present-day North for the discrete samples from the upper 162 m; but there was no control on the declination of the samples below 162 m due to rotations of pieces during the borehole coring process. For the unconsolidated sediments, paleomagnetic samples were taken by pushing non-magnetic cubes directly into the center of the working halves; whereas for semi-consolidated to consolidated sediments, a non-magnetic extruder was inserted, and then the sediment plug was pushed out into aluminum foil pieces and loosely wrapped before putting into a plastic vial.

Shipboard paleomagnetism and magnetostratigraphy

Shipboard paleomagnetic analyses were conducted on archive-half sections with the pass-through superconducting rock magnetometer with alternating field (AF) demagnetization steps at 5, 15 and 25 mT. The maximum field strength of in-line AF demagnetization used on the archive-half sections is limited because of the destructive nature of the treatments and our limited ability to measure weak magnetizations in the magnetically noisy shipboard environment. As a consequence, the pass-through shipboard data are usually not sufficient to isolate accurate characteristic remanent magnetization (ChRM) directions. A small set of shipboard discrete samples was subjected to AF and thermal demagnetization, and the remanence was measured on the spinner magnetometer. We adopted a combination of stepwise AF and thermal demagnetization steps to fully demagnetize these pilot samples to obtain ChRMs.

A preliminary and slightly ‘over-interpreted’ shipboard magnetostratigraphy (Fig. A.1) had been constructed based on the raw paleomagnetic data with stable and clear demagnetization behaviors. The core orientation tool enabled partial correction of paleomagnetic declinations in the upper 162 m; below that, our interpretation is only based on inclination data from both archive halves and a few discrete samples. Typical demagnetization behaviors of those few discrete samples that were measured shipboard are shown in Fig. A.2. AF demagnetization of those samples displayed demagnetization paths that were easier to interpret than the results from thermal demagnetization, probably because of the absence of a magnetically-shielded lab

environment on board; and thermal demagnetization at higher temperatures lacked clear trends. Therefore, no reliable ChRM directions could be achieved, although both treatments indicated the removal of a near-vertical positive component at low-temperature or low-AF steps. This steep-downward component is frequently attributed to a drilling-induced remanent magnetization that is dominantly carried by multi-domain grains (Allerton et al., 1995).

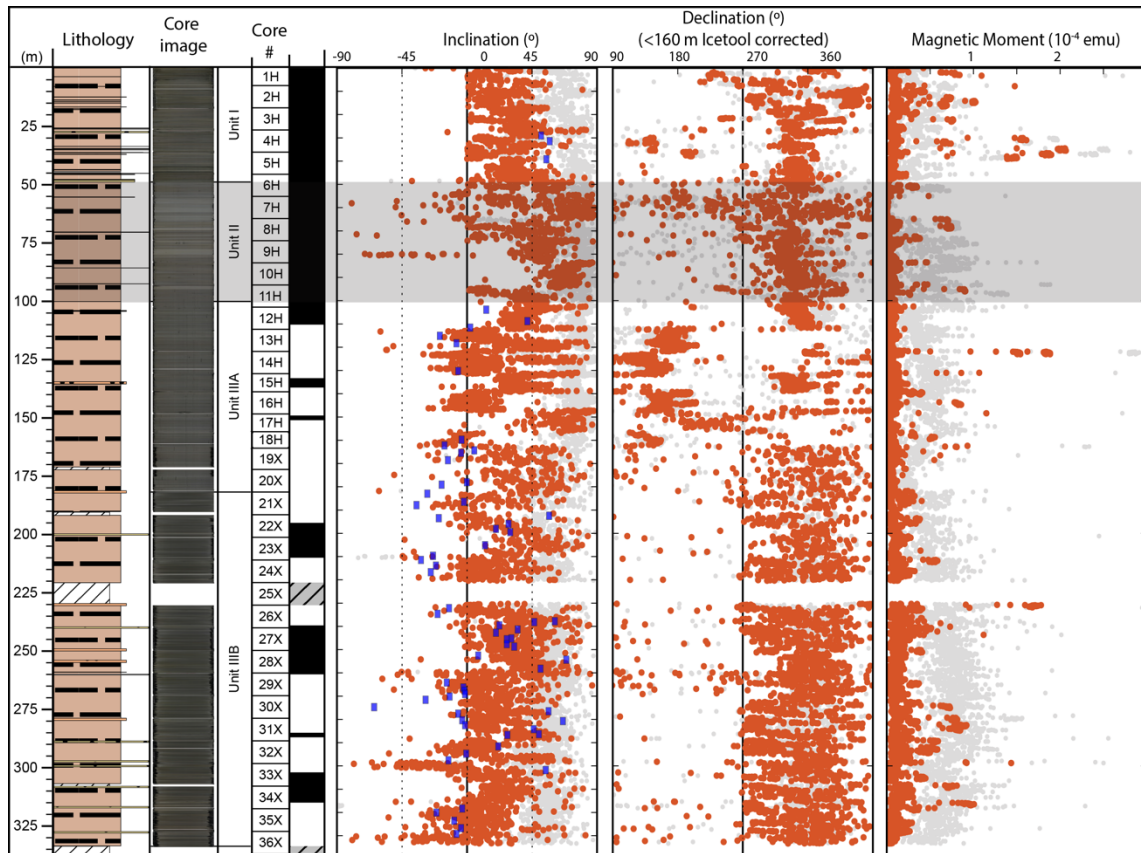


Figure A.1. Shipboard magnetostratigraphy data (NRM in light gray and 20 mT in orange dots) on meter scale. Core declinations above 160 m were partially corrected using the Icefield MI-5 core orientation tool; therefore, the main declination clusters could be used for polarity interpretation. ChRMs from discrete samples measured on board are marked by blue squares. The slump-deposit interval of Unit II (48.85–100.04 m, U1499A-6H-3 to 11H-5) is shaded in gray, according to that interpretation by both microfossils and sedimentology; and it seems that portions of that slump seemed to have acquired a normal-polarity magnetization during its syndimentary settling.

When comparing to the reference geomagnetic time scale of GTS2016 (Ogg et al., 2016), several tie points were achieved with the shipboard measurements: an assignment of the Brunhes/Matuyama Chron boundary (0.78 Ma; which is the current working definition for the Middle/Early Pleistocene boundary) at ~110 m, and the middle of C2An.3n subchron (Late/Early

Pliocene; 3.6 Ma) at ~260 m. This suggested placement of the Pleistocene/Pliocene boundary (~2.6 Ma) at ~220 m and the Pliocene/Miocene boundary (5.33 Ma) at ~370 m (Sun et al., 2018; and Fig. A.3). However, post-expedition paleomagnetic measurements were necessary to enhance and verify the shipboard polarity interpretation.

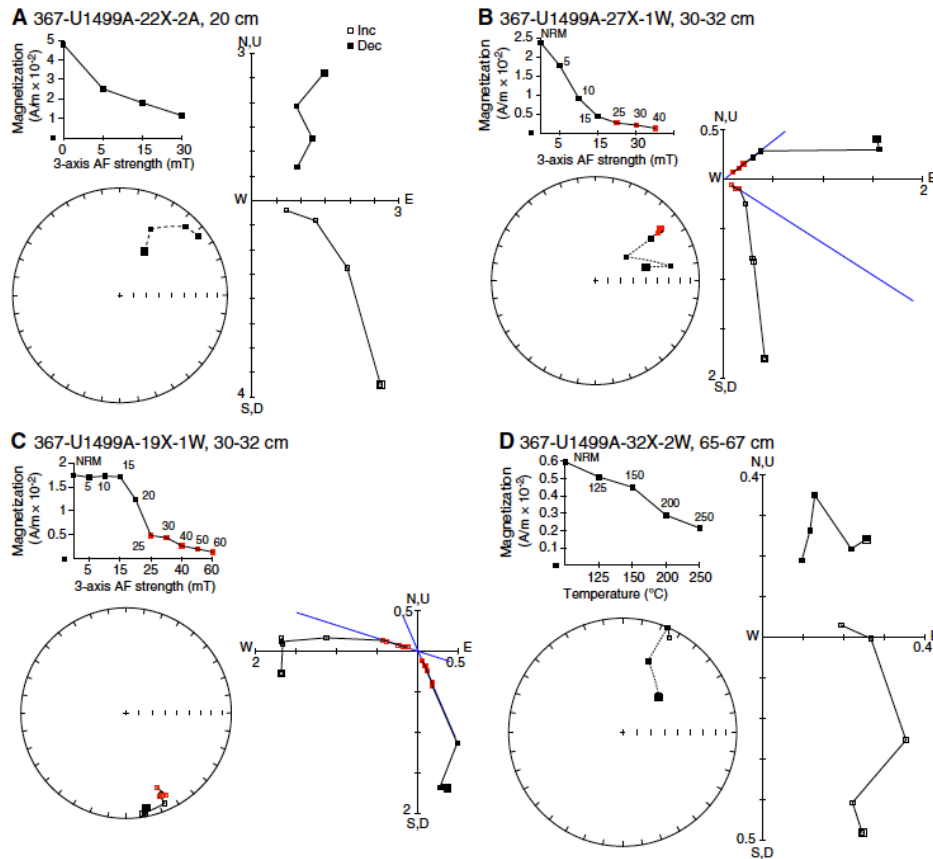


Figure A.2. Shipboard demagnetization plots of (A) archive-half section and (B–D) discrete samples, Hole U1499A. Stereographic plots: solid squares = positive (downward) inclination, open squares = negative (upward) inclination. (A, B) Samples interpreted as normal polarity; ChRM of sample in B (blue line; red squares = measurements used in calculation of PCA) has 51° declination and 21° inclination. (C) Reversed-polarity sample with ChRM declination of 156° and inclination of -16°. (D) A sample interpreted as potential reversed-polarity based on its inclination that progressively shallowed and then became negative at 250°C.

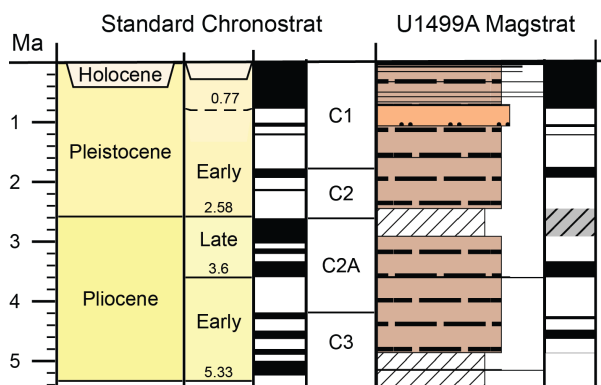


Figure A.3. Shipboard magnetostratigraphy and its pattern-match-based correlation to the magnetic polarity time scale in GTS 2016.

Post-cruise paleomagnetism and magnetostratigraphy

The stereo-plot projection of all NRM and ChRM from discrete samples (Fig. A.5) shows the inclination shallowing (and inverting to negative inclination for reversed-polarity samples) as these overprints are removed to unblock the interpreted primary magnetization. However, many of the trends toward negative inclinations only attained $\pm 10^\circ$ (Fig. A.4B), which is much shallower than the expected Pleistocene value of -25° . This is similar to the reported situation for shallow negative inclinations in coeval similar lithology facies at IODP Site 1148 to the northeast of Site U1499 (Wu et al., 2014). In these cases, the polarity interpretations are made accordingly to the combined inclination-declination trend upon stepwise demagnetization and/or the context (e.g., Fig. A.4B).

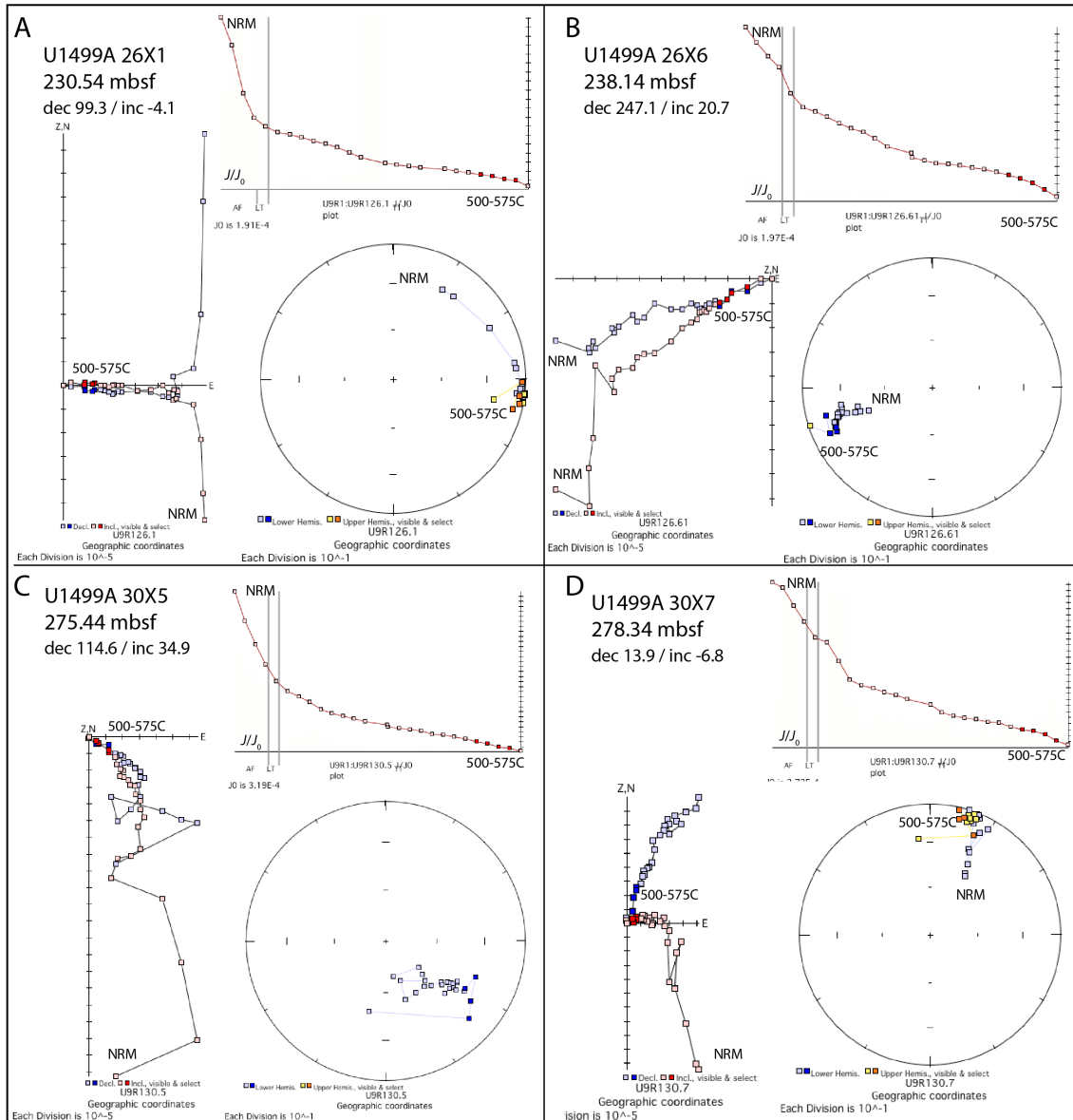


Figure A.4. Examples of samples that constrain placement for two of the boundaries between polarity zones. Reversed-polarity samples (A and D) show a progressive trend of inclination during demagnetization from an initial downward direction to an upward direction, although the ChRM inclination is still shallower than predicted from this site paleolatitude. However, these trends are clearly opposite to those of the inclination behavior during demagnetization of the normal-polarity rated samples (B and C).

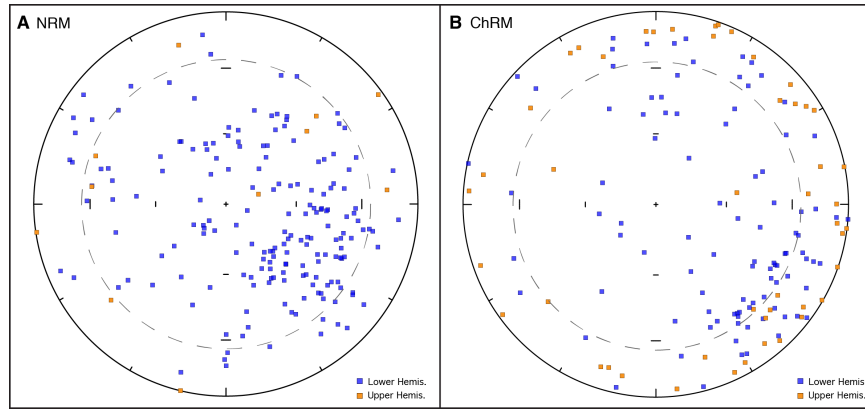


Figure A.5. Stereo-plot projection of NRM (A) and ChRM (B) of all the post-cruise samples. The removal of a steep-downward drilling-induced component is clearly recognized. The dashed circle marks the present-day magnetic inclination of this locality.

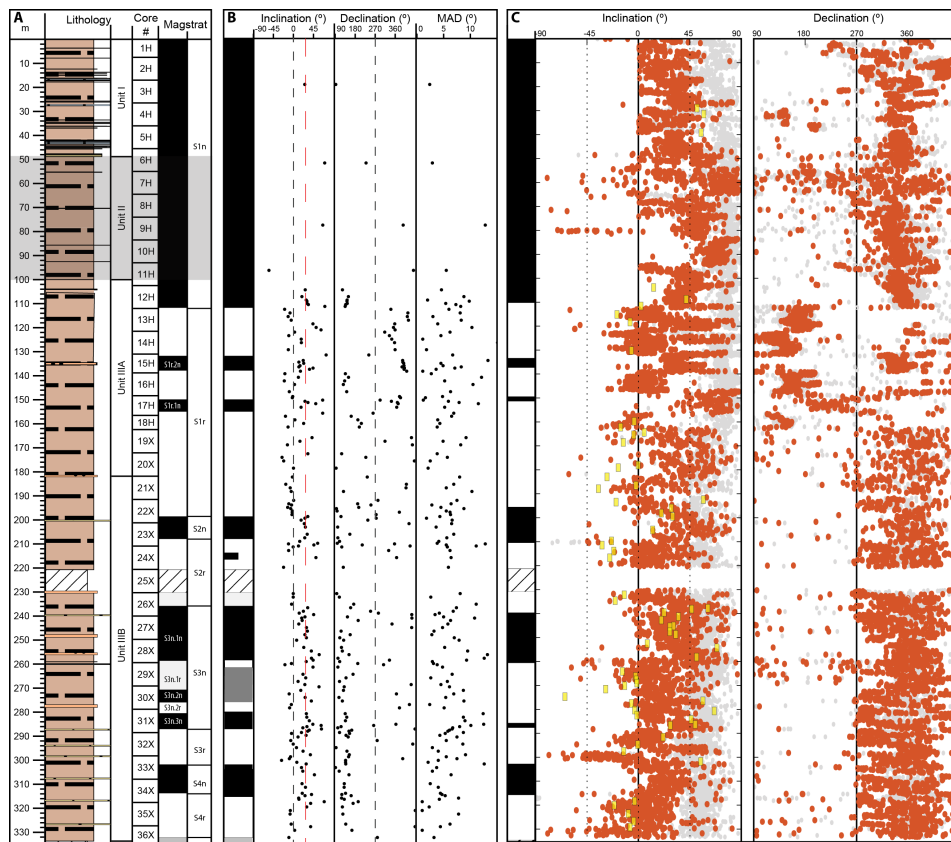


Figure A.6. Composite magnetostratigraphy of U1499A (0-333 m) that was constructed based on the merger of the post-expedition magnetostratigraphy of discrete samples and shipboard pass-through magnetometer results (Fig. A.1). Magstrat = magnetostratigraphy. MAD = maximum angular deviation. The dashed red line in the Inclination column indicates the present-day magnetic inclination at this location. “S” of the magnetozones S4r to S1n is for South China Sea. Note that almost all of the MADs are $\leq 15^\circ$ indicating high-quality data for polarity interpretation.

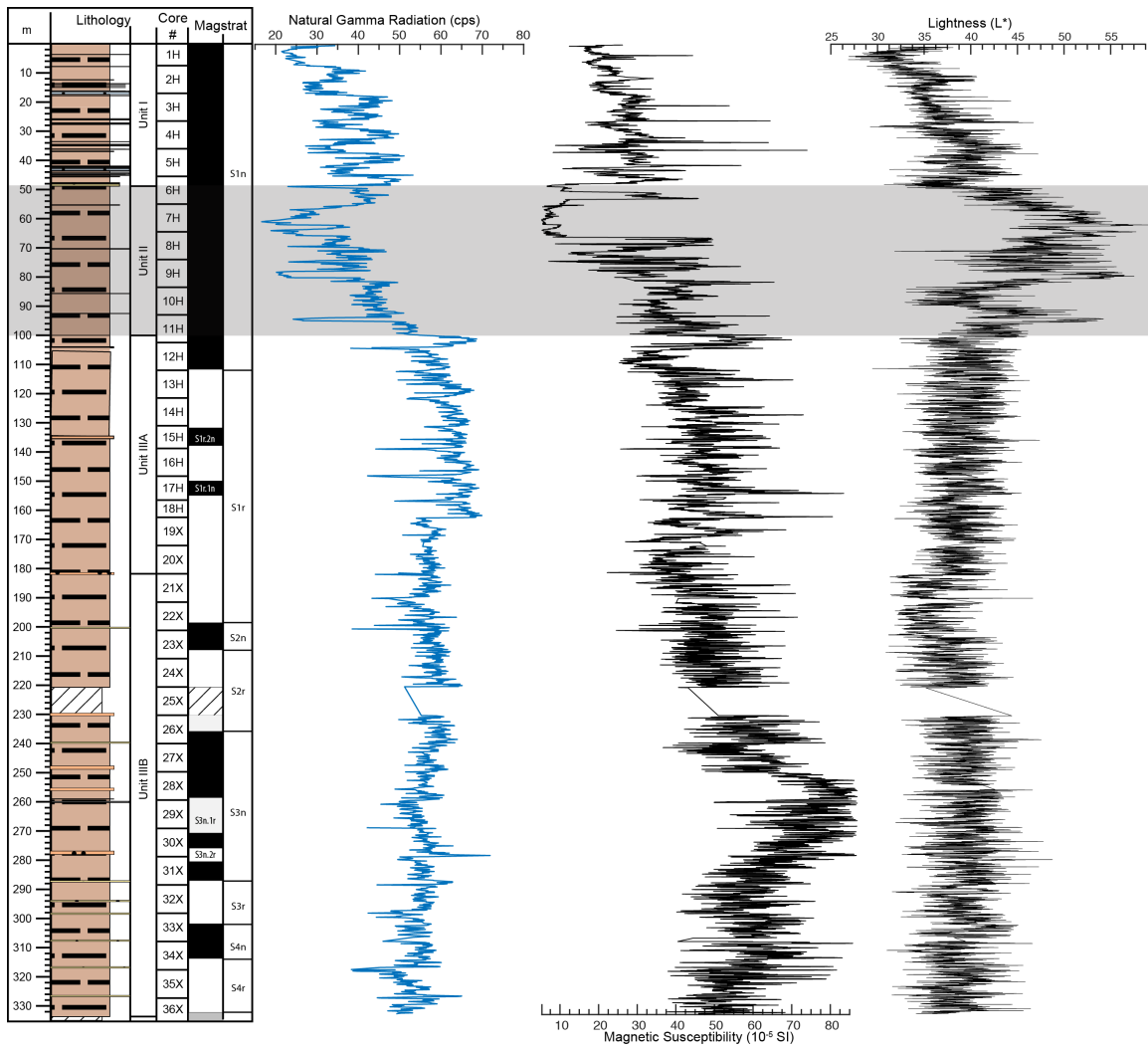


Figure A.7. Complete data series of natural gamma radiation (NGR), magnetic susceptibility and reflectance parameter lightness (L^*) with the lithology and composite magnetostratigraphy of this study. The shaded area denotes the slump deposit interval, evidenced by the anomalous values in all three data sets.

Cycle analysis of the natural gamma ray data of Site U1499 (0-333 m)

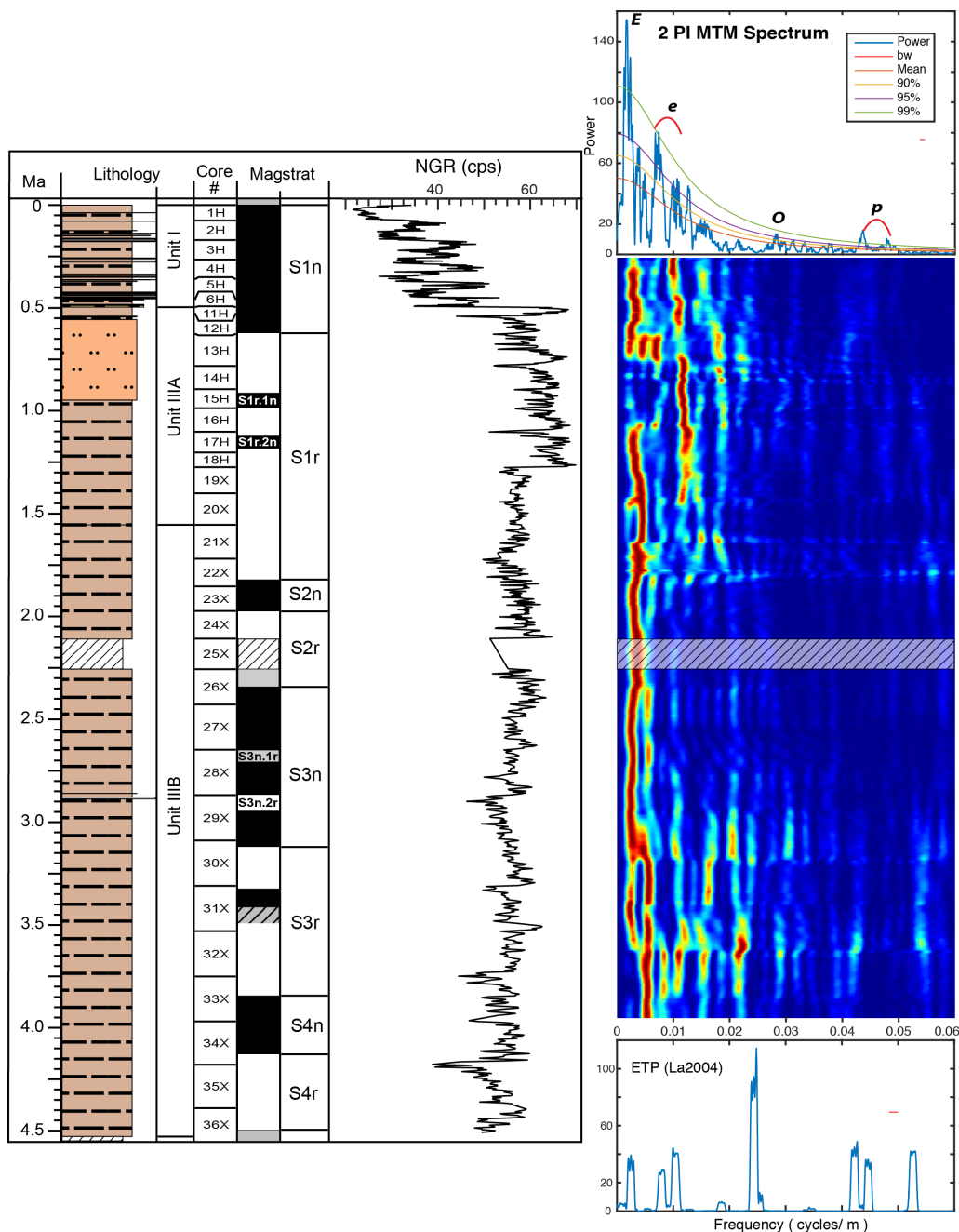


Figure A.8. Complete NGR series projected into the time domain with its power spectra showing the dominating cyclicality. For reference, the MTM power spectrum of the astronomical ETP (La 2004) model is shown in the lower-right diagram. The lithostratigraphy, coring record and magnetostratigraphy of U1499A have also been projected into the time domain.

Age model and sediment accumulation rates of Sites U1499 (0-333 m), 1148 and 1143

Site U1499 (this study)

Table A.1. Depth-to-age model used to convert the magnetostratigraphy of Site U1499. The meter scales below the dashed line have been adjusted to compensate for the missing time (~200-300 kyr) in the recovery gap of Core 25X as implied by the correlation of magnetostratigraphy to the geomagnetic polarity time scale; and this plus other correlations, are indicated by the sediment accumulation rates (Sed. Acc. Rate).

Depth (m)	Age (ka)	Depth (m)	Age (ka)	Depth (m)	Age (ka)	Sed. Acc. Rate (cm/kyr)
25.00	250.00	59.09	606.22	128.27	1512.58	
26.00	260.03	61.09	628.22	129.27	1530.17	
27.01	269.86	66.11	716.29	130.27	1548.07	
28.01	279.88	69.11	767.13	131.28	1565.98	
29.01	289.91	86.16	970.11	132.28	1583.57	
30.01	299.93	96.18	1089.45	133.28	1601.16	
31.02	309.96	97.19	1102.14	134.28	1618.15	
32.02	319.99	98.19	1114.83	135.29	1635.14	
33.02	330.11	99.19	1127.36	136.29	1652.43	
34.02	340.34	101.20	1151.52	137.29	1668.86	
35.03	350.68	102.20	1163.75	138.29	1685.30	
36.03	361.12	108.22	1237.11	139.30	1702.01	
37.03	371.57	109.22	1249.19	140.30	1717.93	
38.03	382.01	110.22	1261.42	142.30	1749.26	
39.04	392.45	111.22	1273.50	143.31	1764.68	
40.04	402.90	112.23	1285.72	146.31	1806.46	
41.04	413.34	113.23	1297.95	147.32	1820.00	
42.04	423.79	114.23	1310.64	160.35	1980.92	
43.05	434.23	115.23	1323.49	161.35	1993.29	
44.05	444.67	116.24	1336.35	162.36	2006.48	
45.05	455.12	117.24	1349.37	163.36	2019.68	
46.05	465.78	118.24	1363.10	169.37	2106.86	
47.06	476.68	119.24	1376.84	170.38	2121.39	
48.06	487.58	120.25	1390.76	178.40	2494.79	2.15
49.06	498.60	121.25	1405.29	184.65	2590.00	6.57
50.06	511.45	122.25	1420.04	235.35	3600.00	5.02
51.07	522.00	123.25	1434.78	250.85	4100.00	3.10
52.07	532.56	124.26	1449.31	262.85	4300.00	6.00
53.07	543.11	125.26	1463.84			
54.08	553.89	126.26	1478.58			
55.08	564.44	127.26	1495.29			

Site 1148 (Tian et al., 2008)

Table A.2. Depth-to-age model and sediment accumulation rate of Site 1148 based on the tie points of the Marine Isotope Stages (MIS) noted in Figure 4a of Tian et al. (2008), which uses visual comparison of the benthic foraminiferal (*Uvigerina*) $\delta^{18}\text{O}$ from Site 1148 to Shackleton's *Uvigerina* $\delta^{18}\text{O}$.

MIS stages (peak) of Site 1148	Depth (m)	Age (Ma) according to Shackleton et al.	Sed. Acc. Rate (cm/kyr)
5	16	0.11	14.55
6	17	0.13	5.00
12	31	0.4	5.19
16	43	0.62	5.45
22	61	0.88	6.92
52	99	1.52	5.94
96	139	2.43	4.40
100	143	2.5	5.71
M2	156	3.3	1.63
Gi16	172	4	2.29
Si6	183	4.86	1.28

Site 1143 (Ao et al., 2011)

Table A.3. Depth-to-age model and sediment accumulation rates of Site 1143 according to the detailed cycle analysis by Ao et al. (2011).

Depth (m)	Age (ka)	Sed. Acc. Rate (cm/kyr)	Depth (m)	Age (ka)	Sed. Acc. Rate (cm/kyr)	Depth (m)	Age (ka)	Sed. Acc. Rate (cm/kyr)
0.2	10	--	83.5	1727	5.71	151.5	3503	2.88
0.8	21	5.45	85.8	1801	3.11	152.7	3523	6.00
4.3	73	6.73	91.1	1862	8.69	153.7	3547	4.17
7.2	114	7.07	92.9	1886	7.50	154.2	3563	3.13
9	140	6.92	93.8	1914	3.21	156	3603	4.50
10.7	161	8.10	94.6	1938	3.33	156.3	3624	1.43
12.5	188	6.67	95.3	1959	3.33	157	3661	1.89
15.5	227	7.69	95.8	1981	2.27	157.6	3698	1.62
18.9	281	6.30	96.3	1995	3.57	158.2	3719	2.86
19.9	303	4.55	97	2018	3.04	159.5	3759	3.25
21.4	327	6.25	97.4	2035	2.35	160.1	3784	2.40
22	349	2.73	98.3	2086	1.76	160.7	3812	2.14
24	400	3.92	101.9	2153	5.37	162.8	3860	4.38
26.8	439	7.18	103.7	2203	3.60	163.7	3903	2.09
28.3	473	4.41	105.1	2244	3.41	164.3	3927	2.50
30.8	515	5.95	106.5	2267	6.09	164.6	3943	1.87
32.6	570	3.27	108.4	2315	3.96	165	3978	1.14
34.1	608	3.95	109.8	2353	3.68	165.2	4000	0.91
35.6	637	5.17	111.2	2411	2.41	165.6	4020	2.00
38.4	685	5.83	112.7	2446	4.29	166.5	4056	2.50
41	723	6.84	114.4	2485	4.36	167.3	4096	2.00
42.9	780	3.33	116	2512	5.93	168	4121	2.80
43.8	814	2.65	118	2561	4.08	168.6	4139	3.33
45.6	854	4.50	120.8	2603	6.67	170.4	4210	2.54

Table A.3. continued

46.6	876	4.55	121.6	2625	3.64	172.1	4251	4.15
48	928	2.69	123.8	2669	5.00	173.1	4292	2.44
50.5	967	6.41	125	2691	5.45	174	4323	2.90
52.4	1037	2.71	125.6	2715	2.50	174.4	4344	1.90
53.4	1063	3.85	126.7	2740	4.40	175	4374	2.00
55	1088	6.40	127.6	2768	3.21	175.7	4421	1.49
57.4	1142	4.44	129.6	2809	4.88	176.4	4456	2.00
59.4	1183	4.88	130.2	2841	1.87	177	4496	1.50
60.6	1220	3.24	130.7	2862	2.38	178.7	4539	3.95
62.4	1254	5.29	131.5	2896	2.35	179.3	4584	1.33
65.8	1329	4.53	132.4	2940	2.05	180.4	4627	2.56
66.9	1350	5.24	133.6	2983	2.79	181.2	4653	3.08
67.4	1370	2.50	134	3005	1.82	182.7	4727	2.03
68	1390	3.00	135.3	3052	2.77	183.1	4752	1.60
69.9	1443	3.58	137.3	3093	4.88	183.4	4773	1.43
71.7	1483	4.50	138.6	3143	2.60	184.2	4815	1.90
72.7	1502	5.26	139.8	3182	3.08	184.9	4849	2.06
73.9	1540	3.16	141.8	3239	3.51	185.3	4870	1.90
75.9	1579	5.13	143.4	3283	3.64	185.7	4900	1.33
76.6	1598	3.68	144.3	3313	3.00	186.7	4925	4.00
77.3	1618	3.50	146.9	3356	6.05	188.6	4966	4.63
79.4	1654	5.83	148	3390	3.24	189.7	4995	3.79
81.5	1692	5.53	150	3451	3.28			

Site 1143 (Wu et al., 2017)

Table A.4. Depth-to-age model and sediment accumulation rates of Site 1143 according to the magnetostratigraphy in Wu et al., (2017).

Polarity subchron	Lower boundary age (Ma)	Depth (mcd) Upper	Sed. Acc. Rate (cm/kyr)
C1n (Brunhes)	0.781	42.37	5.43
C1r.1r (Matuyama)	0.988	50.12	3.74
C1r.1n (Jaramillo)	1.072	54.19	4.85
C1r.2r	1.173	–	
C1r.2n (Cobb Mountain)	1.185	–	
C1r.3r	1.778	85.13	5.22
C2n (Olduvai)	1.945	91.69	3.93
C2r.1r	2.128	–	
C2r.1n (Reunion)	2.148	–	
C2r.2r (Matuyama)	2.581	119.41	6.40
C2An.1n (Gauss)	3.032	134.68	3.39
C2An.1r (Kaena)	3.116	–	
C2An.2n	3.207	140	5.85
C2An.2r (Mammoth)	3.33	144.59	3.73
C2An.3n (Gauss)	3.596	154.42	3.70
C2Ar (Gilbert)	4.187	171.14	2.83
C3n.1n (Cochiti)	4.3	174.94	3.36
C3n.1r	4.493	180.84	3.06

CHAPTER 5. SUMMARY

“Temporal relations are the key to causality arguments in Earth’s history” (Westerhold et al., 2012). “With the acceptance of a reliable time scale, geology will have gained an invaluable key to further discovery. In every branch of science its mission will be to unify and correlate, and with its help a fresh light will be thrown on the more fascinating problems of the Earth and its Past.” (— Arthur Holmes, 1913, *The Age of the Earth*)

Quotes from these two great geologists manifest the importance and necessity of geologic time scale construction throughout the Earth’s history. Among the multiple stratigraphic tools used to establish a geologic time scale, the combination of magnetostratigraphy and cyclostratigraphy have proved to be one of the most powerful strategies, especially for more continuously exposed sedimentary successions.

Chapter I give a brief introduction of the philosophy of building a geologic time scale and the two stratigraphical tools that have been utilized for the PhD research. Specifically, the background of each time interval of interest is also summarized.

Chapter 2 The Carnian time scale

The highlights of the Carnian paper could be summarized as below:

1. The geomagnetic polarity time scale for the entire Carnian is established
2. Onset of the humid Carnian Pluvial Episode (CPE) is coeval worldwide
3. Newark Basin magnetic polarity series begin at about 20% up in Late Carnian
4. The ca. 231 Ma ash bed in S. Italy is above a second humid interval

Chapter 3 The Age of the Barremian-Aptian Boundary

The novelties and significance of the Barramian-Aptian paper are:

1. Unifying the mag-strat, bio-start, and radiometric ages all on one section (Svalbard core), reducing many of the ambiguities of OAE1a and Stage boundary from global correlations
2. Resolving the age of the base Chron M0r (proposed to be the base Aptian) to be at 121.2 ± 0.4 Ma, ca. 5 myr younger compared to GTS212
3. Revising the earlier-published astrochronology of the Piobbico core, which confirms a shorter Aptian Age of ca. 8 myr compared to 13 myr

4. Merging the post-2012 radiometric dates with magnetostratigraphy, biostratigraphy, and cyclostratigraphy for the Aptian, which could be used to calibrate the entire M-sequence and the sea floor spreading rates
5. To calibrate the evolution of dinosaurs and the earliest birds to events and environmental-trends in the marine record.

Chapter 4 Quaternary time scale and Mid-Pleistocene Transition

The highlights of the Quaternary paper include:

1. Visit the Table of Contents that is currently in this document.
2. First astronomical-tuned magnetostratigraphy from South China Sea (SCS) IODP cores
3. Lower accumulation rates during late Zanclean, early Gelasian and early Calabrian
4. Mid-Brunhes Event (500 ka) marks the onset of major coarser-grained clastic input
5. Astronomical-tuned NGR events correlate to global benthic foraminifer $\delta^{18}\text{O}$ curve
6. Apparent synchronous sediment accumulation trends in northern and southern SCS.

In brief, the combination of cyclo-and-magnetostratigraphy succeeds in constructing a high-resolution cycle-scaled time scale and thus helps put the geologic and climate events (Carnian Pluvial Episode, Cretaceous OAEs, and major Quaternary paleoclimate shifts etc.) back to a reasonably correct chronological order, which allows a better understanding of the underlying cause and effect. Integration with other stratigraphy tools, such as radiometric dating, biostratigraphy, geochemistry etc., is also necessary especially when astronomical signals are ambiguous and when rocks/sediments get re-magnetized.

VITA

Yang (Wendy) Zhang

Department of Earth, Atmospheric & Planetary Sciences, Purdue University
550 Stadium Mall Drive, West Lafayette, IN 47907-2051

<https://scholar.google.com/citations?user=tZKN7tMAAAAJ&hl=en>

Professional Preparation

China University of Geosciences Wuhan, China Marine Science M.S. 2015

Ocean University of China Qingdao, China Environmental Engineering B.S. 2012

Appointments

Academic:

2015-2019- Doctoral student, Purdue University, West Lafayette, IN (to complete Fall 2019)

2019 Fall/Spr, 2018 Spring, 2017 Fall and 2016 Fall/Spr Teaching assistant in undergraduate courses (EAPS 100,111 and 112; and three times EAPS 301 OIL!)

2018 Spring/Summer Guest lectures in Southeast Asia special course

2016 Spring Research assistant assembling public databases of China stratigraphy (<https://engineering.purdue.edu/Stratigraphy/tscreator>)

2014 Summer Teaching assistant for Integrated Stratigraphy workshop (under Profs. Linda Hinnov and James Ogg)

International Ocean Drilling Program:

2020, Jan-Mar (confirmed) USA NSF-supported paleomagnetist, IODP Expedition 378 (South Pacific Paleogene Climate)

2017, Feb-Apr USA NSF-supported paleomagnetist, IODP Expedition 367-368 (South China Sea)

Publications

Peer Reviewed Publications

Yang Zhang, James G. Ogg, Matthias Franz, Gerhard H. Bachmann, Michael Szurlies, Heinz-Gerd Röhlings, Christian Rolf, and Karsten Obst, in review. Carnian Magnetostratigraphy from the Germanic Basin and global correlation of the Carnian Pluvial Episode – (*Earth and Planetary Science Letters* to be resubmitted with incorporation of the requested revisions)

- Yang Zhang, James G. Ogg, Daniel Minguetz, Mark W. Hounslow, Snorre Olausen, Felix M. Gradstein, and Selen Esmeray-Senlet, in review. Magnetostratigraphy of U/Pb-dated boreholes in Svalbard, Norway, implies that the Barremian–Aptian boundary (beginning of Chron M0r) is 121.2 ± 0.4 Ma – (*Geology to be resubmitted with incorporation of the requested revisions*)
- Yan Chen, Haishui Jiang, James G. Ogg, Yang Zhang, Yifan Gong, Chunbo Yan, in-review. Early-Middle Triassic Boundary Interval: Integrated chemo-bio-magneto-stratigraphy of potential GSSPs for the base of the Anisian Stage in South China (*accepted by EPSL after incorporation of minor revisions*)
- Yang Zhang, Liang Yi, James G. Ogg, Pliocene-Pleistocene magneto-cyclostratigraphy of IODP Site U1499 and implications for climate-driven sedimentation in the northern South China Sea, *Palaeogeography, Palaeoclimatology, Palaeoecology* 527: 118-132.
- Mingsong Li, Chunju Huang, James Ogg, Yang Zhang, Linda Hinnov, Huaichun Wu, Zhong-Qiang Chen, Zhuoyan Zou, 2019. Paleoclimate proxies for cyclostratigraphy: Comparative analysis using a Lower Triassic marine section in South China. *Earth-Science Reviews*, 189: 125-146.
- H. C. Larsen*, G. Mohn*, M. Nirrengartenb, Z. Sun, J. Stock, Z. Jian, C. Alvarez-Zarikian, J. Boagag, S.A. Bowden, A. Briais, Y. Chen, D. Cukur, K. Dadd, W. Ding, M. Dorais, E. Ferre, F. Ferreira, A. Furusawa, A. Gewecke, J. Hinojosa, T. Hoefig, K. Hsiung, B. Huang, E. Huang, X.Huang, S. Jiang, H. Jin, B. Johnson, A. Klaus, R. Kurzwanski, C. Lei, B. Li, L. Li, Y. Li, J. Lin, C. Liu, C. Liu, Z. Liu, A. Luna, C. Lupi, A. McCarthy, L. Ningthoujam, N. Osono, D. Peate, P. Persaud, N. Qiu, C. Robinson, S. Satolli, I. Sauerlich, J. Schindlbeck, S. Skinner, S. Straub, X. Su, C. Su, L. Tian, F. van der Zwan, S. Wan, H. Wu, R. Xiang, R. Yadav, L. Yi, P., C. Zhang, J. Zhang, Y. Zhang, N. Zhao, G. Zhong, L. Zhong, 2018. Rapid transition from continental breakup to igneous oceanic crust in the South China Sea, *Nature Geoscience* 11(10): 782.
- Sun, Z., Jian, Z., Stock, J.M., Larsen, H.C., Klaus, A., Alvarez Zarikian, C. A., and Scientists, T.E., 2018, South China Sea Rifted Margin: *Proceedings of the International Ocean Discovery Program*, 367/368: College Station, TX (International Ocean Discovery Program). (I sailed as an onboard paleomagnetist)

- Dal Corso, J., Benton, M., Bernardi, M., Franz, M., Gianolla, P., Hohn, S., . . . Zhang, Y. (2018). First workshop on the Carnian Pluvial Episode (Late Triassic): A report: *Albertiana*, v. 44, p. 49-57.
- Mingsong Li, Yang Zhang, Chunju Huang*, James Ogg, Linda Hinnov, Yongdong Wang, Zhuoyan Zou, Liqin Li, 2017. Astronomical tuning and magnetostratigraphy of the Upper Triassic Xujiahe Formation of South China and Newark Supergroup of North America: implications for the Late Triassic time scale, *Earth and Planetary Science Letters* 475: 207-223.
- Shi, Z., N. Preto, H. Jiang, L. Krystyn, Y. Zhang, J. G. Ogg, X. Jin, et al, 2017, Demise of Late Triassic sponge mounds along the northwestern margin of the Yangtze Block, South China: Related to the Carnian Pluvial Phase? *Palaeogeography, Palaeoclimatology, Palaeoecology* 474: 247-263.
- Mingsong Li, James G. Ogg, Yang Zhang, Chunju Huang*, Linda Hinnov, Zhong Qiang Chen, and Zhuoyan Zou, 2016, Astronomical tuning of the end-Permian extinction and the Early Triassic Epoch of South China and Germany, *Earth and Planetary Science Letters* 441: 10-25
- Mingsong Li, Linda Hinnov*, Chunju Huang*, Zhong-Qiang Chen, James Ogg, and Yang Zhang, 2016, Obliquity-forced climate during the Early Triassic hothouse in China, *Geology*, 44(8): 623-626.
- Yang Zhang, Mingsong Li, James G. Ogg*, Paul Montgomery, Chunju Huang, Zhong-Qiang Chen, Zhiqiang Shi, Paul Enos, Daniel J. Lehrmann, 2015. Cycle-calibrated magnetostratigraphy of middle Carnian from South China: Implications for Late Triassic time scale and termination of the Yangtze Platform. *Palaeogeography, Palaeoclimatology, Palaeoecology* 436: 135-166.
- Papers in preparation:*
- Yang Zhang, Yan Chen, James Ogg, Mingsong Li, Haishui Jiang, ZhongQiang Chen, Early Triassic scaling enhanced by cycle-scaled magnetostratigraphy from South China. (*Data analysis completed, presented at GSA and Wuhan conferences, to be submitted*)
- Jean Self-Trial, Yang Zhang, David Powars, James G. Ogg, Marci Robinson et al., Hyperthermals recorded in eastern coast of US evidenced by high-resolution bio-magnetostratigraphy, *presented at CBEP 2017 (Utah) and GSA annual meeting 2019.*

Yang Zhang, Eocene-Oligocene Transition Recorded in the South China Sea evidenced by the Time-calibrated Magnetostratigraphy.

On-going projects:

01/1/2019 – 12/31/2019 Open Project Proposal 2019 funded by the State Key Laboratory of Marine Geology (Tongji University) (PI)

Conference presentations (since 2015):

Yang (Wendy) Zhang, James G. Ogg, Daniel Minguez, Mark W. Hounslow, Snorre Olausen, Felix M. Gradstein, and Selen Esmeray-Senlet, Magnetostratigraphy of U/Pb-dated boreholes in Svalbard, Norway, implies that the Barremian–Aptian boundary (beginning of Chron M0r) is 121.2 ± 0.4 Ma [Oral; Abstract submitted to AGU Fall meeting 2019]

James G. Ogg, Yang (Wendy) Zhang (presenter), Felix M. Gradstein, Andy Gale, Frits Agterberg, Daniel Minguez, Mark W. Hounslow, Snorre Olausen, and Selen Esmeray-Senlet, Revised M-sequence of Late Jurassic through Early Cretaceous Polarity Chrons Based on New U-Pb Dates and Cyclostratigraphy [Poster; Abstract submitted to AGU Fall meeting 2019]

Yang (Wendy) Zhang, Daniel Minguez, James Ogg, Snorre Olausen, the Geological Society of America 130th Annual Meeting 2018, Magnetostratigraphy across U-Pb-Dated Horizons in Svalbard Boreholes to Partly Resolve the Debated Age of Barremian/Aptian Boundary [Oral]

Yang (Wendy) Zhang, May 2018. Applying Cycle-scaled magnetostratigraphy for global correlation and time scales of paleoclimatic events in the Triassic, Eocene and Quaternary. South China Sea Institute Of Oceanology (Guangzhou, China) [invited talk]

Yang (Wendy) Zhang, April 2017. Ocean drilling cruise to the South China Sea and my “Chocolate” life. Chengdu University of Technology (Sichuan, China) [invited talk]

Mingsong Li, Yang (Wendy) Zhang, James Ogg, Linda Hinnov, Chunju Huang, Zhong-Qiang Chen, 2017. Triassic Time Scale from Astronomical-tuned Magnetostratigraphy. GSA Annual Meeting 2017 in Seattle, US [Oral]

Yan Chen, Yang (Wendy) Zhang, James Ogg, Mingsong Li, Zhong-Qiang Chen, Chenyi Tu, Daoliang Chu, 2017. Magnetostratigraphy of the Continental Reference Section for Latest Permian Through Early Triassic of North China at Dayulin (Henan Province). GSA 2017 in Seattle, US [Oral]

- Jean Self-Trial & Yang (Wendy) Zhang, David S. Powars, James G. Ogg, and Megan K. Fung, 2017. A Very (Very) Preliminary Chronostratigraphic Framework of an Expanded and Structurally Controlled Early Eocene Section from the Knapps Narrows Core, Salisbury Embayment, USA, Climatic and Biotic Events of the Paleogene (CBEP) 2017 in Utah, US [Poster]
- James Ogg and Yang (Wendy) Zhang, 2017. Cycle Calibrated Magnetostratigraphy of the Carnian and Implications for the Global Coincidence of the Carnian Humid Episode. Workshop on The Carnian Pluvial Episode (Late Triassic): Climate Change and Evolutionary Innovations, Institute for Advanced Study in Delmenhorst, Germany [Oral]
- Yang (Wendy) Zhang, Mingsong Li, James Ogg, Linda Hinnov, Chunju Huang, Zhong-Qiang Chen, 2016. Applying cycle-calibrated magnetostratigraphy for time scales and correlation of major climate excursions of the Early and the early-Late Triassic. 35th International Geological Congress in Cape Town, South Africa [Oral]
- Yang Zhang, James Ogg, Mingsong Li, et al, 2015. Cycle-calibrated Magnetostratigraphy of middle Carnian from South China: Implications for Late Triassic Time Scale and Termination of the Yangtze Platform. GSA Annual Meeting 2015 in Baltimore, US [Oral]
- Yang Zhang, Mingsong Li, James G. Ogg, Paul Montgomery, Chunju Huang, Zhong-Qiang Chen, Zhiqiang Shi, et al, 2015. Cycle-calibrated Magnetostratigraphy of middle Carnian from South China, State Key Laboratory of Biogeology and Environmental Geology Academic Forum. Wuhan, China. [Oral]

Field and Lab Experiences

- 2019/03 and 2016/03 Field Geology in North America –Big Bend National Park and Death Valley, respectively (led by Prof. Kenneth Ridgeway)
- 2018 Summer Field work: magnetostratigraphy for Late Triassic in Sichuan Province, China
- 2017 Summer Field work: cyclostratigraphy and magnetostratigraphy for Early Triassic in Sichuan Province, China.
- 2016/08 Two-week Field Excursion on Permian-Triassic in Karoo Basin, South Africa
- 2016/05-07 Field-work: Late Triassic cyclostratigraphy and magnetostratigraphy, Guizhou Province, South China
- 2015/09 Workshop “Sedimentary cycles and Geologic time: A cyclostratigraphy (work) excursion to Sicily”, Italy

2015/09 Field-work: Terrestrial Triassic cyclo-magnetostratigraphy in Grubenhagen core repository (managed by LBEG Hannover) and Sternburg core repository (managed by LUNG M-V), Germany.

2015/05-06 Field-work: Early and Middle Triassic cyclo-magnetostratigraphy, Guizhou Province, SW China (two field sessions)

2015/04 Field-work: Early Triassic magnetostratigraphy, Anhui Province, Central China.

2012/10 to 2014/06 Field-work: Extensive Triassic cyclostratigraphy, South China

Since 2014 Because Purdue University does not have a paleomagnetic lab, I did my paleomagnetism measurements in several other Paleomagnetic labs, including:

Black Mountain Paleomagnetism Laboratory (Australian National University, Canberra)

Paleomagnetism Lab in Lehigh University (hosted by Prof. Kenneth Kodama)

Beijing's China University of Geoscience (hosted by Prof. Huaichun Wu)

Beijing's Chinese Academy of Science (hosted by Prof. Zhiming Sun)

University of Texas at Dallas (hosted by Prof. John Geissman)

Lancaster University (UK, hosted by Dr. Mark Hounslow)

Tongji University (Shanghai, hosted by Prof. Xixi Zhao)

Kirschvink Laboratory at Caltech (hosted by Prof. Joe Kirschvink)

Grubenhagen lab (BGR Germany, hosted by Dr. Christian Rolf)

Awards

2018/Spring EAPS Michael C. Gardner Memorial Award

2018/06 Urbino Summer School in Paleoclimatology (USSP) funded by the U.S. Graduate Student Scholarships

2017/09 Travel Grant from Department of Earth, Atmospheric & Planetary Sciences, Purdue Univ. to attend the Climatic and Biotic Events of Paleogene in Utah

2017/08 to 2018/08 Post-Expedition Award of serving as a paleomagnetist on IODP Expedition 367

2018/Spring EAPS Cedric J. Newby Scholarship and Donald W. Levandowski Memorial Scholarship in Geology

2016/03 Travel Grant from the Geological Society of America Foundation to the 35th International Geological Congress (IGC) in South Africa

2016/05 Travel Grant from Department of Earth, Atmospheric & Planetary Sciences, Purdue Univ.

2015/11 Travel Grant by Women in Science Programs and College of Science

2015/09-2017/05 Fellowship for the initial two years of PhD research at Purdue University, Indiana, USA (from Geologic TimeScale Foundation).

Synergistic Activities

Spring 2018 Guest lectures in Southeast Asia special course; besides TA for Sedimentary and Stratigraphy course.

2017/09 Departmental outreach event: AP Environmental Science class on campus learning about Soils

Fall 2017 Teaching assistant in an undergraduate lecture (EAPS 100 Planetary and Earth Sciences)

2017/02-04 Serving as a paleomagnetist on IODP Expedition 367 at South China Sea

Fall 2016 Teaching assistant in an undergraduate lecture (EAPS 301 OIL!)

2016/05 Assembling databases of China stratigraphy to support the Geologic Time Scale development (<https://engineering.purdue.edu/Stratigraphy/tscreator/index/index.php>)

2014/06 Teaching assistant in the Integrated Stratigraphy workshop in my Masters' university lectured by Dr. Linda Hinnov (George Madison University) and my current advisor (Dr. Jim Ogg)

Relevant Courses

Masters (09/2012-06/2015, China University of Geosciences in Wuhan, China)—

Basin Geodynamics/Marine Resources/Advances in Marine Science/Sedimentary Geology/Biogeology/Isotope Geochemistry

PhD (Purdue University, Fall 2015 to Spring 2019)—

- Fall 2015/Spring 2016 Triassic Stratigraphy/ Field Course in Climate Cycles/ Computer - Analysis in Geosciences/Field Geology in North America (Death Valley)/Paleomag and Magstrat

- Fall 2016/Spring 2017 South China Sea Geology (Participation on IODP Expedition 367)

- Fall 2017 SE Asia Geology, Climate & Oil

- Spring 2018 Field Geology in North America (Utah)

- Spring 2019 Basin Analysis/Field Geology in North America (Big Bend National Park)

- Fall 2019 Geologic Dating Methods